
NEW DEVELOPMENTS AND TECHNIQUES
IN RADIO TO X-RAY OBSERVATIONS OF AGN

NEUE ENTWICKLUNGEN UND TECHNIKEN
ZUR BEOBACHTUNG VON AGN IM RADIO- BIS RÖNTGENBEREICH

Der Naturwissenschaftlichen Fakultät
der Friedrich-Alexander-Universität Erlangen-Nürnberg
zur Erlangung des Doktorgrades Dr. rer. nat.
vorgelegt von

Christoph Großberger

aus Nürnberg



ERLANGEN CENTRE
FOR ASTROPARTICLE
PHYSICS



FRIEDRICH-ALEXANDER
UNIVERSITÄT
ERLANGEN-NÜRNBERG

NATURWISSENSCHAFTLICHE
FAKULTÄT

Als Dissertation genehmigt
von der Naturwissenschaftlichen Fakultät
der Friedrich-Alexander-Universität Erlangen-Nürnberg

Tag der mündlichen Prüfung:

19.09.2014

Vorsitzender des Promotionsorgans:
Gutachter:

Prof. Dr. Johannes Barth
Prof. Dr. Jörn Wilms
Prof. Dr. Eduardo Ros

Abstract

I present my work related to the most luminous persistent sources in the known Universe – Active Galactic Nuclei (AGN). The term AGN refers to the central “active” region of a galaxy which can be very bright and even outshine their host galaxy. We typically observe these objects across the whole electromagnetic spectrum (from radio to γ -rays).

In our current understanding of AGN a supermassive black hole resides in the center of each galaxy, with typical masses on the order of millions of solar masses. This black hole is thought of as the engine powering the AGN and is “fueled” by surrounding material (dust and gas). The strong gravitational field of the black hole causes the material to be accreted, where accretion is a highly efficient process which converts the gravitational potential energy of material into radiation. Due to the conservation of angular momentum the material will not accrete directly onto the black hole, building instead an accretion disk. The accretion mechanisms explain most of the observed emission from AGN. However, observations show that the radio emission and parts of the high energy emission originate from jets. Jets are highly relativistic collimated outflows perpendicular to the accretion disk, which can reach velocities close to the speed of light. With radio interferometers we can create highly resolved images of these jets, reaching spatial resolutions on the sub-lightyear scale. Evolutionary studies show traceable features in these jets, with apparent motion faster than the speed of light which can be explained by relativistic Doppler boosting. The phenomenon of AGN is not fully understood and many questions remain such as the detailed physics of the accretion process, underlying physical processes for the emission at various wavelength, the evolution of AGN, or the launching, formation, and composition of the jets.

The eROSITA instrument on-board the future mission *Spektrum-Roentgen-Gamma* (SRG), will address some of these questions by an all-sky survey in the soft X-rays. For eROSITA I developed and implemented necessary data processing steps prior the Near Real Time Analysis (NRTA) and the Science Analysis Software System (SASS). The data processing is split into multiple parts such as the conversion of binary telemetry data streams to FITS files, the merging and splitting of these, and archiving tasks.

With Very Long Base Interferometry (VLBI) I studied the structural evolution of the jet in 3C 111 during 2007 and 2012.5. I found the ejection of multiple ballistic components associated with outbursts in the lightcurve at mm wavelengths. The number of ballistic components appear to be correlated to the strength of these outbursts. The ballistic components can usually be traced a short period of time before vanishing or a change in their trajectory is observed.

In a second source study I analyzed the flux density evolution in the structure of the jet in 3C 84 at various wavelengths. Based on the long-term radio lightcurves an increase in flux density is observed since 2008 and rapidly increasing since early 2011. I find that the flux density is not increasing in the core region, which is constant, but rather in the southern region ~ 2 mas away from the core. Using simultaneous observations at

24 GHz and 43 GHz I could determine the frequency core shift. I can also confirm the limb-brightened structure seen in a previous study of the source.

Furthermore I present a new software package which I developed to overcome the shortcomings of the typical software used for model fitting the VLBI data, DIFMAP. I show that we are able to reproduce the fits produced by DIFMAP or find even better fits. I demonstrate the possibilities for a thorough error analysis in the new software package. Moreover, I show that one can simultaneously fit models to multiple VLBI data sets at once based on an example kinematic analysis of a source from the MOJAVE program. I was able to reproduce the established apparent motions. Investigation of the uncertainties revealed a strong correlation between the vector speed parameter and the ejection time in the ballistic model, demonstrating the need for an in-depth error analysis.

Zusammenfassung

Ich stelle meine Arbeit zu den leuchtstärksten und durchgehend beobachtbaren Quellen im Universum vor – Aktive Galaktische Kerne (AGN). Unter dem Begriff AGN versteht man die “aktive” Region im Zentrum einer Galaxie, die so hell ist, dass sie sogar ihre Wirtsgalaxie überstrahlen kann. In der Regel können wir diese Objekte im gesamten elektro-magnetischen Spektrum (von Radio- bis Gammastrahlung) beobachten.

Nach heutigem Erkenntnisstand über AGN befindet sich ein supermassives schwarzes Loch, dessen Masse im Bereich von ein paar Millionen Sonnenmassen liegt, im Zentrum einer jeden Galaxie. Man kann dieses schwarze Loch als eine Art “Motor” für die AGN verstehen, der Staub und Gas aus der Umgebung als “Treibstoff” verwendet. Durch das starke Gravitationsfeld des schwarzen Loches wird Materie akkretiert. Akkretion ist ein hocheffizienter Prozess bei dem die potentielle Gravitationsenergie von Materie in Strahlung umgewandelt wird. Die Materie wird jedoch aufgrund der Drehimpulserhaltung nicht direkt auf das schwarze Loch akkretiert sondern bildet eine Akkretionsscheibe. Der Großteil der beobachteten Emission von AGN kann durch diese Akkretion erklärt werden. Die Radio- und ein Teil der hochenergetischen Strahlung jedoch stammt von Jets. Jets sind hochrelativistische, gebündelte Teilchenausflüsse, senkrecht zur Akkretionsscheibe, die Geschwindigkeiten bis hin zur Lichtgeschwindigkeit erreichen können. Mit Hilfe von Radiointerferometrie kann man hochaufgelöste Bilder, mit einer Auflösung im Bereich von Lichtjahren, dieser Jets erzeugen. Studien der Entwicklung zeigen verfolgbare Komponenten im Jet mit scheinbarer Überlichtgeschwindigkeit, die sich durch den relativistischen Doppler Effekt erklären lassen. Das Phänomen der AGN ist noch nicht vollständig geklärt und viele Fragen zum Akkretionsprozess, zu den zugrundeliegenden physikalischen Prozessen bei verschiedenen Wellenlängen, zur Entwicklung von AGN, der Entstehung und Komposition von Jets, bleiben bestehen.

Einige dieser Fragen soll mit dem eROSITA Instrument, in dem man den gesamten Himmel im weichen Röntgenbereich studiert, auf der Mission *Spektrum-Roentgen-Gamma* (SRG) geklärt werden. Ich habe die wichtige Datenprozessierung für die zeitnahe Analyse Software (Near Real Time Analysis – NRTA) und der wissenschaftlichen Analyse Software (SASS) des eROSITA Instruments entwickelt und implementiert. Die Prozessierung der Daten ist dabei in mehrere Bereiche unterteilt: die Umwandlung des binären Telemetrie-Datenstroms in das FITS Dateiformat sowie in Folge deren Gruppierung, Aufteilung und Archivierung.

Ich habe die strukturelle Entwicklung des Jets in 3C 111 zwischen 2007 und Mitte 2012 mit interferometrischen Beobachtungen, bei der die Entfernung zwischen den Teleskopen sehr groß ist (VLBI), studiert. Ich konnte die Entstehung von ballistischen Komponenten mit Ausbrüchen in der mm Lichtkurve assoziieren. Die Anzahl der ballistischen Komponenten scheint mit der Stärke der Ausbrüche korreliert zu sein. Typischerweise kann man diese ballistischen Komponenten nur für eine kurze Zeit verfolgen, bevor diese entweder verschwinden oder man eine Veränderung ihrer Trajektorie beobachtet.

In einer zweiten Studie habe ich die Entwicklung der Flussdichte des Jets in 3C 84 bei verschiedenen Wellenlängen analysiert. Die Langzeit-Lichtkurve zeigt einen Zuwachs der Flussdichte seit 2008, der seit 2011 stärker geworden ist. Ich habe herausgefunden, dass der Flussdichte-Zuwachs nicht in der Kern-Region, die einen konstanten Wert in dieser Zeit hatte, stattgefunden hat, sondern in der ~ 2 mas entfernten, südlichen Region. Basierend auf simultanen Beobachtungen bei 24 GHz und 43 GHz habe ich die frequenzabhängige Verschiebung der Kern-Region bestimmt. Zusätzlich konnte ich die bereits in einer früheren Studie beobachtete Randaufhellung des Jets bestätigen.

Außerdem präsentiere ich ein neues Software-Paket, das die Unzulänglichkeiten der etablierten Software (DIFMAP) zur Entwicklung von Modellen für VLBI-Daten behebt. Wir sind damit in der Lage, die mit DIFMAP gefundenen Modelle zu reproduzieren oder auch Bessere zu finden. Ich zeige die Möglichkeiten einer genauen Fehlerberechnung mit diesem Software-Paket. Außerdem demonstriere ich die Option einer simultanen Anpassung eines Modells an mehrere VLBI Datensätze am Beispiel der kinematischen Analyse einer Quelle aus dem MOJAVE-Programm. Ich bin in der Lage, die bereits etablierten Geschwindigkeiten in dieser Quelle zu reproduzieren. Eine Untersuchung der Unsicherheiten zeigt eine starke Korrelation zwischen der Vektor-Geschwindigkeit und dem Zeitpunkt der Entstehung im ballistischen Modell, welches den Bedarf einer tiefergehenden Fehleranalyse unterstreicht.

Contents

1	Introduction	1
1.1	AGN	1
1.2	Historical overview	2
1.3	Structure	4
1.4	Classification	5
1.5	Unification	8
1.6	Accretion Disk	9
1.7	Broad Line Region	12
1.8	Jets	12
1.9	The importance of multiwavelength observations	21
1.10	Evolution of AGN	23
2	eROSITA	25
2.1	Mission and Design	25
2.2	Data processing	30
2.3	Pre-processing	34
3	VLBI	45
3.1	Fundamentals of Radio Interferometry	46
3.2	Data analysis	50
3.3	Advanced model fit options for VLBI data	56
4	Kinematics of the jet in 3C 111	73
4.1	Source overview	73
4.2	Radio lightcurves	75
4.3	VLBI observations	77
4.4	Model fitting and identification	80
4.5	Summary & Outlook	113
5	Multi-frequency evolution study of the jet in 3C 84	115
5.1	Source overview	115
5.2	Data & Fit	118
5.3	Morphology	119
5.4	Light curves	124
5.5	Discussion	127
A	Tables for Chapter 3.3	135
A.1	Model parameters and uncertainties	135
A.2	Comparison of model parameter uncertainties with conservative estimates	136

1 Introduction

The term AGN, short for Active Galactic Nucleus, refers to an object with a size smaller than our solar system. It is located in the central regions of galaxies and harbors a super-massive black hole (SMBH) typically a million times more than our sun. This black hole devours everything from the smallest particle up to stars. This region is a very violent place. Intense electromagnetic fields are formed even stronger than everything we can artificially create on earth. Particles get accelerated close to the speed of light and emission over the whole electromagnetic spectrum is produced. Therefore it is no surprise that AGN are hosts of a variety of different energetic phenomena and can even outshine the rest of its host galaxy.

Chapter 1.1 gives an introduction to AGN theory and phenomenology. The second section gives an overview of future X-ray instrument eROSITA (extended ROentgen Survey with an Imaging Telescope Array) on-board the mission *Spektrum-Roentgen-Gamma* (SRG). It is designed to answer the questions on the topic of cosmology but is also a great instrument to discover nearly all AGN visible on the X-ray sky. The main focus in this chapter is about the necessary data processing steps before the data can be even used for analysis. Chapter 3 starts with an introduction to the Very Long Baseline Interferometry (VLBI) technique which can reveal the jet structures in AGN. The chapter is concluded with an introduction to a new analysis technique which can be used in future source studies using VLBI data. I next discuss the individual sources studies of the objects 3C 111 and 3C 84. The jet in 3C 111, typically known for its superluminal features and trailing components, is discussed in the context of strong outbursts in the radio regime while the focus of the study of 3C 84 is on the connection to the outbursts in the γ -regime.

1.1 AGN

Active Galactic Nuclei are among the most fascinating objects in the universe and significant effort has been put into studying them (more than 10000 publications in the

ADS database¹ with the title consisting of the keywords AGN or active galactic nucleus/nuclei). Based on this high number of publications AGN are evidently interesting to continue to study. Yet even giving the definition of an AGN is not as easy it seems. A suitable definition is given in [Peterson \(1997\)](#):

“... the term active galactic nucleus, or AGN, refers to the existence of energetic phenomena in the nuclei, or central regions, of galaxies which cannot be attributed clearly and directly to stars.”

1.2 Historical overview

The story of AGN is quite a brief one in the history of Astronomy. It began only a little over 100 years ago with the discovery of the first AGN by [Fath \(1909\)](#), who reported on bright emission lines in the spectrum of NGC 1068. At that time neither the term AGN was used nor was it known that the observed object was indeed of extragalactic origin. [Curtis \(1918\)](#) was the first to actually image an AGN (M87) and described the optical jet by

curious straight ray lies in the nebulosity in P.A. (position angle) 20° apparently connected with the nucleus by a thin line of matter. The ray is brightest at the inner end, which is $11''$ from the nucleus

An image of the jet in M87 by the Hubble Space Telescope (HST) in the optical is shown in Fig. 1.1. A little bit more than a decade after Fath, [Hubble \(1929\)](#) found the first indications for an expanding Universe by investigating the relation between distance and radial velocity among extra-galactic “nebulae”. To honor his work the constant describing this expansion is now named Hubble’s constant. In the work of [Seyfert \(1943\)](#) a similarity of the emission in the nuclei of six “extragalactic nebulae” with planetary and gaseous nebulae was reported. The reported properties of the optical spectra in this paper led to the now-established optical classification of AGN into Seyfert 1 and Seyfert 2 galaxies. In 1954 [Baade & Minkowski](#) identified the radio source Cygnus A with a magnitude 18 galaxy, making this the first detected radio galaxy. Using a balloon experiment as a transport vessel for their instruments, [Giacconi et al. \(1962\)](#) discovered the cosmic X-ray background (CXRb). One year later [Schmidt \(1963\)](#) shed light into the mystery of unknown spectral lines in the optical counterparts of radio sources. Using observations of the source 3C 273 during a lunar eclipse by [Hazard et al. \(1963\)](#), the object could be resolved into two components. One of these coincided with the position of a star, for which Schmidt obtained spectra and realized that the unknown lines were the reminiscent lines of the Balmer series of hydrogen but at a redshift of $z = 0.16$. Afterwards the term quasar, i.e., “quasi stellar radio source” was introduced by [Schmidt & Matthews \(1964\)](#) to describe this type of object. This term is still used today. A general implication of this discovery was that these objects have to have a high intrinsic luminosity but no known process at that time could explain it. Already one year afterwards [Salpeter \(1964\)](#) and [Zel’dovich & Novikov \(1964\)](#) independently proposed the mechanism of accretion onto a

¹<http://www.adsabs.harvard.edu>

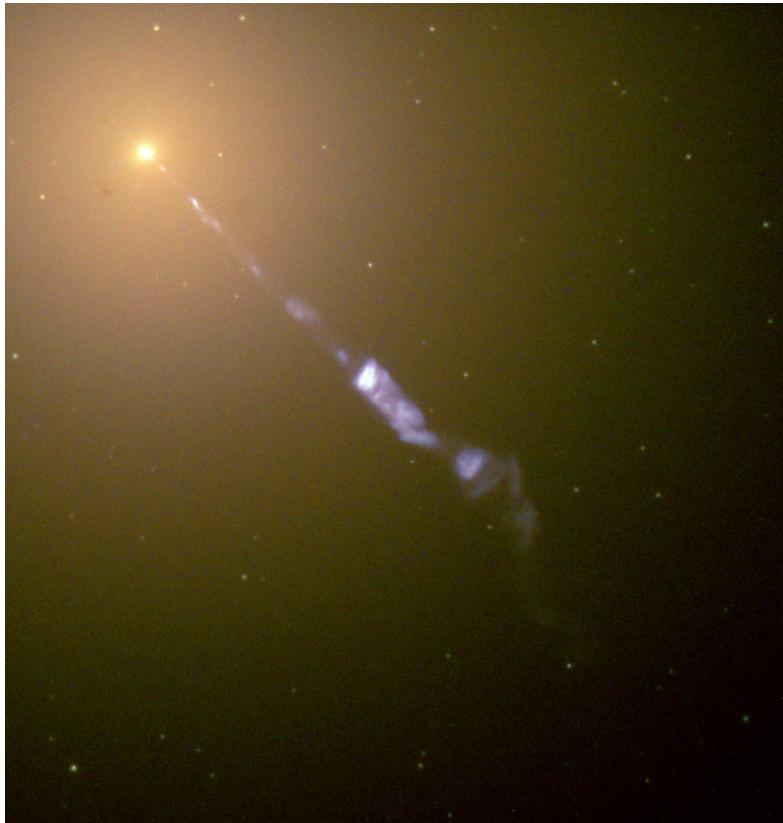


Figure 1.1: The jet of M87 (rotated by 90°, counter-clockwise) in the optical by the Hubble Space Telescope (HST). (Credit: J. A. Biretta et al., Hubble Heritage Team, NASA)

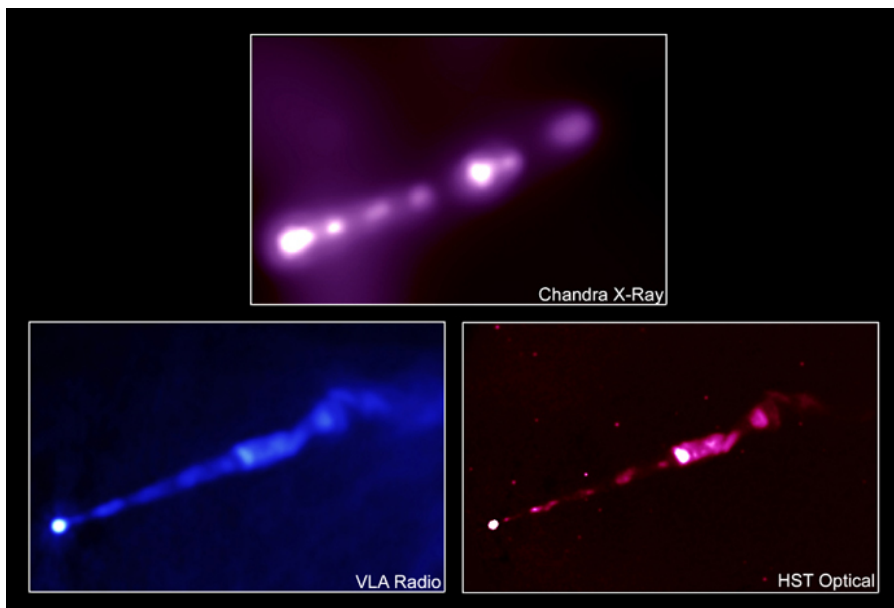


Figure 1.2: The jet of M87 is visible across the electromagnetic spectrum. (Credit: X-ray: NASA/CXC/MIT/H.Marshall et al. Radio: F. Zhou, F.Owen, J.Biretta, Optical: NASA/STScI/UMBC/E.Perlman et al.)

massive object, requiring the mass to be in the order of millions of solar masses or more to explain the luminosities. The dimension of these regions were estimated to be on the order of milliarcseconds based on arguments of light travel times and AGN showing radio variability on timescales of months (Dent, 1965; Sholomitskii, 1965). The development of a technique called VLBI, using magnetic tapes to store the signal of radio telescopes and later correlating these and thus building an artificial interferometer, allowed to analyze sources at these scales. One of the first to report on observations of AGN with VLBI were Cohen et al. (1968). This method quickly led to the discovery of apparent superluminal motion in the sources 3C 273 and 3C 279 by Cohen et al. (1971) and Whitney et al. (1971). At about the same time the first X-ray satellite *Uhuru* (e.g., Giacconi et al., 1972) revealed the isotropic nature of the cosmic X-ray background (CXRb), which led to the conclusion of its extragalactic origin. Swanenburg et al. (1978) were one of the first to report on the discovery of γ -rays from an AGN. This was followed by the discovery that the soft CXRB could be resolved into discrete sources, which could be associated with AGN (Giacconi et al., 1979). More detailed information about the history of AGN and their discoveries can be found in Shields (1999) and Kellermann (2013).

1.3 Structure

AGN are highly luminous objects with typical luminosities of $10^{10} L_{\odot}$ (Baade & Minkowski, 1954) which outshine their host galaxies on a regular basis. They sources show variability on timescales of days to decades and emission over the whole electromagnetic spectrum (Soldi et al., 2008; Fossati et al., 1998; Abdo et al., 2010a). In our general picture, AGN (see Fig. 1.3) are powered by a central engine, an accreting supermassive black hole with typical masses on the order of $10^6 - 10^9 M_{\odot}$ with accretion rates of $\dot{M} \sim 1 - 2 M_{\odot} \text{yr}^{-1}$ (Woltjer, 1959; Woo et al., 2010). Accretion is a mechanism to convert gravitational potential energy of matter into radiation. This accreted material is e.g., interstellar dust and gas surrounding the AGN, which then form an accretion disk due to the conservation of angular momentum. This accretion disk is surrounded by a dusty torus, whose configuration is still debated (Elitzur, 2007). The broad line region (BLR) in its most simple model is thought of as a region of ionized gas clouds with the addition of winds originating from the accretion disk. For a review on the nature and configuration of the BLR see Gaskell (2009). The narrow line region (NLR) is thought of as a similar region as the BLR except that the velocities of the ionized gas clouds are smaller and the region is less dense (e.g., Kraemer & Crenshaw, 2000). In the case of radio loud AGN collimated relativistic outflows (jets) can be observed (see Fig. 1.2). Individual components of an AGN will be discussed later.

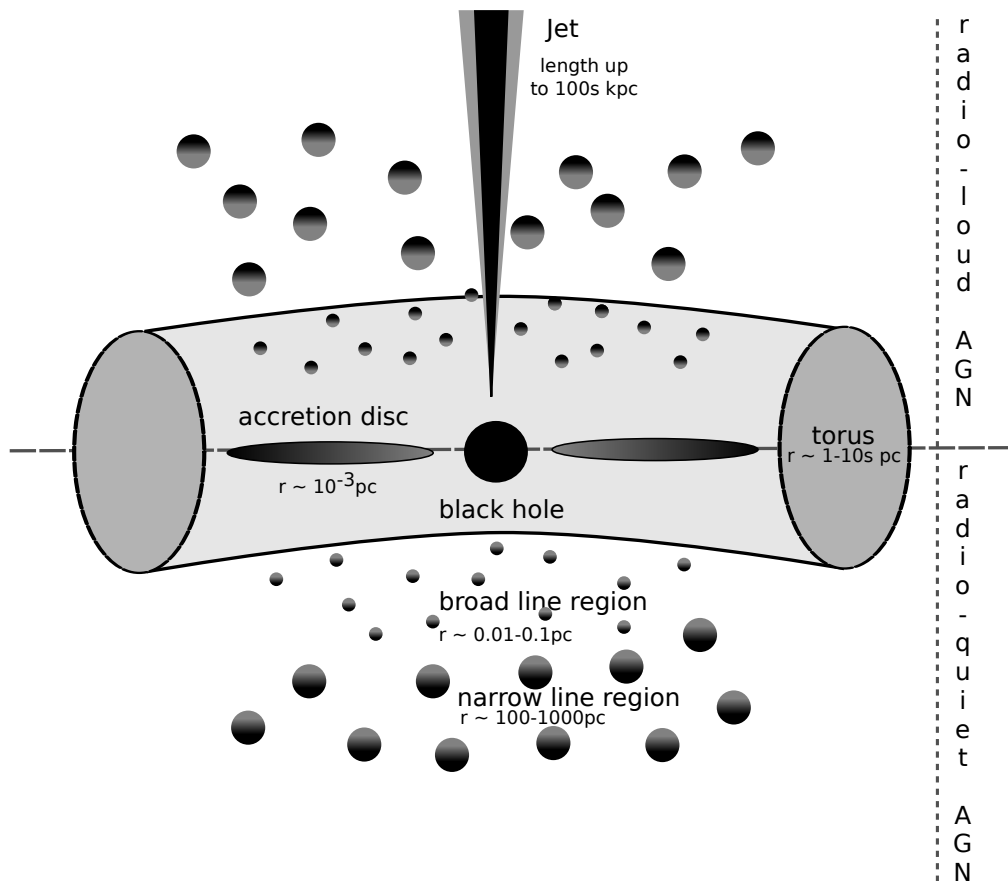


Figure 1.3: Schematic overview of the structure of an AGN and its main components. The separation between radio-loud and radio-quiet is used to explain the two types which are thought to be symmetric along the orbital plane.

1.4 Classification

In this section I give an overview of the important AGN classes. In-depth reviews of AGN and their nomenclature are given in the textbooks by Krolik (1999) and Beckmann & Shrader (2012) which are also used as the basis of this chapter. One has to note, though, that a clear classification is extremely difficult since no clear definition is given to differentiate between all existing types. In addition, AGN display a variety of properties which can be attributed to multiple classes. To make matters worse, AGN are variable objects, which leads to changes in their classifications during their lifetime.

1.4.1 Seyfert galaxies

Seyfert galaxies as a class are found to be the most common of all AGN. Their identification is traditionally based in the optical regime by observing their spectra (e.g., Osterbrock & Ferland, 2006). The spectrum of a Seyfert galaxy shows emission lines of

highly ionized material. One usually differentiates between two types of Seyfert galaxies, Seyfert 1 and Seyfert 2, by investigating their emission lines (Urry & Padovani, 1995). In Seyfert 1 types profiles of lines from the Balmer series are usually broader than forbidden lines. Typical derived velocity distributions from profiles of Seyfert 1 show a full width at half maximum (FWHM) of the order of a few thousands of km s^{-1} but can reach 10^4 km s^{-1} . The velocity distributions are obtained with the Doppler effect $\Delta\lambda/\lambda = v/c$ at rest wavelength λ and the speed of light c . The narrow lines only have a FWHM of a few hundred km s^{-1} . Seyfert 2 galaxies are defined as showing only narrow lines. Due to the nature of AGN a lot of intermediate types of Seyfert galaxies were introduced, which are based on the ratio of their emission profiles (e.g., Osterbrock & Koski, 1976; Cohen, 1983; Winkler, 1992). Using the unified model of AGN (see Sect. 1.5) a second method to differentiate Seyfert types can be performed in the X-rays by measuring the intrinsic absorption, given as the column density of hydrogen N_H (atoms per cm^2) in the light of sight.

1.4.2 LINER

LINERs are AGN with low-ionization nuclear emission-regions. They usually show a faint core but strong emission lines. In principle they closely resemble Seyfert 2 types but with stronger forbidden lines and low bolometric luminosity of $L_{\text{bol}} < 10^{40} \text{ erg s}^{-1}$ (Heckman, 1980). This type of class is suitable to fill the gap of objects with intermediate luminosity higher than that of our own Galaxy Sgr A* ($L_{\text{bol}} = 10^{37} \text{ erg s}^{-1}$) but less than that of Seyfert galaxies.

1.4.3 Radio galaxies

AGN are typically divided into radio-quiet and radio-loud types (Kellermann et al., 1989). This division is historically based on the ratio between radio flux density at 5 GHz ($\lambda \sim 6 \text{ cm}$) and the flux density at 4400 \AA , with a typical ratio of 0.1 – 1 for the radio-quiet regime and 10 – 1000 for the radio-loud regime (Kellermann et al., 1989). The class of radio galaxies can be seen as the equivalent to Seyferts with high radio emission. They are also divided into two types: Broad Line Radio Galaxy (BLRG) and Narrow Line Radio Galaxy (NLRG), which like their Seyfert counterparts have either broad or narrow emission lines. Radio galaxies are typically found in elliptical galaxies and have higher luminosities than found in Seyferts.

1.4.4 The classification of Fanaroff and Riley

A second classification in the radio regime of spatially resolved radio galaxies is based on the radio jet morphology. It was introduced by Fanaroff & Riley (1974) and differentiates between the low-luminosity FR-I class and the high-luminosity FR-II class. To determine the class of an object, the distance between the two brightest spots in the jet separated by the nucleus was measured and put in relation to the span covering whole radio emission.

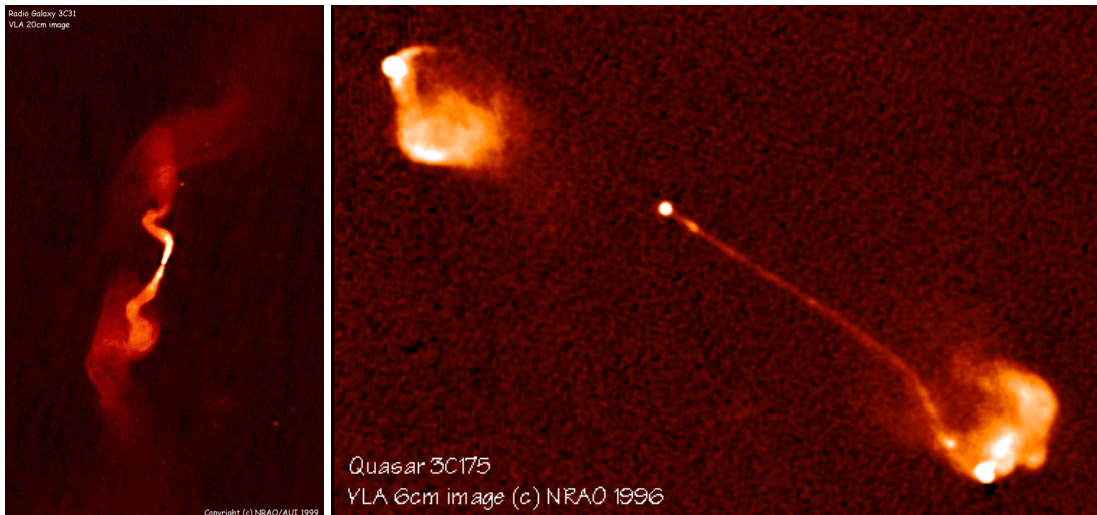


Figure 1.4: The FR-I type radio galaxy 3C 31 is shown on the left and the FR-II type radio galaxy 3C 175 is displayed on the right.

A ratio of 0.5 or less was classified as FR-I while a higher ratio as FR-II. In their analysis they found that a division of these types could also be given by the luminosity of the object

... those with luminosities at 178 MHz below $\approx 2 \times 10^{25} \text{ W Hz}^{-1} \text{ sr}^{-1}$ (...) are nearly all of class I, and those above nearly all class II.

In FR-I galaxies, mostly two sided jets are observed. The jet shows a very bright inner region including the nucleus while the jets of FR-II types are mostly one sided ending in plumes. An image showing examples for these types is shown in Fig. 1.4.

1.4.5 Quasars

Quasars, “quasi-stellar radio sources”, are the most luminous AGN. The name of this class was coined based on the observation that these sources are bright, point-like optical counterparts with strong optical emission lines. However, astronomers could not resolve these objects in optical images, which resembled blue stars. Consequently these objects show analogies to Seyfert galaxies but are apparently brighter. To separate these types [Schmidt & Green \(1983\)](#) introduced a dividing line which put objects into the class of Quasars if they exceeded an absolute magnitude of $M_B > 23 \text{ mag}$.

1.4.6 Blazars

Blazars are characterized by their large-amplitude flux variability, showing changes in their luminosity by orders of magnitude as well as a strong intraday variability (e.g. [Sarma Kuchibhotla et al., 2010](#)). They emit throughout the whole electromagnetic spectrum ranging from the radio regime up to γ -rays. Another attribute of this type is its

high degree of polarization in the radio and optical regime (Beckmann & Shrader, 2012). Blazars are divided into the sub-types BL Lac and Flat Spectrum Radio Quasar (FSRQ). BL Lac is named after BL Lacertae and was originally classified as a variable star (Schmitt, 1968). BL Lac and FSRQ are typically differentiated by the equivalent width (EW) of the observed emission lines. As a rule of thumb, values of the EW more than or less than 5 denote FSRQs and BL Lacs, respectively (e.g., Stocke et al., 1991), with BL Lacs having lower values. A more detailed discussion about the classification of blazars is given by e.g. Giommi et al. (2012a).

1.5 Unification

A large body of work has been dedicated on the subject of explaining the different AGN types and their observed properties with one unified model (e.g., Urry & Padovani, 1995; Fossati et al., 1998). The structure of a generic AGN was previously shown in Fig. 1.3. Already in the simplest model by taking only the viewing angle into account one can explain most of the observed discrepancies between the various AGN classes.

In the general picture of an AGN, a supermassive black hole is located in the center and surrounded by an accretion disk. Materials with high velocity distributions and therefore broad emission lines have to be close to the black hole and are forming the BLR. Narrow emission lines stem from material with low velocities and thus further away from the central black hole, in the NLR. This structure is surrounded by a dusty torus. In the case of radio-loud AGN jets are symmetrically launched perpendicular to the accretion disk are (note that in Fig. 1.3 and 1.5 only one jet is displayed, because solely the top part resembles the type of radio loud AGN).

The different classes of AGN can be explained by different lines of sights to that object. For instance an observation made edge on will not allow us to detect a BLR, since it is obscured by the dusty torus. A slight change in the inclination angle allows a direct observation of the BLR. This explains the differences in the observed emission line properties of Seyfert 1 and Seyfert 2 galaxies as well as in BLRG and NLRG. One can test the viability of this model using the prediction that polarized emission from the BLR can be detected even though the region is obscured (Antonucci, 1984; Antonucci & Miller, 1985). Polarized emission gets scattered in the NLR and into the direction of the observer, while the NLR itself does not show any polarization. Roughly 40% of Seyfert 2 types were found to harbor a hidden BLR and had a powerful AGN with high accretion rates (Gu & Huang, 2002).

Changing the inclination angle even further will lead to a line of sight which is nearly face on. The jet is observed with a small inclination angle to the line of sight. Jets are relativistic outflows and thus are boosted in the direction of their movement. As a consequence the jet will dominate the emission of other components. This boosting also explains the high apparent luminosity and the short variability of these AGN classes.

The geometrical explanation for the different types of AGN seem to work quite well but other obvious influencing parameters like the mass of the black hole and the accretion rate need to be taken into account to explain observed discrepancies.

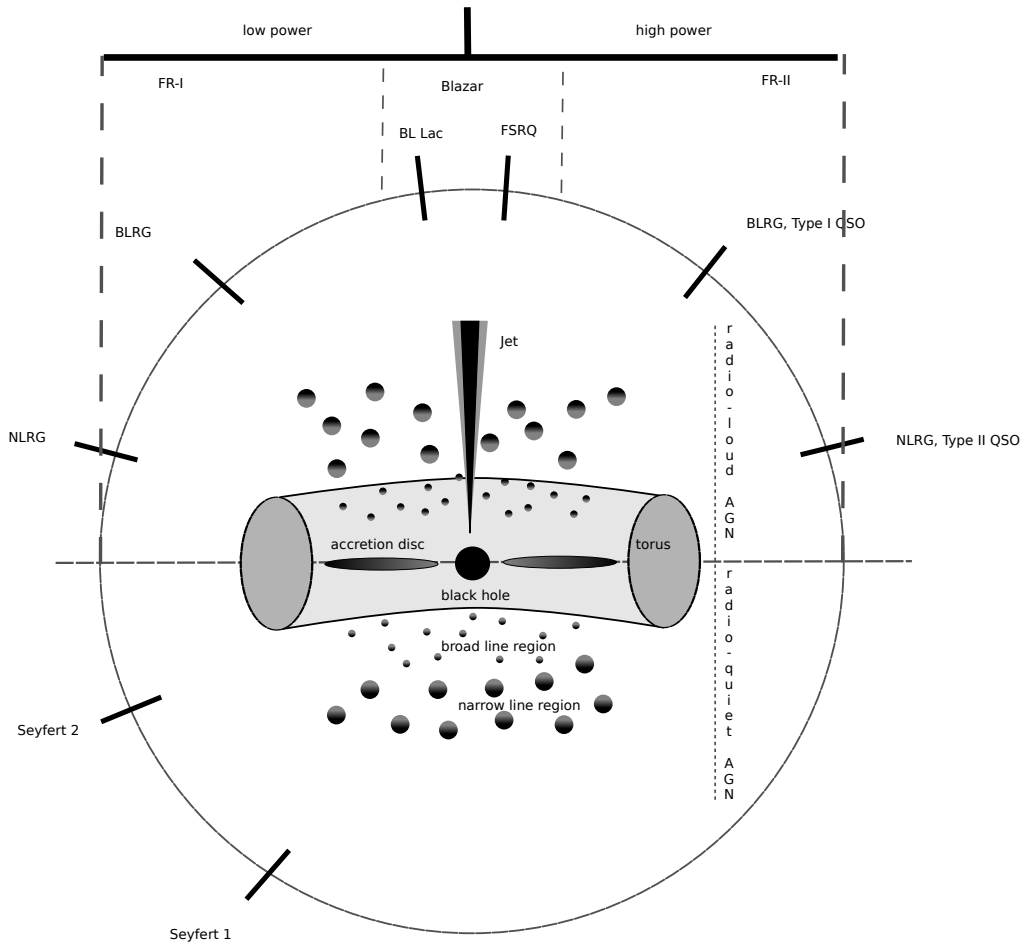


Figure 1.5: Illustration of different AGN types in the unification model. In this model the various types are explained by different viewing angles indicated by tics on the enclosing circle and the dependency on the power of the AGN. Figure after [Beckmann & Shrader \(2012\)](#).

1.6 Accretion Disk

Matter in the gravity field of a massive object like a supermassive black hole will fall onto it unless it possesses sufficient angular momentum. Taking conservation laws into account, this would lead to the fact that the matter is moving on Keplerian orbits around this object and forming an accretion disk. This holds true only as long as the angular momentum cannot be extracted by other means like viscous heating in a medium.

The standard model for accretion disks is the assumption of a geometrically thin, radiatively-efficient disk, considered to be optically thick within a constant accretion rate. Geometrically thin means that for any given radius r of the accretion disk, the thickness H is far less than that. This was already proposed in the 1970s by [Shakura & Sunyaev \(1973\)](#) and a review on the topic of accretion disks is given by [Pringle \(1981\)](#). The textbooks by [Beckmann & Shrader \(2012\)](#) and the lecture by [Kadler & Wilms \(2010\)](#) are the basis of

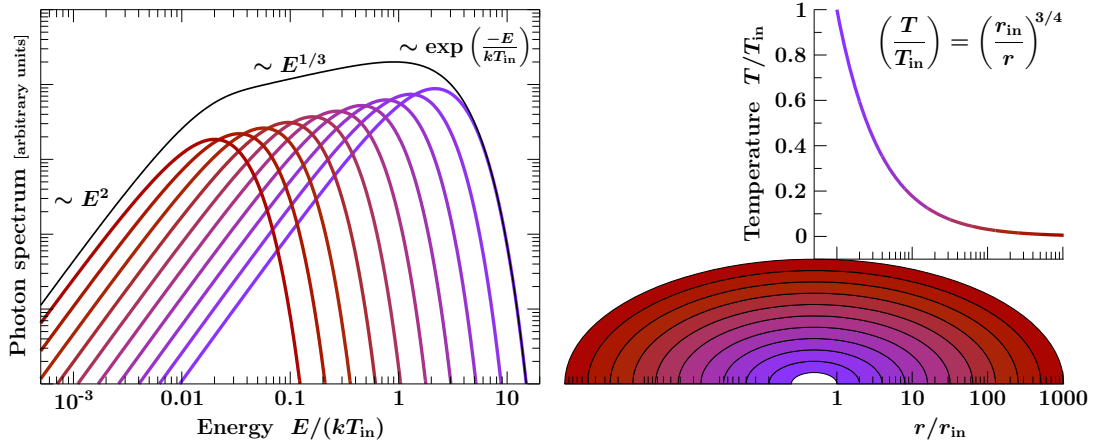


Figure 1.6: *Left:* Combined spectrum of an accretion disk with contributions of different radii. *Right:* Temperature and model of an accretion disk split in 10 rings. (Credit: Hanke, 2011, Fig. 1.6)

this section.

If the disk is optically thick, it can be considered to be in thermodynamic equilibrium and thus at any given radius the emitted luminosity, L , is

$$L \propto T^4 \quad (1.1)$$

where T is the temperature at this radius. The thermal profile of an accretion disk (see Figure 1.6) follows by considering a $1/r$ gravitational potential

$$T(r) \propto r^{-3/4} \quad (1.2)$$

and the single black body spectrum is given by Planck's law:

$$B_\nu(T) \propto \nu^3 [e^{h\nu/(k_B T)} - 1]^{-1} \quad (1.3)$$

with B denoting the spectral radiance. The observed energy spectrum of a disk is the superposition of the thermal spectra for all radii starting at the inner radius r_{in} up to the outer radius r_{out} (see Figure 1.6):

$$S_\nu \propto \int_{r_{in}}^{r_{out}} B_\nu 2\pi r dr \quad (1.4)$$

1.6.1 Emission line diagnostics in the X-ray regime

An accretion disk is thought to be directly surrounded by a hot corona (Haardt & Maraschi, 1993). Photons in that region are thermal comptonized and result in a power-law X-ray

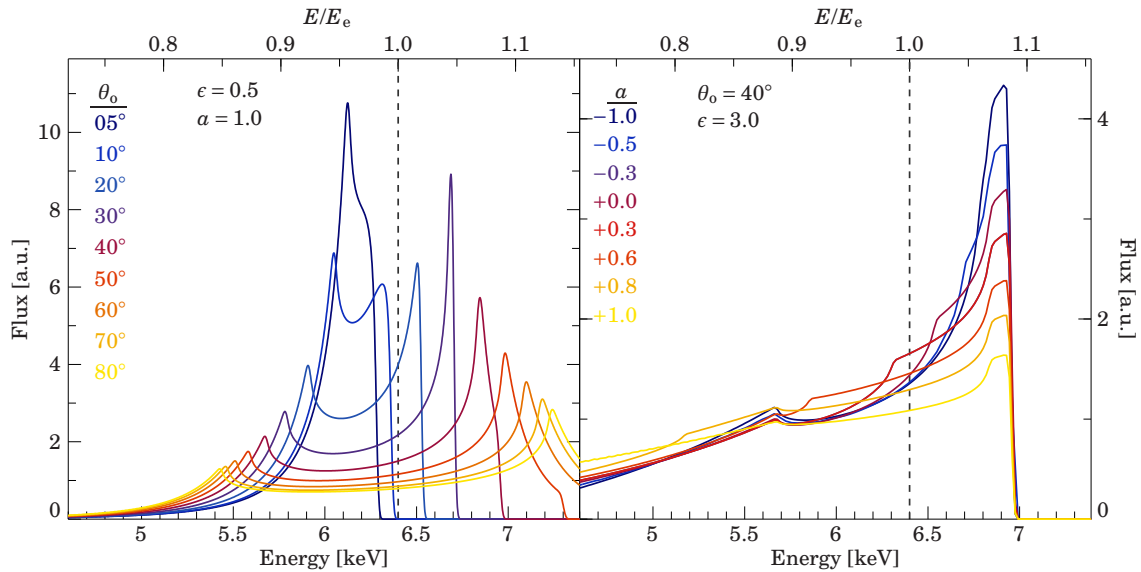


Figure 1.7: Relativistic broadened Fe $K\alpha$ lines *Left:* Line profiles for a maximal spinning black hole ($\alpha = 0$) with an emissivity $\epsilon = 0.5$ for different inclinations of the accretion disk. *Right:* Line profiles at a fixed inclination angle of $\theta_0 = 40^\circ$ and an emissivity $\epsilon = 3.0$ with varying spin. (Credit: Thomas Dauser, priv. comm.)

spectrum irradiating the accretion disk (e.g., Dove et al., 1997; Gierlinski et al., 1997; Malzac & Jourdain, 2000). These photons will undergo scattering processes or get photoelectrically absorbed. The first process leads to a Compton Reflection Hump while the second one to emission lines in the spectrum (e.g., Ghisellini et al., 1994; Turner & Miller, 2009, and references therein), the most prominent one being the Fe $K\alpha$ at 6.4 keV. For an in-depth review on this topic refer to Fabian et al. (2000a).

Photons produced in an accretion disk will receive a relativistic Doppler boost with respect to the line of sight of the observer. In addition, light bending and a gravitational redshift due to being close to a supermassive black hole changes the energy of these photons. The spin of the black hole changes the innermost stable orbit for the accretion disk (Bardeen et al., 1972). This leads to different line profiles as discussed by Dauser et al. (2010). Taking into account an emissivity of the accretion disk will further influence the emission lines. An example showing different line profiles for changing inclination angles and spins are shown in Fig. 1.7.

These lines are ideal candidates to be used as diagnostic tools to study these objects but the signal to noise ratio of the spectra obtained so far are not yet at that point to allow a differentiation between all influencing parameters.

1.7 Broad Line Region

The BLR is the region in which the broad observed optical emission lines are thought to be created through photoionization. The basic questions about this region are still viable today, “what is the geometric configuration?”, “what are the kinematics of the BLR?”, and “what is the origin of BLR clouds”. The basic picture of this region is a sphere of clouds which are illuminated by an ionized radiation from a central object. This model is able to explain many of the observed properties in AGN and yet there are also observational evidence that this picture is incorrect (Gaskell, 2009).

An interesting technique to measure the size of the BLR and to determine the mass of the black hole is reverberation mapping (Peterson, 2006, and references therein). The concept of this method is that a change in the radiation from the central object will also alter the emission profile of the BLR with a certain time lag. By measuring this time lag and the Doppler-broadened width of the line one is able to derive the size of the BLR and the mass of the central black hole.

1.8 Jets

As per the unified model the presence of a jet denotes an AGN as radio loud, since jets are most prominent in the radio band. The introduction of methods such as VLBI allowed observations of these jets in the radio with unsurpassed angular resolution in the order of milliarcseconds. An introduction to this technique is given in chapter 3.

An important observational fact is that jets show linearly polarized emission with some regions even reaching a polarization degree of more than 50% (e.g. Lister & Homan, 2005)). This is the strongest argument for non-thermal emission processes in jets, such as synchrotron and the inverse-Compton mechanism. However the latter process does not necessarily lead to the observed polarization values (Krolik, 1999).

Monitoring campaigns on individual jets and across samples of AGN have revealed that distinct features in the jet are moving such that the outflow appears to have relativistic speeds. This was first reported as mentioned in section 1.2 by Cohen et al. (1971) and Whitney et al. (1971) for 3C 279. The most sophisticated program in monitoring jets today is the Monitoring Of Jets in Active galactic nuclei with VLBA Experiments (MOJAVE) project (Lister, 2003).

This section is based on the lecture by Kadler & Wilms (2010) and the publications by Boettcher et al. (2012), Krolik (1999), Bridle & Perley (1984), and Rybicki & Lightman (1979).

1.8.1 Radiative processes

Jets are mainly observed in the radio regime but they can also be seen at other wavelength such as in the X-rays (Hogan et al., 2011). In this section I discuss the governing radiative processes to explain the observed multi-wavelength occurrence of jets – syn-

chrotron radiation and inverse Compton scattering. The first one dominates the lower part of the spectrum while the latter one dominates the high energies. For in-depth reviews on the processes involved in the theory of jets and AGN refer to [Boettcher et al. \(2012\)](#), [Krolik \(1999\)](#), [Bridle & Perley \(1984\)](#), and [Rybicki & Lightman \(1979\)](#).

Synchrotron radiation

Incoherent synchrotron radiation was the first process thought of able to produce the observed radio emission and was proposed as early as in the 1950s by [Alfvén & Herlofson](#). This process was also able to theoretically reproduce the observed polarization, which was a strong constraint in finding possible explanations.

Synchrotron radiation is produced when a charged particle is accelerated, e.g. it moves through a magnetic field on a path not anti/-parallel to the magnetic field lines around it. The motion of a relativistic particle with mass m , charge q in a magnetic field B can be described by the equation

$$\frac{d\vec{v}}{dt} = \frac{q}{cm\gamma} \vec{v} \times \vec{B} \quad (1.5)$$

with v the velocity of the particle, $\gamma = (1 - \beta^2)^{-1/2}$ and $\beta = v/c$. This particle receives a force perpendicular to the magnetic field causing it to spiral along the same direction as the magnetic field lines and is thus constantly accelerating, causing the production of synchrotron radiation. Assuming a non-thermal incident population of electrons $n(\gamma)$ with a power law distribution

$$n(\gamma)d\gamma \propto \gamma^{-p}d\gamma \quad (1.6)$$

one finds that the spectrum produced P_ν is also a power law

$$P_\nu \propto \nu^\alpha \quad (1.7)$$

with $\alpha = (1 - p)/2$ the spectral index. The resulting power law is the superposition of all spectra produced by the incident power law distribution of the electrons. Therefore by measuring the spectral index one can infer the distribution of the underlying population of electrons.

Inverse Compton scattering

The process of a photon scattering with a charged particle and thereby losing energy is called Compton scattering while the reverse process, a photon gaining energy when scattering with a charged particle is called inverse Compton scattering or Compton cooling. In the non-relativistic regime, an approximation of the energy change of a photon scattering with electrons that follow a thermal distribution is given by

$$\frac{\Delta E_{\text{ph}}}{E_{\text{ph}}} = \frac{4k_B T_e - E_{\text{ph}}}{m_e c^2} \quad (1.8)$$

with k_B the Boltzmann constant, T_e the temperature of the electron, and m_e the mass of the electron.

In the case of jets, special cases of Compton scattering exist, such as the synchrotron self-Compton (SSC) and external Compton (EC) scattering. In SSC a population of electrons produces synchrotron radiation. The photons produced then scatter off of the incident electron population. This leads to the interesting fact that the ratio of the peak luminosities from inverse Compton and synchrotron radiation is the same as the ratio of the photon density to the magnetic field density. Moreover, the resulting inverse Compton spectrum has the same spectral index as the synchrotron radiation. For more details refer to e.g. [Beckmann & Shrader \(2012\)](#).

The EC model can be described as an SSC model plus an additional external photon population e.g., produced in the accretion disk or the BLR (e.g., [Sikora et al., 1994](#)), off which the electrons can scatter.

1.8.2 Jet kinematics

VLBI observations of the jets in AGN have revealed that the flux density of these are not only variable in time but that discrete features are moving in these jets. These emission components are often referred to as "knots" or "blobs". Measuring the apparent motion of these features lead to our inferring a velocity higher than the speed of light; this is called superluminal motion. Among the first to discover this phenomena were, as mentioned in section 1.2, [Cohen et al. \(1971\)](#) and [Whitney et al. \(1971\)](#).

An example showing superluminal motion are the observations of 3C 111 by [Kadler et al. \(2008\)](#) as presented in Fig. 1.8. Individual jet features were found to have an apparent velocity of $3c$ up to $5c$. Ideas explaining the superluminal motion were reviewed in [Blandford et al. \(1977\)](#), who concluded that these velocities are not real but apparent due to the geometry of the system.

The principle of superluminal motion is given in the following and illustrated in Fig. 1.9. Consider a jet with an inclination α to the line of sight. At an arbitrary time t_0 , a feature traveling with constant velocity \vec{v} is observed along the jet axis. In a time interval Δt , this feature will have traveled the distance Δd_{\perp} projected on the plane of the sky of the observer. The distance to the jet can be considered at a quasi-infinite point for the change of the inclination angle due to the movement of the feature. Therefore the inclination angle can be treated as constant for all observations and the distance traveled by the feature is given by

$$\Delta d_{\perp} = v \Delta t \sin \alpha. \quad (1.9)$$

At time $t_1 = t_0 + \Delta t$, the feature is observed again. During the time Δt , it also moved in the direction of the observer, thus leading to a reduction of the distance to this feature,

$$\Delta d_{\parallel} = v \Delta t \cos \alpha. \quad (1.10)$$

Therefore the light emitted by this feature will not be observed at time Δt later but instead at

$$\Delta t_{\text{obs}} = \Delta t - \frac{\Delta d_{\parallel}}{c} = \Delta t \left(1 - \frac{v \cos \alpha}{c} \right) \quad (1.11)$$

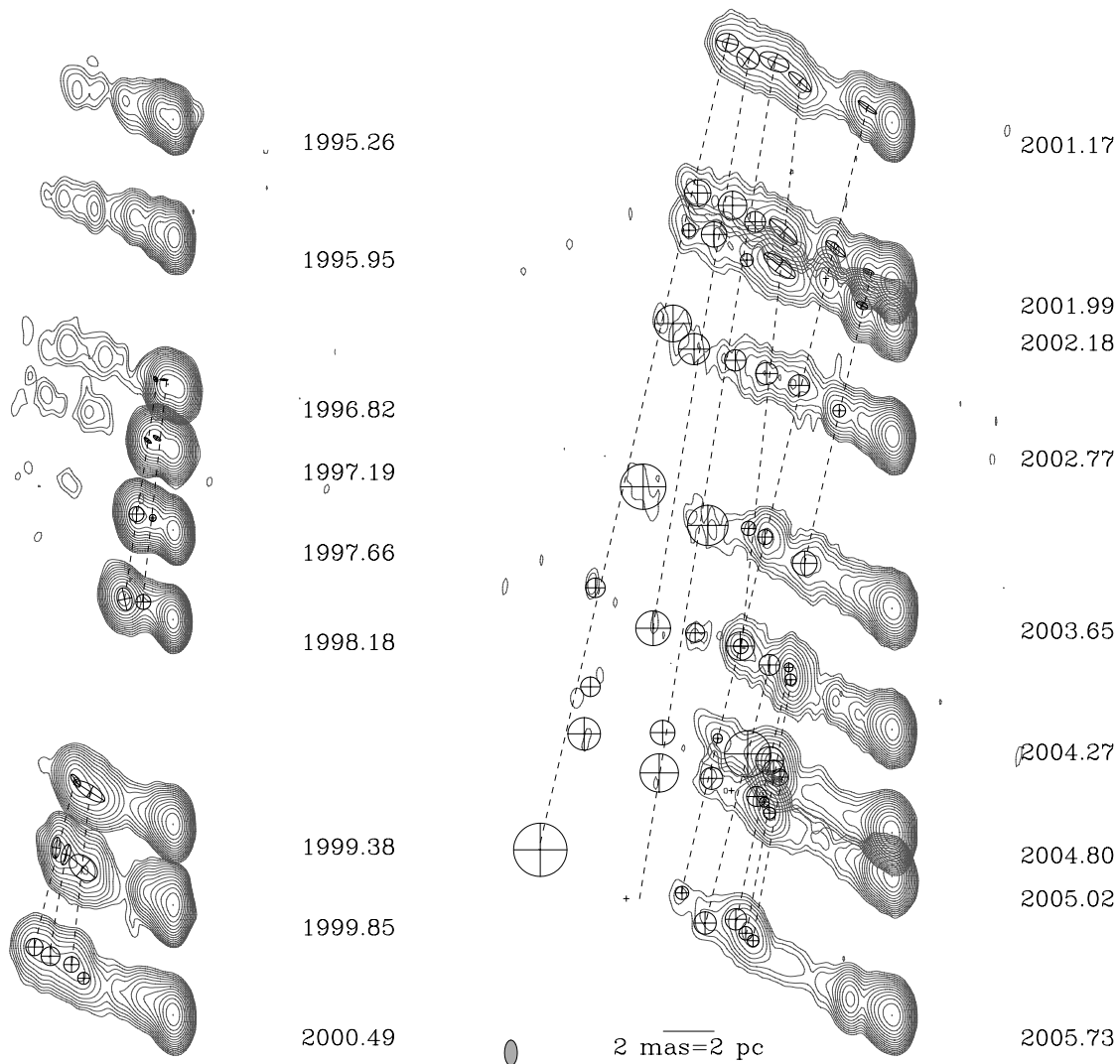


Figure 1.8: The 10 year evolution of the jet in 3C 111 from 1995 to 2005 by Kadler et al. (2008). Identifying and tracking individual features (dashed lines) of the jet showed apparent velocities of up to 5 c.

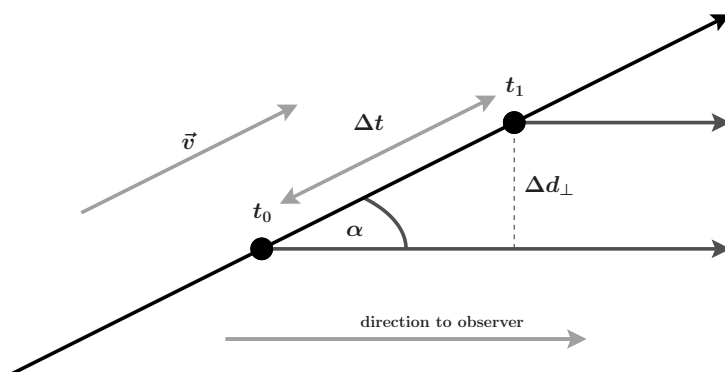


Figure 1.9: Sketch to illustrate the principle of superluminal motion. A bright feature moves with velocity \vec{v} moves along the jet stream with an inclination α to the line of sight. See text for further explanations.

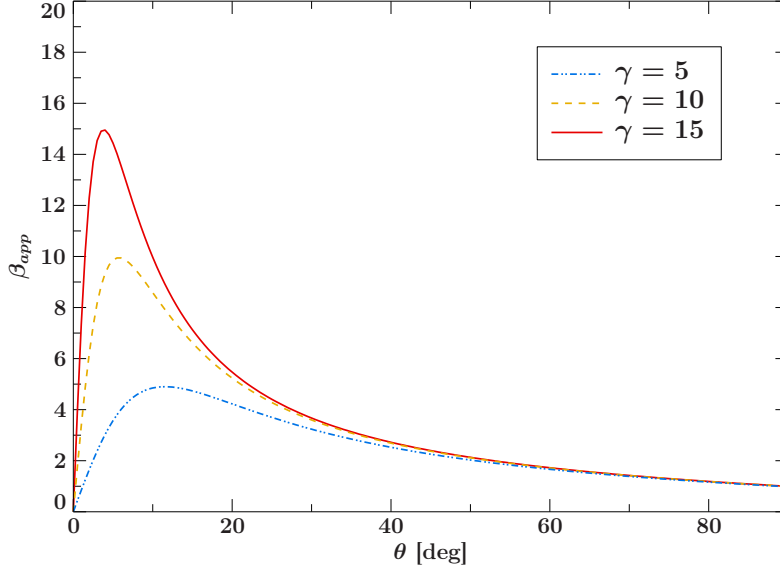


Figure 1.10: Dependency of apparent velocity on the viewing angle for different Lorentz factors.

leading to an apparent velocity of

$$v_{app} = \frac{d_{\perp}}{\Delta t_{obs}} = \frac{v \sin \alpha}{\left(1 - \frac{v}{c} \cos \alpha\right)} \quad (1.12)$$

From equation 1.12, it is clear that the maximum apparent velocity only depends on the inclination angle α and the velocity v . This can be seen in Fig. 1.10 for different Lorentz factors $\gamma = \frac{1}{\sqrt{1-\beta^2}}$ with $\beta = \frac{v}{c}$.

The angle for which the apparent velocity becomes maximal is given by

$$\cos \alpha_{v,max} = \beta. \quad (1.13)$$

Using $\sin \alpha_{v,max} = \sqrt{1 - \cos^2 \alpha_{v,max}} = \sqrt{1 - \beta^2} = \gamma^{-1}$, one finds that the maximum apparent velocity for a certain Lorentz factor γ is given by

$$v_{max,app} = \frac{v}{\gamma(1 - \beta^2)} = \gamma v = c \sqrt{\gamma^2 - 1}. \quad (1.14)$$

Therefore the Lorentz factor for any observed apparent velocity v_{app} must be at least

$$\gamma \geq \sqrt{\beta_{app}^2 + 1} \quad (1.15)$$

with $\beta_{app} = v_{app}/c$. Using equation 1.12, one finds that the maximum apparent velocity for any inclination angle α is reached when $\beta \rightarrow 1$, thus

$$\beta_{max,app} = \frac{\sin \alpha}{1 - \cos \alpha}. \quad (1.16)$$

This translates to a maximum value of the inclination angle for which a jet with an apparent superluminal motion v_{app} can be observed:

$$\cos \alpha_{max} = \frac{\beta_{app} - 1}{\beta_{app} + 1}. \quad (1.17)$$

1.8.3 One-Sided and Two-Sided Jets

As described in section 1.4.4 the Fanaroff-Riley classification was introduced to differentiate between two jet morphologies. In the FR-I type, a two-sided jet is observed, while the jets of FR-II types are one-sided. In the unified model, both classifications have two jets but in FR-II only one jet can be observed due to relativistic Doppler boosting. The relativistic Doppler factor, defined as

$$D := \frac{1}{\gamma(1 - \beta \cos \alpha)} \quad (1.18)$$

depends on the inclination angle α . Figure 1.11 illustrates this dependency for various Lorentz factors. In the limits of v being close to the speed of light the Doppler factor becomes very large.

It can be shown that the quantity S_ν/ν^3 is Lorentz invariant (e.g., [Rybicki & Lightman, 1979](#)) where S_ν is the flux density at frequency ν . Therefore the observed flux density can be written as

$$S(\nu_{\text{obs}}) = D^3 S(\nu_{\text{em}}). \quad (1.19)$$

If the flux density of a feature can be described by a power law of $S(\nu) = C\nu^\phi$ with C being a constant and taking time dilation into account ($\nu_{\text{obs}} = D\nu_{\text{em}}$), one finds

$$S(\nu_{\text{obs}}) = D^{3-\phi} S(\nu_{\text{em}}). \quad (1.20)$$

Assuming that the ejection of a feature is simultaneous in both jets as in the picture of the unified model with the additional constraints of both features being isotropic radio emitters, have the same luminosity, and the same ejection velocities, the ratio of the received fluxes (S_{ap} and S_{re} – approaching and receding) is

$$\frac{S_{\text{ap}}}{S_{\text{re}}} = \left(\frac{1 + \beta \cos \alpha}{1 - \beta \cos \alpha} \right)^{3-\phi}. \quad (1.21)$$

Therefore even small relativistic speeds and large angles can lead to high values of the ratio explaining the observed one-sidedness.

1.8.4 Jet formation and structure

The launching and formation of relativistic jets is still a highly-discussed topic (e.g. [Meier, 2003](#)). In general, the launching of the jet is thought to occur in the vicinity of the black hole at distances of a few tens of gravitational radii ([Meier, 2009](#)). The two prevailing mechanisms to create jets are based on the process described by [Blandford & Znajek \(1977\)](#) and [Blandford & Payne \(1982\)](#). The Blandford-Znajek mechanism extracts energy and angular momentum from a spinning central black hole while the Blandford-Payne mechanism only requires a rotating accretion disk with a magnetic field. Both ideas work similarly, with the difference being that in the Blandford-Znajek mechanism, the spinning black hole causes the rotation of confined magnetic field lines in the accretion disk due to “frame-dragging” arguments, while for the Blandford-Payne process no black hole is

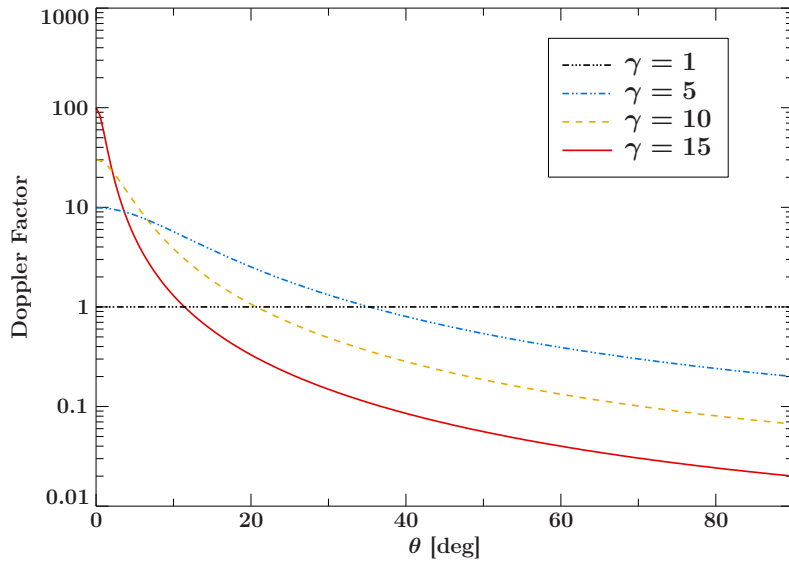


Figure 1.11: Dependency of the relativistic Doppler factor on the viewing angle for different Lorentz factors

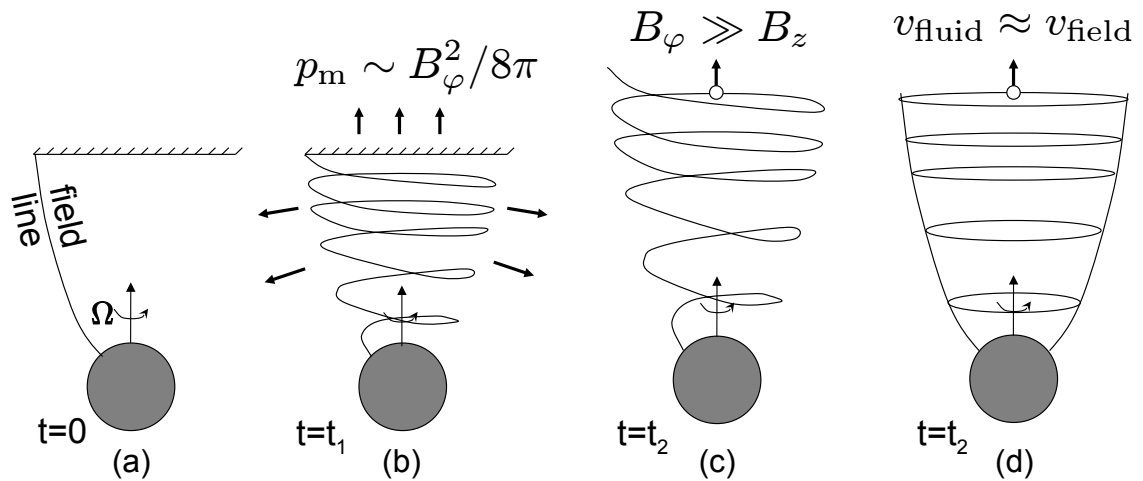


Figure 1.12: Illustration of the jet launching mechanism due to magnetic field lines. *a*: a magnetic field line is attached to a filled circle (representing the black hole / accretion disk) and to a stationary “ceiling” (representing the ambient medium). *b*: the magnetic field lines coil up due to rotation, thus building pressure. *c*: at some point, the pressure is so high that the “ceiling” is pushed away and plasma attached to the magnetic field is accelerated, forming the jet. *d*: in a steady state, the production rate of toroidal loops is equal to the rate of moving loops. (Credit: Tchekhovskoy et al., 2012)

needed. As the black hole or the accretion disk spins so will the surrounding space-time, thus forcing the magnetic field lines into a helical spring pattern. This creates a kind of pressure which at some point will be released and accelerating any plasma attached to the magnetic field lines (see Fig. 1.12 for illustration) leading to the jet formation.

Tchekhovskoy et al. (2012) performed three-dimensional magnetohydrodynamic (MHD) simulations on the Blandford-Znajek mechanism, finding that in the extreme case of a maximally spinning black hole and with a large magnetic flux a magnetically-arrested

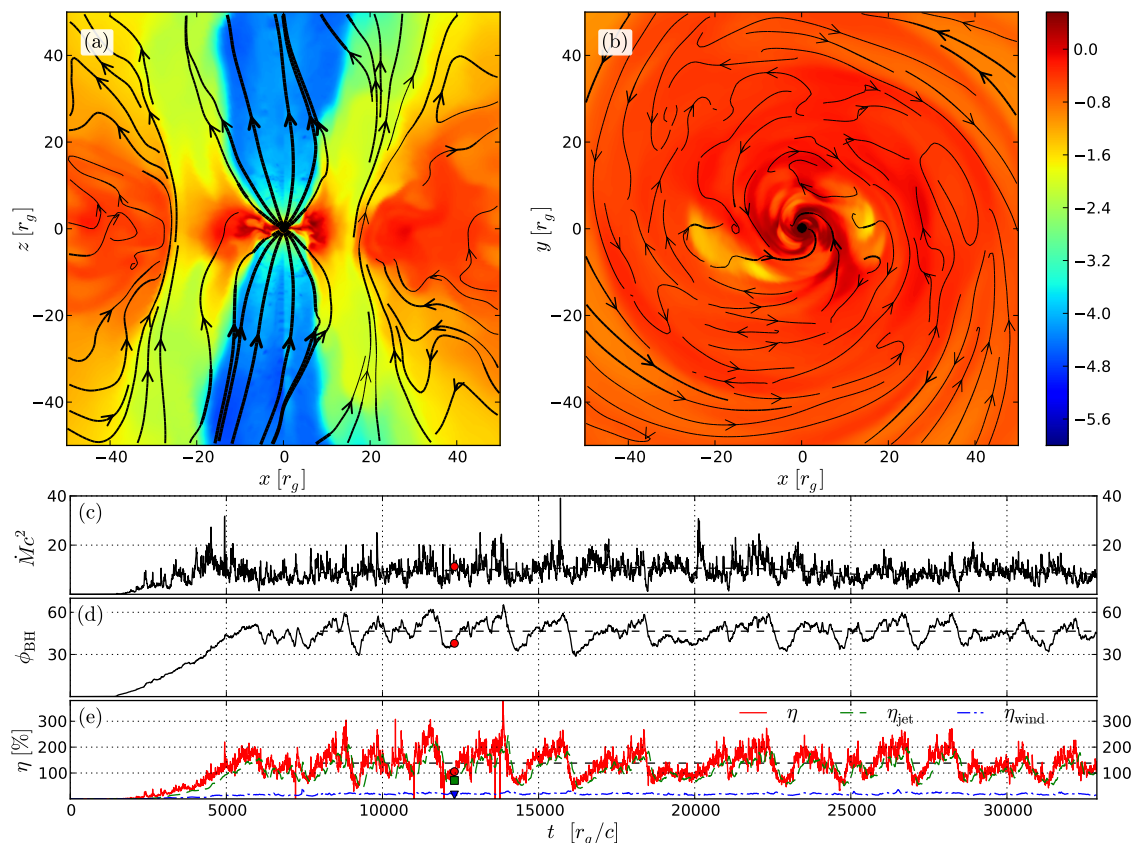


Figure 1.13: Snapshot of a MHD simulation with a maximal rotating black hole showing a magnetically-arrested accretion disk. The lowest panel shows the jet efficiency showing values of more than 100%. (Credit: Tchekhovskoy et al., 2012).

accretion disk is formed and the energy released into the jet is more than the amount gained by accretion (see Fig. 1.13). The extraction of spin energy via the Blandford-Znajek mechanism is therefore a plausible scenario in the launching of jets.

The classical picture of a jet is depicted in Fig. 1.14, showing the acceleration and collimation of the jet due to a helical magnetic field at the jet launch point. As the magnetic field expands, the magnetic pressure declines, leading to a pressure gradient along the jet axis, which accelerates the flow (Marscher, 2010). The standard model to explain the observed emission of radio jets is the one given by Blandford & Königl (1979) consisting of a quasi-steady jet and induced emission of propagating shock waves. This model was de-facto only the starting point and a lot of effort is still put into that field to explain the observed phenomena of jets.

A good review on jet dynamics and stability is given by Perucho (2014), who explains that these parameters depend on pressure differences between the jet and the ambient medium, as well as on the jet itself. These pressure differences lead to expansion and recollimation of the jets resulting in the production of conical shocks or Mach disks. In case of asymmetric pressure in the jet, helical patterns coupled to kink current-driven or Kelvin-Helmholtz instabilities can occur.

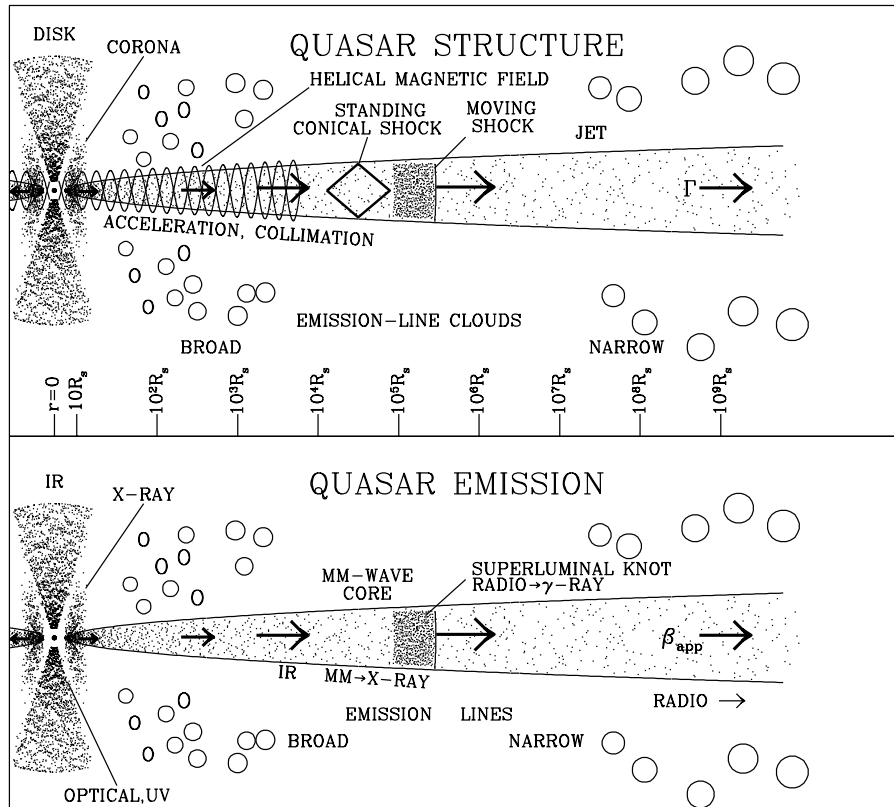


Figure 1.14: Classic illustration of an extragalactic jet showing various physical and emission components. (Credit: Marscher, 2010)

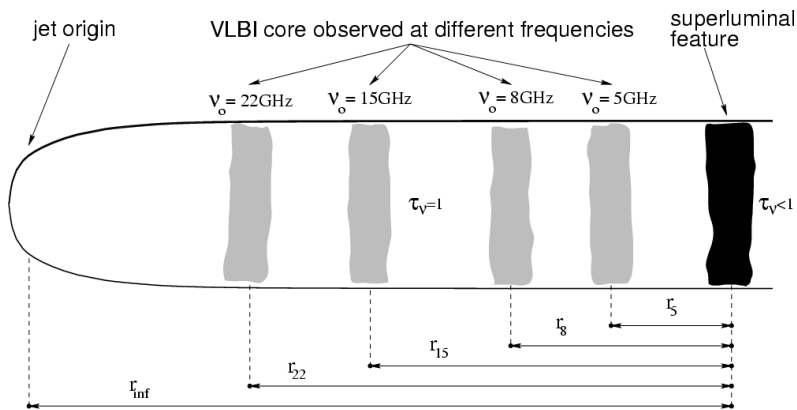


Figure 1.15: Illustration of the frequency dependent core shift as in Kovalev et al. (2008a) adopted from Lobanov (1996).

One common term appearing when talking about the structure of jets is the word “core”. In the model of Blandford & Königl (1979), the core is regarded as the surface of a photosphere with an optical depth of unity (e.g., Pudritz et al., 2012). The location of this region depends on the observed frequency with $r \propto \nu^{k_r}$ with r being the distance from the jet base (Königl, 1981). An illustration of the core shift is given in Fig. 1.15.

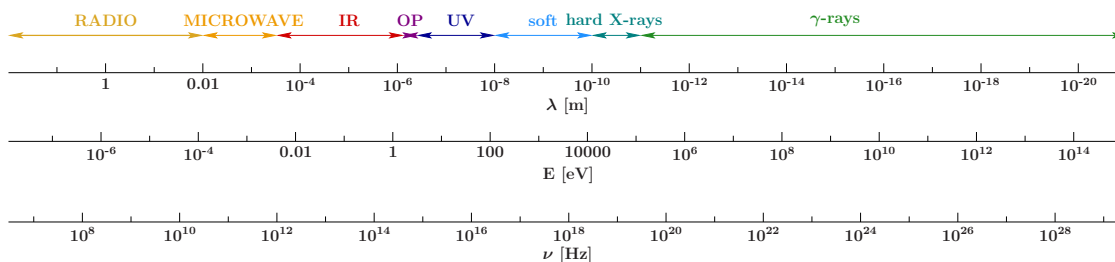


Figure 1.16: The electromagnetic spectrum and its representation in wavelength, energy, and frequency. (Credits: F. Krauß and C. Müller, private comm.)

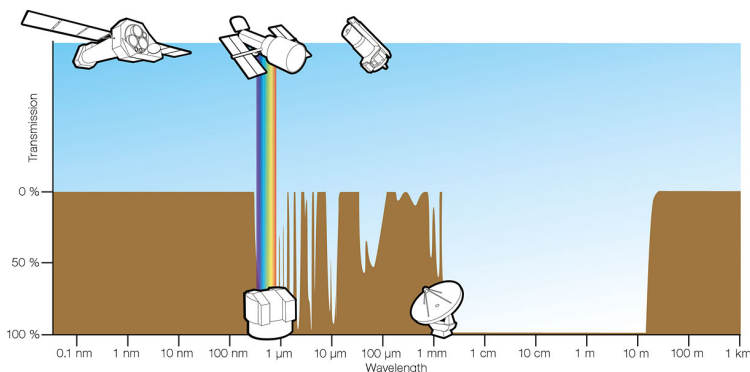


Figure 1.17: Atmospheric opacity on earth for different wavelength. (Credits: ESA/Hubble, F. Granato)

1.9 The importance of multiwavelength observations

The previous sections discussed important radiative processes related to AGN, including synchrotron and inverse Compton emission from the jet, blackbody radiation, and emission lines from the accretion disk. Our understanding of these individual processes is quite good but our understanding of their relative contributions is not. Therefore observations over the whole electromagnetic spectrum (see Fig. 1.16) are important to understand the sources of emission and identify the prominent physical processes in them.

Obtaining observations across the full range of wavelengths is quite challenging. The earth's atmosphere has an opacity which depends on wavelength, as depicted in Fig. 1.17. Based on this illustration it is clear that only for certain observing frequencies ground-based instruments are viable, mainly in the optical and radio regime, while in the infrared, X-ray and γ -rays regime instruments on spacecrafts or balloons are required to get above the atmosphere.

Nonetheless if this is not complicated enough, we know that AGN are variable on timescales of days, and even shorter. If physical processes are influencing each other and one wants to disentangle their connection, multiwavelength observations have to be performed nearly simultaneously.

The spectral energy distribution (SED) for two sources are shown in Fig. 1.18 as examples. The left panel shows the collected archival observations of the source 3C 111. The right panel shows the SED of 3C 273 as presented by [Giommi et al. \(2012b\)](#), with red crosses marking a simultaneous measurement at different wavelength and in gray the

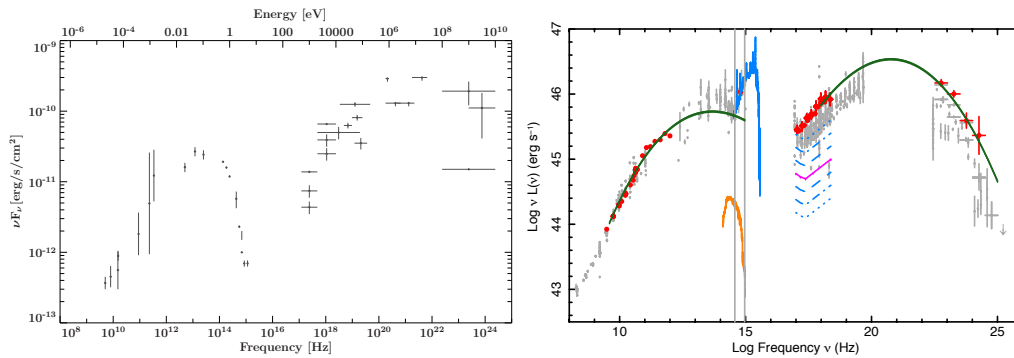


Figure 1.18: *left:* SED of 3C 111 based on archival data. *right:* SED of 3C 273 as shown in [Giommi et al. \(2012b\)](#), red data points are from simultaneous observations and gray from archival data.

archival data. It is immediately clear that the SED is variable in time when considering the archival data points, making simultaneous observations a necessity. Although the SED is different for various objects in the case of quasars, a typically double hump structure is seen due to boosted emission. The lower energy hump is attributed to the synchrotron radiation while the higher energy one to various Comptonization models.

The blazar sequence

Studying the SEDs of a sample of blazars, [Fossati et al. \(1998\)](#) found a correlation between the observed bolometric luminosity and their spectra. This became known as the “blazar sequence”. The peak positions of the two humps are shifted towards higher frequencies with decreasing bolometric luminosity. Moreover, a second correlation was found: the ratio of the peak luminosity of the high energy peak to that of the lower peak decreases towards relatively lower bolometric luminosities.

This topic is still heavily discussed, with many theories trying to explain the mechanism for the blazar sequence, while others suggest that this sequence is just a selection effect on the used blazar sample (using a combination of different radio- and X-ray selected samples). For instance, [Padovani \(2007\)](#) rules out the existence of the sequence in its simplest form when taking these selection effects into account, while [Ghisellini & Tavecchio \(2008\)](#) discuss the nature of the sequence being linked to the mass of the black hole and the accretion rate. [Meyer et al. \(2011\)](#) found an envelope of the sequence with an upper limit given by highly aligned blazars to our line of sight and radio galaxies to populate the lower peak luminosities and frequencies. In addition they suggest that the sequence is due to a two-population scenario, and they discuss these populations with regard to the Fanaroff-Riley classification scheme.

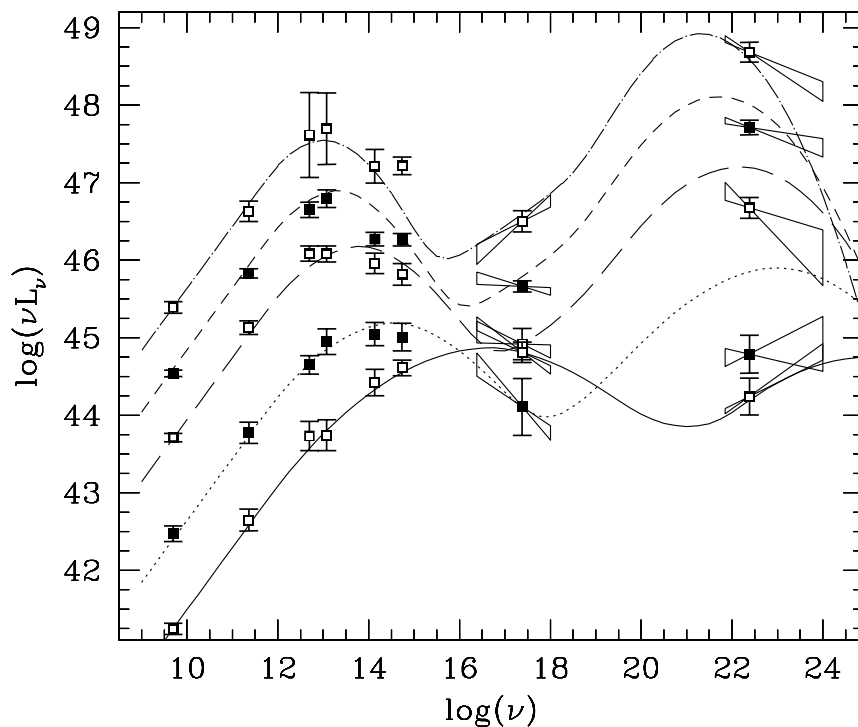


Figure 1.19: The blazar sequence as shown in [Fossati et al. \(1998\)](#). With decreasing luminosity the peaks are shifted towards higher frequencies and the ratio of the twin peaks change.

1.10 Evolution of AGN

Optical observations of nearby active and inactive galaxies e.g., by [Ferrarese & Merritt \(2000\)](#), [Ferrarese et al. \(2001\)](#) and [Gebhardt et al. \(2000\)](#) revealed that the masses of SMBHs are correlated with the velocity dispersion of their host bulges and the bulge luminosity. These findings suggests a link between the evolution of a SMBH and the host bulge. The underlying physical mechanisms are still unknown but typically include “AGN feedback” ([Sanders et al., 1988](#); [Di Matteo et al., 2005](#); [Springel et al., 2005](#); [Fabian, 2012](#)). Studying the accretion history of SMBH by measuring the X-ray luminosity function allows the derivation of the SMBH mass as a function of redshift ([Merloni & Heinz, 2008](#)) therefore placing constraints on evolutionary models of AGN (e.g., [Fanidakis et al., 2011](#)). One of the tools to study the development of AGN is the luminosity function and its evolution with cosmic time ([Hasinger et al., 2005](#)). This function counts the number of AGN in a given volume and luminosity range. Assuming a maximum observable flux S_{\max} in an Euclidean universe, the number of sources per unit volume and luminosity is given by:

$$N(> S_{\max}) = \int \frac{\Omega}{3} \phi(L) dL = \frac{\Omega}{3(4\pi)^{3/2}} S^{-3/2} \int L^{3/2} \phi(L) dL \quad (1.22)$$

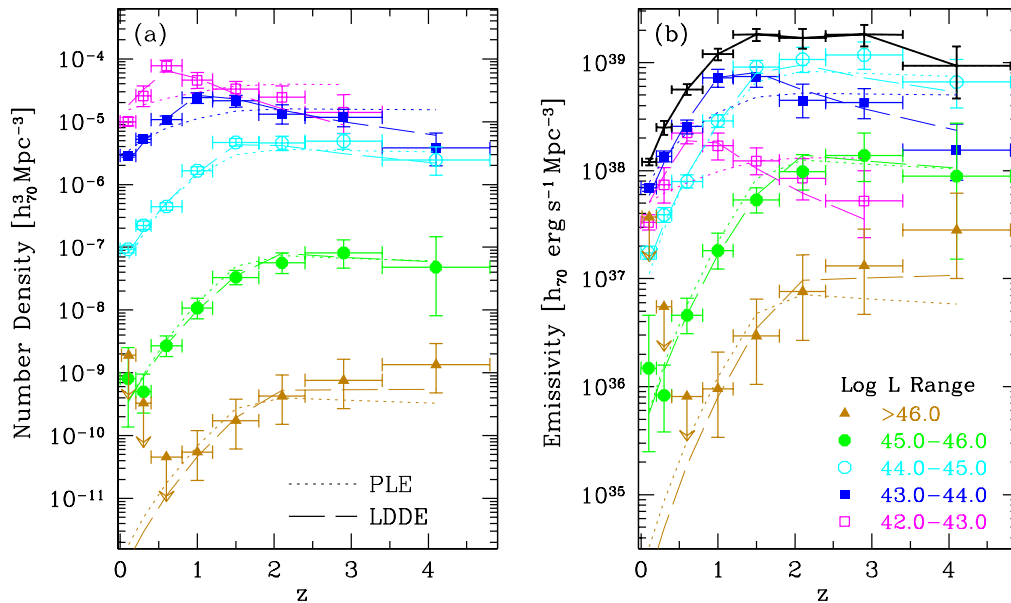


Figure 1.20: *left:* Number density of AGN as a function of redshift for different luminosity classes. *right:* as in *left* with emissivity instead of number density. (Credit: [Hasinger et al., 2005](#))

with Ω the solid angle (e.g., [Merloni & Heinz, 2013](#)). Observations in the soft X-rays e.g., by [Hasinger et al. \(2005\)](#) and in the hard X-rays e.g., by [Ueda et al. \(2003\)](#) lead to the finding that the evolution of the number counts depends on the intrinsic luminosity (see Fig. 1.20) of the AGN, suggesting evolutionary models for the development of AGN. Moreover, the peak in space density moves to lower redshifts with smaller luminosities and is known as “AGN downsizing” ([Hasinger et al., 2005](#)). This relation holds up to a redshift of $z \sim 2$ and is not unique to the X-rays (e.g., [Hasinger et al., 2005](#); [Massardi et al., 2010](#); [Merloni & Heinz, 2013](#)). To get a precise luminosity function large survey experiments, such as the future X-ray instrument eROSITA ([Merloni et al., 2012](#)), are needed. The hard X-rays being particularly important since they include heavily obscured, compton-thick, sources ([Merloni & Heinz, 2013](#)).

2 eROSITA

As was discussed in chapter 1, AGN emit over the whole electro-magnetic spectrum. X-rays are therefore an important regime to study the physics of these objects. Today we live in a golden age for X-ray astronomy, with instruments like *XMM-Newton*, *Swift*, *Chandra*, *Suzaku*, *INTEGRAL* and *NuSTAR* currently operating (Jansen et al., 2001; Burrows et al., 2005; Weisskopf et al., 2002; Mitsuda et al., 2007; Winkler et al., 2003; Harrison et al., 2013) and for the next years to come. All of these instruments have in common that they are built and used almost exclusively for pointed observations. Many missions were launched since the end of *ROSAT* (Trümper, 1982, 1992) in 1998, the first imaging all-sky survey in the soft X-rays, but none were successfully conducted afterwards. A *Broadband Imaging X-ray All-Sky Survey (ABRIXAS)* was planned as the successor mission of *ROSAT*, but could never be used for scientific studies. A design error caused problems in the power supply of *ABRIXAS*, which lead to the loss of its main battery (Predehl, 1999). However the lack of any soft X-ray all-sky survey over more than 15 years will change with the hopefully successful launch of the eROSITA instrument (Predehl et al., 2006, 2007, 2010, 2011; Predehl, 2012; Merloni et al., 2012) opening unique opportunities in studying AGN.

2.1 Mission and Design

eROSITA (extended ROentgen Survey with an Imaging Telescope Array, Predehl et al., 2006, 2007, 2010, 2011; Predehl, 2012; Merloni et al., 2012) is an X-ray telescope developed under the leadership of the Max-Planck-Institute for extraterrestrial Physics (MPE) in cooperation with the following institutes: Dr. Karl Remeis-Observatory in Bamberg, Institut für Astronomie und Astrophysik Tübingen, Leibniz-Institut für Astrophysik Potsdam, Hamburg Observatory, Argelander-Institut für Astronomie at the University of Bonn, the Max-Planck Institut für Astrophysik (MPA), and the Universitäts-Sternwarte München. It is the primary of two instruments designed for the Russian mission *Spektrum-Roentgen-*

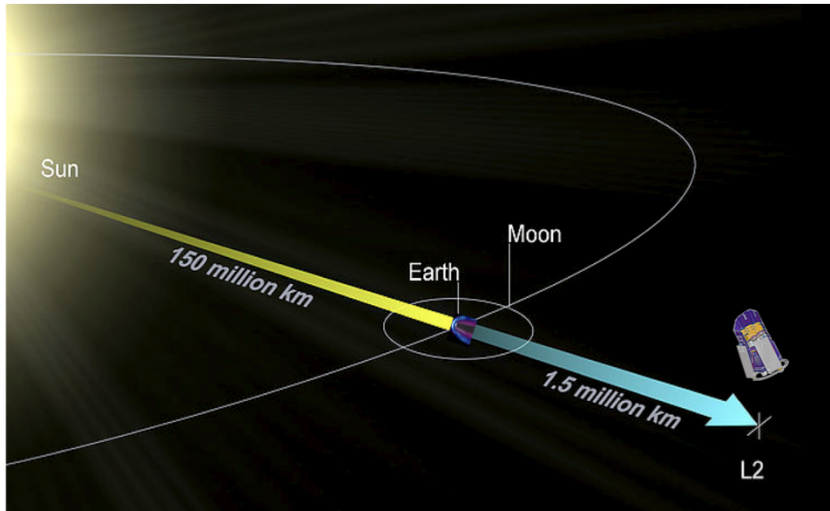


Figure 2.1: The eROSITA telescope will be the first X-ray telescope to view the X-ray sky in an orbit around Lagrange point L_2 , which is a non-stable location of zero gravity. L_2 is positioned on a straight line of the Sun and Earth connection, 1.5 million km behind the Earth not facing the Sun. (Credit: <http://www.stsci.edu/jwst/overview/design/orbit>)

Gamma (Pavlinisky et al., 2007, 2011, 2012, (SRG)), with the second being the *Astronomical Roentgen Telescope – X-ray Concentrator* (ART-XC, Pavlinisky et al., 2006, 2008, 2009). The spacecraft will be launched from Baikonur with a Zenith-Fregat rocket (e.g., Predehl & eROSITA Team, 2013). The planned orbit is around the second Lagrangian point L_2 of the Sun-Earth system (see Fig. 2.1). The choice was made in order to avoid heat radiation from Earth and it allows for longer and stable observations (Merloni et al., 2012). According to the latest (4th) eROSITA bulletin¹ the expected launch of SRG is in December 2015/January 2016.

Three months later the vessel will reach L_2 , and the planned four year all-sky survey will be conducted by both instruments (Merloni et al., 2012). The survey itself will be done by drift scan observations providing a complete scan of the celestial sphere every 180 days. During this slew the satellite is rotating with a scanning axis pointing towards the sun and a complete rotation will take about four hours (Predehl et al., 2011). Thus, a source in a typical field will be observed to move on a track in the detector plane. Taking into account the slew and rotation speed of the satellite a source will be observed a few times in a row on tracks that are offset from each other in the detector plane (see Fig. 2.2). The Point-Spread-Function (PSF) is degrading with the off-axis angles and leads to a widening of the observed tracks at the detector edges (Merloni et al., 2012). The currently planned satellite rotation axis – facing the sun – leads to a deep exposure > 50 ks at the ecliptic poles. Other regions will have a roughly uniform coverage with an average exposure of ~ 2.5 ks² (Merloni et al., 2012). The calculated orbits of SRG are

¹http://www.mpe.mpg.de/5394374/eROSITA_Bulletin4.pdf

²The average exposure is calculated by the survey duration of 4 years times the field of view for eROSITA of 0.833 deg² divided by the square degrees of the sky of 41253 deg²

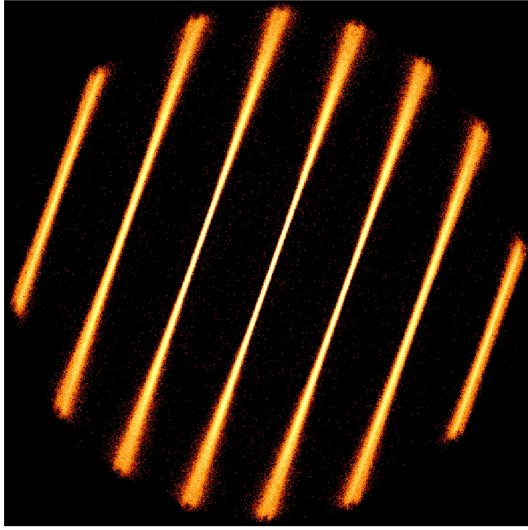


Figure 2.2: Simulated traces for one bright X-ray source caused by the continuous slew of the eROSITA satellite (Schmid, 2012). The traces become wider towards the edges of the FoV caused by the degradation of the PSF for large off-axis angles.

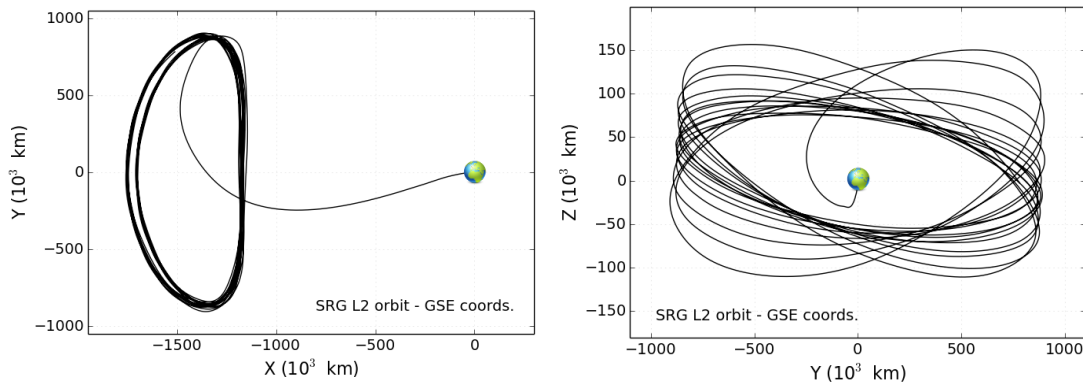


Figure 2.3: The calculated orbits of SRG at L2 (Earth not to scale). (Credit: J. Robrade; orbit data by Applied Math. Inst., Moscow, obtained via I. Lapshov, IKI; http://www.mpe.mpg.de/5394374/eROSITA_Bulletin4.pdf)

depicted in Fig. 2.3. After this all-sky survey program, an estimated time of 3.5 years is currently planned to be dedicated to pointed observations (Merloni et al., 2012).

The key science driver for eROSITA, motivated by cosmology, is to study dark energy by means of detecting all massive galaxy clusters in the observable Universe (Merloni et al., 2012). In addition questions of cosmological models will be addressed by determining the cosmological constants with at least one order of magnitude higher statistics in the

X-rays than before, including a study of the large scale structure in the Universe.

To study the nature of this large scale structure a complete catalog of *eROSITA* detected X-ray sources and information about their characteristics, e.g., redshifts, is required. The expected majority of these objects will be AGN. The current prediction for this mission is the discovery of more than 3 million AGN (Merloni et al., 2012). This large number of predicted AGN is also the subject of a set of questions and is as an additional science driver, e.g., the question on the physical mechanism/s coupling the evolution of super-massive black holes and their host galaxies (Merloni et al., 2012). Besides these main goals a series of other questions will be addressed with *eROSITA* and are explained in the *eROSITA* science book by Merloni et al. (2012).

The technical details and implementation of the *eROSITA* instrument are given in depth by e.g., Predehl et al. (2006, 2007, 2010, 2011), Merloni et al. (2012), and references therein. Based on these a short summary of important technical properties is provided in the following. The *eROSITA* instrument, see Fig. 2.5, is built to be sensitive in the soft X-rays from 0.2-10 keV. It consists of 7 identical mirror modules with 54 gold coated mirror shells each and overall coaligned optical axis Predehl et al. (2006). The design of these mirror shells follows the Wolter-Type I geometry (Wolter, 1952). An X-ray baffle is placed in front of each module to reduce the number of stray photons by single reflection for bright sources outside the field of view (FoV). More than 90% of these photons will be suppressed and the effective area of the instrument is only reduced by $\sim 2\%$ (Friedrich, 2013). Since the mirror system is sensitive to heat and cold, a temperature of $20 \pm 2^\circ\text{C}$ has to be maintained otherwise the mirrors will become subject to deformation and image degradation (Merloni et al., 2012). The on-axis angular resolution for each mirror module is in the order of 15 arcsec half energy width at 1.5 keV and becomes rapidly worse with increasing off-axis angles. A large field of view with 61 arcmin in diameter is achieved for each telescope, which is necessary when performing an all-sky survey.

All seven mirror modules possess their own camera systems which consist of a CCD-module and processing electronics, allowing them to operate independently. Thus in the event of a malfunction of one or more mirror modules, the remaining ones can continue to take data. The *eROSITA* detector is a back illuminated frame-transfer CCD based on the XMM-Newton pn-CCD (Meidinger et al., 2011). An illustration of the CCD-module is shown in Fig. 2.4. X-ray photons will illuminate the CCD from the back producing charges in the pixels. After an integration time of 50 ms this charge will be shifted to a frame-store CCD in $115 \mu\text{s}$ which is shielded against X-rays. Three analog signal processors (CAMEX) will simultaneously read-out the frame-store CCD in 9 ms. This type was chosen to reduce the amount of out of time events to 0.2% (Meidinger, 2013). Out of time events are photons hitting the detector during the time when the signal charges are shifted to the anodes for readout. Therefore they are assigned to wrong pixel values which leads to a wrong reconstruction of their origin.

The size of the imaging CCD-detectors is $28.8 \times 28.8 \text{ mm}^2$ and has 384×384 pixels, the size being $75 \times 75 \mu\text{m}^2$. The frame store CCD inherits the same number of pixels but of a smaller size. The CCD-modules will be kept at a proposed working temperature of -90°C (Merloni et al., 2012). A temperature control system will try to maintain the CCD temperature within $\pm 0.5^\circ\text{C}$. The camera system will be shielded against particle radiation by a copper housing and an additional graded shield will protect the CCD modules from

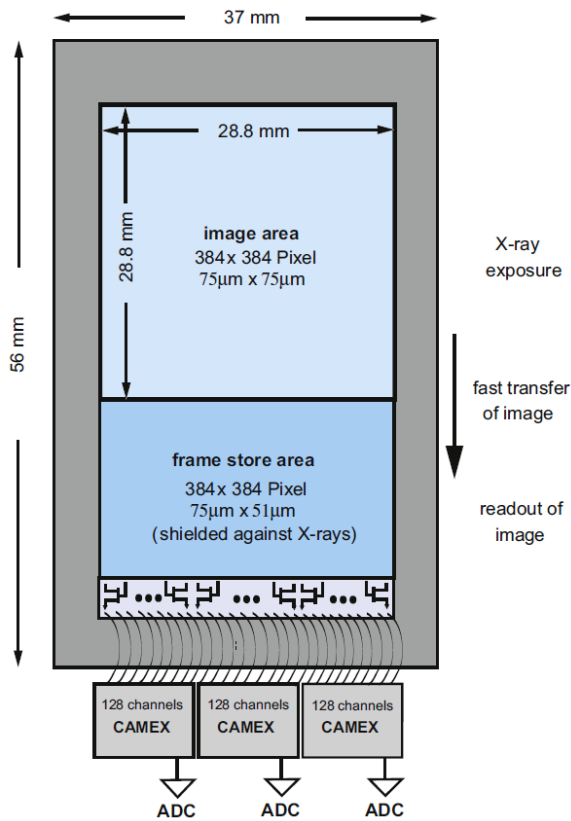


Figure 2.4: Illustration of the eROSITA frame-store CCD. Incident photons produce charges in the pixels of the image area. After an integration time of 50 ms the charges are shifted to the frame store area in ~ 0.1 ms and then readout by the CAMEXs, analog signal processors. [Meidinger et al. \(2011\)](#)

fluorescent X-rays generated in the instrument. An energy resolution of 138 eV at 6 keV is expected for the CCD ([Predehl et al., 2011](#)). As calibration sources radioactive ^{55}Fe and a Al/Ti target will be used, which will produce prominent lines, e.g., at 1.5 keV and 4.5 keV.

The camera system has only three operational modes: standby, checkout, and normal ([Merloni et al., 2012](#)). Only radiation hard components were used for the electronics. The tasks of the electronics for each mirror module is to:

- digitize the CAMEX output
- provide correct timing signals
- process the events, e.g., by applying a threshold
- act as a control unit, collecting telemetry data and executing commands

The expected telemetry rate of events is ~ 3.6 kbits/s and is based on the assumption of a typical photon rate of $30\text{--}40\text{ s}^{-1}$. This also takes into account the production of split events (see [Schmid, 2012](#), for a good explanation on this topic), and the 30 bit encoding for each event. The typical telemetry data rate is increased to ~ 10 kbits/s with the addition of housekeeping data and some overhead ([Merloni et al., 2012](#)).

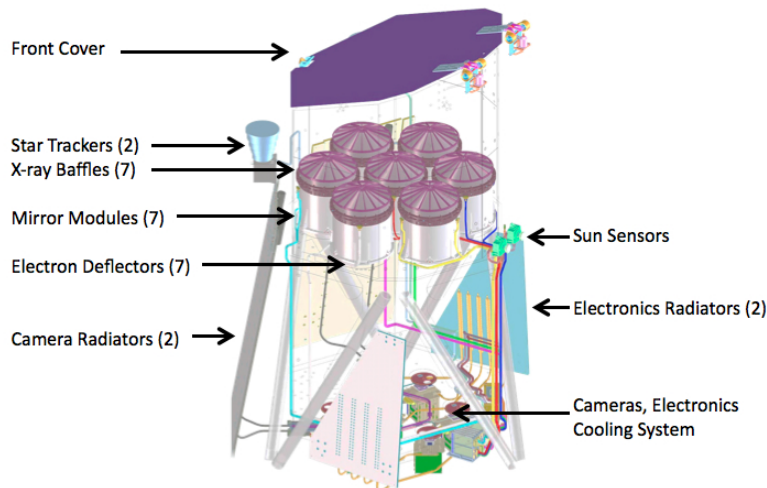


Figure 2.5: Schematic illustration of the eROSITA telescope structure with its various components. [Predehl \(2013\)](#)

2.2 Data processing

The focus in this section is set on my work for the eROSITA mission, which is the management of the data processing prior the dedicated Science Analysis Software System (SASS) and the Near Real Time Analysis (NRTA) and usually referred to as the preprocessing of the data (Preprocessor).

2.2.1 Data flow

Before any data can be scientifically analyzed and new results be generated, the recorded data of each telescope must be prepared for scientific use (e.g., calibration). As a first step the data will be transmitted as a binary telemetry stream to a ground station (see Fig. 2.6 and 2.7). At the time of writing two ground stations (Spectrum-X) with a TNA-57 12 m antenna in Baikonur and Bear Lakes are planned to be used ([Predehl, 2013](#)). For the early phase of the mission and its corrections the additional ground station Fobos with a P-2500 antenna in Ussuriysk can be used. As an additional back-up antenna system the TNA-1500 (Cobalt-M-FG) 64 m in Bear Lakes can be engaged to increase the radio link stability to the spacecraft. The data which will be transmitted to the ground stations include ([Wilms et al., 2009](#)):

- scientific data from the CCDs – photon event list containing the information about the time, position, etc.
- diagnostic data from the camera system – noise maps, offset maps, etc.
- time resolved sensor information – voltages, temperatures, etc.
- other housekeeping data – state of instruments, etc.
- data from the attitude sensors
- data from the star trackers

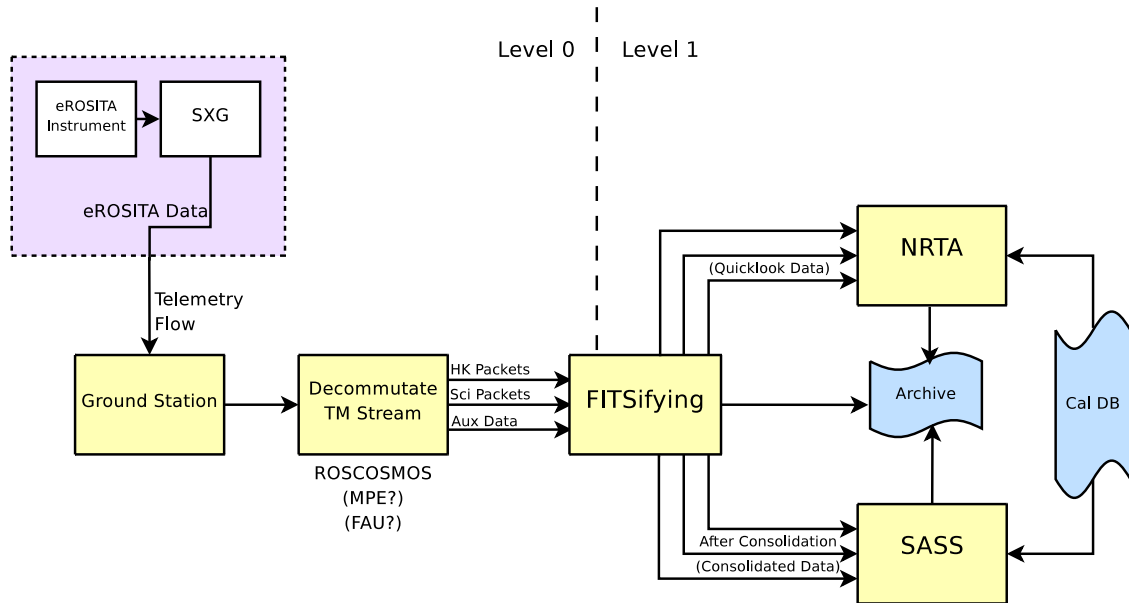


Figure 2.7: Illustration of the data flow starting on-board the eROSITA satellite transmitted to the ground station, processed and ending in the NRTA and SASS pipelines. [Wilms et al. \(2009\)](#)

of utility programs to create, examine, or modify data files in the FITS (Flexible Image Transport System) format” ([Pence, 1992](#))⁵. The work-flow within SASS can be described as a data-processing pipeline using the products of the preprocessing stage as an input and performing the tasks of event calibration, image and exposure map creation, source detection and characterization, and the extraction of source specific products (see Fig. 2.8). The pipeline will be set up to process pointed and survey-mode observations. The data of the all-sky will be organized in fields of equal size ($3.6^\circ \times 3.6^\circ$) with a total of 4700 overlapping regions.

2.2.3 Near Real Time Analysis – NRTA

The Near Real Time Analysis (NRTA) is a pipeline software package with the primary goal to continuously monitor the status of the eROSITA instrument ([Wilms et al., 2009](#)). A secondary purpose is to provide a quick scientific look at the data. Therefore the NRTA is divided into two parts, one with the main focus on the housekeeping data, and the other focusing on the event data of the latest observation. The health monitoring of the eROSITA instrument involves many different tasks with a subset given in the following:

- checking housekeeping parameters to be in their allowed limits
- monitoring the state of the instrument (e.g., data mode) and providing warnings in case of unexpected behavior
- automated search for malfunctioning in imaging, e.g., bad pixel detection, cold

⁵https://heasarc.gsfc.nasa.gov/lheasoft/ftools/ftools_quicky.html

eROSITA data processing pipeline

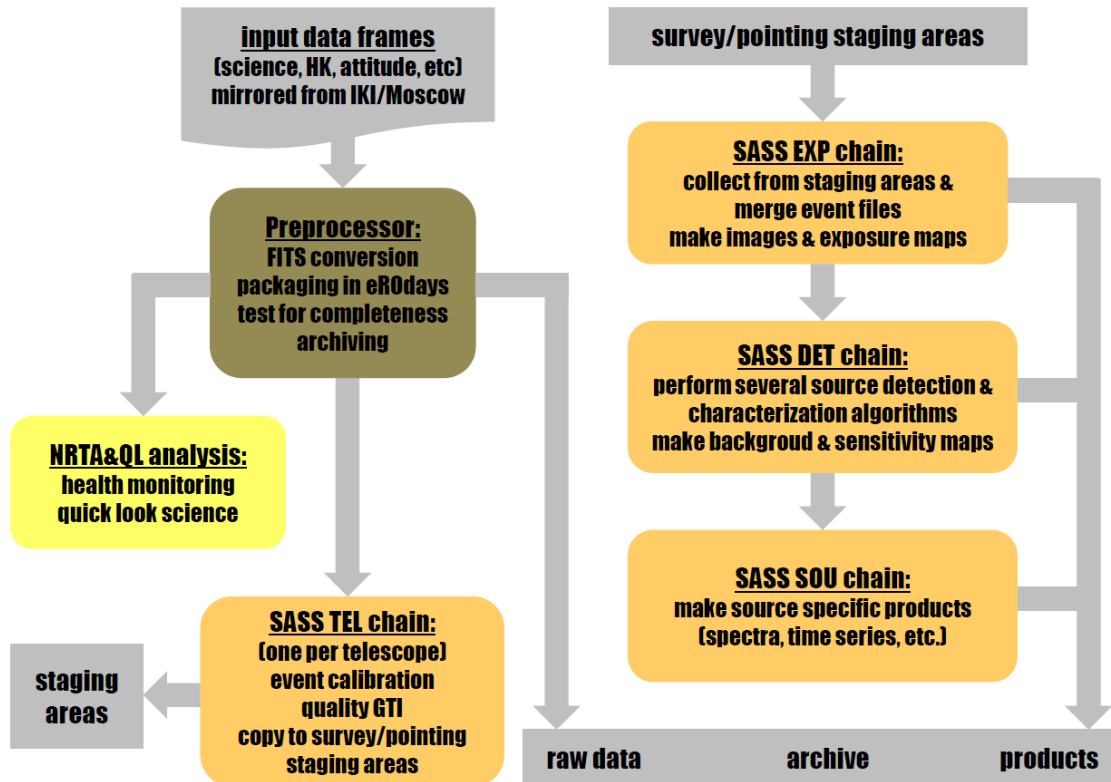


Figure 2.8: SASS processing pipeline as developed for the eROSITA satellite. priv. comm. Hermann Brunner

pixel detection, dead columns and others (Wille, 2011)

- providing overview plots for the time evolution of housekeeping parameters

It is important that the health monitoring is performed promptly after receiving the data to ensure the safety of the instrument. The scientific part of NRTA makes use of the SASS pipeline for providing a first preliminary scientific analysis. The tasks include the search for transient behavior in the initial images by generating lightcurves and spectra, and identification of sources and comparison to the expected values of a catalog. In case of missing information such as the attitude, mission planning files and interpolations will be used to provide SASS with the necessary information. A similar fast processing of the event data is required for these science tasks of the NRTA as well to immediately identify interesting events and potentially trigger follow up programs.

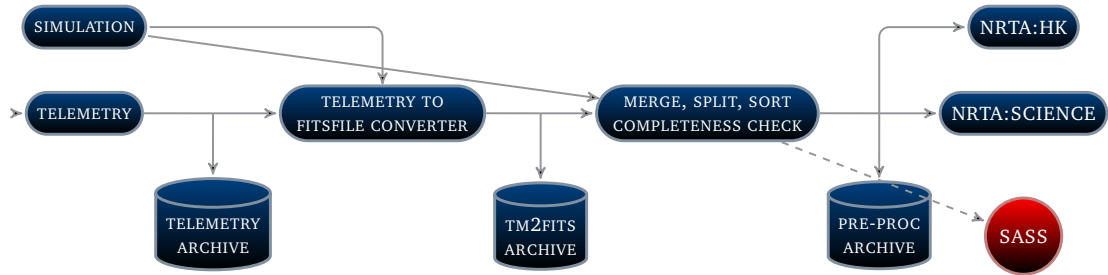


Figure 2.9: The pre-processing pipeline. The incoming telemetry data is converted into certain FITS files, which will be merged, split, sorted according to the requirements of the SASS or different parts of the NRTA.

2.3 Pre-processing

The main purpose of the pre-processing pipeline is to take the incoming telemetry data stream (prior to launch simulated data) as an input in order to create FITS files, prepare these according to the standard required by the SASS and NRTA pipelines, and archive the data (see Fig. 2.9). Each step in the pipeline was written as a stand-alone program to ensure maximum flexibility, in case new tasks have to be added in the future, or become obsolete. Parameters to all programs can be either provided by command line or by parameter files using the Parameter Interface Library (PIL) or the All-purpose Parameter Environment (APE). The source code makes extensive use of the HEASoft package provided by HEASARC especially using routines of the CFITSIO and FITSIO libraries. The task, concepts, and implementation of the main programs will be presented in this section.

2.3.1 Telemetry to FITS File conversion

Task

As explained above, a binary telemetry data stream will be received at the ground station. The data will then be made available to the German eROSITA team by means which are currently under discussion. We assume that the binary data will arrive with a certain time delay at the data center and therefore do not guarantee a timely order. These binary data have to be decoded into the various data types:

- Housekeeping Data (HK) – voltages, state of instruments, etc.
- Event Files (EVT) – photon list
- Maps (MAP) – noise maps, offset maps, etc.
- Star Trackers

A separate FITS file with columns sorted in time is be written for each package including a Good Time Intervall (GTI). Figure 2.10 illustrates the task of the telemetry to FITS file conversion. For each telescope a separate FITS file is produced.

ing for the sync-word marking the start of a package on a bit by bit basis. The search on a bit level was chosen to account for potential bit shifts, truncated records, etc. If a record is found it is read into memory and corrections are applied (offsets and scaling factors). The program then fills the appropriate data structures for EVT, HK and MAPS with the content of this record and continue to collect information of new packages until either a user-defined limit is reached or the whole binary file has been processed. Afterwards a FITS file is created and the data, sorted in time, is written to disk (Wilms et al., 2009). The GTI of the data are derived and appended as a GTI extension to the FITS file. In a last step new header keywords specifying the type of the data are added.

2.3.2 Merge and Split

Task

The second major task of the pre-processing pipeline is to take the output files of the TM2FITS task and use them to create new FITS files which comply to the requirements of the archive, SASS and NRTA. The current design of the archive structure requires that each input FITS file contains only data for one specific eroday defined as 4 h which is approximately the expected revolution time of the satellite. The counting of these erodays starts at a specified time, which is not yet defined, but we currently consider it to be the start of the survey. In a current discussion a change to the strict split after 4h of data was proposed. The argument for this change is that some data, e.g., parameters for the calibration, will not be available in every frame but only in every few frames. These parameters are valid from that point on until a new value is received. In a different scenario the SASS derives new parameters in every frame by interpolating the sparsely sent parameter values. Thus by continuing with the current design, splitting the data exactly after 4h, most files would contain some frames for which the value of these parameters is unknown. As a way to solve this problem the content of a FITS file should be expanded by extending the 4h with data before and after the eroday. This additional time will be in the order of a few seconds and based on the lowest rate at which crucial parameters will be transmitted.

An additional requirement on the merge and split task is given by the NRTA, which requires the data to be well structured such that an easy inspection is possible. There is no guarantee that the data packages received by the TM2FITS converter contain information of consecutive frames and might be even distributed over multiple binary files. In this scenario the TM2FITS task produces multiple output FITS files and an operator studying the time evolution of one the parameters, e.g., temperature of the mirrors, has to inspect all files.

Therefore the merge and split task merges all files containing the same application identification and splits them into multiple files containing the information of one eroday.

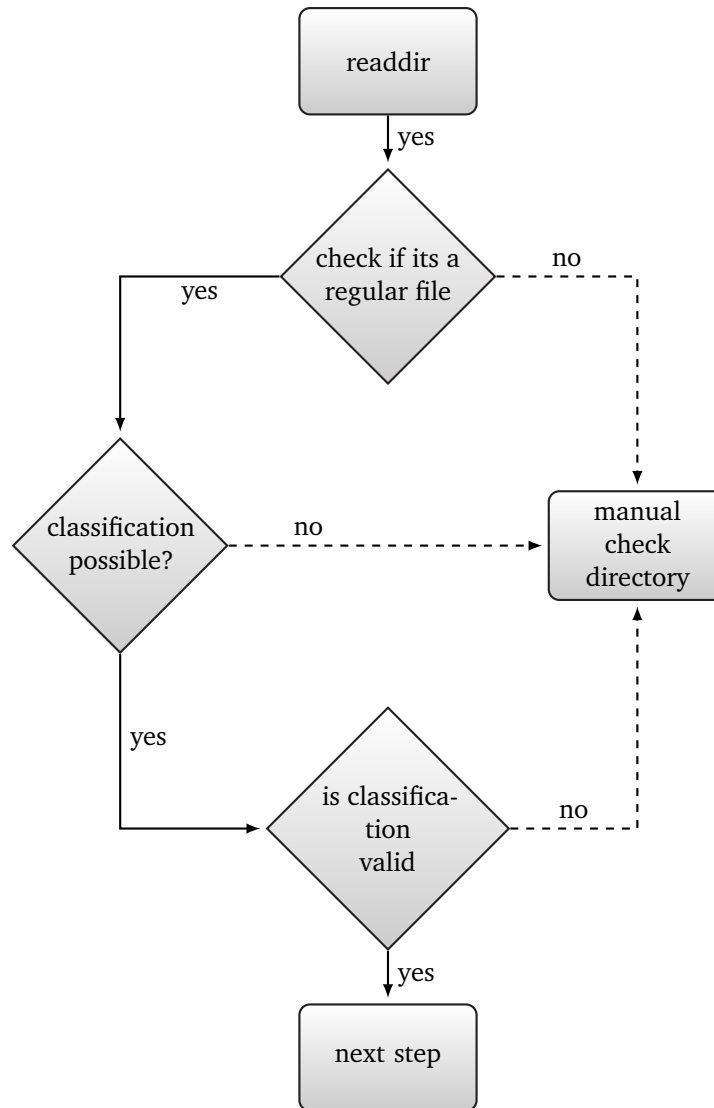


Figure 2.11: Validation step

Concept

The merge and split program operates on all files found in an input directory (e.g., the output directory of TM2FITS). At first the program validates each file by checking against a certain standard and classifying it. The definition of classes is provided in a separate FITS file. If a file is invalid it is marked for manual inspection and moved to a separate directory. A flow diagram of this concept is depicted in Fig. 2.11. A file passing the validation is processed. Depending on the class of a file and the contained time information, multiple files are created and some parts of the contained data are merged with preexisting files.

Implementation

Like the TM2FITS converter the program first reads the parameters provided by command line or by use of a parameter file. Afterwards a log file in the FITS format is created to report any incidents occurring during the program. The default name of the log file consists of the date when the program is executed. The log file contains the time, error code and a text describing the incidents.

The merge and split task operates on four directories which are by default:

- an input directory, usually the output directory of TM2FITS
- a processing directory, new files will be created here or data will be merged with the files in this directory
- a log directory, to store the log files
- a manual inspection directory, all files which are either corrupt or do not comply to the standards will be put here

At first any preexisting files from the processing directory are checked for the FITS format and compliance to classification. This step is referred to as the *validation check* and is used for multiple directories and other programs as well. I describe it once and refer to this procedure later on. The validation check verifies that a file contains a certain HDU extension depending on the data type (EVT, HK, MAP) and includes an additional GTI extension. In addition, certain header keywords are read and the erodays of the data are calculated on the basis of the GTI extension. The determined parameters and values are then cross-checked with the ones given in a FITS file describing all valid data types and formats. If one of these steps fail the file is assumed to be invalid and will be moved to the manual inspection directory. Future work will expand the validation check by having the additional requirement that each data type has a fixed number of columns and fixed column names.

After the validation check on the processing directory, the input directory is checked. Any telemetry file (TM file) passing this test is further processed by the merge and split task. For each determined eroday a file name is generated. Amongst others, the file name contains information about the data type and the eroday. The program continues by searching in the processing directory for the possible existence of a file with this specific name. Such a file could have been created by previous runs of the program and was neither deleted or moved by other programs at later stages.

The next steps only apply to EVT and HK files, while MAP files are copied to the processing directory. If no FITS file with this name was found, a new one (with this name) is created, by copying the TM file to the processing directory with the exception of the GTI extension. All files produced by the merge and split program are henceforth called PP files (preprocessed). A new temporary file with a reduced GTI matching that of the eroday currently being processed is created afterwards. The temporary GTI file is then applied as a filter to the newly created PP file, reducing the data to only contain data of this particular eroday. Afterwards the GTI extension is appended to the PP file and header keywords updated to prepare it for further processing. Finally the processing directory is cleaned by removing all temporary products. The flow diagram of this part in the merge

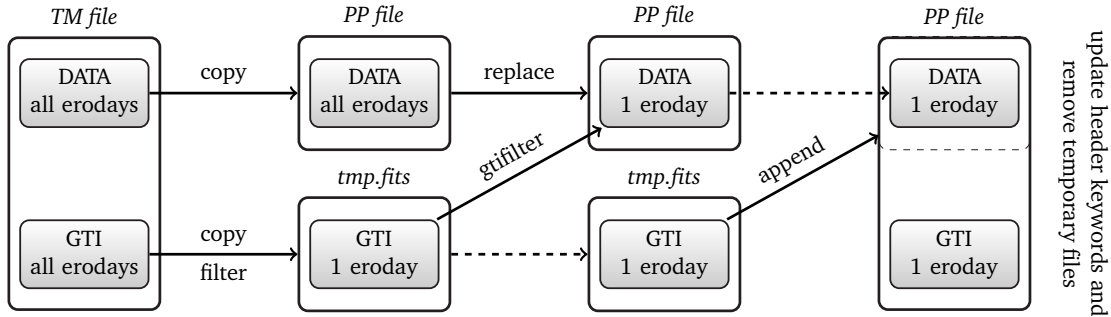


Figure 2.12: Processing of *TM file* if no *PP file* with the same specifications exists. The black boxes indicate a *FITS file*, while the shaded boxes the *HDU extensions*.

and split task is depicted in Fig. 2.12.

In the case that a *PP file* with the specific name already exists in the processing directory, a different course of action is performed (see Fig. 2.13). The program merges the data extensions of the *PP* and the *TM file* into a new temporary file. Necessary header keywords are copied to that temporary file as well. Afterwards, the merge and split task creates a second temporary file by merging the *GTI* extension of both files and filtering it to only contain the *GTI* values of the eroday being processed. The program then appends the temporary *GTI* file to the temporary *PP file* before it applies the *GTI* extension as a filter on the data. Thus only data for the eroday remains and the initial *PP file* is overwritten by the merged file. In the final step the program updates the header keywords (i.e. with the time when the file was created) and disposes the created temporary files.

This course of action is executed for each determined eroday in the *TM file*. Each *TM file* which is completely processed by the merge and split task is removed from the input directory.

2.3.3 Completeness check

Task

After the merge and split task is finished, the produced *PP files* are checked for completeness and if so marked for archive ingestion. A second test is performed in case a file is incomplete to check whether the file is eligible to be treated as complete. The reason for this second test is that a possibility exists for files to be incomplete forever, or at least a very long time. This scenario might be happening due to packet losses in the transmission process to the ground station, when transferring the data to the processing side, or due to huge time delays by the prioritization of data. Therefore to avoid these files to be stuck forever in the processing directory and never to be analyzed, this second test is executed.

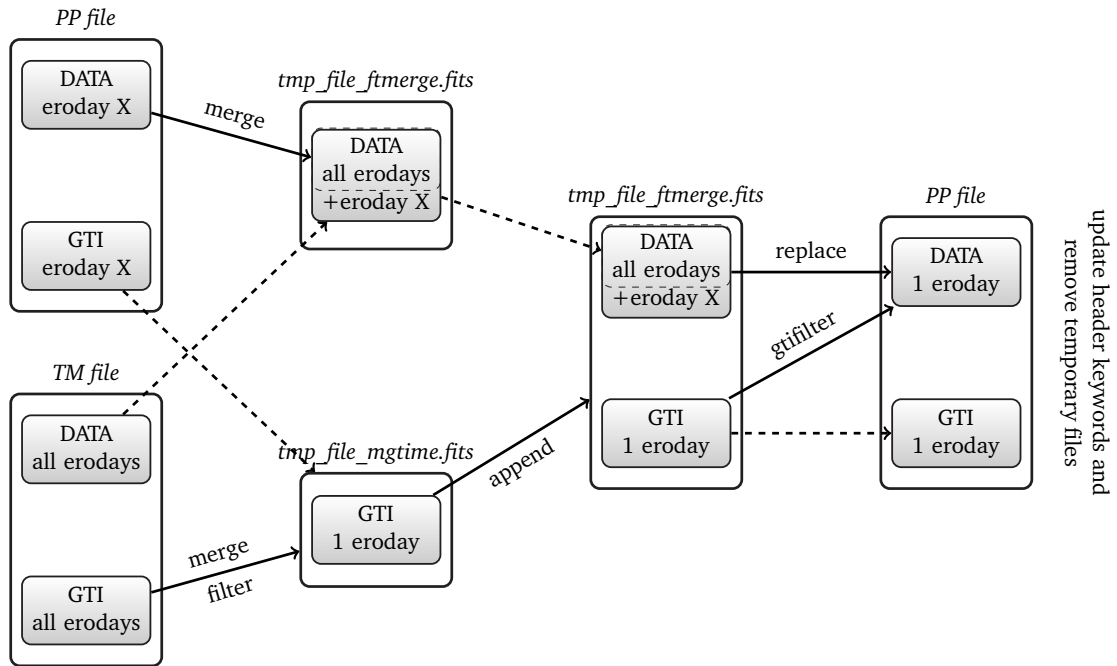


Figure 2.13: Processing of *TM file* if a *PP file* with the correct name already exists in the processing directory. The black boxes indicate a *FITS file* while the shaded boxes its HDU extensions.

Concept and Implementation

Like all programs parameters are read in first before the logging is set up. The completeness check task begins with a validation check on the processing directory. Afterwards it tests the completeness of each PP file in this directory. A PP file is considered to be complete if the GTI extension contains only one row and the start/stop entry complies to the onset and end of the eroday, given in as header keyword in the file. In the case of the GTI extension being complete, a header keyword of the PP file is updated to reflect its new status. If the PP file is incomplete a header keyword which contains the date when the file was first processed by merge and split is read. If the difference between that date and the current date is large enough, currently set to a total of three days, the file is also marked as complete.

2.3.4 Archive ingestion

Task

The archive ingestion task operates on the files found in an input directory which is by default the processing directory. All files marked for as complete are then transferred to the archive and the SASS is triggered to process the data type and eroday of that file.

Concept

In principle the input directory is processed on a “per file” basis. The FITS files are validated and the header keyword, which contains the status of the files, is read. In the case that a file has to be archived the program cross-checks with a separate FITS file containing the information of all files moved to the archive for whether a record for a file of this data type and eroday already exists in the archive. If at least one file transfer is found, a merged file is produced and copied to the archive instead of a plain copy to the archive. Regardless of the way in which the data is copied to the archive, the SASS is triggered afterwards.

Implementation

The program reads the parameters and a log file are set up. Before any data are transferred to the archive the validation check is performed on the input directory, which is the processing directory by default. Once the status of a file, by reading of the appropriate header keyword, is determined only data with the correct status are processed while all others just remain in the directory. The archive ingestion task continues by checking the current archive structure (see Fig. 2.14) if the appropriate directories to which the data will be copied already exist and creates them if necessary. The archive structure includes different directories depending on the eroday of a file and its data type.

Afterwards an archive index file which contains the information (classification, eroday, etc.) of all files in the archive and complies to the FITS format is opened. This archive index file is searched for entries of the same eroday and classification. If no matching entries are found the file, which is currently processed, is moved to the archive and a record in the archive index file is created. In the case that one or multiple matching transfers are found, a merging procedure as in Fig. 2.13 is executed. The constituents of the merging are the files which are currently processed and the latest file in the archive with the same data type and eroday. This merged file is then copied to the archive and removed from the pre-processing directory. This course of action only applies to FITS files containing a binary table, namely EVT and HK data files. In the case of MAP files, it is plainly copied to the archive with a new name reflecting the number of versions of this file. Finally, the archive index file is updated and the SASS is then triggered by creating a certain file in an appropriate directory.

2.3.5 Test of the pre-processing tasks

The pre-processing is a crucial task in the data flow of the mission, being the first to convert the telemetry data into a human readable format and preparing it for the use of the sophisticated pipelines SASS and NRTA. Therefore, all tasks should be subject to extensive testing prior to the launch of the mission. At the moment we have performed early tests on the functionality of the tasks by using data from the TRoPIC camera, the prototype camera for eROSITA ([Freyberg et al., 2008](#)). The TRoPIC camera is also a back-illuminated frame-store CCD with pixels of the same size as the ones being used in

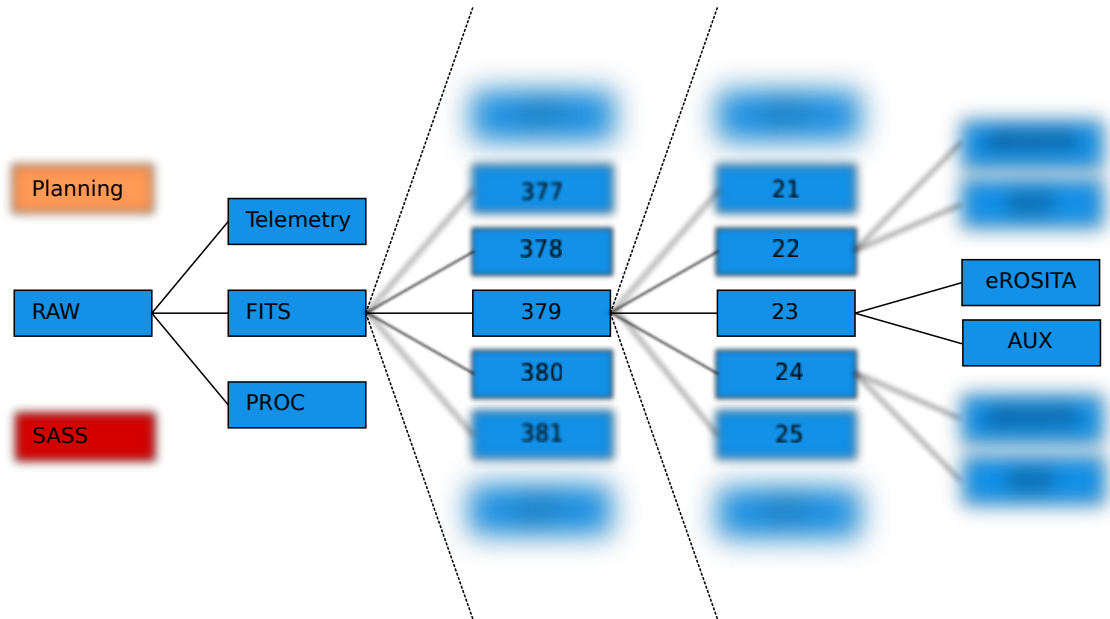


Figure 2.14: Archive structure for the eROSITA data. On a first level directories exist for the planning files, files produced by the SASS, and raw files. Files produced by the pre-processing tasks are ingested into the RAW directory hierarchy which includes separate folders for telemetry, processing and FITS files. The FITS files are sorted into different directories depending on the eroday. The first three out of five digits of an eroday define the first level while the last two the second level. The third level divides the FITS files into eROSITA relevant data and auxiliary files.

eROSITA. The only difference is that the number of pixels is only 256×256 instead of the 384×384 for the real camera.

A set of binary telemetry data files for which the FITS file representation was known (provided by MPE) was fed into the TM2FITS converter using a XML file describing the TRoPIC format. The resulting FITS files were compared with the FITS file representations showing no unexpected differences. Artificially created errors, e.g., changing the number of bits for packages, lead to the expected result of the generation of a log message stating that this package is corrupt.

The merge and split tasks were tested with the generated FITS files by TM2FITS ensuring that the programs can be operated in a pipeline like behavior. Executing the program lead to the correct creation of files and header keywords. This was tested for different duration values of an eroday and no temporary files remained in the processing directory. We also tested the task to correctly move “wrong” files into the manual check directory by putting various other files in the input directory. Amongst these were files which did not comply to the FITS format or for which the data type was not allowed. All of these files have been successfully moved to the directory for manual inspection.

The completeness check task was then operated on the files created by the merge and split program. Instead of the expected 3 days waiting time we changed it to a reasonable timescale. In our test file sample we had complete files and also incomplete ones. Check-

ing the header keyword after the first run showed that all complete files were marked for archive ingestion and the others were not, since not enough time had passed since their creation. We reran the program multiple times and always checked the header keywords, and only after the waiting time was over were the status of the incomplete files changed. Thus the program worked as intended.

The archive ingestion tool was tested with the same files as above but only some were marked for archive ingestion. Every marked file was correctly put into the archive with the archive directory structure being created at first, if necessary. We then tested the case of a file with the same data type already present in the archive by copying that file to the processing directory and marking it for archive ingestion. After running the program again, we confirmed the second entry in the archive log file and a second file with the correct naming convention in the archive. Verifying the content of that file showed the expected duplicate entries. Although, it must be noted that duplicate entries is a behavior which is not desirable at launch date.

2.3.6 Outlook

Future work for the pre-processing pipeline includes the use a sophisticated simulation to test our tools. A simulation framework was written for eROSITA and other satellites by [Schmid \(2012\)](#). We already made use of this, simulating the AGN population at one ecliptic poles by using a XLF to distribute the AGN according to their redshift (see Fig. 2.15) . We will expand this work by simulating a full four year all-sky survey of eROSITA including AGN sources, transient X-ray sources, and galaxy clusters. This will allow us to test the performance of our programs by processing the whole simulated data set. This is also important in the prospect that a (re-)processing of a whole survey is not unlikely to happen based on our experience with other missions.

We will also continue to test the functionality of our programs by artificially creating new errors. In additional we will ask other people to modify and corrupt files to maximize the number of possible problems which our tools could encounter.

As was already pointed out in the sections above, we will add an additional classification scheme in the validation check. This criteria is based on the number and names of the columns which will be defined for each data type. Moreover we will write another tool to search the PP files for duplicate entries and handle these. Although the way of treating these entries is still under discussion, the basic idea is to remove them from the file and generate a detailed log message.

This summarizes the upcoming plans for the pre-processing pipeline but more work will be done since our responsibility also includes the NRTA. As was already pointed out in section 2.2.3 the main task of the NRTA is to monitor the health of the instrument and provide a first scientific analysis. Sophisticated tools for the NRTA like a program to detect bad pixels, bad lines, etc. by [Wille \(2011\)](#) were already produced. The latest addition to these was a program with the task to check whether parameters are within certain limits and produce an output containing the information. A future program will then work on these results producing warnings and in case of emergencies contacting the operator by any means possible.

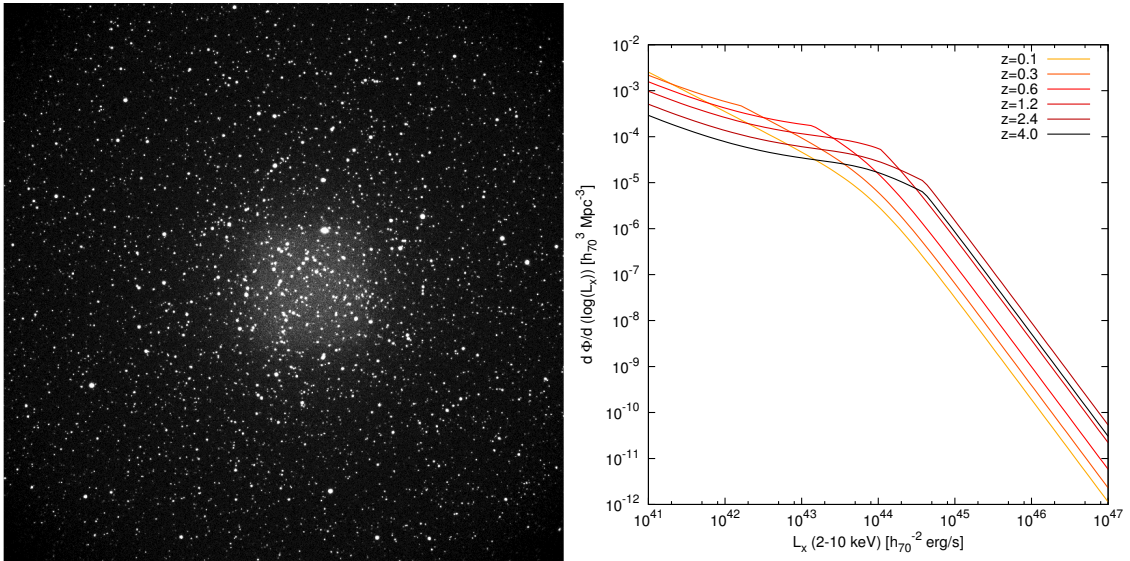


Figure 2.15: *left:* Simulation of a full 4 year survey polar field of AGNs. *right:* X-Ray Luminosity Function describing the number density of AGN in relation to their intrinsic luminosity for different redshifts. (Credits: Christian Schmid and Thorsten Brand, priv. comm.)

In addition we started the development of a web interface to display a series of overview plots and which is flexible enough to provide a more detailed view on parameters, maps, and more if necessary. This interface will also grant access to preliminary scientific results of an early analysis of the EVT data performed by the NRTA. It will include the image of the current X-ray sky as seen by eROSITA, a list of detected sources, marking and displaying new found objects, and reporting strong flares observed in transient sources. To achieve this, new sophisticated tools to produce images, perform source detection runs, match found sources with catalogs and search for unusual behavior of known objects will be created. All of these programs will be designed to make extensive use of the SASS framework, which shares the same tasks. Thus using the SASS will significantly reduce the amount time needed to develop these programs. The difference between the tools of the SASS and the NRTA is that the SASS has access to more information, e.g., the attitude. Therefore, tools in the NRTA will derive necessary information from files or extrapolation, e.g., in the case of the attitude, by extracting the missing information from mission planning files.

3 VLBI

[Jansky \(1933\)](#) measured for the first time radio waves from outside the solar system with a single antenna at a wavelength of 14.6 m. The position of this radio emission was close to the Galactic center of our Milky Way but the uncertainties on the angular resolution was high at 30°. Today we are able to observe objects with an angular resolution better than 1 milliarcsecond with radio interferometry arrays (a review on the historical development is given by [Kellermann & Moran, 2001](#)) in comparison. This is pretty amazing considering the fact that the angular resolution θ of a telescope is given by the Rayleigh criterion:

$$\sin \theta \approx 1.22 \frac{\lambda}{D} \quad (3.1)$$

with D denoting the diameter of a telescope and λ the observing wavelength. Thus, radio observations with telescopes should have the least resolution. With the ability to combine several radio telescopes into an interferometric array, the diameter of the array is not given by the diameter of a single telescope but by the distance between the telescopes. Using telescopes which are separated by a few thousand kilometers would thus increase the angular resolution to the order of milliarcseconds or even better. A dedicated synthesis array, the Very Long Baseline Array (VLBA, [Napier et al., 1994](#)) of the National Radio Astronomy Observatory (NRAO), has been build using this technique which is referred to as Very Long Baseline Interferometry (VLBI). The VLBA (see Fig. 3.1) was used for all observations analyzed in this thesis. It consists of 10 antenna located in the USA with a maximum separation of over 8000 km. It is a dedicated instrument for VLBI, i.e. all telescopes are identical, having a 25 m dish each which reduces the amount of work needed for correlating and calibrating the data in comparison to heterogeneous arrays.

Other radio interferometer synthesis arrays not dedicated to VLBI are the Atacama Large Millimeter/submillimeter Array (ALMA, [Wootten & Thompson, 2009](#)) in Chile with more than 60 telescopes, the Jansky Very Large Array (JVLA, formerly EVLA, [Perley et al., 2011](#)) in the USA and the e-MERLIN¹ in the UK. Radio interferometer arrays are a few

¹<http://www.merlin.ac.uk/e-merlin/>

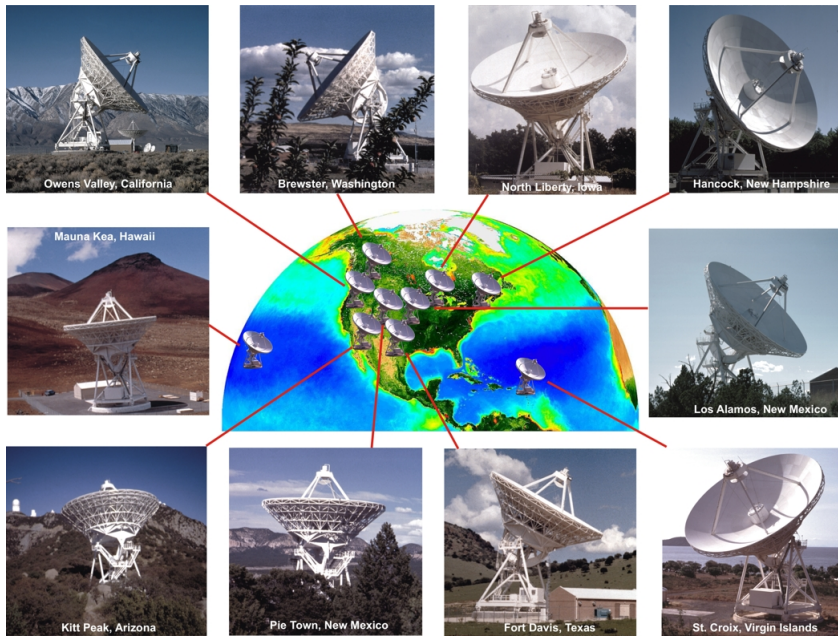


Figure 3.1: The VLBA radio telescopes and their locations in the USA. (Image courtesy of NRAO/AUI and Earth image courtesy of the SeaWiFS Project NASA/GSFC and ORBIMAGE)

times a year combined with individual radio telescopes to form even larger instruments e.g., the European VLBI Network (EVN, [Venturi, 2010](#)) or the Global Millimeter VLBI Array (GMVA, [Krichbaum et al., 2008](#)). A way to even further increase the resolution capabilities of these arrays is the addition of a space radio telescope such as the Russian RadioAstron (baselines $\sim 300\,000$ km, [Kardashev et al., 2013](#)) or the Japanese VLBI Space Observatory Programme (VSOP, [Hirabayashi et al., 2000](#)).

In the following sections the fundamentals of VLBI will be explained with the main literature being the textbook by [Taylor et al. \(1999\)](#) on the topic of synthesis imaging.

3.1 Fundamentals of Radio Interferometry

The techniques to obtain highly resolved images by synthesis arrays can be understood from the concepts of basic two-element interferometers ([Swenson, 1969](#); [Thompson, 1999](#)). We assume a source to be located at a distance such that: the far-field approximation is valid, the incoming electro-magnetic radiation can be considered parallel, and the emission from different parts in a source is uncorrelated. Two antennas, as displayed in Fig. 3.2, will point in the direction to this source given by the unit vector \mathbf{s} and the distance between the telescopes is usually referred to as **baseline** and is given by \mathbf{b} . The plane wavefront of the incoming radiation is registered at different times at the antennas

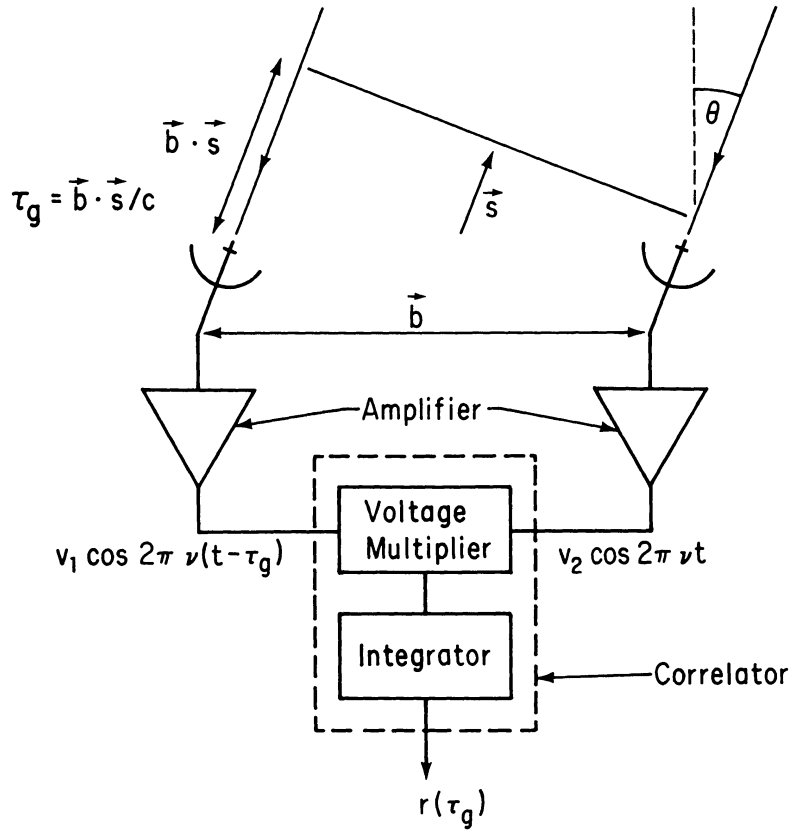


Figure 3.2: Two element interferometer with the baseline \vec{b} pointing in direction \vec{s} , and the expected geometric delay depending on θ . [Thompson \(1999\)](#).

which can be expressed in the form of a geometrical delay τ_g given by

$$\tau_g = \frac{\vec{b} \cdot \vec{s}}{c} \quad (3.2)$$

with c denoting the speed of light. The incoming signal of the antennas is amplified and a bandpass filter $\Delta\nu$ on the central frequency ν is applied ([Thompson, 1999](#)). The voltages (signals) can then be expressed as $V_1(t) = v_1 \cos 2\pi\nu(t - \tau_g)$ and $V_2(t) = v_2 \cos 2\pi\nu t$ and the correlator output can be written as:

$$R(\tau_g) = v_1 v_2 \cos 2\pi\nu\tau_g \quad (3.3)$$

The geometrical delay τ_g slowly changes in time due to the rotation of the earth which leads to an oscillating correlator output that can be understood as the source moving through the fringe pattern of the interferometer (Thompson, 1999). The output R can also be written in the form of

$$R = \Delta\nu \int_S A_{\text{eff}}(\mathbf{s}) I(\mathbf{s}) \cos \frac{2\pi\nu \mathbf{b} \cdot \mathbf{s}}{c} d\Omega \quad (3.4)$$

with $I(\mathbf{s})$ being the source brightness in units of $\text{Wm}^{-2}\text{Hz}^{-1}\text{sr}^{-1}$, $A_{\text{eff}}(\mathbf{s})$ the effective area, $d\Omega$ the source element and the integral taken over the surface of the entire sky S . One usually defines the center of the synthesized field of view as \mathbf{s}_0 , which is typically the position of the source and referred to as the phase tracking center (Clark, 1999). One therefore writes $\mathbf{s} = \mathbf{s}_0 + \boldsymbol{\sigma}$ with $\boldsymbol{\sigma}$ as the displacement of the emission from the phase tracking center. With Equation 3.4 the correlator output becomes

$$\begin{aligned} R = \Delta\nu \cos\left(\frac{2\pi\mathbf{b} \cdot \mathbf{s}_0}{c}\right) \int_S A_{\text{eff}}(\boldsymbol{\sigma}) I(\boldsymbol{\sigma}) \cos \frac{2\pi\mathbf{b} \cdot \boldsymbol{\sigma}}{c} d\Omega \\ - \Delta\nu \sin\left(\frac{2\pi\mathbf{b} \cdot \mathbf{s}_0}{c}\right) \int_S A_{\text{eff}}(\boldsymbol{\sigma}) I(\boldsymbol{\sigma}) \sin \frac{2\pi\mathbf{b} \cdot \boldsymbol{\sigma}}{c} d\Omega. \end{aligned} \quad (3.5)$$

As a measure of the spatial coherence of the incoming electric field one defines the complex visibility V as:

$$V = |V| e^{i\Phi_V} = \int_S A_N(\boldsymbol{\sigma}) I(\boldsymbol{\sigma}) e^{-2i\pi\nu \mathbf{b} \cdot \boldsymbol{\sigma}/c} d\Omega \quad (3.6)$$

with $A_N(\boldsymbol{\sigma})$ the normalized antenna reception pattern. It is defined as $A_N(\boldsymbol{\sigma}) \equiv A_{\text{eff}}(\boldsymbol{\sigma})/A_0$ with A_0 the effective area in direction \mathbf{s}_0 (Thompson, 1999). After some transformations of Equation 3.6 and substitutions in Equation 3.5 one can write the correlator output as:

$$R = A_0 \Delta |V| \cos\left(\frac{2\pi\nu \mathbf{b} \cdot \mathbf{s}_0}{c} - \Phi_V\right). \quad (3.7)$$

The amplitude and phase of the fringe pattern, the cosine term in Equation 3.7, are the typically measured observables (Thompson, 1999). To reconstruct an image of a source Fourier transformation is essential, since the visibility V is the Fourier transform of the brightness distribution of a source $I(\boldsymbol{\sigma})$ (see Equation 3.6). It is convenient now to introduce a new coordinate system to explain more details necessary for the image reconstruction (see Fig. 3.3, Thompson, 1999). The baseline vector \mathbf{b} is expressed with the components (u, v, w) given in units of observing wavelength $\lambda = c/\nu$ (i.e. $\mathbf{b} \cdot \mathbf{s}_0/\lambda = w$ and $\mathbf{b} \cdot \boldsymbol{\sigma}/\lambda = ul + vm + w\sqrt{1-l^2-m^2}$). The w component points towards the phase tracking center \mathbf{s}_0 , later becoming the center of the synthesized image, and the (u, v) -plane perpendicular to it. The direction of u and v is east- and north-wards, respectively. The coordinates l and m define the position on the celestial sky and are represented by the direction cosine in the (u, v) -plane (Thompson, 1999). Assuming that all baselines are in the same (u, v) -plane one can write the complex visibility as:

$$V(u, v) = \iint I(l, m) e^{-2i\pi(ul+vm)} dl dm \quad (3.8)$$

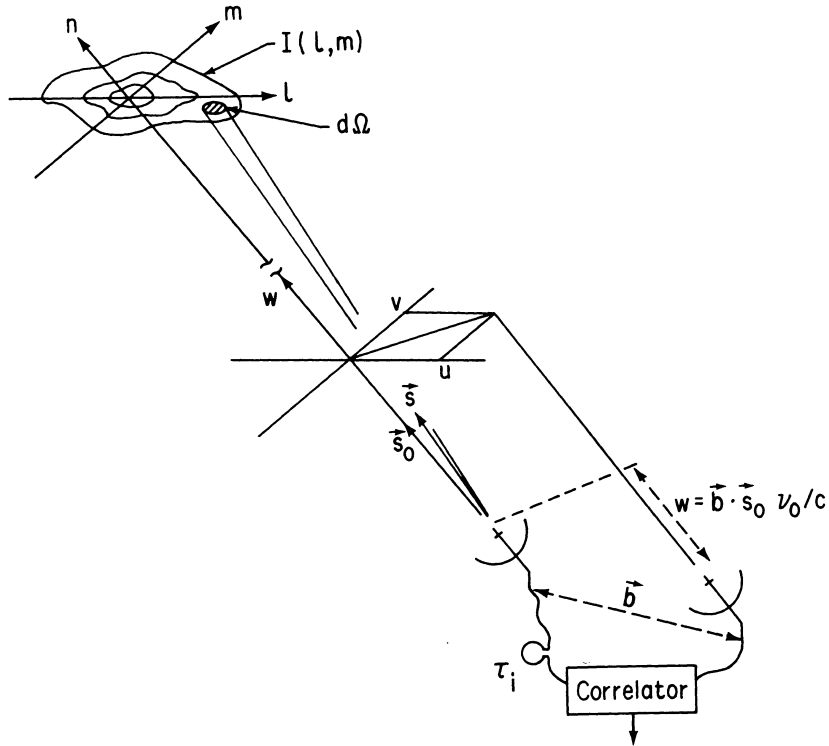


Figure 3.3: A diagram illustrating the different coordinate systems relevant for an interferometer. [Thompson \(1999\)](#)

and therefore using a Fourier transformation, the brightness distribution can be written as

$$I(l, m) = \iint V(u, v) e^{2i\pi(ul+vm)} du dv. \quad (3.9)$$

Thus, measuring the complex visibility throughout the (u, v) would allow the reconstruction of a perfect image, assuming perfect measurements. But in reality the (u, v) -plane is only sampled at certain places, depending on the synthesis array. This can be improved by taking the rotation of the earth into account which changes the baselines and thus improves the (u, v) -coverage ([Ryle & Hewish, 1960](#); [Scott et al., 1961](#); [Ryle & Neville, 1962](#)). This is limited by the fact that sources are only visible for a certain time. An example of the (u, v) -coverage of a VLBI observation with the VLBA is shown in Fig. 3.4. The observed brightness distributions are thus modified by a sampling function $S(u, v)$, which is zero at the (u, v) -positions where the source was not observed, and leads to the *dirty image* $I_D(l, m)$ given by

$$I_D(l, m) = \iint V(u, v) S(u, v) e^{2i\pi(ul+vm)} du dv = I(l, m) * B(l, m). \quad (3.10)$$

The resulting image can be understood as the convolution (represented by the asterisk) of the true brightness distribution of the source $I(l, m)$ with the reception pattern of the synthesis array, the synthesized beam $B(l, m)$. This beam is also referred to as the point

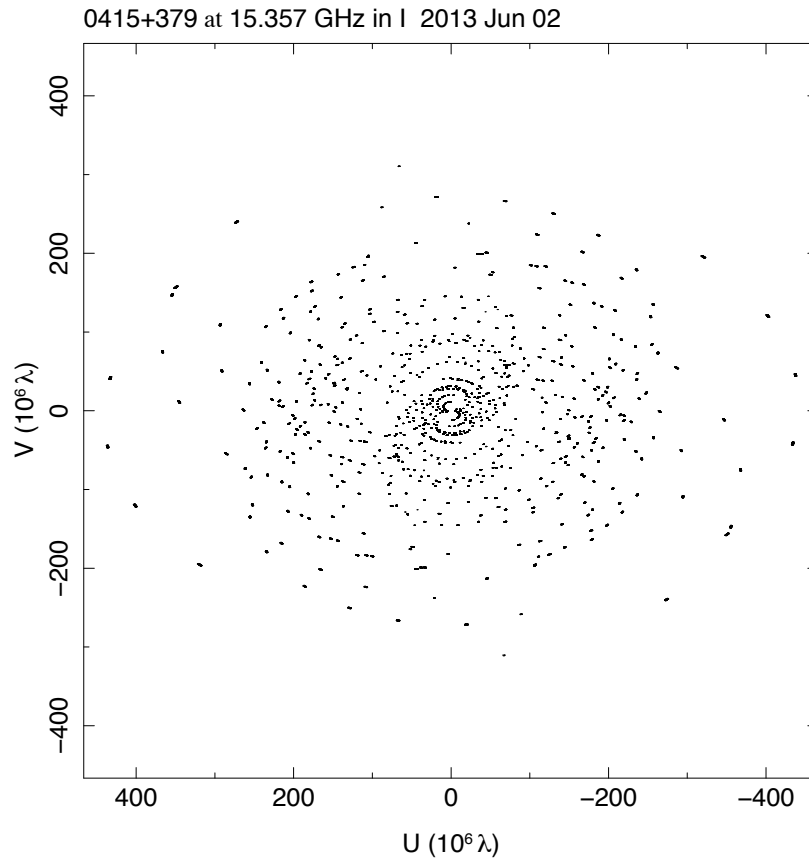


Figure 3.4: Example (u, v) coverage for an observation with the VLBA at 15.4 GHz of the source 3C 111, with each dot representing one complex visibility measurement.

spread function determined by the sampling function $S(u, v)$. The true source brightness distribution cannot be obtained directly (inversion problem) but different methods exist, with the most prominent being the CLEAN algorithm developed by Högbom (1974).

3.2 Data analysis

To create the high resolution images of the sources with VLBI, the data have to be carefully calibrated and must undergo a series of complex post-processing steps. The two main software packages used for these are AIPS (Greisen, 1990, 1998, Astronomical Image Processing System) and DIFMAP (Shepherd, 1997).

3.2.1 Calibration

The calibration of the data is usually performed with AIPS. AIPS provides a means to create calibration and flagging tables, account for atmospheric effects, for usage of cal-

ibrator sources, an interactive working environment, and the display and analysis of astronomical images. As a first step the data are pre-calibrated, which includes steps to select a reference antenna for which the phases are taken and to flag data of bad quality. The next steps are typically referred to as a-priori amplitude and phase calibration and e.g., accounts for instrumental effects. For more detailed information about the data-reduction and (self)-calibration steps refer to [Diamond \(1995\)](#), [Cornwell & Fomalont \(1999\)](#), [Kadler \(2002\)](#), and [Schinzel \(2011\)](#). In this work only data were used which were calibrated according to [Jorstad et al. \(2005\)](#), [Lister et al. \(2009a\)](#), or were of private communication but calibrated following the guidelines from the AIPS cookbook.

3.2.2 Imaging with CLEAN

For the imaging of VLBI data the program DIFMAP was used which allows for further data inspection, (self)-calibration, deconvolution and creation of images. It makes use of the CLEAN algorithm for imaging which creates an image based on a list of point sources convolved with the “clean beam”, usually the Gaussian fit to the main lobe of the dirty beam. It was originally devised by [Högbom \(1974\)](#) and, although more advanced implementations of the algorithm exist, they are not available in DIFMAP. The principle working scheme of the CLEAN algorithm based on Chapter 8 in [Taylor et al. \(1999\)](#) is outlined here:

1. Select a field (CLEAN window) in the dirty image.
2. Find the peak strength and position in that window.
3. Subtract the dirty beam multiplied by the peak strength and a dampening factor γ (loop gain) from the dirty image / residuals at the peak position. This creates a new image termed residuals.
4. Record the position of the peak and the subtracted magnitude, which is basically a point source
5. Repeat from (2) unless a user-defined number of subtractions were performed or a threshold of the remaining peak intensity in the residuals was reached.
6. Convolve the list of point sources with the “clean beam” to create an image
7. Add the residuals to the image in step (6) resulting in the CLEAN image

Depending on the source, especially for weak extended sources, additional windows will be most likely added during the CLEAN process.

Before cleaning, one first selects a grid to sample the map and the beam in the image plane in DIFMAP. Weighting schemes like natural and uniform are applied to individual visibilities as they are gridded, prior to Fourier inversion into the image plane. In contrast to natural weighting, uniform weighting takes into account the reciprocal number of visibilities in the local vicinity of a baseline in the (u, v) -grid and is typically set to 2 pixels in DIFMAP. The resulting CLEAN images strongly depend on the chosen weighting. Natural weighting is more susceptible to extended emission while uniform weighting is able to pick up more small scale structures.

As part of the imaging process one usually self-calibrates the data to improve the quality

of the image. This step is performed after CLEAN and is used in an iterative way with CLEAN until a robust image is found.

3.2.3 Self-calibration

The following introduction to self-calibration is based on the [Cornwell & Wilkinson \(1981\)](#); [Cornwell & Fomalont \(1999\)](#) and the commentary in the DIFMAP source code.

“Self-calibration is a means to finding self-consistent telescope based amplitude and phase corrections, through comparison of the observed data to an approximate model of the source structure”

is the description of the task self-calibration in DIFMAP. This task is performed by minimizing the sum of the squares of the residuals S from the model and the observed visibility \tilde{V}_{ij} adjusted by the complex gains g_i and g_j and is given by

$$S = \sum_t \sum_{i,j} w_{ij}(t) |\hat{V}_{ij}(t)|^2 \left| \frac{X_{ij}(t)}{\sigma_{x,ij}^2} - g_i(t)g_j^* \right|^2 \quad (3.11)$$

where

$$X_{ij}(t) = \frac{\tilde{V}_{ij}(t)}{\hat{V}_{ij}(t)} \quad (3.12)$$

and $i \neq j$ with \hat{V}_{ij} denoting the model visibilities, $\sigma_{x,ij}^2$ the variance of $X_{ij}(t)$, and t the solution bin. This equation can be interpreted as the to be imaged object being transformed into a pseudo-point source. In addition it can be solved independently and analytically for phase and amplitude which is shown in depth by [Cornwell & Wilkinson \(1981\)](#) but it is beyond the scope of this work.

Since the algorithm only alters the element gains, closure quantities (phase and amplitude) must be conserved. If we consider a telescope array of N elements and therefore $N(N-1)/2$ baselines and assume complex gain errors affecting each station, we are left with $N(N-1)/2 - N$ closure quantities to reconstruct the true source brightness distribution ([Cornwell & Fomalont, 1999](#)). The phase of the baseline in an array can be written as

$$C_{ij} = \phi_{ij} + \phi_i - \phi_j + \epsilon_{ij} \quad (3.13)$$

with ϕ_i and ϕ_j denoting the instrumental error at the specific station, ϕ_{ij} the phase of the baseline and ϵ_{ij} a noise term. The closure phase C_{ijk} is then given by a loop consisting of three baselines from the elements i , j , and k :

$$\begin{aligned} C_{ijk} &= C_{ij} + C_{jk} + C_{ki} \\ &= \phi_i - \phi_j + \phi_{ij} + \epsilon_{ij} + \phi_j - \phi_k + \phi_{jk} + \epsilon_{jk} + \phi_k \phi_i + \phi_{ki} + \epsilon_{ki} \\ &= \phi_{ij} + \phi_{jk} + \phi_{ki} + \epsilon_{ij} + \epsilon_{jk} + \epsilon_{ki} \end{aligned} \quad (3.14)$$

²This is a modified version of equation 10.5 by [Cornwell & Fomalont \(1999\)](#)

and thus free of instrumental effects. An array of N telescopes has $N(N - 1)/2 - (N - 1)$ independent closure phases since the phase is defined as the phase difference between to stations and therefore an absolute phase is not needed (Cornwell & Wilkinson, 1981). A similar concept is applied on the closure amplitude $\Gamma_{ijkl}(t)$ for which one defines a loop of four elements

$$\Gamma_{ijkl}(t) = \frac{|\tilde{V}_{ij}(t)||\tilde{V}_{kl}(t)|}{|\tilde{V}_{ik}(t)||\tilde{V}_{jl}(t)|} \quad (3.15)$$

in which the amplitudes of the complex gains vanish (Cornwell & Fomalont, 1999).

3.2.4 Non-Imaging Data Analysis – Model fit

This section is based on chapter 16 in the textbook Taylor et al. (1999). As was already shown in Sect. 1.8.2 features in VLBI images can be identified and tracked over several epochs. The image domain though is not the one in which the measurements have been performed and thus errors might not be easily identified. Moreover since Fourier transforms, (u, v) -grids, etc., are involved in creating these images errors in the data will be spread across the image and thus pixels most likely have correlated errors. A far better approach for a quantitative analysis is to directly use the measured complex visibility.

One of the techniques to work on this is called model fitting. The general idea is to create a parametric model of the assumed sky brightness distribution and use the equations from Sect. 3.1 to derive the complex visibility for each baseline. By fitting these models to the data on the basis of χ^2 -statistics, one finds the best model parameters can evaluate the goodness of the fit and calculate the uncertainties of the mode parameter. A good introduction to least-squares fitting and algorithms is given by Bevington & Robinson (1992). An example of a derived model and the data as depicted in the (u, v) -plane is shown in Fig. 3.5.

The first condition to use χ^2 -statistics is that the uncertainties of the data have to be Gaussian. For VLBI this is only the case if one were to use the real and imaginary parts of the observed visibility (Pearson, 1999). The second condition is that the uncertainties of the data have to be known. In principle the uncertainties could be derived by various means e.g., the measured system temperatures or by the scatter of points within an integration.

3.2.5 Model fit in DIFMAP

The program which we used for the model fitting of the sources 3C 111 and 3C 84 (see chapter 4 and 5) was DIFMAP, which fulfills the requirements given by the χ^2 -statistics. In addition a modified version of DIFMAP, `DifmapRemeis` was used in conjunction with a personally written module for the X-ray fitting software ISIS (Houck et al., 2013) to derive parameter uncertainties and tie/constraint parameters (see Sect. refchap:Methods) for which the stand-alone original DIFMAP has none or only limited options. In all of these analysis DIFMAP was used for the management of the data and the evaluation of

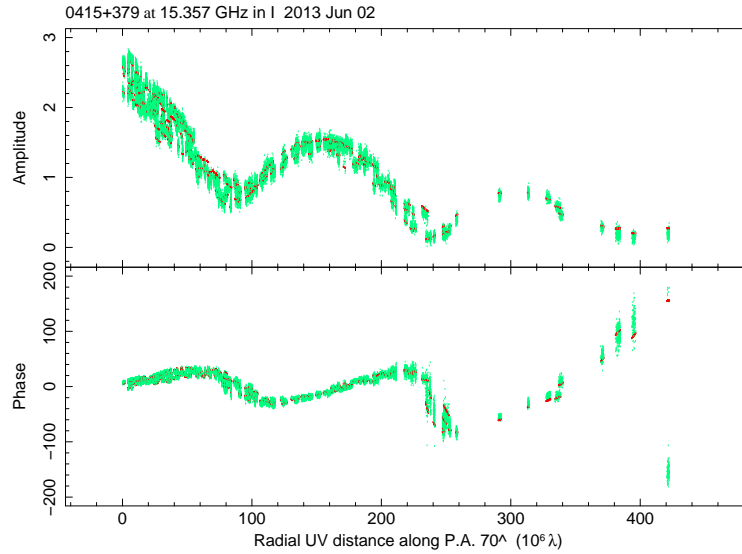


Figure 3.5: Example observation of 3C 111, showing the model and data for amplitude and phase. The data is represented in green while red marks the model values.

the model on the basis of χ^2 -statistics.

First the data are read in. The complex visibilities are averaged with a reasonable time interval (integration) which results in new data points and new weightings determined by the scatter of the data during the integration time. Although AIPS does provide an averaging function the weighting is not stored in the produced files and thus this task is typically performed in DIFMAP during the calibration process.

The model of a source is established by the superposition of multiple model components for which DIFMAP offers delta functions, Gaussian, uniformly bright disks, optically thin spheres and rings. All of these models have in common that they are parametrized in the image-plane, but an analytic function exists to calculate their Fourier-plane representation at all baselines. The generic model component is a Gaussian with the parameter: flux S , Cartesian coordinates x and y , the full width half maximum (FWHM) of the major axis, the ratio of the two axis, and the orientation angle ϕ . Throughout the thesis mainly circular Gaussian components were used. Note that these model components may not be real physical features but are simply needed to properly describe the complex source brightness distribution (Lister et al., 2009b).

When located at the origin of the image coordinate system the transformation of these model components are given by:

Gaussian

$$f(r) = \frac{1}{\sqrt{\pi/4 \ln 2} a} \exp\left(\frac{-4 \ln 2 r^2}{a^2}\right) \quad (3.16)$$

$$F(\rho) = \exp\left(\frac{-(\pi a \rho)^2}{4 \ln 2}\right) \quad (3.17)$$

Delta Function

$$f(x, y) = \delta(x, y) \quad (3.18)$$

$$F(u, v) = 1 \quad (3.19)$$

with a denoting the FWHM, $r = \sqrt{l^2 + m^2}$, and $\rho = \sqrt{u^2 + v^2}$. More detailed analytic expressions for commonly-used model components are given by [Purcell \(1973\)](#). The χ^2 of a model is derived by:

$$\chi^2 = \frac{1}{\sigma^2}(A^2 + A_m^2 - 2AA_m \cos(\phi - \phi_m)) \quad (3.20)$$

with A and ϕ referring to the amplitude and phase of the complex visibility, while A_m and ϕ_m mark the respective model values. σ is the derived uncertainty from the statistical scatter of the integrated complex visibilities in the calibration step. Note that the weighting as described in the CLEAN task does not contribute in the calculation of the χ^2 value. To find the best fit of the model, DIFMAP makes use of the Levenberg-Marquardt least-square-fit algorithm (e.g., [Bevington & Robinson, 1992](#)) which operates on the knowledge of the partial derivatives of the model functions in the (u, v) -plane.

The typical procedure of finding a good model representation of the data used is similar to that of CLEAN:

1. Find the peak strength and position in the residual / dirty image
2. Add a new model component to the model by placing a new Gaussian component at the peak position, with a flux density equaling the peak strength and a size of the minor axis of the clean beam
3. Fit the model to the data
4. Store the model component(s) in a list
5. Restart (1) until a reasonable good fit is achieved

As an alternative one can adopt the model from a previous analysis if the observations were executed close in time or the expected morphology change between two observations is small and fit this model. Afterwards one deletes all components which show a non-physical behavior (e.g., negative flux density) and start with (1) again. Note that these two procedures are just guidelines and one can use different ways to find a good model.

In this thesis self-calibration (see e.g., [Cornwell & Fomalont, 1999](#)) of the phases was used once a good model was already established to even further improve the quality of the fit. This enabled us to model regions of low brightness which were observed in the CLEAN-images but could not be modeled before.

3.3 Advanced model fit options for VLBI data

As I pointed out above DIFMAP is not able to calculate the uncertainties of model parameters based on χ^2 -statistics. Some effort was made to overcome this problem with the software package `Difwrap` (Lovell, 2000) which allows the inspection of the χ^2 -space for one or two parameters by fitting and storing the resulting model fit for small variations of these parameters on a user-defined grid. The uncertainties could then be derived by manually selecting “good” fits. A major drawback of this approach becomes evident in the case of the best fit being in a local minimum of the χ^2 -landscape. The real (global) minimum is then only found by pure chance since the probed parameter space is limited by the user’s impression of the χ^2 -landscape.

3.3.1 `DifmapRemeis` & `ModelFitPack`

To overcome the limitations of DIFMAP and `Difwrap`, such as the one mentioned above as well as not being able to handle function dependent model parameters and constraints, I developed a software module MFP (**ModelFitPack**) for the X-ray fitting tool ISIS (Houck et al., 2013) and **DifmapRemeis** (a modified version of the original DIFMAP). These tools also provide the framework for simultaneous fits of multiple data sets (e.g., observations at different frequencies) and thus the possibility to test time and frequency dependent models.

`DifmapRemeis` extends the functionality of DIFMAP by enabling it to exchange information with ISIS. The communication is based on pipes of the standard streams (stdin, stdout, stderr) and the option to transfer information from DIFMAP to ISIS via memory maps. MFP provides the necessary functions for ISIS to read the memory maps, control `DifmapRemeis`, create models to be evaluated by `DifmapRemeis` and various plot options. In general all commands of DIFMAP are available in ISIS.

3.3.2 Fitting with ISIS and the `ModelFitPack`

In the following I will explain how to fit (u, v) -data with the MFP in ISIS and provide examples for fits to multiple data sets and how one can apply constraints to parameters. Most of the communication between ISIS and an instance of `DifmapRemeis` is performed by the two function. `difmap_command` sends a plain string via stdout to the stdin of `DifmapRemeis` and the command is then carried out as if it was executed on the command line interface of DIFMAP. `difmap_get_output` reads the stdout of `DifmapRemeis` and returns it as a string. It is important to note that due to buffering issues new strings from the stdout of `DifmapRemeis` can only be read after invoking the `print` command in `DifmapRemeis` via `difmap_command`.

A default set up for fitting (u, v) -data with ISIS is to start ISIS, load the memory mod-

ule included in MFP, the Remeis ISISscripts³, and the MFP. **set_difmap_statistics** is now used to add the models *map*, **cmp_circ**, **cmp_ell**, **cmp_delta**, and **cmp_line_circ** to ISIS and changes the statistic to **difmapchisq** which allows the models to be evaluated.

New data sets can then be added to ISIS by using **load_difmap_data** opening a pipe to a new instance of DifmapRemeis for each data set. Moreover, the data sets are also added to the correct instances of DifmapRemeis with the usual DIFMAP commands, e.g., **observe** and **select**. Thus this set up allows ISIS to have access to multiple data sets without the need to reload data sets if one were to use only a single instance of DifmapRemeis. In ISIS a fake spectrum for each data set with the number of bins set to twice the number of visibilities (real and imaginary part of the complex visibility) is created which is necessary to store the residuals during the fit process. The command **savePar** is used to save the current model and the location of the data while **loadPar** is used instead of **load_difmap_data** to import a saved model into ISIS which includes the data. In principle the standard ISIS commands are available as well, but should be used with care.

After all data sets are loaded, memory maps have to be set up with the command **mfp_shm_init** if an implementation of the Levenberg-Marquardt least-square-fit algorithm in ISIS should be used for fitting. The memory maps are used to exchange to the residuals of the model and data from DifmapRemeis to ISIS. All process communication is handled through routines provided with the MFP package and do not require an additional programming effort by the user.

MFP models

Models provided by the MFP should only be used in an additive way, e.g., “**cmp_ell(1) + cmp_ell(2)**”. Model parameter values can be accessed and modified via the ISIS standard routines. The models **cmp_delta**, **cmp_circ** and **cmp_ell** are variants of the Gaussian model component introduced in section 3.2.5. The generic model component is **cmp_ell** requiring the parameters:

- flux – the flux density of the model component in Jy
- x, y – the *x* and *y* position of the model component in mas
- major – the size of the major axis in mas
- ratio – the ratio between major and minor axis
- phi – the orientation angle of the ellipse in degrees

The parameters **freq** (the frequency at which the observation was carried out), **date** (the date of the observation), **tb** (the brightness temperature) are optional parameters and are not needed to derive the χ^2 value of the model. All other models are subsets of the generic Gaussian model component representing a point source or a circular Gaussian model component. **Cmp_line_circ** is a circular Gaussian model component exclusively used in multiple data sets and has additional parameters which can be used to describe its ballistic trajectory over time:

³<http://www.sternwarte.uni-erlangen.de/isis/>

- v – the vector speed of the model component
- α – the position angle of the trajectory
- x_0, y_0 – the starting position
- t_0 – the ejection time

The model **map** has the parameters **dx**, **dy**, **date**, **freq**. The parameters **dx** and **dy** are offsets added to the position of every defined model component which enables an easy way to align the position of model components and should typically be frozen. The frequency and date parameter (freq and date) are optional and not used to calculate the χ^2 -value.

ISIS statistics – difmapchisq

When evaluating or fitting a model with the **difmapchisq**-statistics in ISIS, **DifmapRemeis** functions e.g., **addcmp** are used to add new model components to the appropriate instances of **DifmapRemeis** and return the χ^2 -values for each data set. If memory maps were initiated the residuals between the complex visibilities and the model are returned as well.

Overcoming the limitations of DIFMAP

ISIS provides some powerful options to place constraints on model parameters by using e.g., **set_par**, **set_par_fun**, **tie**. These functions are all used by taking a parameter id as an input (each parameter id is unique) and in the case of **set_par** and **set_par_fun** the use of regular expressions, which can include wildcards characters, is also possible. **Set_par** allows the user to set the value and range of a parameter. With **set_par_fun** a fit-parameter can be defined as an arbitrary function depending on other parameters allowing the development of very complex models. **Tie** instead ties one or multiple parameters to one parameter. Usually the defined model in ISIS is applied to every data set but by using the parameter **Isis_Active_Dataset** in the model description one can change the model for every data set, e.g., “**cmp_circ**(100 + **Isis_Active_Dataset**)”. More details on how to use these are given in the ISIS manual⁴. ISIS also provides routines to derive the uncertainties for model parameters and more advanced versions of these routines are available in the **Remeis ISISscripts**, which allow the use of computer clusters for a faster computation of the uncertainties.

Examples for using MFP

In this section I give an example on how to use the MFP with ISIS. I will start with demonstrating how one can load the data, defines the model and sets parameter values.

Listing 3.1: Load data with ISIS using the MFP and defining a model

⁴<http://space.mit.edu/cxc/isis/manual.html>

```

1 import("memory"); % load the memory module of the ModelFitPack
2 require("isiscripts"); % load the Remeis ISISscripts
3 require("mfp.sl"); % load the ModelFitPack
4 set_difmap_statistics; % change the statistics
5 load_difmap_data("example_data_1.uvf"); % load a first data set
6 load_difmap_data("example_data_1.uvf"); % load a second data set
7 % create a model for both data sets, consisting of two circular components
  (cmp_circ) and the map offsets (map)
8 % Isis_Active_Dataset is a number corresponding to the number of the data set
  which is currently active
9 fit_fun("map(Isis_Active_Dataset) + cmp_circ(100 + Isis_Active_Dataset)");
10 % the model includes now the following independent parts: map(1), map(2),
  cmp_circ(101), cmp_circ(102)
11 % the last two digits in individual model names correspond to the data set
  number
12 % to set the value of a parameter one access them by the use of set_par()
13 set_par("cmp_circ(101).flux", 1); % the flux density of the first component
  in data set 1 is changed to 1 Jy
14 % to imitate the "normal" way of model fitting, one can alternatively use
  functions such as MF_init_Cmp(); to initialise new model components with
  default values
15 % frequency, position, date, flux density, size are set according to some
  rules, e.g., the position of the peak in the residual map in DifmapRemeis
16 MF_init_Cmp(301);
17 % to finally fit the model parameters
18 fit_counts();

```

After the data were loaded and a model established one can constrain parameter values.

Listing 3.2: Constraint parameter values

```

1 % set a minimum and maximum value for a parameter
2 set_par("cmp_circ(101).flux", 1; min=0, max=2);
3 % tie parameter values, e.g., the x position of component 101 and 102 are now
  tied, thus one connects information from one data set to the other
4 tie("cmp_circ(101).x", "cmp_circ(102).x")
5 % use set_par_fun to constraint a parameter with a function
6 set_par_fun("cmp_circ(101).x", "cmp_circ(102).x + 3");
7 % e.g. when using multiple data sets and the cmp_line_circ model component
  one can set the position of a component to be calculated by another
  function
8 % in this case to be positioned on a straight line defined by some parameters
9 set_par_fun("cmp_circ(201).x", "calcPosOnLine(cmp_line_circ(201).date,
  cmp_line_circ(201).v, cmp_line_circ(201).alpha, cmp_line_circ(201).x0,
  cmp_line_circ(201).y0, cmp_line_circ(201).t0; x)");
10 % in the MFP if one were to derive a ballistic fit of a model component one
  can use functions like replace_with_line_circ(); to change a cmp_circ(xxx
  + Isis_Active_Dataset) model component into a cmp_line_circ (xxx +
  Isis_Active_Dataset) component for which the initial values are already
  determined
11 replace_with_line_circ(200)
12 % this will change the position of all components cmp_circ(200 +
  Isis_Active_Dataset) to be placed upon a ballistic trajectory
13 % use of fit_counts will thus fit the parameters of the ballistic trajectory
  to all data sets at once

```

With this set up one can already start developing complex models, e.g., frequency dependent models, ballistic models, accelerating models. Moreover, one can make use of the routines and scripts to derive the uncertainties for model parameters in parallel using the Message Passing Interface (MPI)⁵, e.g., `mpi_fit_pars`.

3.3.3 Testing the module – reproducing the model fit

To demonstrate that the quality of a fit performed with ISIS and ModelFitPack is at least as good as a fit solely done with DIFMAP I chose two data sets of 0202+319 from September 2005 which were calibrated as part of the MOJAVE project. The source 0202+319 is a flat-spectrum radio source (Healey et al., 2007) at a redshift of 1.466 (Burbidge, 1970). The object inherits a moderate complex jet structure showing a compact core region and an isolated feature which is depicted in Fig. 3.6. Superluminal motion is observed with a maximum vector speed of less than 0.15 mas/yr at 15.4 GHz (Lister et al., 2013). Thus the positions of model components are stable within 0.01 mas in the selected data set, since the observations were carried out within 18 d from each other.

For each observation I used the calibrated visibility data available from the MOJAVE website and fit the data with models consisting of four two dimensional Gaussian components. In order to prove that I could reproduce the established fits, I used the model and parameter values as presented by Lister et al. (2013) and refit the model with difmap (model 0) and isis (model 1).

The fitted model parameters of model 0 and model 1 matched in both data sets. However calculating the uncertainties of the model parameters with ISIS led to an improved quality of the fit in one data set. The χ^2 -value changed from 26501.30 to 26464.67. A comparison of the model parameters shows a major difference in the y position of the C2 component (see Table A.1). An inspection of the χ^2 -landscape for this parameter (see Fig. 3.7 left) reveals two local minima at 1.14 mas and 1.76 mas, suggesting that the fit algorithm was stuck in the minimum with the higher χ^2 -value.

These fits demonstrate that my set up is capable of reproducing the results produced by DIFMAP and in addition a thorough investigation of the uncertainties.

3.3.4 Comparing models and uncertainties for single observations

From this point on all fits are exclusively performed with ISIS and include the calculation of uncertainties for all model parameters, which usually improves the fit. In literature (e.g., Pearson, 1999) one finds the statement of non-uniqueness of models in this type of analysis. To compare different models I fit two additional models (model 2 and model 3) to the same data set.

In model 2 all “delta” components (major axis of 0) are replaced with circular Gaussian components and the core with an elliptical Gaussian component. Model 3 solely consists of circular Gaussian components.

The best fit values are presented in Table 3.1 and 3.2. A comparison of the χ^2 -values

⁵e.g., <http://www.open-mpi.org>

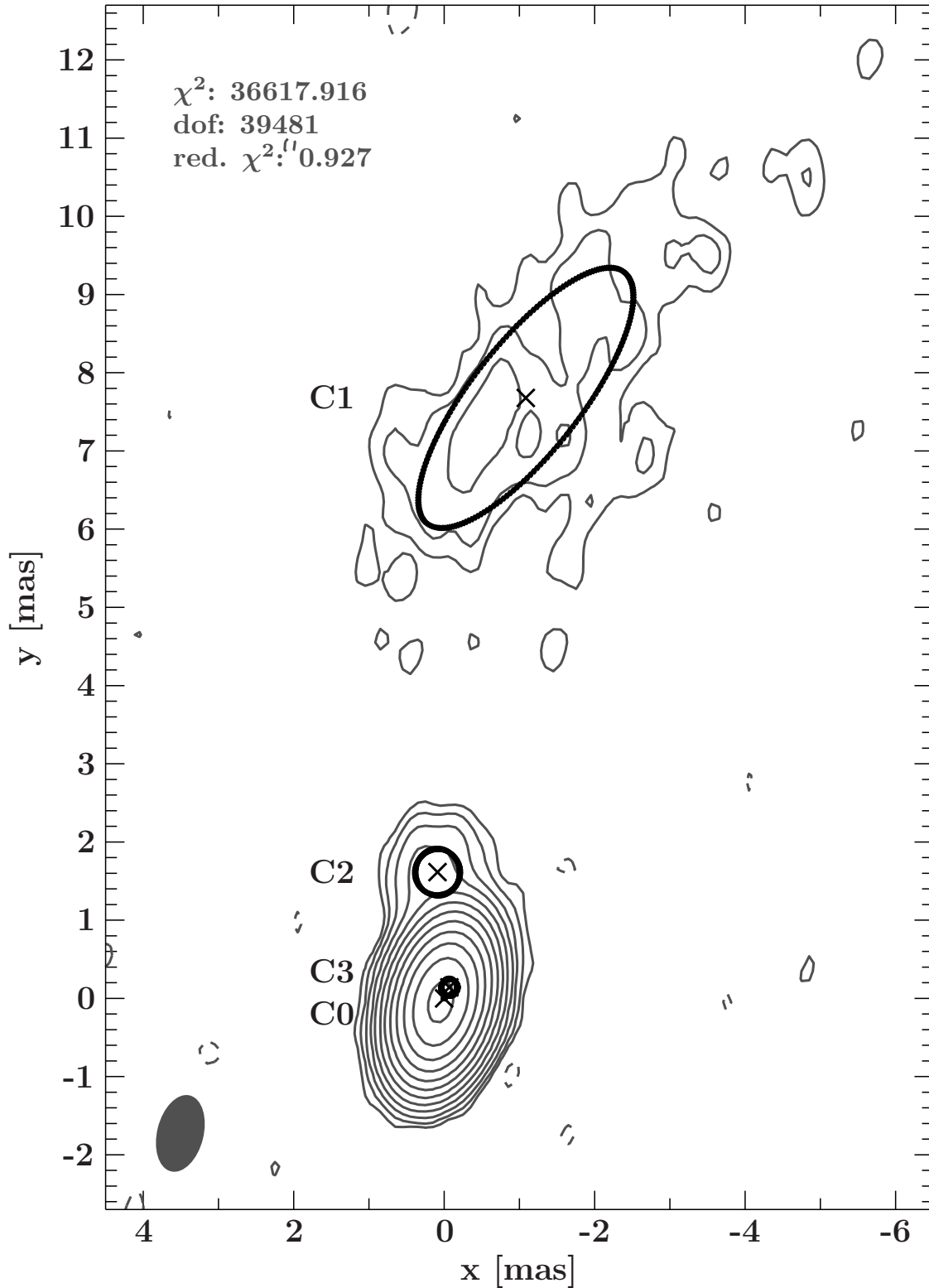


Figure 3.6: Contour map of the source 0202+319 at 15 GHz from the observation at 05 September 2005. The continuous lines show the logarithmic flux density levels starting at the 3σ , while the dashed contours show the negative flux density levels. Label numbers are in analogy to the ones by [Lister et al. \(2013\)](#) (0, 1, 2, 3 – here C0, C1, C2, C3). Information of the statistics for this model fit are shown at the top left while the restoring beam is shown at the bottom left.

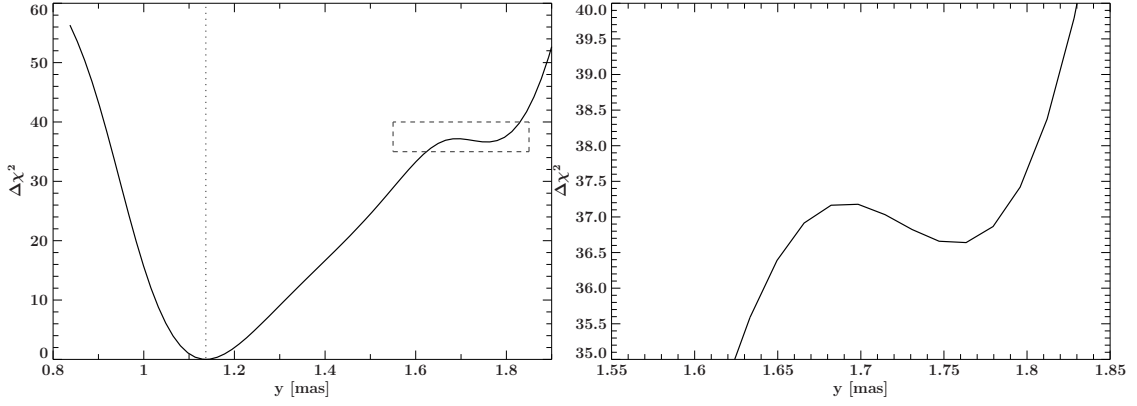


Figure 3.7: The $\Delta\chi^2$ landscape of the y position parameter for component C2 in the observation 23 September 2005.

Table 3.1: The χ^2 value, the degrees of freedom and the number of free parameters are presented for each model for the observation of 0202+319 at 05 September 2005.

model	χ^2	dof	nfree
0	36617.92	39481	17
1	36617.92	39481	17
2	36599.89	39478	20
3	36826.16	39482	16

shows that all models are viable representations of the data.

3.3.5 Uncertainties of model parameters

I used the models 1-3 to derive the model parameter uncertainties using χ^2 -statistics by determining the multidimensional contour level for each parameter, which satisfies the condition of $\chi^2 = \chi_{min}^2 + \Delta\chi^2$ and $\chi_{min}^2 = 1$ in the case of 1σ errors (Bevington & Robinson, 1992). This contour is projected on the 1D plane of the parameter with the maximum and minimum value defining the upper and lower value of it. The fit parameters and their uncertainties are given in Table 3.3 for model 1 in the data set of the observation 05 September 2005. All other values are shown in Table A.1.

Table 3.2: The χ^2 value, the degrees of freedom and the number of free parameters are presented for each model for the observation of 0202+319 at 23 September 2005.

model	χ^2	dof	nfree
0	26501.30	28966	16
1	26464.67	28966	16
2	26116.35	28962	20
3	26306.96	28966	16

Table 3.3: Fit parameters for model 1 of the observation 05 September 2005. The positional parameters x and y are given in respect to the core position. Parameter values for which no uncertainties are given were frozen in this particular model.

id	date	S [Jy]	x [mas]	y [mas]	major [mas]	ratio	ϕ [deg]
C0	2005.68	1.236 ± 0.008	$(0.00^{+0.26}_{-0.25}) \times 10^{-3}$	$(0.0 \pm 0.5) \times 10^{-3}$	0	1	—
C1	2005.68	0.0329 ± 0.0011	-1.08 ± 0.05	7.68 ± 0.06	$4.15^{+0.16}_{-0.15}$	$0.345^{+0.025}_{-0.022}$	-39.5 ± 1.6
C2	2005.68	0.0133 ± 0.0005	$0.089^{+0.015}_{-0.016}$	1.613 ± 0.020	0.59 ± 0.04	1	—
C3	2005.68	$0.570^{+0.008}_{-0.007}$	-0.0685 ± 0.0007	0.1412 ± 0.0012	$0.2144^{+0.0019}_{-0.0018}$	1	—

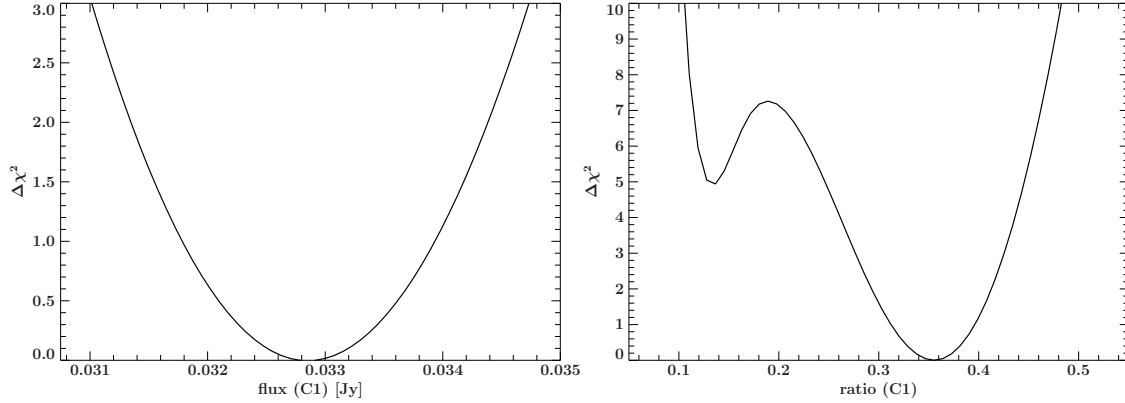


Figure 3.8: $\Delta\chi^2$ landscape for component C1 in model 1. Left: the flux parameter for the Gaussian component C1 in the observation 05 September 2005. Right: $\Delta\chi^2$ landscape of the ratio parameter for the Gaussian component C1 in the observation 23 September 2005.

In case of Gaussian errors the χ^2 -landscape is expected to have the shape of a parabola close to the minimum. Therefore I investigated these for the parameters of the different models. I found that most of the calculated parameters are well behaved (parabolas) while some have multiple minima but maintain the parabola shape in the close vicinity of it (see Fig. 3.8). If these extrema have the same χ^2 values then more than one configuration of parameter values exists which are viable representations of the data. In the particular case of Fig. 3.8 the $\Delta\chi^2 = 5$, which is reasonably close and thus strengthens the statement that multiple models exist which describe the data equally well.

Comparison with conservative estimates

To probe the reliability of the derived uncertainties I compared them with conservative estimates following the works by (e.g., [Homan et al., 2002](#); [Lister & Homan, 2005](#); [Lister et al., 2009b](#); [Piner et al., 2007](#)). The position uncertainty can be guessed by taking the scatter in position of the components. This is only viable if two observations of the same source are close in time and have a constant jet structure. The uncertainty of the flux density is typically in the order of 5% but can be even smaller for bright components. Other estimates of the uncertainties exist but are not used for comparisons in this thesis.

Table 3.4: Comparison of C1 component parameter values in model 1 with uncertainties and conservative estimates. The conservative flux estimate is a 5% error, while the position uncertainty is the scatter of the values. No conservative estimate on the major axis, phi and the ratio is found in literature.

parameter name	value 05 Sep 05	value 23 Sep 05	conservative uncertainty
S [Jy]	0.0329 ± 0.0011	0.0360 ± 0.0013	0.002
x [mas]	-1.08 ± 0.05	-1.03 ± 0.05	0.058
y [mas]	7.68 ± 0.06	7.65 ± 0.07	0.023
major [mas]	$4.15^{+0.16}_{-0.15}$	$4.93^{+0.08}_{-0.20}$	-
phi [deg]	-39.5 ± 1.6	$-26.9^{+1.9}_{-2.0}$	-
ratio	$0.345^{+0.025}_{-0.022}$	0.36 ± 0.05	-

Lister et al. (2009b) state that the position uncertainty is 1/5 FWHM of the beam and Fomalont (1999) give estimates on the uncertainties of components which are fit directly in the image-plane. Fomalont (1999) also states that these uncertainties have to be treated with great caution, since one has to assume that the image errors are stochastic and independent. In the used data set of 0202+319 the contribution to the uncertainty of component positions is less than 0.01 mas, and thus, they are suitable to derive conservative estimates on the errors of the model parameter values. I find that the typical position uncertainty is less than the ones given by conservative estimates which also applies to the flux density. An example of the parameter values and their uncertainties, including conservative estimates, is presented in Table 3.4 while the others are given in Table A.2 and A.3. Regardless of the model used the uncertainties of model parameters were found to be similar, except for the parameters not used to describe the component (e.g., size in the case of a delta component).

I note a strong discrepancy between the positions of component C2 of more than 0.4 mas. This cannot be explained by the derived uncertainties nor by the observed apparent motion in the source. Moreover the discrepancy is evident in all models. This suggests that the identification of C2 component might be wrong and the C2 must be treated with care when performing a kinematic study of this source. One has to add though that the strong difference became apparent only after the uncertainties were derived. Before that the minimization algorithms of DIFMAP and ISIS were most likely stuck at a local minimum (see Fig. 3.7).

Confidence maps

A more general understanding of model parameters and their dependencies can be derived by the calculation of confidence maps for a parameter pair. These maps are created by stepping the χ^2 -space of two model parameters over a certain range and the contours of constant χ^2 yield information about the dependency of these parameters (Bevington & Robinson, 1992). A contour of circular shape denotes that these parameters are independent from each other.

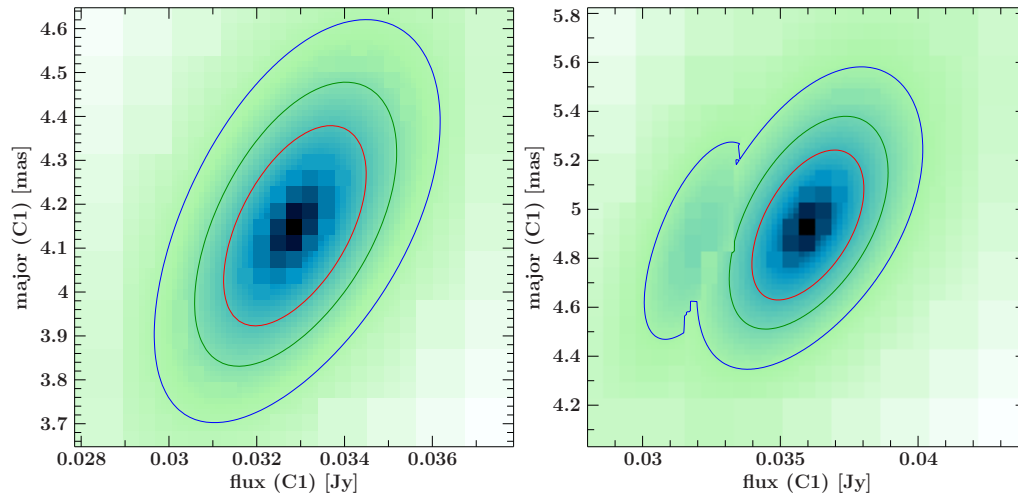


Figure 3.9: Confidence maps of the component parameters flux and major axis for the isolated C1 component for the observation 05 September 2005 (left) and 23 September 2005 (right). The contours are based $\Delta\chi^2 = 2.30, 4.61$ and 9.21 , corresponding to a confidence of 68%, 90%, and 99% confidence for the two parameters of interest.

Parameter dependencies of single model components

I calculated these confidence maps for parameters of single model components e.g., flux density and the major axis of C1. I find a general correlation of the flux density and the major axis parameter of circular Gaussian components. An example of this is depicted in the left plot of Fig. 3.9. One would expect an anti-correlation for these Gaussian parameters if the fit and the parameters would reside in the same plane (image or (u, v)) but since the data and the fit are performed in the (u, v) -plane and the parameters are defined in the image-plane we observe the opposite, a correlation.

In Fig. 3.8 I already showed that a single parameter could have multiple local minima, which are also displayed in the confidence maps e.g., Fig. 3.9 for the flux and the major axis of component C1 in the observation of 23 September 05.

I find no general dependency for the parameters of single model components besides the flux density and the major axis.

Dependencies between model components

[Homan et al. \(2001\)](#) stated the effect of “cross-talk” between spatially close components however this was never quantitatively shown. I therefore calculated the confidence maps of the flux density parameters for all parameters. A strong correlation was found for the flux densities of component C0 and C3, spatially speaking the closest components in all models and observations. This strong dependency of the parameters is shown in Fig. 3.10 for model 1 of the 05 September 2005 data set. I did not find the other pairs

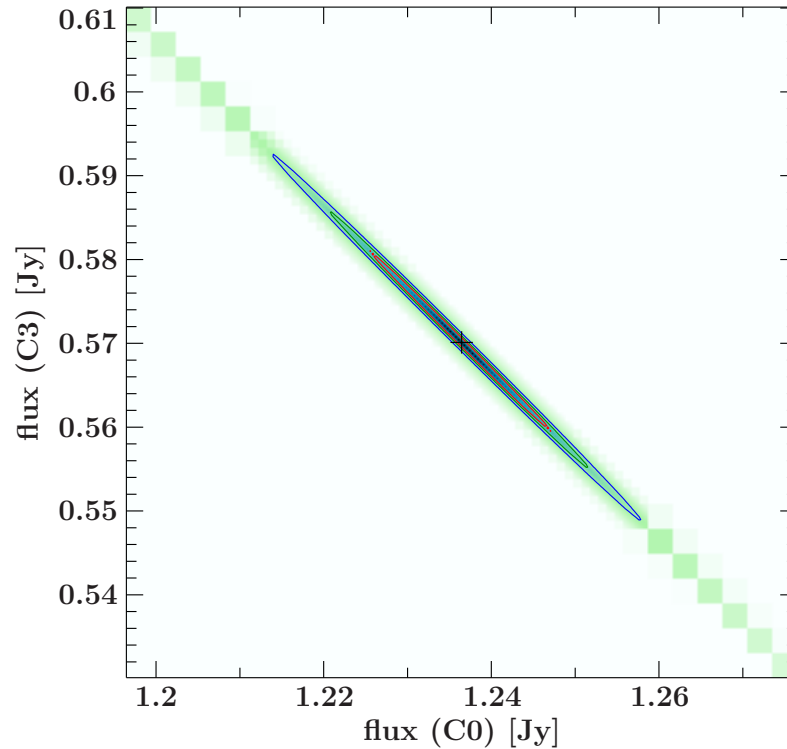


Figure 3.10: The confidence map of the flux density parameters for the spatially close components C0 and C3 in the observation of 05 September 2005. The contours are based $\Delta\chi^2 = 2.30, 4.61$ and 9.21 , corresponding to a confidence of 68%, 90%, and 99% for the two parameters of interest. The black cross mark the position of the best fit values.

of flux density parameters being correlated. It was beyond the scope of this work to search for other potentially correlated parameters between model components and will be performed in future works.

3.3.6 Models for multiple observations – simultaneous fits

As will be demonstrated in chapter 4 for the analysis of 3C 111, kinematics of jets are usually derived by

1. fitting various Gaussian model components to the data
2. identification and association of components
3. fits (mainly linear regression) to the fitted positions of identified model components.

This approach comes with the drawback that the uncertainties of model component parameter are unknown and the weights uniformly rescaled such that the reduced $\chi^2 = 1$. Therefore one cannot determine if a model is a suitable representation of the data. Moreover each component is weighted equally and thus effects due to e.g., calibration, sparse

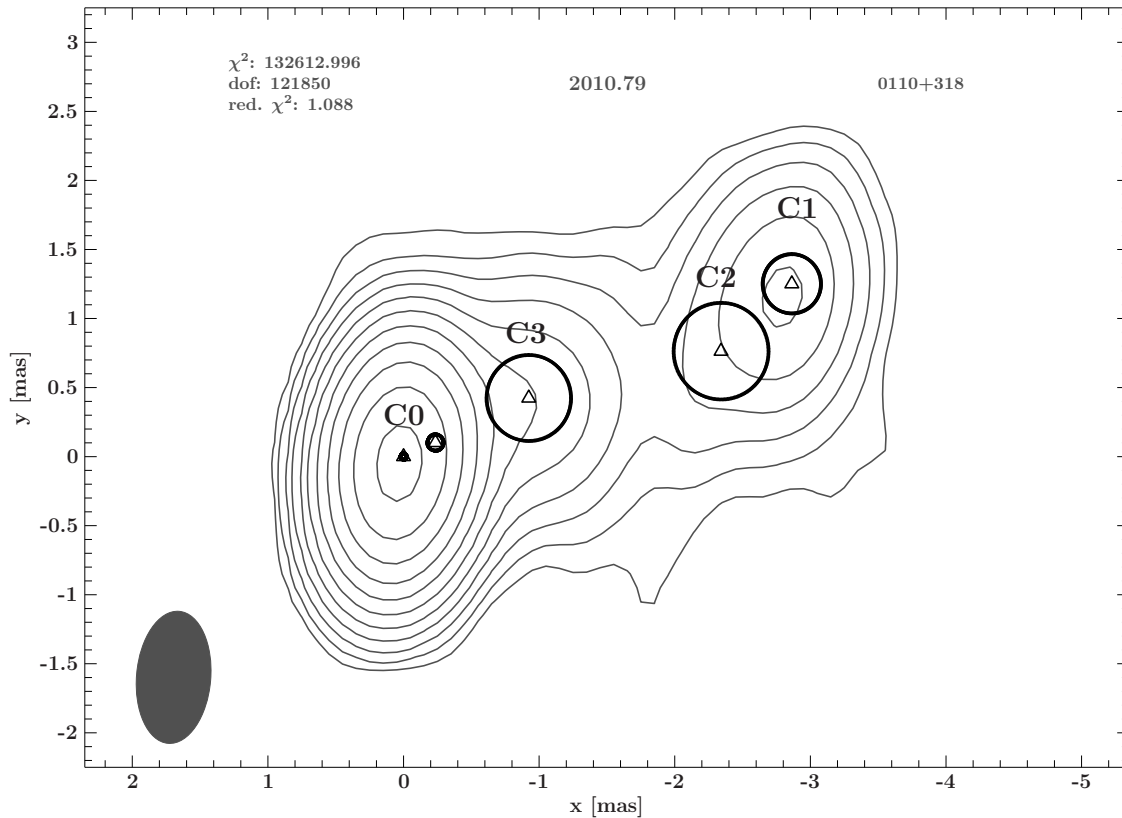


Figure 3.11: Contour map of the source 0110+318 at 15 GHz. The solid lines show the logarithmic flux density levels starting at the 3σ , while the dashed contours show the negative flux density levels. Gaussian components were added to illustrate the fitted model. The label numbers are in analogy to the ones by [Lister et al. \(2013\)](#) (0, 1, 2, 3 – here C0, C1, C2, C3). Information on the statistics of this model fit are shown at the top left while the restoring beam is shown at the bottom left

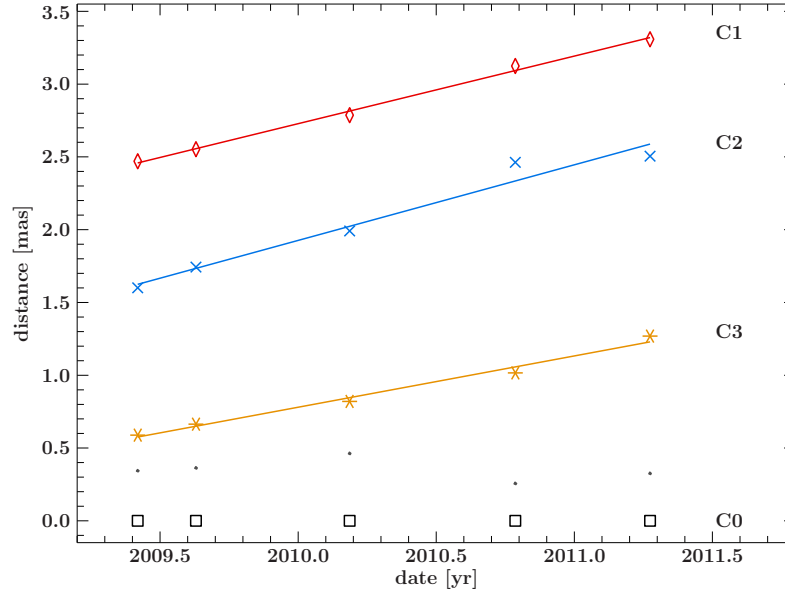
sampling of the (u, v) -plane, and the flux density evolution of components (bright components have smaller uncertainties (e.g. [Lister et al., 2009b](#))) are neglected.

The chosen setup with the MFP, ISIS, DifmapRemeis was designed to overcome these issues. One can fit a model to multiple data sets at once and is able to constraint parameters with functions. In addition, multiple methods for error analysis are available which were already demonstrated for single observations.

To showcase the possibilities of MFP and compare them with the traditional approach I selected the 5 observations of the source 0110+318, for which a kinematic model was already established ([Lister et al., 2013](#)). The object 0110+318 is a flat-spectrum radio source ([Healey et al., 2007](#)) at a redshift of $z = 0.603$ ([Wills & Wills, 1976](#)) and inherits only a moderate complex jet morphology (see Fig. 3.11) which allows an easy identification of components.

Table 3.5: The apparent motions for the components C1, C2 and C3 derived from literature, individual fits and simultaneous fits.

component name	app. motion Lister et al. (2013) [$\mu\text{as yr}^{-1}$]	app. motion indiv. fit [$\mu\text{as yr}^{-1}$]	app. motion simult. fit [$\mu\text{as yr}^{-1}$]
C1	464 ± 13	464 ± 26	465 ± 5
C2	521 ± 58	520 ± 91	492^{+27}_{-20}
C3	342 ± 26	352 ± 24	361 ± 5

**Figure 3.12:** The distance evolution of components in 0110+318. Linear regression fits were applied to components identified by [Lister et al. \(2013\)](#). The dots represent components which were not identified. No uncertainties of the distances are shown since they are too small (~ 0.01 mas).

Reproducing the ballistic fit

Before attempting simultaneous fits I verified that my set up can reproduce the established ballistic model, based on standard techniques, by using a linear regression fit on the date and distance of refitted identified model components with the core component (C0) shifted to (0/0). For the refitting I used the models and the parameter values for the single observations as given in the online supplement by [Lister et al. \(2013\)](#) and included an error calculation for each model parameter. The uncertainty of model component positions is typically very small in the order of 0.01 mas. The derived ballistics (see Fig. 3.12), based on the refitted position values, are in good agreement with the previous results (see Table 3.5). Minor differences can be explained by the different applied weightings of model components and slightly different positions.

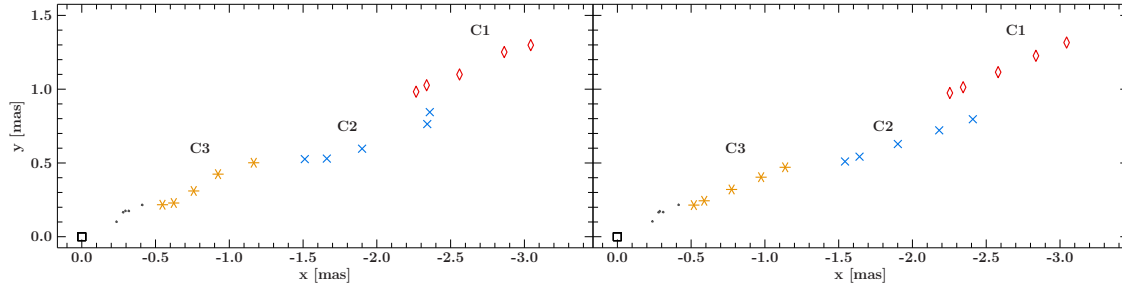


Figure 3.13: The position of all model components for the individually fit data sets (*left*) and for the simultaneous fit (*right*). The same color and symbols are used for the identified components (C0, C1, C2 and C3), while the dots mark the position of unidentified components.

Simultaneous kinematic fit – ballistic

The Cartesian position x, y of a single ballistic model component can be described by

$$x = x_0 + \cos(\alpha)v(t - t_0) \quad (3.21)$$

$$y = y_0 + \sin(\alpha)v(t - t_0) \quad (3.22)$$

with x_0, y_0 as the starting position, α the ejection angle, t_0 the ejection date, and v the apparent motion. I simultaneously fit the kinematic of the identified components C1, C2, and C3 using Eq. 3.21 and 3.22 with the available data set. The ejection position was set to (0, 0) and other starting parameters were derived from the previous non simultaneous fit. The position of all model components in Cartesian coordinates is displayed in Fig. 3.13 for the individual and simultaneous fits to showcase the difference between them.

A comparison of the sum of the χ^2 -values for the individual fits with the combined χ^2 of the simultaneous fit (see Table 3.6) shows that there is only a minor difference and thus one can conclude that the ballistic model is an appropriate description of the data.

The fitted apparent motions (Table 3.5) are in good agreement with the previous works but one has to note that a strong correlation of the vector speed and the ejection date is apparent for all components (C1, C2 and C3). This is depicted in the confidence maps in Fig. 3.14, showing the parameters vector speed and ejection date for the components C2 and C1.

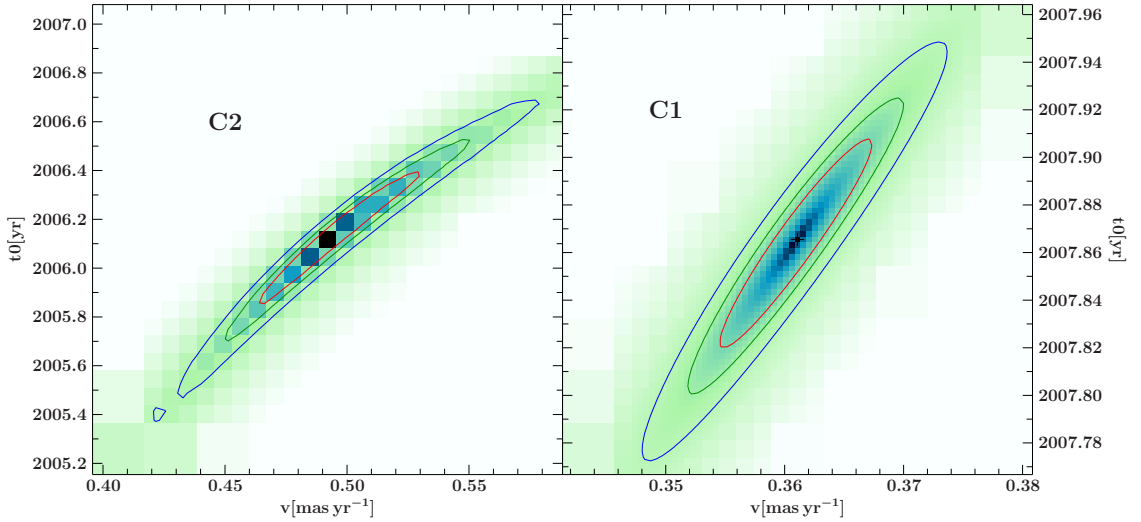
3.3.7 Summary & Outlook

In this Chapter I presented a new module (DifmapRemeis) for the X-ray fitting tool ISIS to fit models to VLBI data using a modified version of DIFMAP. Using this module I was able to reproduce the model fits of the source 0202+319 obtained solely with DIFMAP. Moreover, I demonstrated that the DifmapRemeis is capable of calculating the statistical uncertainties for model parameters, which were found to be in agreement with the conservative estimates.

I find that the χ^2 -landscape inherits multiple local minima and plainly fitting the data

Table 3.6: Comparison of the χ^2 -value of the fits to the individual observations and evaluated for the observations in the simultaneous fit of the ballistics.

observation	single fit	sim. fit (ball.)
date	$[\chi^2]$	$[\chi^2]$
2009 06 03	107133.1	107162.2
2009 08 19	129240.2	129289.9
2010 03 10	143648.7	143681.4
2010 10 15	132613.0	132724.8
2011 04 11	111227.2	111275.2
all	623862.2	624133.4

**Figure 3.14:** The confidence maps of the vector speed and ejection date for the components C2(*left*) and C1(*right*). The contours are $\Delta\chi^2 = 2.30, 4.61$ and 9.21 , corresponding to a confidence of 68%, 90%, and 99% for the two parameters of interest. The black cross marks the position of the best fit values

without error calculation creates a tendency where a fit becomes stuck in these. Error analysis is shown as a possibility to overcome this. Finding the global minimum is important in the aspect of component identification, since small changes in the parameter values can already change the association and thus potential kinematics. For most model components I note a correlation of the flux density and size. No other general correlations were found but I was able to show the effect of a flux density “cross-talk” between components (Homan et al., 2001).

In the second part I demonstrated the capability of DifmapRemeis to simultaneously fit a model to multiple data sets at once by fitting the ballistic kinematics of a jet. This method is different to the usual practice of fitting a kinematic model to the fitted positions of model components, thus ignoring other influential parameters like the flux density. The found apparent motion is in good agreement with the previous analysis of the source but I note a strong correlation between the ejection date and vector speed parameter.

In future works we will use this module fit more complex models, e.g., with accelerating kinematics. Moreover, we will use this module to fit the frequency core shift of sources by simultaneously fitting multi-frequency observations and tying the position of all optically thin components. I will also explore the option to include systematic effects in the calculation of the χ^2 -values therefore affecting the best fits and parameter uncertainties.

4

Kinematics of the jet in 3C 111

4.1 Source overview

The broad-line radio galaxy 3C 111 is situated behind a heavily obscured region identified with the Galactic dark cloud complex Taurus B (Ungerer et al., 1985; Dame et al., 2001) at a position in J2000 coordinates according to the NASA/IPAC Extragalactic Database (NED) of $\alpha=04\text{ h }18\text{ m }21.3\text{ s}$ and $\delta=+38\text{ d }01\text{ m }36\text{ s}$ (J2000). Consequently, very few morphological details about the host galaxy are known in the optical besides being an elliptical galaxy dominated by a bright point-like nucleus. Sargent (1977) measured a redshift of $z = 0.0485$ and classified it as Seyfert 1 due to the broad lines in the optical spectrum. Latest measurements of the redshift by Eracleous & Halpern (2004) show only a slight difference with a value of $z = 0.049$. In the 13th edition of the catalog of quasars and active nuclei by Véron-Cetty & Véron (2010) 3C 111 is still listed as a classical Seyfert 1 galaxy, showing no evidence for a sub-class between Seyfert 1 and 2. The central black hole of 3C 111 was initially estimated to have a mass of $M_{\text{BH}} = 3.6 \times 10^9 M_{\odot}$ (Marchesini et al., 2004) based on the empirical correlation of the mass of a black hole and the velocity dispersion of stars in the host bulge (e.g., Ferrarese et al., 2001). New $\text{H}\alpha$ measurements lead to a lower derived mass of about $1.5 \times 10^8 M_{\odot}$ to $2.4 \times 10^8 M_{\odot}$ (Chatterjee et al., 2011). The different values for M_{BH} were explained by Chatterjee et al. (2011) due to differences in the assumed extinction.

As the name 3C 111 implies, the source is listed in the revised 3rd Cambridge catalog of radio sources by Bennett (1962) although it was not part of it in previous versions (Edge et al., 1959) and is thus detected in the radio regime. Early studies of 3C 111 in the radio with synthesis imaging reveals a triple structure at kilo-parsec scales which consists of a central component and two lobes positioned NE and SW (Laing, 1981). The radio morphology on parsec scales (see Fig. 4.1) was classified as FR II (Fanaroff & Riley, 1974), exhibiting a highly collimated one-sided jet, a few knots and two lobes (e.g., Linfield & Perley, 1984). More details focusing on the radio jet will be given in the upcoming section 4.1.1.

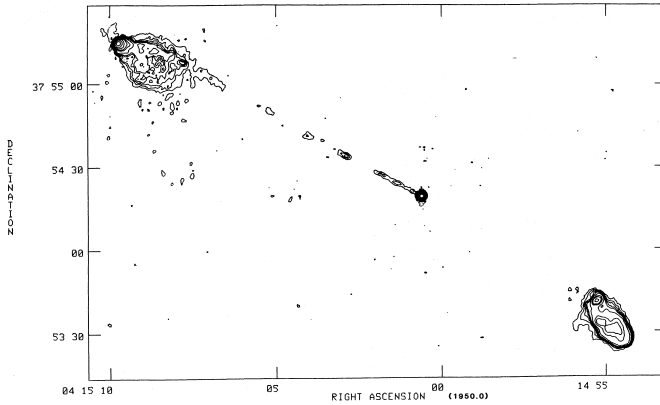


Figure 4.1: Total intensity contour image of 3C 111 with the VLA at 1.4 GHz from [Linfield & Perley \(1984\)](#).

[Golombek et al. \(1988\)](#) found significant flux of 3C 111 in the far-infrared, and it was observed by 2MASS in the J, H, and K band ([Skrutskie et al., 2006](#)).

3C 111 was first detected in the X-rays by [Marshall et al. \(1978\)](#) with the A2 detector on-board of HEAO-1. Recent results by [Hogan et al. \(2011\)](#) with *Chandra* show a one-sided jet structure in the soft X-rays, finding X-ray emission in 3 out of 4 radio knots and in its terminal point. An iron K complex and a weak reflection component were detected in the X-ray spectrum with *Suzaku* and *XMM-Newton* by [Ballo et al. \(2011\)](#).

The source was first detected in the γ -rays by [Hartman et al. \(2008\)](#) associating 3C 111 with the *EGRET* source 3EG J0416+3650. Studies of the first 15 months with the *Fermi*-satellite ([Abdo et al., 2010a](#)) listed 3C 111 as a misaligned AGN in the γ -regime but the source was later omitted from the 2nd *Fermi*/LAT catalog ([Nolan et al., 2012](#)).

A historical multi-wavelength SED was compiled by [Sguera et al. \(2005\)](#) describing the source as a blazar-like object, inheriting a flat spectrum in the radio [Bloom et al. \(1994\)](#) with a strongly polarized core and a blazar-like X-ray spectrum due to the lack of all features.

These results lead to a controversy in the context of the unified model of AGN ([Urry & Padovani, 1995](#)), since a blazar should not show a FR II morphology or be classified as Seyfert 1. Thus 3C 111 is a unique object to study the gap between these different AGN classes.

4.1.1 Radio morphology of 3C 111

The kilo-parsec scale morphology in the radio is composed of a central component, two lobes positioned NE and SW, a jet from the central component to the lobe NE, and a few knots in the jet [Linfield & Perley \(1984\)](#). Zooming into the central components with VLBI resolutions (parsec scale) reveals a jet which shows a similar P.A. as on kilo-parsec scales [Linfield \(1981\)](#) with no sign of a counter-jet structure.

The jet exhibits superluminal motion on parsec scales which was reported by [Götz et al. \(1987\)](#) and [Preuss et al. \(1988\)](#) making this source one of the first radio galaxies to show this effect. The morphology of 3C 111 was extensively studied by [Alef et al. \(1998\)](#) who found a flux density outburst at 43 GHz in 1996 prior to changes of its parsec scale structure, which could not be explained by moving components. A bimonthly monitoring

campaign of AGN, including 3C 111, was performed at 43 GHz in the period from 1998 to 2001 by [Jorstad et al. \(2005\)](#) finding fast and slow-moving features in the jet, which could be backextrapolated to the outburst in 1996. A good explanation for these observations is given in the shock wave model (e.g., [Hughes et al., 1991](#)). In this the fast and slow moving knots are associated with a forward and reverse shock, which were created due to a disturbance of increased velocity or energy flux. In addition [Jorstad et al. \(2005\)](#) reported on the occurrence of trailing components in 3C 111, which were predicted as a general phenomenon in jets by hydrodynamical simulations (e.g., [Agudo et al., 2001](#)). A disturbance interacting with the underlying jet flow and/or the ambient medium can create the observed variability and multiple shocks can be created in the wake of a strong shock wave, which would be observed as trailing features.

The phenomenon of trailing components was also a major result in the analysis by [Kadler et al. \(2008\)](#) studying the data, obtained within the MOJAVE program at 15.4 GHz, over a time span of a decade. [Kadler et al. \(2008\)](#) observed two prominent components, the primary perturbation associated to the outburst in 2006, which were interpreted as a forward and backward-wave. This is in good agreement with the 1D hydrodynamic simulation by [Perucho et al. \(2008\)](#), who explained this by the injection of a perturbation of dense material followed by a time of decreased injection rate. At later epochs [Kadler et al. \(2008\)](#) found the emergence of multiple trailing components in the wake of the primary perturbation at a distance of 3–5 pc away from the core. Based on the non-detection of a counter-jet in 3C 111 [Kadler et al. \(2008\)](#) derived an inclination angle to the line of the sight of $\sim 19^\circ$ for the jet.

A multi-epoch study at 43 GHz using data between 2004 and 2010, and multi-wavelength data from the optical to the X-rays by [Chatterjee et al. \(2011\)](#) showed that the ejection of radio knots succeed major dips in the X-ray lightcurve. This was discussed in the context of a jet-disk coupling and was motivated by the works on 3C 120 by [Marscher et al. \(2002\)](#).

More than a decade after the outburst in 1996 a similar strong outburst was observed in the mid of 2007 at mm wavelengths by [Trippe et al. \(2011\)](#) with flux densities of more than 10 Jy in the 3 mm band. The radio morphology close to the time of the outburst was investigated by [Schulz et al. \(2013\)](#) at 86 GHz finding a prominent bend at a distance of 0.5 mas from the jet base. Early kinematic analysis indicated that this bend is related to this prominent outburst and has a slower apparent motion than is typically observed in this source.

4.2 Radio lightcurves

The lightcurves of 3C 111 (see Fig. 4.2) obtained by the University of Michigan Radio Observatory (UMRAO, details of calibration by [Aller et al., 1985](#)) show outbursts at different observing frequencies of 4.8, 8.0, and 14.5 GHz in the time range from early 2000 to May 2012. A similar behavior is observed in the MOJAVE data at 15.4 GHz and in the Submillimeter Array (SMA) data at 230 GHz. The details of the calibration of the SMA data is given by [Gurwell et al. \(2007\)](#). A compilation of different lightcurves for 3C 111 is

given in [Chatterjee et al. \(2011\)](#), including the UMRAO 14.5 GHz data and the 230 GHz data of the SMA.

At 14.5 GHz 6 outbursts can be identified between 2005 and 2012 with 4 of them being prominent. The prominent outbursts are shown as dashed lines while the minor ones as dotted lines in Fig. 4.2. At lower frequencies the outbursts are harder to detect, if at all. At 4.5 GHz only two outbursts are observed. The observed variability and different peak times of the outbursts is not atypical for these type of objects. [Angelakis et al. \(2012\)](#) studied the variability of 78 *Fermi* detected blazars (including 3C 111) at frequencies between 2.64 and 142 GHz finding different variability patterns, with the observed pattern of 3C 111 being the second most prevalent pattern. A model to explain the observed frequency depending peak time is given by the shock-in-jet model of [Marscher & Gear \(1985\)](#), which suggests that the variability is caused by shocks propagating down the jet and experiencing – ordered in the time of their appearance – Compton, synchrotron and adiabatic energy losses.

In the 14.5 GHz lightcurve the first outburst starts 2004.6, peaking in 2005.1, and ending at 2005.8. During this time the total flux density increased by about 1 Jy, before settling at a level of about 0.5 Jy higher than before. The onset of the second prominent outburst starts in 2005.8 with the peak a half a year later before declining until 2007. The overall flux density level increased by 1 Jy with a peak increase of 2 Jy at the time of the maximum. The most prominent outburst starts in 2007, peaking in 2008 before declining until 2008.5. At that point a change of the decline rate is observed for 0.2 years before it returns to previous one until 2008.8. This can be seen as a minor outburst at 2008.6. The total flux density nearly doubled during the major outburst from 4.8 Jy to close to 9 Jy, and was at a level of 6.9 Jy at the time of the minor outburst. The last prominent outburst showed an onset of peak flux increase of 1 Jy starting at 5.8 Jy before declining to about 4 Jy. During this outburst a minor outburst appears again and is observed at 2009.4, which also delayed the decline of the flux density for about 0.2 years. The rising phase of the prominent outburst started 2008.8 and lasted only 0.4 years before declining for ~ 1 year. The observed flux density after the prominent outbursts is at a level ~ 500 mJy higher than before the onset of the prominent outburst series, suggesting some kind of change in the source.

The rise time between the prominent outbursts changed starting with 0.5 years, peaking with 1.0 year for the major outburst, and returned to about a half a year afterwards. The decay phases seem to increase from 0.7 to 1.1 years and is most likely caused by the additional appearance of the minor outbursts in the two latest prominent outbursts. The naming of the different outbursts in chronological order is: 2005 outburst, 2006 outburst, 2008a outburst, 2008b outburst, 2009a outburst, 2009b outburst.

The prominent outbursts at 8.0 GHz showed a time delay of 0.2 to 0.4 years to the ones at 14.5 GHz, while the minor ones are not visible. The flux density increments in the outbursts were only about half as strong, which is also true for the netto gain in flux density. At 4.5 GHz an overall increase in the flux density starting at ~ 7 Jy to close to 10 Jy in 2008.6 is observed. This is followed by a time of steady flux at about 9 Jy until 2009.7 ending with a small increase in flux of about 0.5 Jy before the flux density declines and stabilizes at about 7.5 Jy. The minor peaks can be associated with the last two prominent outbursts seen at the higher frequencies.

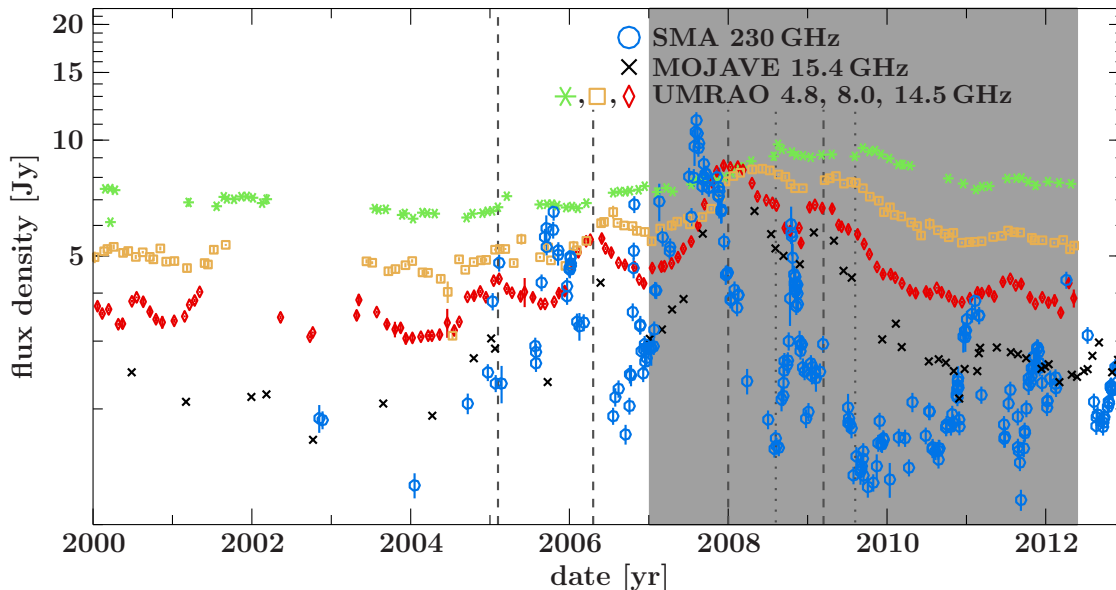


Figure 4.2: Monthly binned lightcurve of 3C 111 at 4.8, 8.0, and 14.5 GHz as observed by the UMR AO. UMR AO funding ended in May 2012, therefore no monitoring exists after that date. Individual VLBI observations of 3C 111 within the MOJAVE program are shown with a black cross. The shaded region marks the time span for VLBI observations obtained in the MOJAVE project are analyzed in this thesis. The dashed lines mark the peak of the prominent outbursts, while the dotted lines mark the peak of minor outbursts in the time range from 2005 to 2012.

The 230 GHz lightcurve (see Fig. 4.2) shows outbursts preceding the above mentioned prominent outburst at 14.5 GHz. In addition smaller peaked outbursts are indicated close to the prominent ones. No apparent sign of an increased flux density level is observed after the prominent outburst series, suggesting that the phenomena only exists at lower frequencies.

4.3 VLBI observations

The MOJAVE program observed 3C 111 for a total of 36 VLBI runs during the period of 2007 to May 2012. The data were calibrated according to [Lister et al. \(2009a\)](#). We fit each data set exclusively with circular Gaussian components, and self-calibrational steps of the phases were applied to improve the quality of the fit. To ensure as much consistency as possible between the models of close in time observations, finished models were used as a starting point if applicable.

The time evolution of the jet structure is displayed in Fig. 4.3. The contours of selected clean images (obtained from the MOJAVE project¹) are separated according to their relative observation date with 1 yr equivalent to a separation of ~ 4 mas. To avoid confusion

¹<http://www.physics.purdue.edu/astro/MOJAVE/>

in the overlay figure, only observations which are close to half a year apart were chosen and the first contour is set to the 10σ noise level. The clean images were restored with the given beam of the respective (u, v) coverage using natural weighting. The contours are overlaid with the positions of the corresponding model fit components marked with a triangle. The size of each component is given by the radius of the circle and is color coded according to its respective brightness temperature with black indicating a $T_{\text{B}} > 10^{11}$ K and white a $T_{\text{B}} < 10^8$ K. In this Fig. 4.3 it can already be seen that moving features show pronounced structural evolution over time.

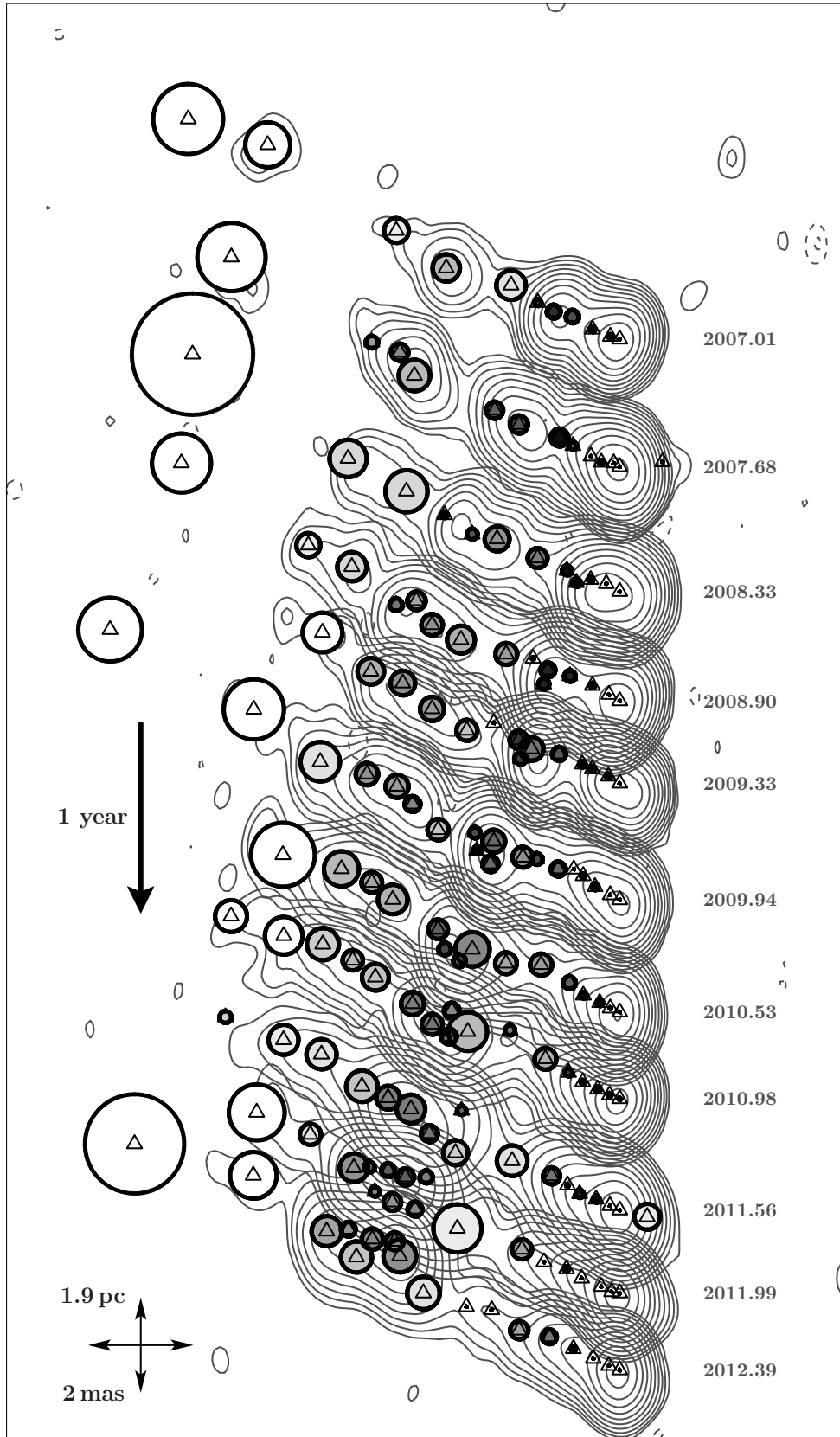


Figure 4.3: Contours of selected clean images starting at 10σ background level and natural weighting. The separation of individual images is scaled to the time of the observation. Position and size of the circular model components for each observation are 79 overlaid and color coded according to their respective brightness temperature (white: $T_B < 10^8$ K and black $T_B > 10^{11}$ K).

4.4 Model fitting and identification

A large number of Gaussian model components (typically 15) are needed to represent the brightness distribution of the jet in one epoch (see Sect. 3.2.4 for an introduction to model fitting), totaling in more than 550 individual Gaussian model components for the whole data set of 36 observations. This representation allows us to study the kinematics and evolutionary behavior of features by comparing the models of consecutive observations. The time evolution is very complex and in many cases it is not possible to uniquely track features over multiple epochs (see, for instance, Fig. 4.3). Focusing on the last model (2012.39) a complex and bright region starting at a position of ~ 5 mas down the jet stream can be observed. This region spans about 2 mas and is modeled with a series of Gaussian components. Comparing the image to previous images reveals that the bright region was traveling along the jet axis with a change in the number and position of model components needed to describe that region. Therefore individual Gaussian components in this complex region cannot be tracked over multiple years, but it is possible to trace the overall emission region back to its origin 2008.33 and clearly associate it with the flux density outburst 2008a. At this time the feature first appears in the Gaussian model as a single component with an offset relative to the locus of the majority of components between 0 mas and 2 mas from the core along $PA \sim 68^\circ$ by 0.2 mas to the south.

The large number of Gaussian components and the changing models make an association of these Gaussian components, between two or more observations, extremely challenging. Therefore the component identification is split into the multiple parts of components associated to any of the prominent outbursts and, if applicable, their successor components which are not necessarily ballistic. The division is displayed in Fig 4.4 showing the distance of each model component to the model component closest to the jet base (henceforth C1) against the time of observation. A dividing line at a distance of 0.8 mas was chosen to separate the inner part of the jet from components. This inner region is usually modeled with two to four components for which no clear associations appear to be possible. The components associated with the prominent outburst 2006, shown as red squares in Fig.4.4, can be observed over the whole data set (Sect. 4.4.1). The components associated with the outbursts of 2008 are shown as orange diamonds (Sect. 4.4.2) and the ones associated with the outbursts of 2009 (Sect. 4.4.3) are shown as blue circles. All other model components which either could not be clearly identified or show no link to any of these outbursts are shown as black dots. Figure 4.4 shows the UMRAO lightcurves for the same time range. The shaded regions mark the periods of the prominent outbursts, with light gray highlighting the rise and dark gray for the decline phases. The maxima of the prominent outbursts are displayed with dashed black lines, while the minor ones are marked with a dotted line.

The naming convention of components is the following. Any component that can be tracked for at least four epochs shows ballistic kinematics, and a model component close to the inner jet region starts with the letter B (ballistic). This is followed by the first two digits of the position angle counted from the north which is derived by a linear regression in the (x, y) plane of all associated Gaussian components. The final letter starts in alphabetical order from A to Z and is used to differentiate between ballistic components

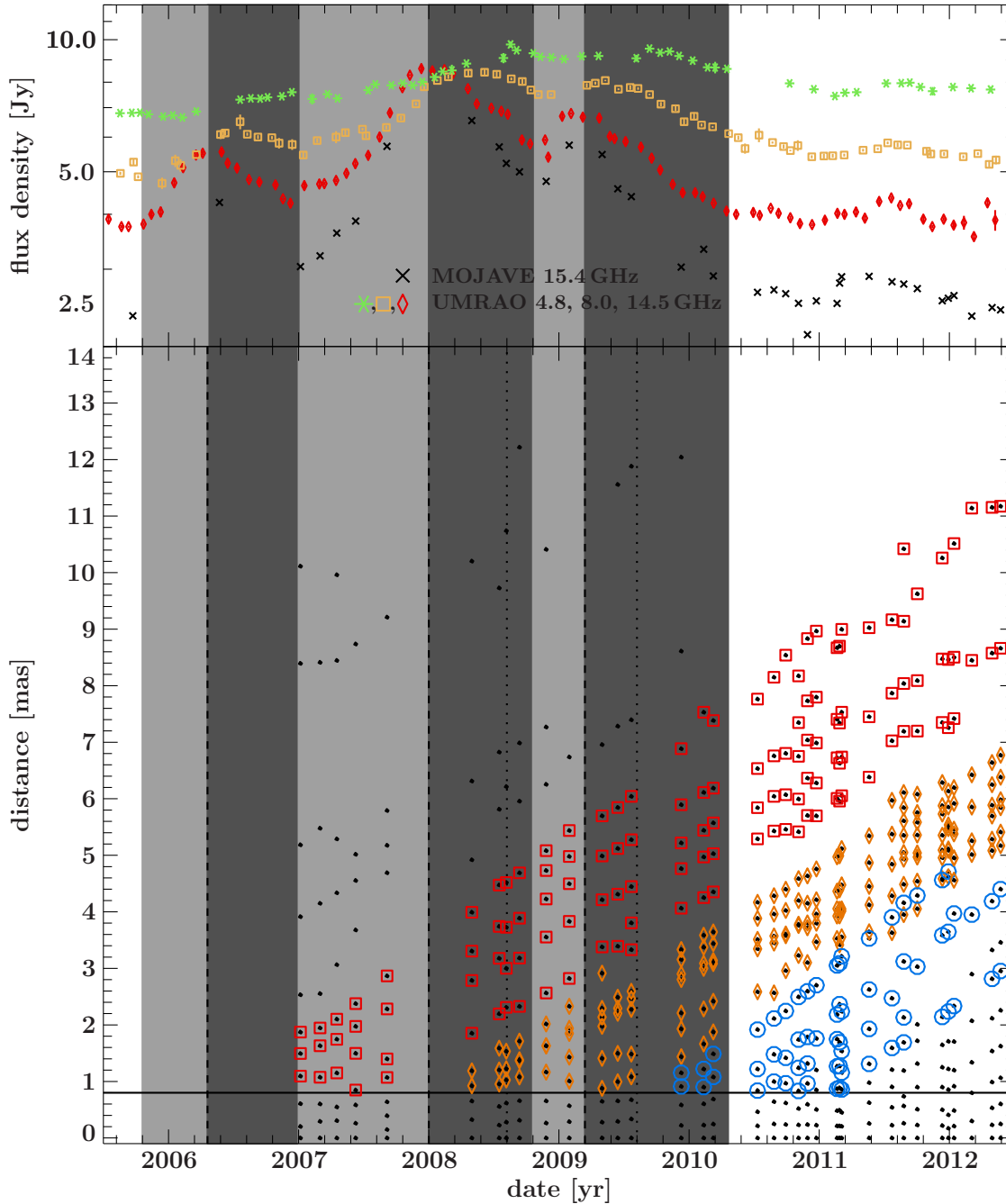


Figure 4.4: The lower panel shows the distance to component C1 over time for all fitted model components (black dots). The model components associated with the outbursts in 2006 are marked in red, while the ones associated with the outbursts in 2008 are marked in orange, and the components associated with the outbursts in 2009 in blue. The top panel shows the lightcurve during the same time range. The shaded regions in light gray mark the rise of the outburst while the dark gray the decline. The vertical dashed lines show the peak time of the prominent outbursts and the dotted lines the ones of the minor outbursts. A solid horizontal line marks the region of the inner jet.

for which the same position angle was derived, but which were ejected at different dates. The kinematics for ballistic components changed at some point and starting from this epoch these components have the additional letter C at the start of their name, i.e. B66a to CB66a. Newly formed components, traceable for more than five epochs but with no model component close to the inner jet region are given the name NX, with X being the increasing number for these new components (N1, N2, ...). All other model components are usually named U (unknown). Some of these components have an additional number attached starting from 1 (U1, U2, ...) in case they are important to explain the observed. In rare cases two model components of one epoch are associated with a single component. This was used when no clear assignment of a single component was possible but the summed flux density of both model components and the mean flux density weighted position of these indicated a viable association to the component. These two to one associations were only used when the change in the model seemed to be temporary (did not occur in more than three consecutive epochs). Sometimes even more complex structural changes in the model occurred, like the evolution from two model components to three but also the reverse can be the case. In these cases the most likely associations are given as well. Unless otherwise noted, these model components were not used to derive any properties like the vector speed of components and are displayed as dots in all upcoming figures.

An explanation for this temporary change of the model composition might be attributed to differences in the (u, v) -coverage between observations which can change the resolution capabilities of the interferometer array. In addition multiple models are able to describe the data equally well (Lister et al., 2009b), so this might be a modeling effect. However a temporary change in the jet structure cannot be ruled out.

The uncertainties of the component parameters cannot be derived with the current analyzing programs such as DIFMAP or AIPS by using χ^2 statistics and are also very susceptible to the calibration of the data see e.g., Lister et al. (2009a). In section 3.3 we developed a new method to compute these uncertainties, but we do not apply it for this analysis due to the complexity of the data set. The uncertainties presented here are derived by rescaling the uncertainties of parameters in fits such that the reduced $\chi^2 = 1$ with an equal weighting of the model components. This is in analogy to the analysis presented by Homan et al. (2002) and Lister et al. (2009b). One has to note that these errors will underestimate the real uncertainties and cannot account for any systematic effects.

For each identified component the P.A. in the (x, y) -plane is derived by a linear regression fit in 2D-space (see Fasano & Vio (1988)) with all component positions shifted such that the mean position is centered at zero (see Fig. 4.5). The vector speed and the ejection date for each component is derived by first calculating a new relative position. In the case of ballistic components originating close to the inner jet region this relative coordinate is defined as the closest position (C1*) on the backextrapolated trajectory and C1 (see Fig. 4.6). For components which are only identified further down the jet stream it is defined as their mean position. From this relative position the distances to the respective model components are determined. A linear regression fit on the observation date with the mean date shifted to zero and the derived distances will then yield the vector speed and, for ballistic components, also the ejection time.

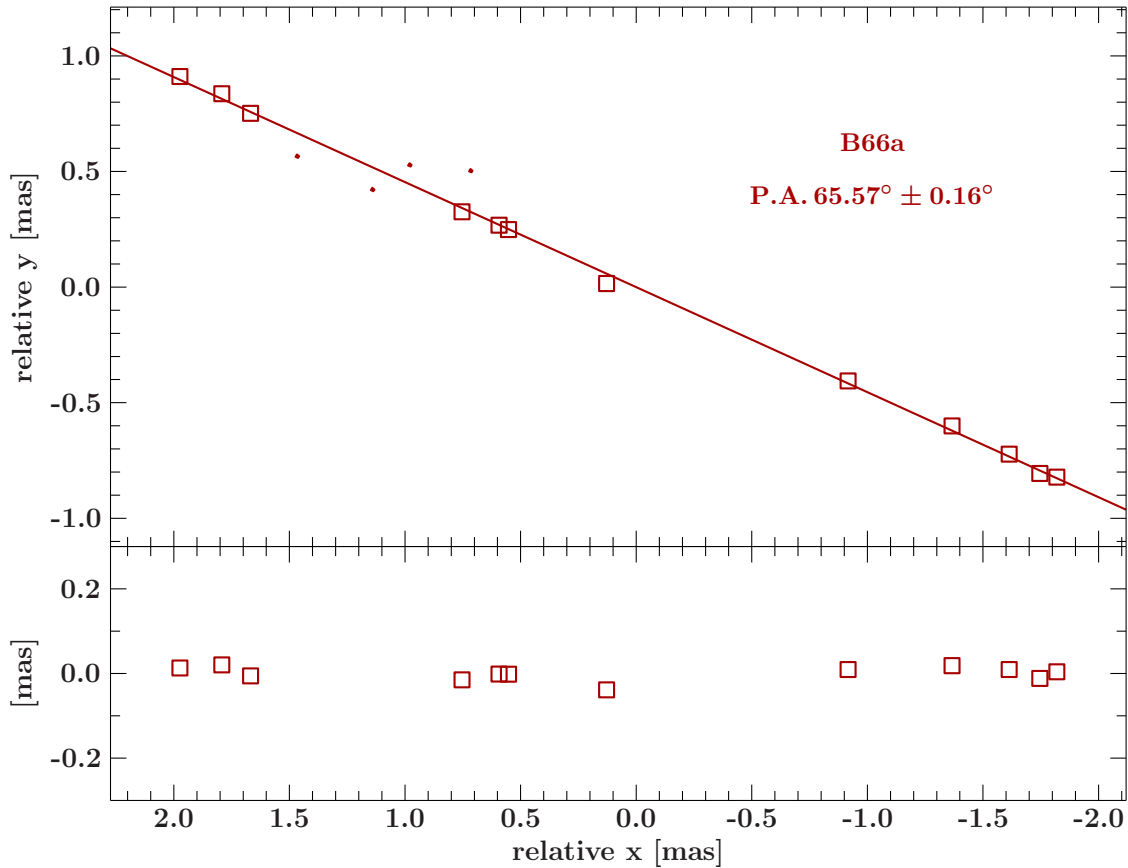


Figure 4.5: In the top panel the shifted x and y position of component B66a, with the mean of x and y centered at zero, is depicted. A two dimensional linear regression fit with the algorithm by [Fasano & Vio \(1988\)](#) is overlaid. The distances of the linear regression fit to the corresponding model component positions are shown in the lower panel.

4.4.1 Kinematics of components associated with the 2006 outburst

In section 4.2 we showed that the lightcurve of 3C 111 (see Fig 4.2) displays multiple prominent outburst. The evolving jet structure associated with the 2006 outburst (see Fig. 4.7) will be discussed in the following. We find the emergence of ballistic components with various vector speeds and position angles close to the inner jet region at the time of this outburst. Analyzing the associated jet structure at later epochs showed that components vanished, changed their kinematics or new ones appeared.

Ballistic jet structure

We find a total of 3 ballistic components which can be associated with the start of the 2006 outburst originating close to the inner jet region. One ballistic component is found at the end of the 2006 outburst. An illustration of these components is given in Fig. 4.8.

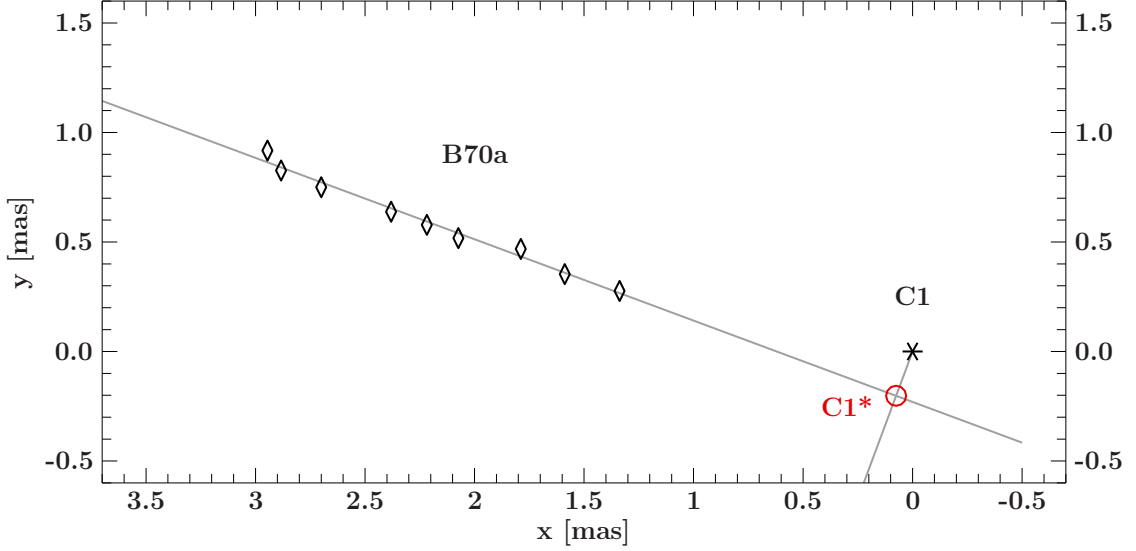


Figure 4.6: Illustration of the C1* position. A two dimensional linear regression fit is applied to the position of model components. The intersection of the backextrapolated trajectory and the normal of it through C1 is called C1*(the closest position on the trajectory to C1.)

Table 4.1: Name and attributes of all emerging ballistic components. The columns in the order of their appearance list the names of the components its, their vector speed, ejection date, and P.A.

name	vector speed [mas yr ⁻¹]	ejection date [yr]	P.A. [deg]	counts
B66a	1.71 ± 0.03	2006.00 ± 0.07	65.57 ± 0.16	12 (14)
B68a	1.50 ± 0.03	2006.09 ± 0.05	68.08 ± 0.68	11
B71a	0.93 ± 0.43	2005.92 ± 0.63	70.68 ± 4.19	4
B68b	1.31 ± 0.03	2006.86 ± 0.07	68.33 ± 4.66	12 (14)

In Table 4.3 the compiled properties of these components i.e. vector speed, ejection date, P.A. and number of identifications (counts) are presented.

B66a was ejected in 2006 with a vector speed of $1.71 \pm 0.03 \text{ mas yr}^{-1}$ at a P.A. of $65.57^\circ \pm 0.16^\circ$. The ejection date coincides with the rise of the 2006 outburst in the lightcurve at 14.5 GHz and a peak at 230 GHz (see Fig 4.9). A comparison of the ejection time and vector speed with the 43 GHz analysis by Schulz (2012) suggests component B16 to be the most likely counterpart. The flux density of B66a (see Fig. 4.10) increased in first three months from $\sim 40 \text{ mJy}$ to $\sim 200 \text{ mJy}$ before being constant for 1.5 years at $\sim 150 \text{ mJy}$. Two model components were fitted to this region in the next two epochs thus no clear identification could be made. Using the summed flux density of these two model components as an estimate (black squares in Fig. 4.10), one finds B66a to become fainter. In the last three epochs the flux density was at a value of 50–60 mJy with a further decline indicated.

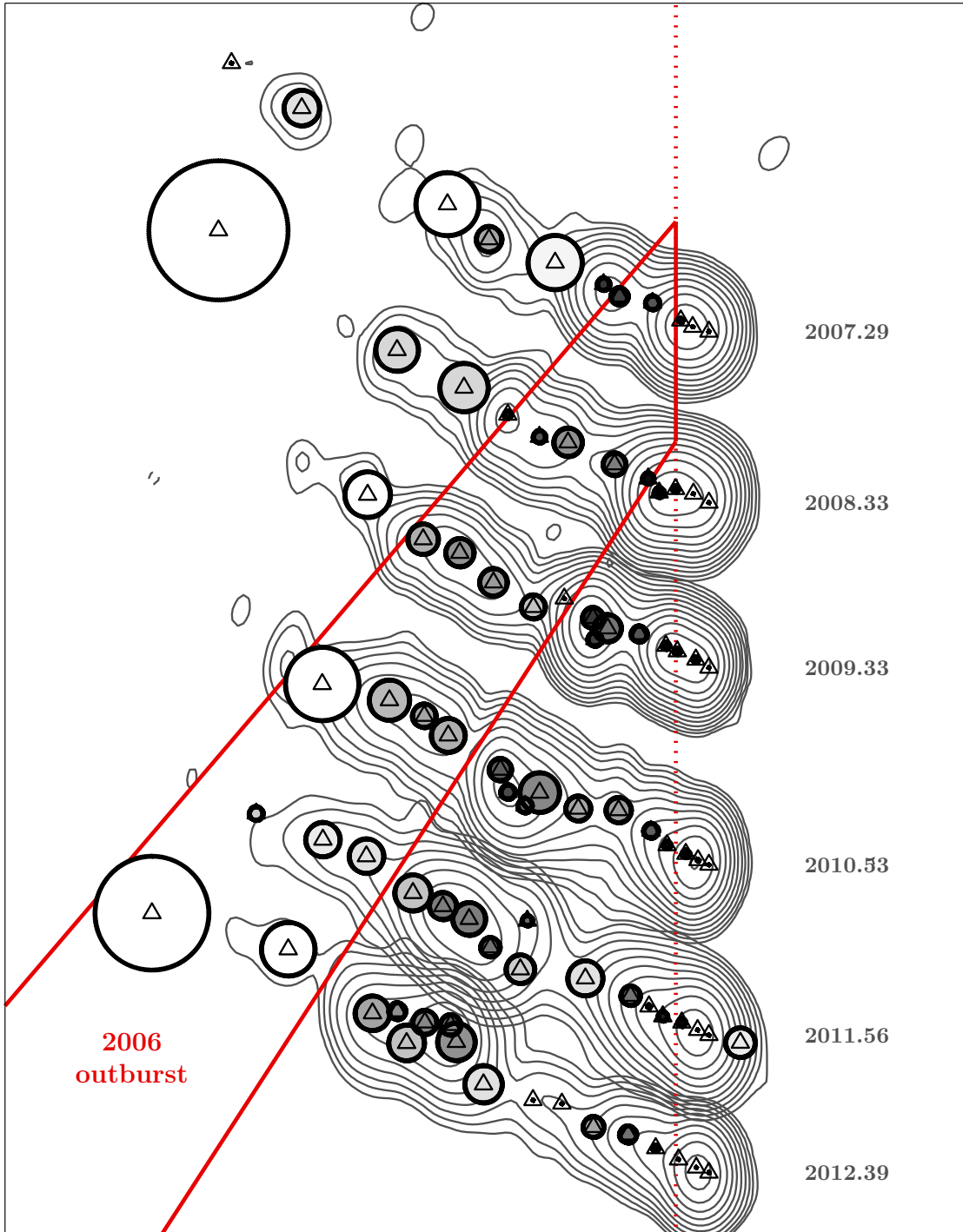


Figure 4.7: Illustration of the region in the jet associated with the 2006 outburst. The contours of selected clean images start at a 10σ background level. The separation of individual images is scaled to the time of the observation. Position and size of the circular model components for each observation are overlaid and color coded according to their respective brightness temperature (white: $T_B < 10^8$ K and black $T_B > 10^{11}$ K).

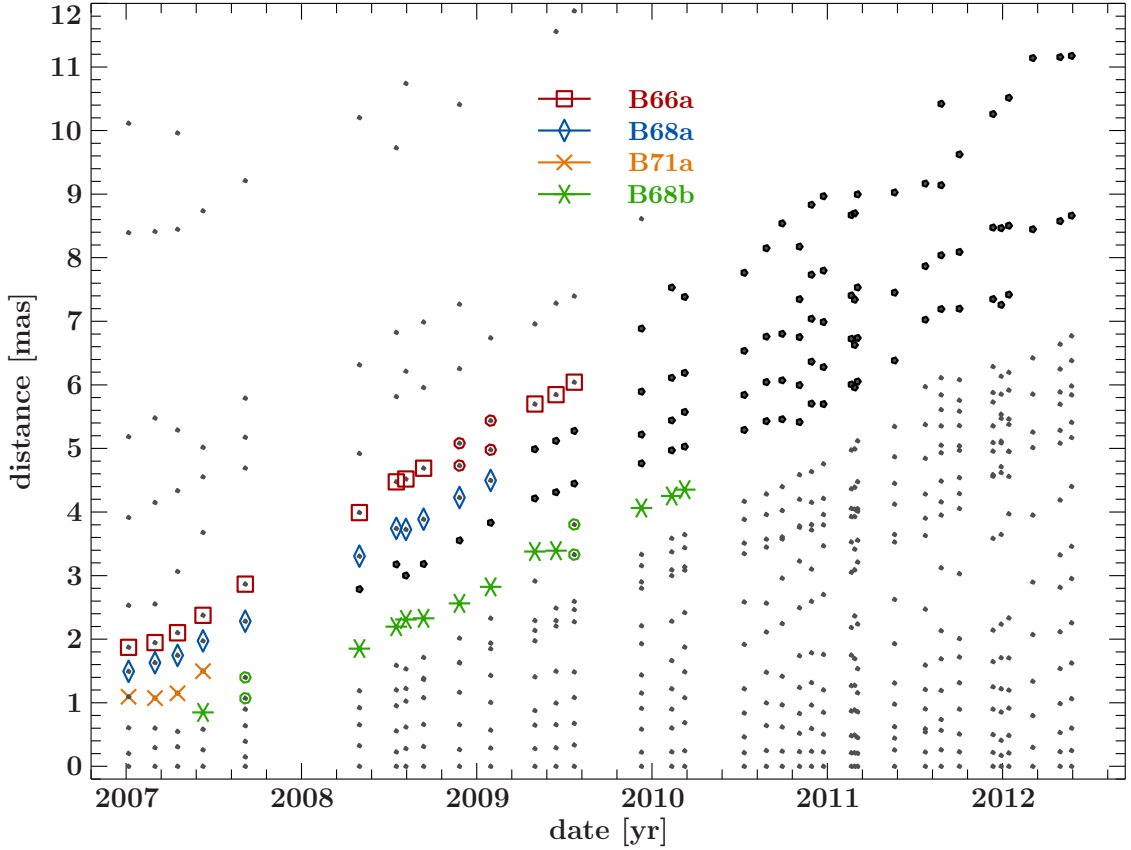


Figure 4.8: The distance of ballistic components to the respective location of C1. The distance of all model components are shown in gray, while the components associated to the 2006 outburst are shown as bold black dots. If multiple components were associated with one particular component they are depicted as circles in the color of the component.

Component B68a was ejected closely after B66a in 2006.09 ± 0.05 (see Fig. 4.9). The vector speed is $1.50 \pm 0.03 \text{ mas yr}^{-1}$, which is slightly slower than for B66a, at a P.A. of $68.08^\circ \pm 0.68^\circ$. The most likely 43 GHz counterpart in the work by Schulz (2012) is B15 which has similar characteristics. During the first five epochs the flux density of B66a is constantly declining. After a break of ~ 0.75 years, for which no observations are available, the flux density is a factor of 3 lower than before. It remains constant for a half a year before a decline is indicated.

A third component which can be potentially associated with the rise of the 2006 outburst is B71a (see Fig. 4.9). It was only identified in four epochs displaying a rapidly decreasing flux density (see Fig. 4.10). The derived characteristics of the ejection date, P.A. and vector speed is not robust but we note that the trend of decreasing vector speeds and larger P.A. values seem to continue. The most likely association at 43 GHz is component B5, which was found to have a slow apparent motion and its position in the (x, y) -plane indicates a change of the P.A. (see Fig. 5.11 in Schulz (2012)).

In 2006.86 ± 0.07 the ballistic component B68b emerged, the date coincides with a plateau

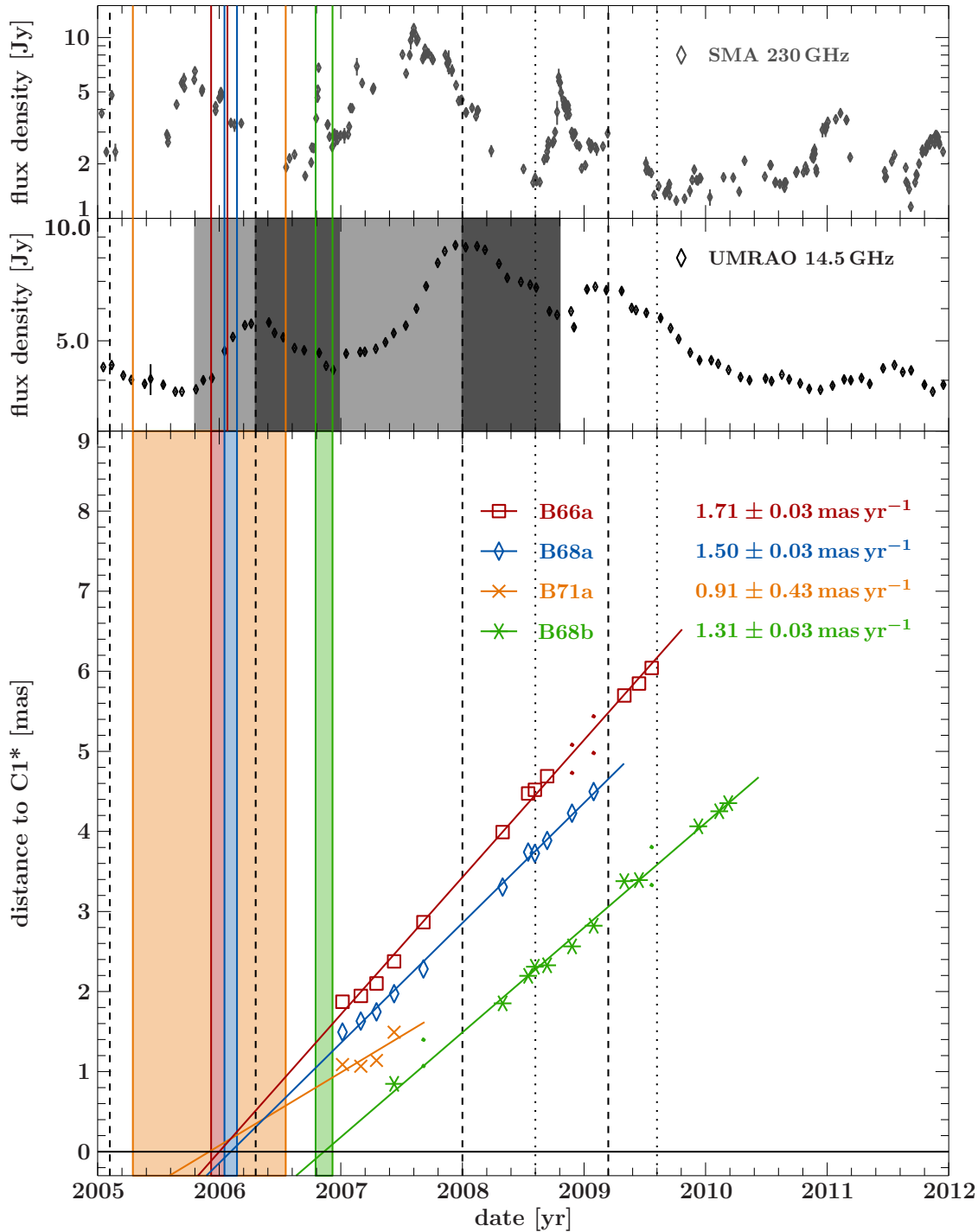


Figure 4.9: *top:* SMA lightcurve at 230 GHz. The colored lines mark the range of ejection dates for all ballistic components shown in the bottom panel. *mid:* UMRAO lightcurve at 14.5 GHz. The shaded regions mark the rise and decline phase of prominent outbursts. The colored lines are the same as in the top panel. *bottom:* The distance of ballistic components to the respective location of C1* over time and overlaid with linear regression fits. The derived ejection times (by extrapolating the fits) are shown as shaded regions in the corresponding color of the component. The dashed black lines mark the peak time of the prominent outburst in the light curve at 14.5 GHz, while the dotted black lines mark minor outbursts.

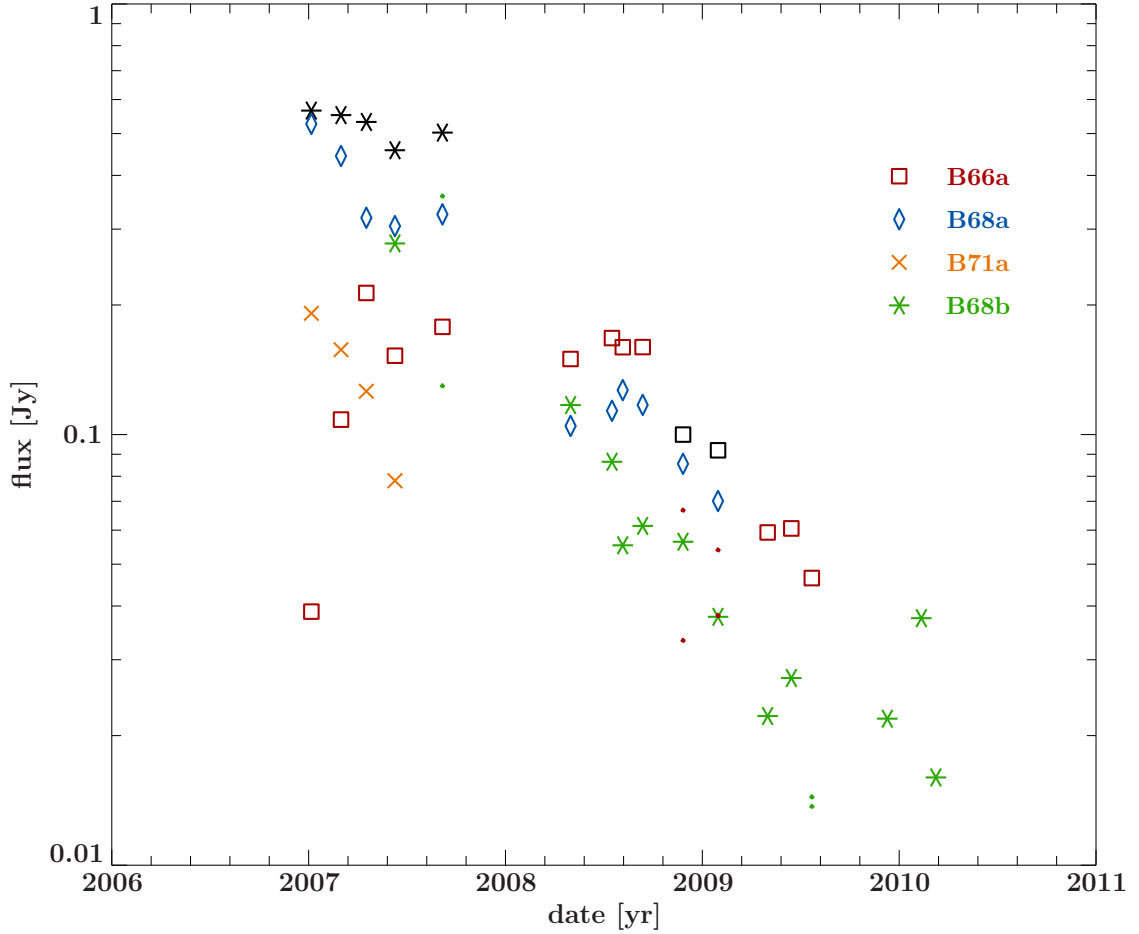


Figure 4.10: Flux density evolution for the different ballistic components before outburst 2008a. The colored dots show associated components that were not considered in the determination of characteristics. The black stars show the sum of the flux densities of component B66a and B68a in the first five epochs. The black squares show also the sum of the flux densities but for the associated components of B66a.

in the lightcurve at 14.5 GHz and a peak at 230 GHz. The component has an apparent motion of $1.31 \pm 0.03 \text{ mas yr}^{-1}$ at a P.A. of $68.33^\circ \pm 4.66^\circ$. Over the course of three years B68b becomes constantly fainter starting at 300 mJy and ending at 15 mJy. No clear counterpart to B68b in the 43 GHz data is found.

Structural changes in the jet region associated with the outburst 2006.

We find that the composition and characteristics of components in the region associated with the outburst 2006 to change over time. New components or the ones which display a change in their properties will have new names according to our naming convention. These components are displayed in Fig. 4.11, showing the distance of all model com-

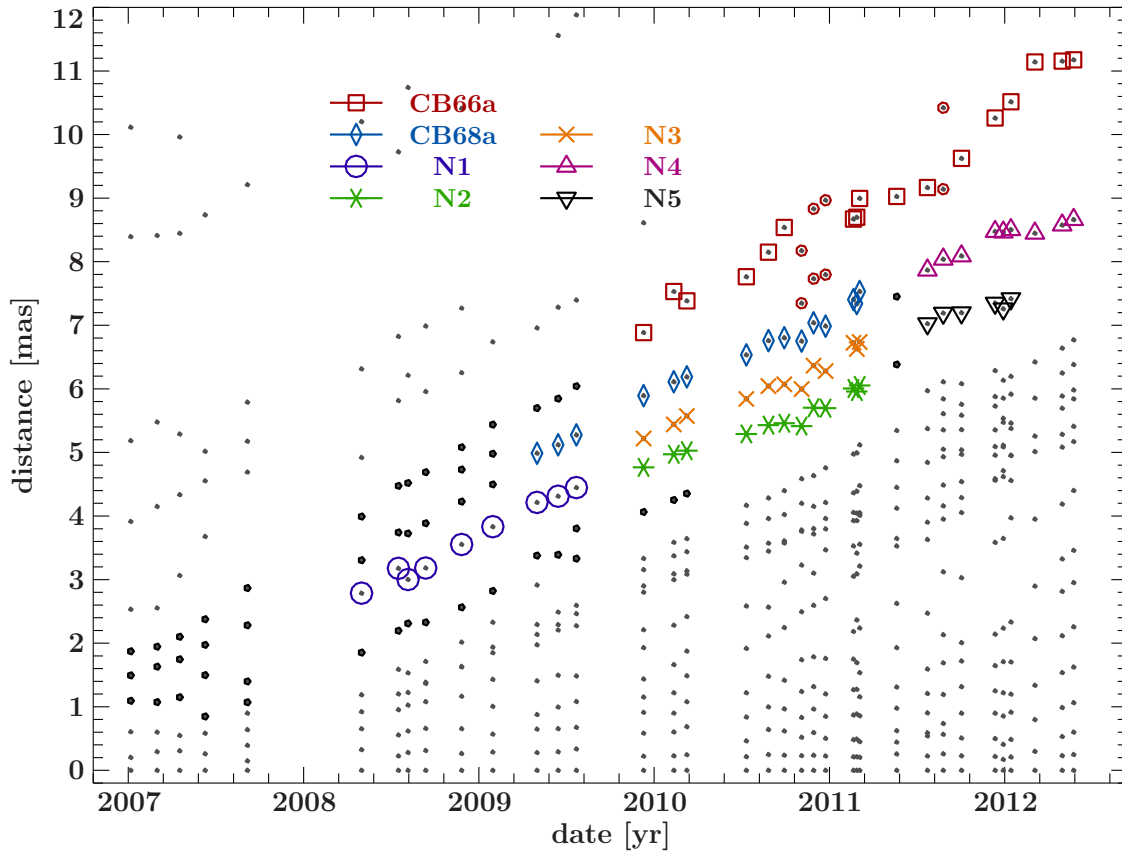


Figure 4.11: The distance to C1 versus the observation date for all model components associated to outburst 2006 which appear down the jet stream. The bold black dots mark the ballistic components associated with the 2006 outburst.

ponents in the context of the identified ballistic component associated with the 2006 outburst. An overview of all characteristic properties for these components is given in Tab. 4.2.

Starting in the order of their appearance, N1 was first identified in the observations starting 2008 with a vector speed of $1.40 \pm 0.07 \text{ mas yr}^{-1}$ (see Fig. 4.12) at a P.A. of $68.33^\circ \pm 4.56^\circ$ in the (x, y) -plane. Besides the first two epochs, which indicate a decline, the flux density increases slightly over the course of 1 year (see Fig. 4.36). The discrepancy of the first two epochs might be due to a modeling effect, which would also explain why we observed the unusual behavior of B68a during that time. This will be investigated in future works and is beyond the scope of this work. N1 could be a trailing component created in the wake of B68a and is a typical component type for this source (Kadler et al., 2008). This is supported by the fact that both components have only minor differences in their vector speeds and the trajectory of N1 intersects the locations of B68a (see Fig. 4.14). Although N1 is different from these trailing features by being observed at distances between 2.5 mas to 4 mas while they usually appear at a distance of ~ 4 mas (Kadler et al., 2008).

A potential predecessor candidate for N1 is found (B71a) by backextrapolating its dis-

Table 4.2: Name and attributes of all components appearing in positions related to ballistic components of 2006. The columns in the order of their appearance list the names of the components, their vector speed, P.A., number of unique identifications, and if applicable the possible predecessor(s).

name	vector speed [mas yr ⁻¹]	P.A. [deg]	counts	pos. predecessor
CB68a	1.29 ± 0.04	57.90 ± 1.09	15	B68a
CB66a	1.69 ± 0.10	64.26 ± 3.81	25	B66a
N1	1.40 ± 0.07	68.33 ± 4.56	9	B71a
N2	0.98 ± 0.07	59.31 ± 2.48	12	N1, B63a
N3	1.15 ± 0.08	62.76 ± 1.00	12	N1, B63a
N4	0.92 ± 0.14	57.70 ± 27.71	9	CB68a
N5	0.68 ± 0.13	56.02 ± 20.66	6	N3

tance evolution, which intersects with the distance of B71a. This is supported by the fact that the trajectory of N1 in the (x, y) -plane also intersects with the positions of B71a (see Fig. 4.14). The trajectory of N1 is not necessarily ballistic but can also be described as curved, indicating acceleration. If B71a is the predecessor of N1, one has to explain why the flux density increases again although B71a is thought to be vanishing.

N1 could only be tracked for 9 epochs before the region was modeled with two components N2 and N3 (see Fig. 4.11). N2 and N3 were found to have a vector speed of $0.98 \pm 0.07 \text{ mas yr}^{-1}$ and $1.15 \pm 0.08 \text{ mas yr}^{-1}$. The trajectories as seen in Fig. 4.15 favor N2 to be the most likely successor of N1, showing a similar curvature, although one has to explain the discrepancy in the apparent motion. N3 seems to be the less likely since the difference between the first component of N3 and the last component of N1 is $\sim 0.9 \text{ mas}$. Taking into account the difference of the observation dates of ~ 0.4 years N1 would have to accelerate to a vector speed of at least 2.0 mas yr^{-1} to explain the spatial distance.

Both components N2 and N3 have similar flux densities and decay with the same rates (see Fig. Fig. 4.13). Moreover we observe the flux density exchange as described in Homan et al. (2001) between model components of N2 and N3 which makes the differentiation of these components complicated.

We find that the summed flux density of N2 and N3 (gray stars in Fig 4.13) in the first three epochs is higher than the extrapolated values for N1. Thus it is unlikely that N1 is the sole predecessor of N2 and N3. Taking into account the additional flux density of CB68a one finds that the summed flux density of N1 and CB68a is in good agreement with CB68a, N2 and N3 (gray left handed triangles in Fig. 4.13). This will be investigated in more details in future works considering uncertainty calculations and dependencies of model parameters.

Component B68a is the predecessor candidate of CB68a based on distance versus observation date arguments (see Fig. 4.12 and 4.9). This is supported by the observed trajectories of the components (see Fig. 4.16). The trajectory of CB68a can be described as slightly curved which becomes linear with increasing distance. In the simple assumption of a ballistic trajectory for CB68a the fitted vector speed is $1.29 \pm 0.04 \text{ mas yr}^{-1}$ which

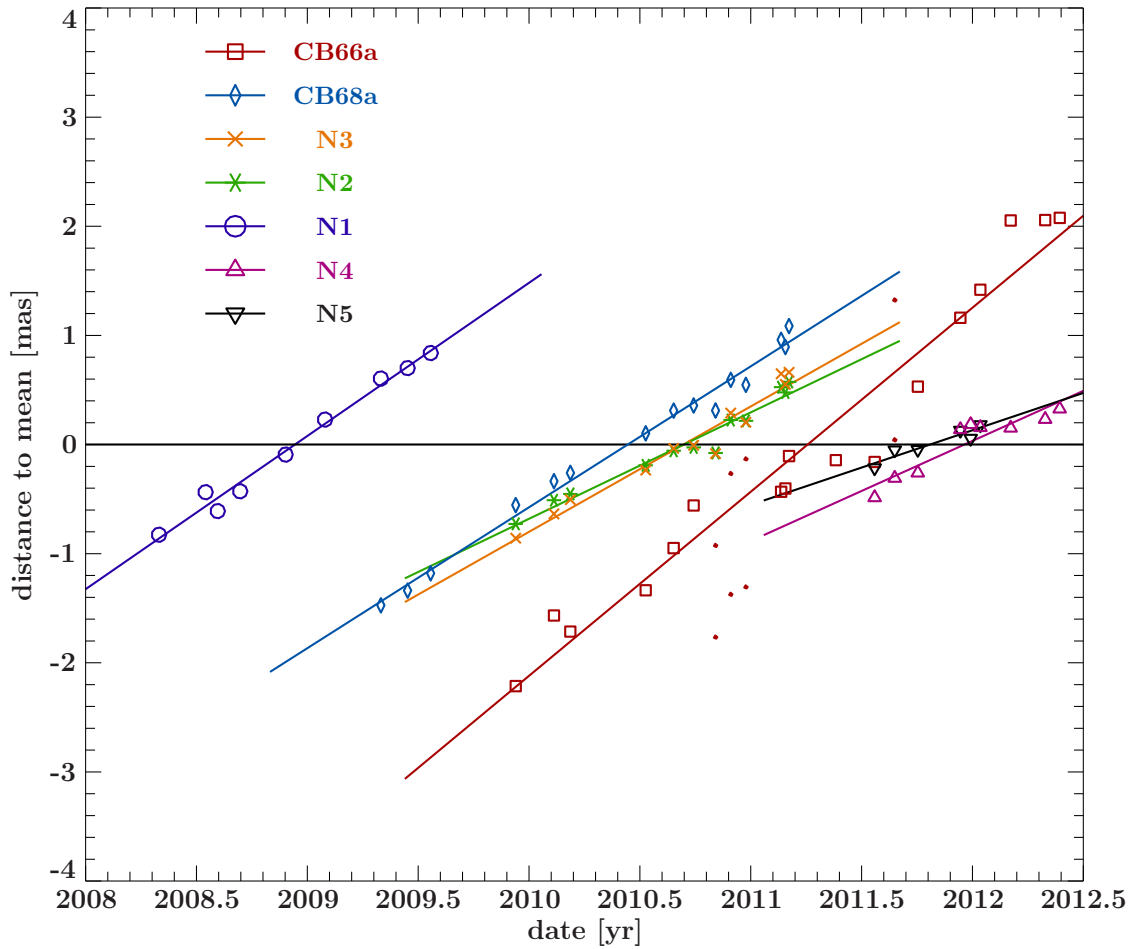


Figure 4.12: The distance of associated components to their mean position for each observation date, overlaid with linear regression fits indicating their respective vector speeds.

is $\sim 0.2 \text{ mas yr}^{-1}$ less than that of B68a. The P.A. of B68a and CB68a differ by more than 10° indicating a strong change of direction during the evolution of the component. In a comparison of the flux density of the last component in B68a and the first one in CB68a an increase in flux density by $\sim 50\%$ from $\sim 70 \text{ mJy}$ to $\sim 110 \text{ mJy}$ has to be noted. In the first six epochs a minor decrease in flux density is observed for CB68a which becomes more rapid afterwards (see Fig. 4.13). The model component position for these six epochs are also the ones indicating the curvature, suggesting a connection between curvature and flux density.

Based on their trajectory (see Fig. 4.17), distance (see Fig. 4.11) and flux density (see Fig. 4.13 and 4.10) component CB66a is most likely B66a. A minor change in the P.A. of $\sim 1.5^\circ$ is found although it is within the uncertainties of the P.A. for CB66a. No change of the vector speed is observed. We still differentiate between these components due to the strong scattering of the position for CB66a model components. The flux density of the model components of CB66a is very low $< 50 \text{ mJy}$ displaying strong variations. Overall

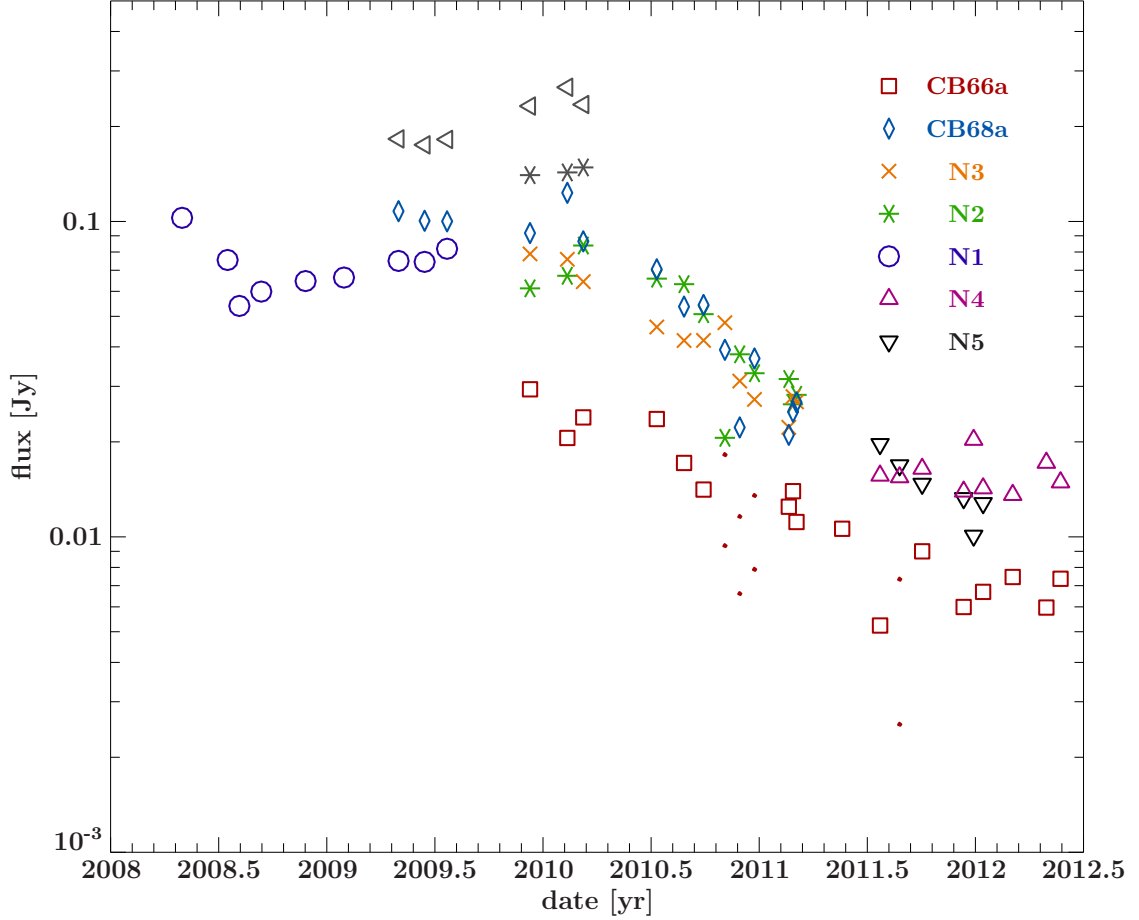


Figure 4.13: The flux density evolution for successor components of the ballistic components associated with the outburst in 2008. The colored dots show associated components but are not considered in the determination of characteristics. The gray left handed triangle show the summed flux density of the displayed components at the same dates while the gray stars show that for component N2 and N3 only.

we find the decay rate of the flux density to be in the order of one magnitude in 3 years (see Fig. 4.10).

In 2011.4 the components CB66a, N2, and N3 could not be identified anymore. Instead of three only two model components (N4 and N5) could be fit at the expected region. The flux density evolution for these two model components, depicted in Fig. 4.10, provides no help in their association with any of the previous three. Both components were fairly constant at a flux density level of 10 – 20 mJy. Based on their trajectories one can identify the potential predecessors CB68a and N3, although the uncertainty of the P.A. is $> 20^\circ$ (see Fig. 4.18). Their respective vector speeds are $0.92 \pm 0.14 \text{ mas yr}^{-1}$ and $0.68 \pm 0.13 \text{ mas yr}^{-1}$ (see Fig. 4.12). Figure 4.11 shows that component N5 disappeared in the last 3 epochs and only N4 can be identified.

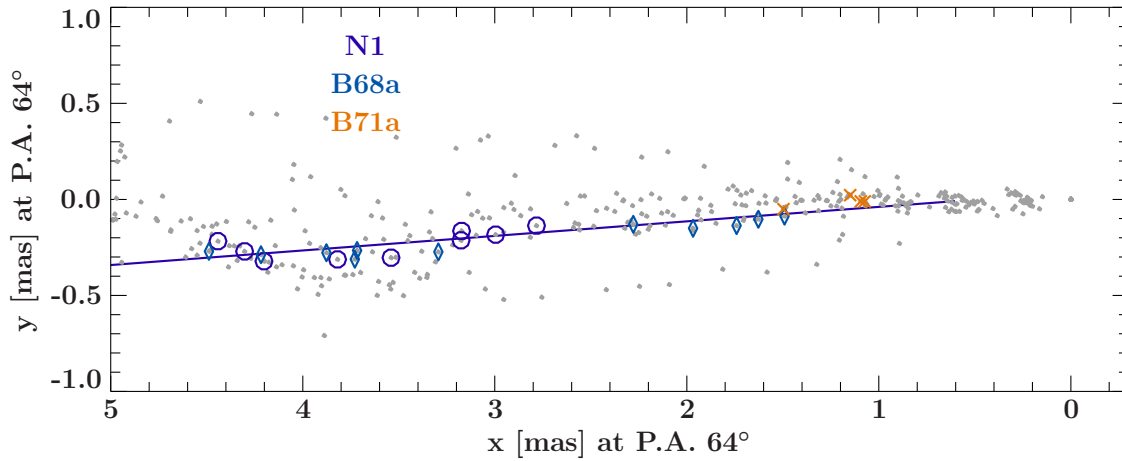


Figure 4.14: The positions of all model components rotated by 64° in gray. In indigo circles the model component positions of N1 are depicted and overlaid with a fitted linear trajectory. The predecessor candidates B68a and B71a are depicted in the same colors and symbols as in the previous figures i.e. Fig. 4.9.

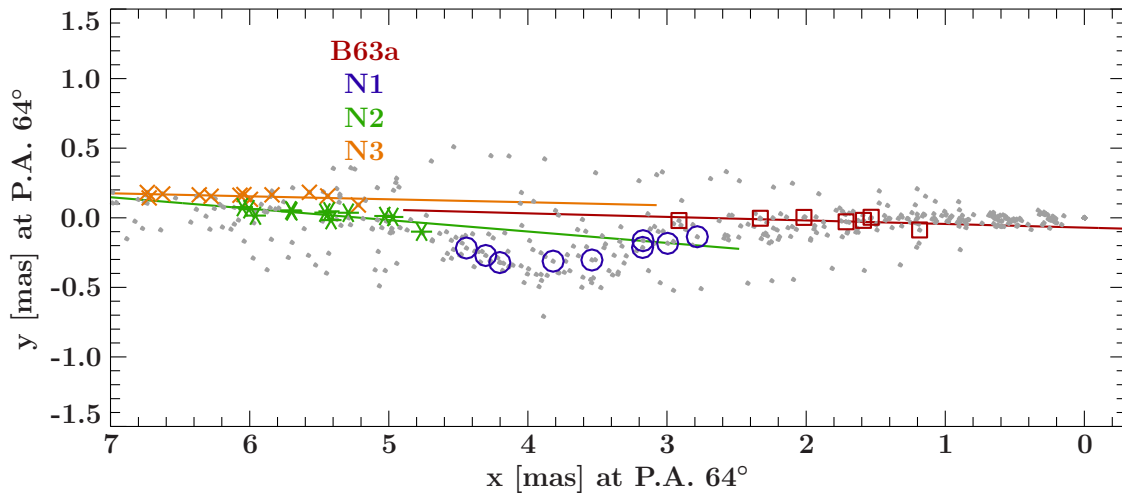


Figure 4.15: The positions of all model components rotated by 64° in gray. In green and orange the model component positions of N2 and N3 are depicted and overlaid with a fitted linear trajectory. The predecessor candidates N1 and B63a are depicted in the same colors and symbols as in the previous figures i.e. Fig. 4.21.

4.4.2 Kinematics of components associated with the 2008 outburst

We find the emergence of new ballistic components which we could associate with the prominent 2008 outburst and form a highly complex and evolving jet structure (see Fig. 4.19). We first discuss the emerging ballistic components close to the inner jet region and later the evolving jet structure. In contrast to the 2006 outburst more components are needed to describe the evolving region.

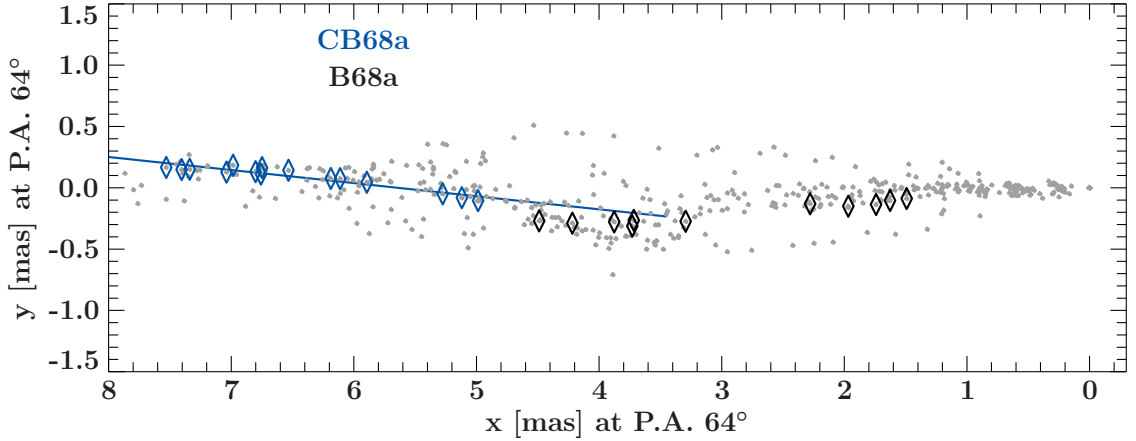


Figure 4.16: The positions of all model components rotated by 64° in gray. In blue diamonds the model component positions of CB68a are depicted and overlaid with a fitted linear trajectory, while the positions of the predecessor component B68a are depicted in black diamonds.

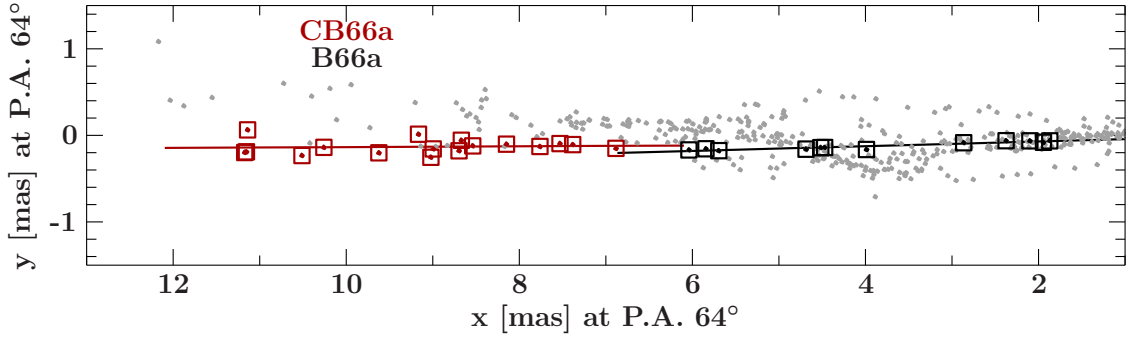


Figure 4.17: The positions of all model components rotated by 64° in gray. In red (black) squares the model component positions of CB66a (B66a) are depicted and overlaid with a fitted linear trajectory.

The ballistic jet structure associated with the prominent outburst 2008a

We find a total of six ballistic components associated with the outbursts 2008a and 2008b (see Fig. 4.20). An overview of their properties is presented in Table 4.3. Continuing the trend of rising vector speeds in the last ejected ballistic components of the 2006 outbursts, B63a has a vector speed of $1.67 \pm 0.10 \text{ mas yr}^{-1}$ at a P.A. $62.54^\circ \pm 1.99^\circ$. The estimated ejection date is 2007.65 ± 0.08 , which corresponds to the rising phase of the 2008a outburst in the lightcurve at 14.5 GHz, and to the peak of the outburst phase at 230 GHz (see Fig. 4.22). B63a shows a rapid decay of its flux density from $\sim 700 \text{ mJy}$ to $\sim 20 \text{ mJy}$ in ~ 1 year (see Fig. 4.22). This suggests that this component is vanishing. In the comparison with the 43 GHz analysis by Schulz (2012) we find component B12 to be the most likely counterpart of B63a although their vector speeds are slightly different. Similar ejection dates to B63a are found for B64a and B70a, although both components

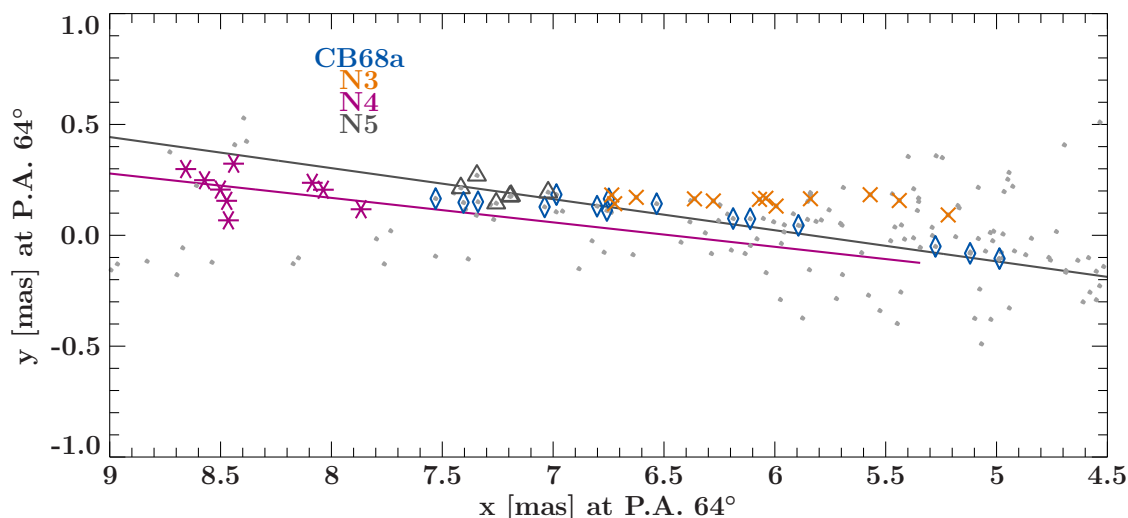


Figure 4.18: The positions of all model components rotated by 64° in gray overlaid with CB68a, N3, N4 and N5. A linear two-dimensional regression fit is overlaid to display the trajectories of N4 and N5 .

Table 4.3: Name and attributes of all emerging ballistic components associated to the outburst 2008a. The columns in the order of their appearance list the names of the components, their vector speed, ejection date, and ejection angle.

name	vector speed [mas yr ⁻¹]	ejection date [yr]	P.A. [deg]	counts
B63a	1.67 ± 0.10	2007.65 ± 0.08	62.54 ± 1.99	7
B64a	1.48 ± 0.02	2007.76 ± 0.08	63.56 ± 0.31	28
B70a	1.15 ± 0.03	2007.49 ± 0.05	69.59 ± 1.14	9
B68c	0.80 ± 0.12	2007.35 ± 0.22	67.61 ± 0.52	5
B67a	1.24 ± 0.08	2008.26 ± 0.09	66.56 ± 1.88	6 (8)
B66b	1.09 ± 0.08	2008.55 ± 0.10	65.65 ± 2.13	6

could not be tracked exactly to the inner jet region. Extrapolating the trajectories of B64a and B70a (see Fig. 4.23) shows that a component U1 is located between these two, suggesting that they could not be resolved before. The y-position of U1 is offset from the majority of component positions observed at similar distances. The idea of U1 being the unresolved B70a and B64a component is supported by the increasing spatial distances between the model components of B70a and B64a (shown as gray lines in Fig. 4.23) with distance to C1 and therefore time. In the work by Schulz (2012) at 43 GHz we identified component B7 to be the counterpart of U1. B7 has an apparent motion of $\sim 1 \text{ mas yr}^{-1}$ and was also found to be located at a lower y-position values than the majority of components in that region. At some point it also disappeared and instead the components B10 and B11 were found, which are the potential counterparts for B64a and B70a.

B64a was found to have an apparent motion of $1.48 \pm 0.02 \text{ mas yr}^{-1}$ and the backextrap-

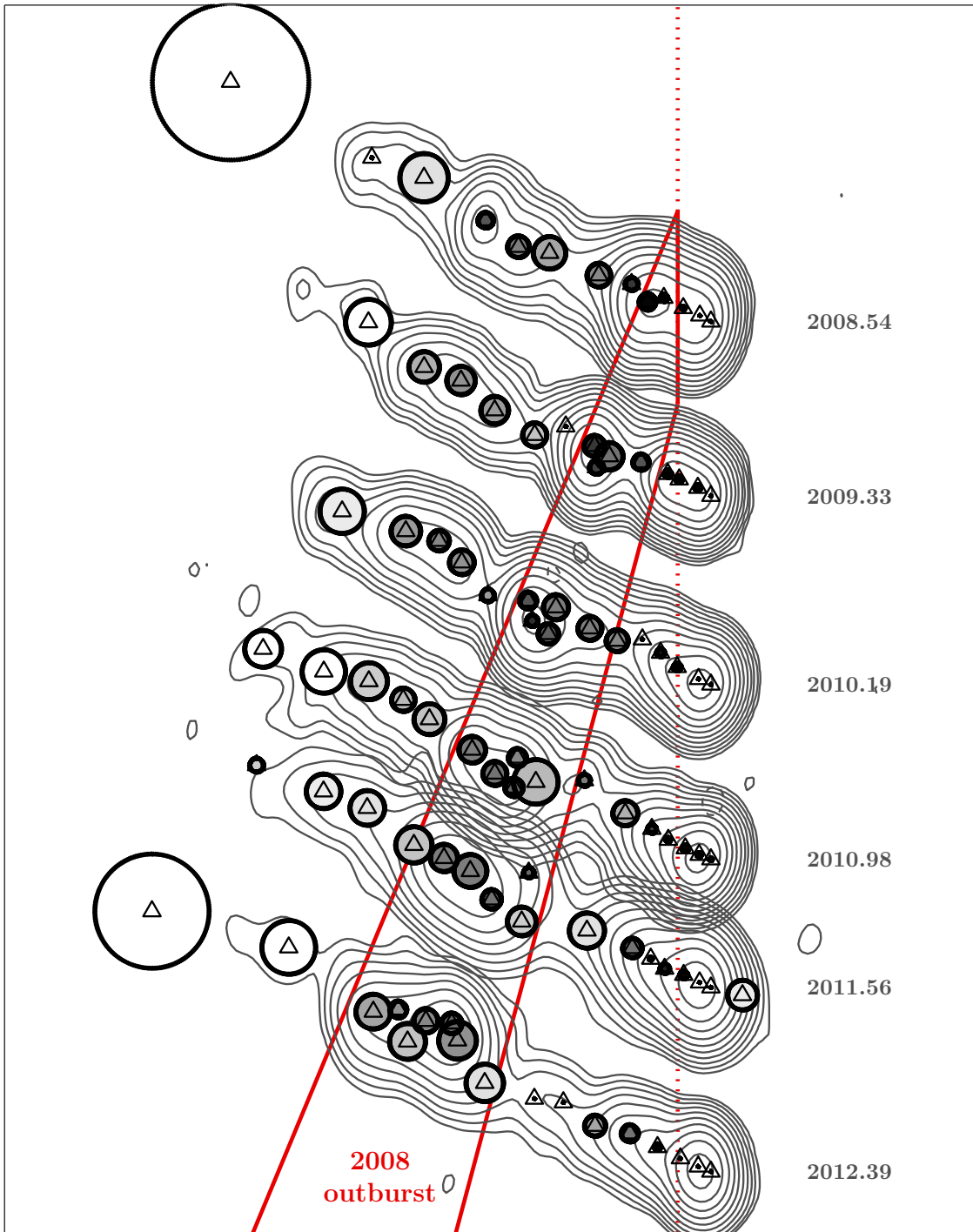


Figure 4.19: Illustration of the region in the jet associated with the 2008 outburst. The contours of selected clean images start at a 10σ background level. The separation of individual images is scaled to the time of the observation. Position and size of the circular model components for each observation are overlaid and color coded according to their respective brightness temperature (white: $T_B < 10^8$ K and black $T_B > 10^{11}$ K).

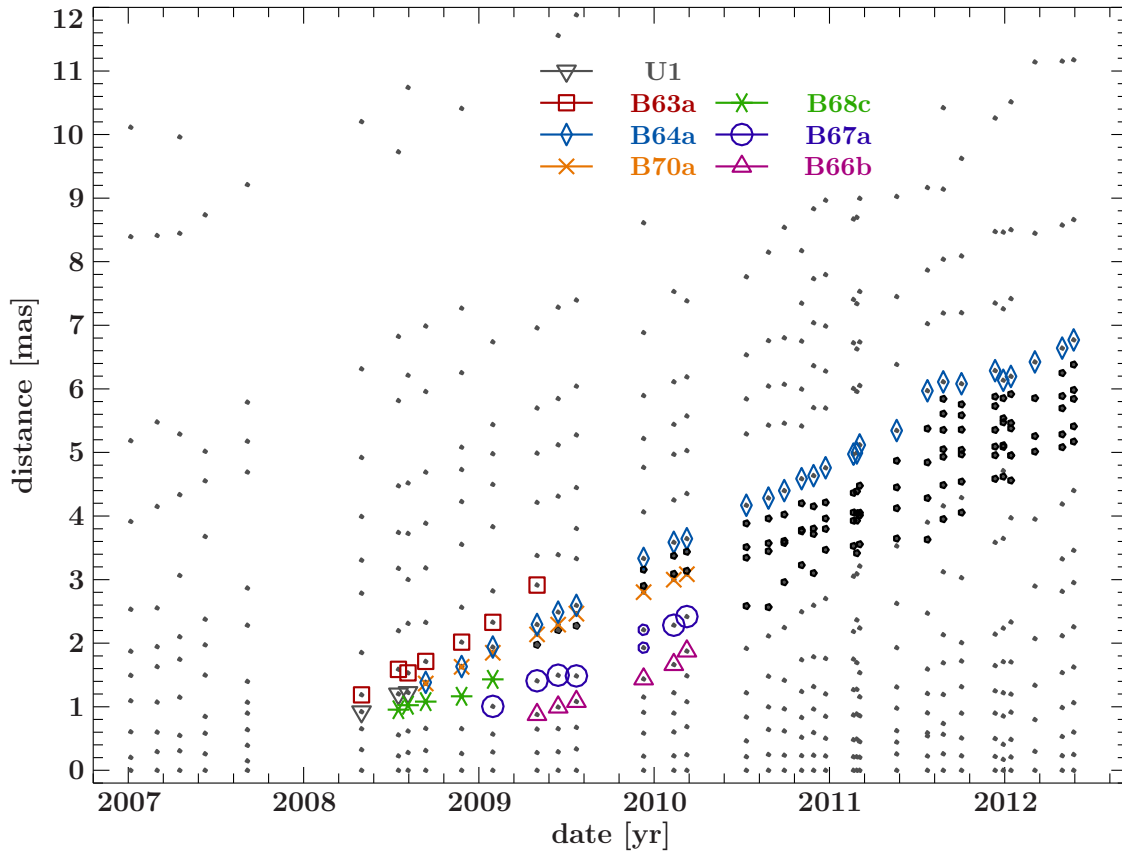


Figure 4.20: The distance of ballistic components to the respective location of C1. The distance of all model components are shown in gray, while the components associated to the 2008 outbursts are shown as bold black dots. If multiple components were associated with one component they are depicted as circles in the color of the component.

olated ejection date coincides with a peak of the lightcurve at 230 GHz (see Fig 4.21, *top panel*). The model component positions can be described by a straight line (see Fig. 4.24) at a P.A. $63.56^\circ \pm 0.31^\circ$. B64a was identified in 28 epochs, no other component could be identified over a similar time range. The flux density evolution (see Fig. 4.22) of B64a shows only a minor decline in the first year with some variability. The variability might be a modeling effect (Homan et al., 2001) due to the spatial close component B70a (see Fig. 4.23). Thus, a decline of flux density in B64a during the first six epochs is seen as a rise in B70a and vice versa. In the first epoch after a gap of 4 months the flux density was at ~ 150 mJy. Over the course of the next 6 months the flux density increased to over 200 mJy again followed by a year of steady decline to 40 mJy. From this minimum the flux density increased again to ~ 150 mJy in 4 months and has been declining since. We identified B10 to be the most likely 43 GHz counterpart in the works by Schulz (2012). From the trajectories in Fig. 4.23 we find that the origin of B64a (C1*) is offset by ~ 0.1 mas to the 0/0 (C1) position. The offset is even more apparent for B70a since the backextrapolated trajectory does not get closer to C1 than ~ 0.2 mas (see Fig. 4.23). We find that y position values of B70a model components are typically 0.3-0.5 mas offset to

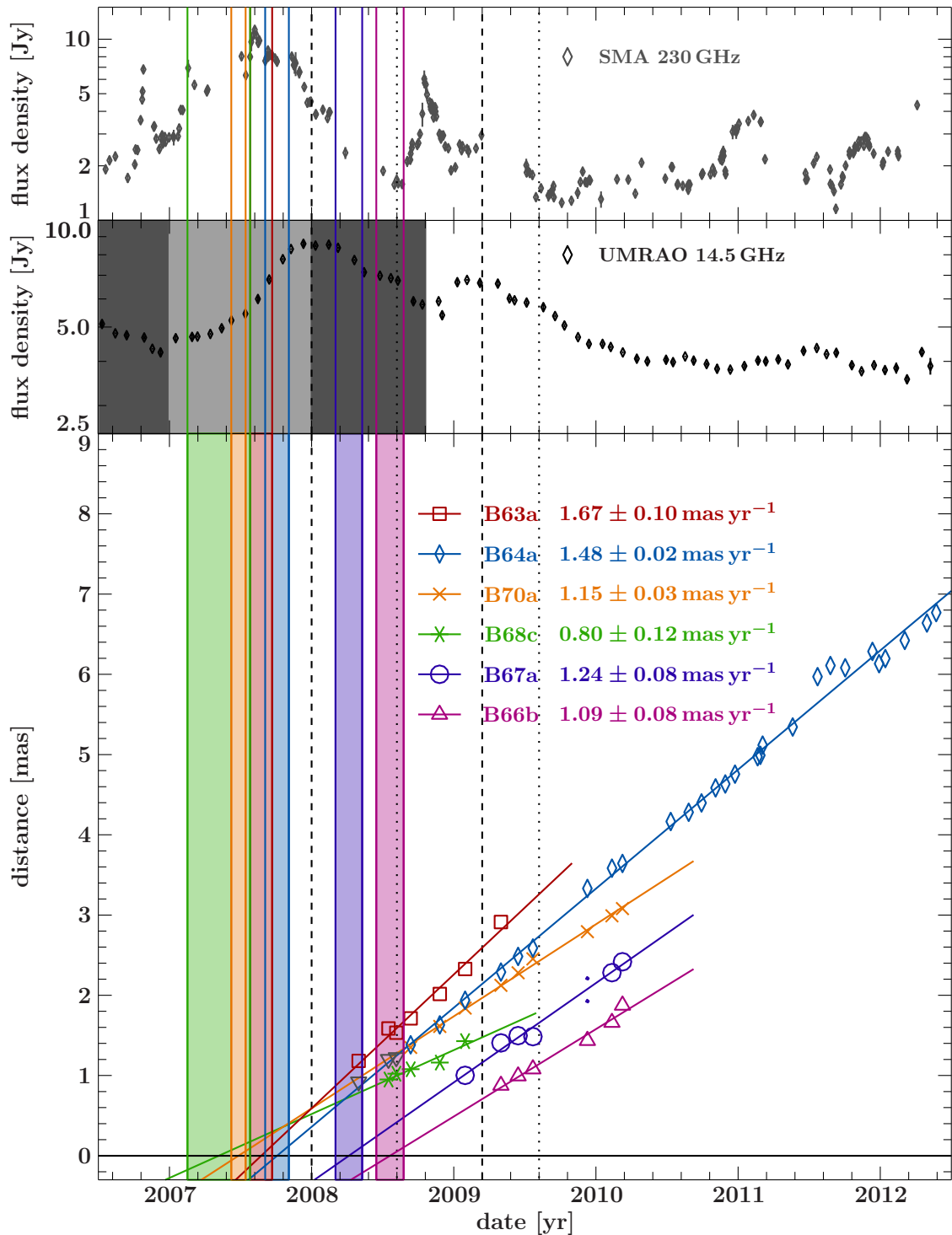


Figure 4.21: *top:* SMA lightcurve at 230 GHz. The colored lines mark the range of ejection dates for all ballistic components shown in the bottom panel. *mid:* UMRAO lightcurve at 14.5 GHz. The shaded regions mark the rise and decline phase of prominent outbursts. The colored lines are the same as in the top panel. *bottom:* The distance of ballistic components to the respective location of C1* over time and overlaid with linear regression fits. The derived ejection times (by extrapolating the fits) are shown as shaded regions in the corresponding color of the component. The dashed black lines mark the peak time of the prominent outburst in the light curve at 14.5 GHz, while the dotted black lines mark minor outbursts.

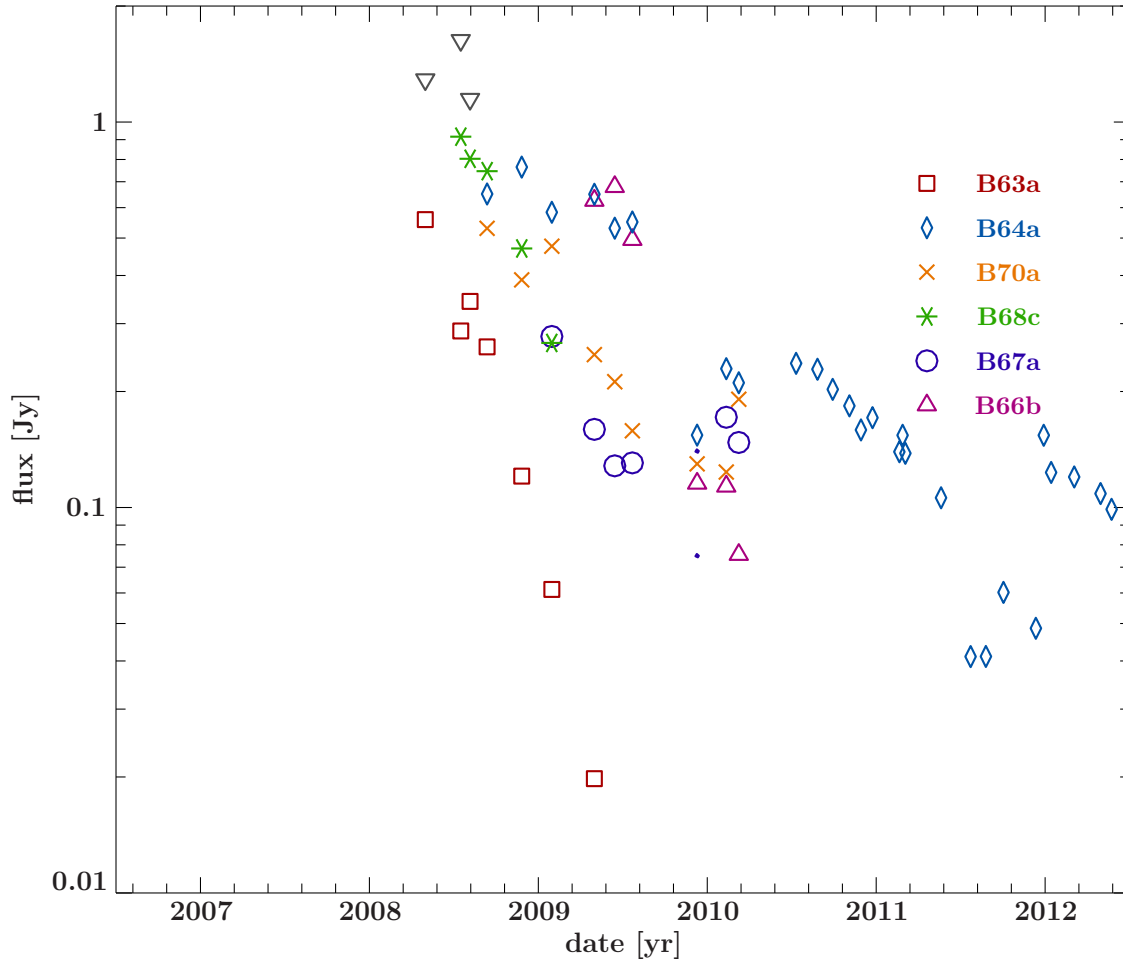


Figure 4.22: The flux density evolution for the different ballistic components associated with outburst 2008a is displayed in color and symbols. The colored dots show associated components but these were not considered in the determination of characteristics.

the ones found for the majority of components located at similar distances. The derived ejection date of B70a is 2007.49 with a vector speed of $1.15 \pm 0.03 \text{ mas yr}^{-1}$ and P.A. of $69.59^\circ \pm 1.14^\circ$. An indication of an outburst in the 230 GHz lightcurve is seen at the time of the ejection time. The decline rate of the flux density of B70a in the first 6 epochs is higher than of B64a dropping from $\sim 500 \text{ mJy}$ to $\sim 150 \text{ mJy}$. Starting from there the flux density decline rate decreases and even shows an increased flux density for the last epoch in which B70a could be clearly identified. In the analysis at 43 GHz by [Schulz \(2012\)](#) component B11 was found to show similar characteristics.

A fourth component B68c can be associated with the rise of the 2008a outburst. It is only identified in 5 epochs and was found to have a P.A. of $67.61^\circ \pm 0.52^\circ$ with a slow vector speed of only 0.80 mas yr^{-1} . The flux density shows a rapid decline from 1 Jy to 250 mJy in 8 months, which is a similar decline rate as found for component B70a. No clear association with a component at 43 GHz in the analysis by [Schulz \(2012\)](#) is found. Component B67a was found to have an ejection date in 2008.26 and coincides with

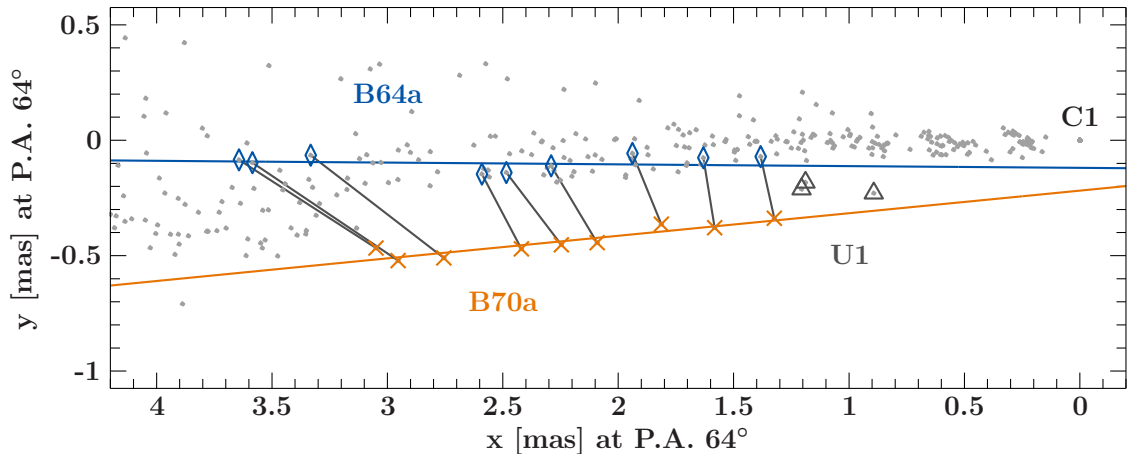


Figure 4.23: The first 9 x and y position of component B64a and B71a projected on P.A. 64° are shown in color. Linear regression fits on the position have been applied to B64a and B71a. All positions of model components are depicted in gray. The position of the U1 model components are marked with dark gray triangles. The spatial distances of model components in the same observation are shown as gray lines.

the onset of the plateau in the lightcurve at 14.5 GHz which marks the beginning of outburst 2008b. The P.A. of B67a is $66.56^\circ \pm 1.88^\circ$ and has an apparent motion of $1.24 \pm 0.08 \text{ mas yr}^{-1}$. The initial flux density was $\sim 300 \text{ mJy}$ and its evolution can be described as decreasing in the first epochs and slight increasing after the first 3 epochs. A second component which can be associated with the outburst 2008b is B66b. It appeared three months after the ejection of B67a. Its measured vector speed is $1.09 \pm 0.08 \text{ mas yr}^{-1}$ with a P.A. of $65.65^\circ \pm 2.13^\circ$. The evolution of the flux density (see Fig. 4.22) shows that the component gets fainter by an order of magnitude in less than a year. At 43 GHz no good association with the components in Schulz (2012) are possible but two candidates are found based on their ejection dates (B9 and B14). Both components show a high apparent motion of $> 2 \text{ mas}$, which is nearly twice the vector speed of B66b and B67a. The large difference in the vector speeds can be explained by different identifications of model components, which is found to be very complex in that region of the jet at that time.

After the ejection of B63a, B64a, B70a, and B68c the region between those components and C1 became more complex to model and identify, since the components were usually fainter. This is depicted in Fig. 4.25, showing the flux density of components between the inner jet region up to a distance of 2.5 mas away from C1 against the date of the observations. The colors and symbols divide the model components in different time regions. The first group (blue, square) displays components which are associated to the 2006 outburst. If at least one model component is associated with outburst 2008a all components are depicted as red diamonds. The model components in the time after the 2008 outburst are shown as black crosses. Although the typical number of model components in this region did not change ~ 3 , the flux densities of model components are in general an order of magnitude lower for components after the outburst 2008a.

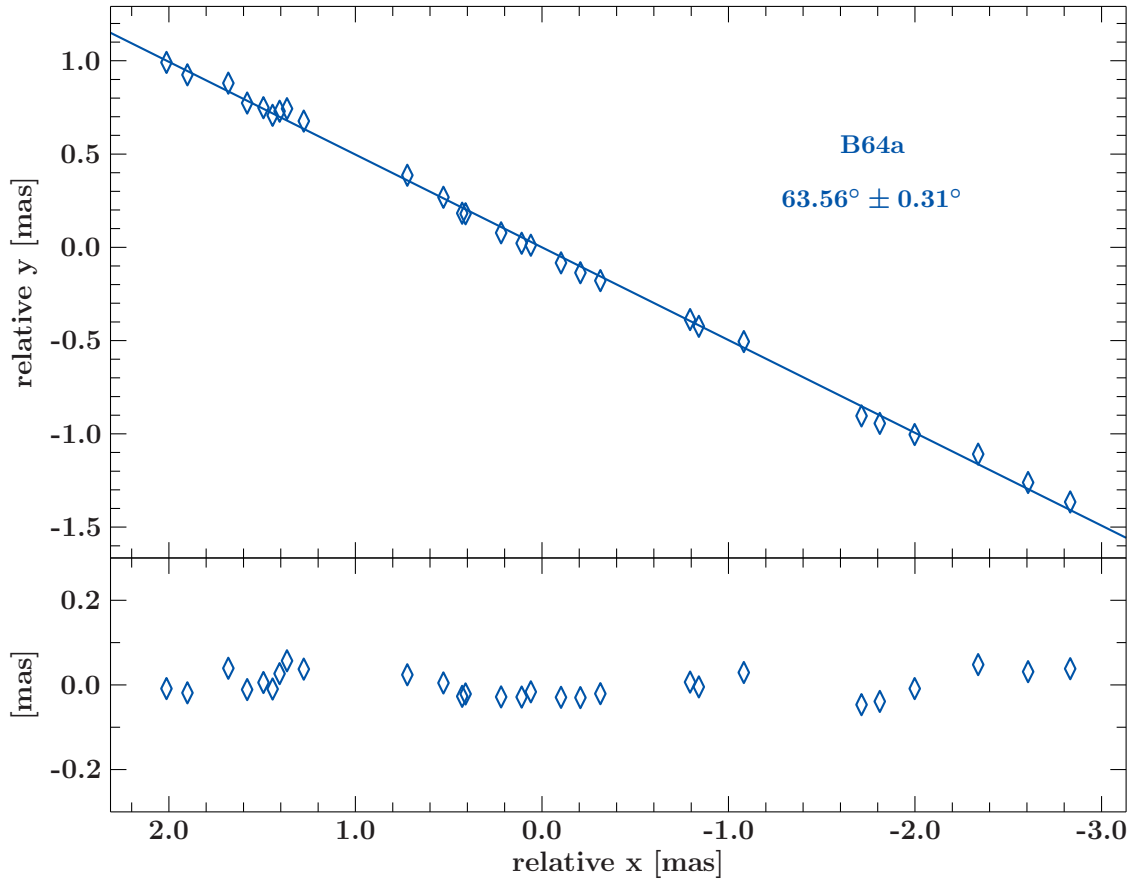


Figure 4.24: In the top panel the shifted x and y position of component B64a, with the mean of x and y centered at zero, is depicted. A two dimensional linear regression fit with the algorithm by [Fasano & Vio \(1988\)](#) is overlaid. The distances of the linear regression fit to the corresponding model component positions are shown in the lower panel.

Structural changes in the jet region associated with the outburst in 2008.

We find that the total number of model components in the region associated to the outburst 2008a increase in time. At its maximum the size of the region is ~ 2 mas times ~ 1 mas, which is 4 times the size of the typical beam, and was modeled with 8 model components. Therefore the effect of flux density exchange plays a major factor and thus we did not use flux density parameters for identification purposes. The complex flux density evolution is depicted In Fig. 4.27 for a phase of ~ 2 years from 2008.5 to 2010.5. The summed flux density (in black) of the individual model components shows only a minor decay of 50% during these 2 years while one can only notice slight trends for some individual components. It is beyond the scope of this work to disentangle and associate all individual components. Only some identified components are shown in the following to demonstrate the complexity of this region (see Fig. 4.26). In Table 4.4 the characteristics of these components is shown. Component N6 was observed from 2009.33 to

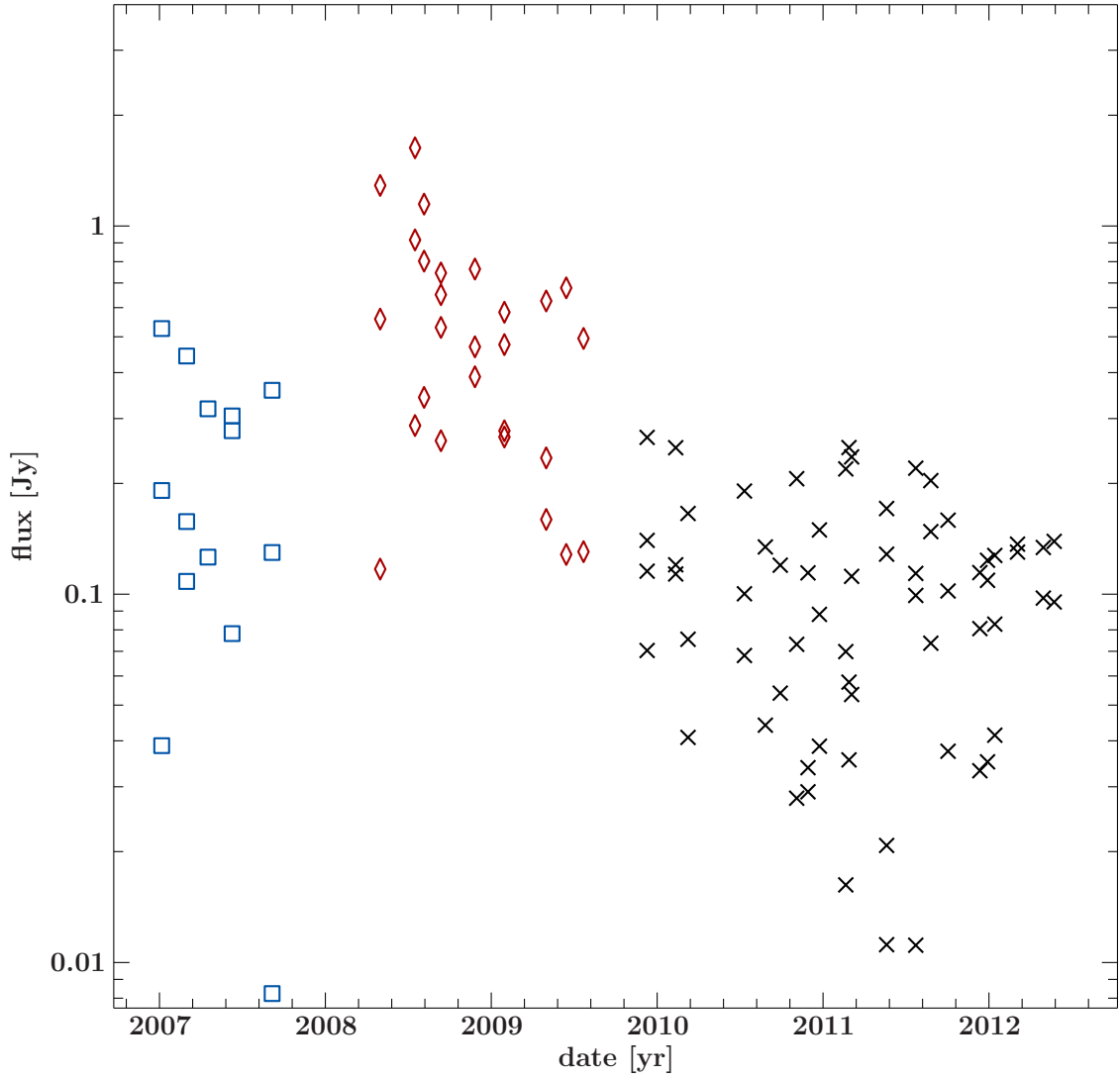


Figure 4.25: The flux density and epoch of all model components between 0.8 mas and 2.5 mas. Blue squares mark model components appearing before the outburst 2008a, red diamonds the model components of the epoch in which at least one model component was associated with the outburst 2008a, and black crosses the components appearing after the 2008 outbursts.

~ 2010.10 . It featured a slightly lower apparent motion than B64a of 1.41 mas yr^{-1} and had a P.A. of $55.56^\circ \pm 4.17$. No preceding component could be identified. The position of N6 at a distance of $\sim 0.4 \text{ mas}$ with respect to B64a can be explained by B64a originally consisting of two unresolved but spatially close components with slightly different vector speeds. This idea is supported by the observed minimum distance of 0.4 mas between the components, which is only slightly less than the average FWHM of the minor beam axis (the best resolution) in these observations. This can be interpreted as an expanding region or alternatively as a trailing feature in the wake of B64a.

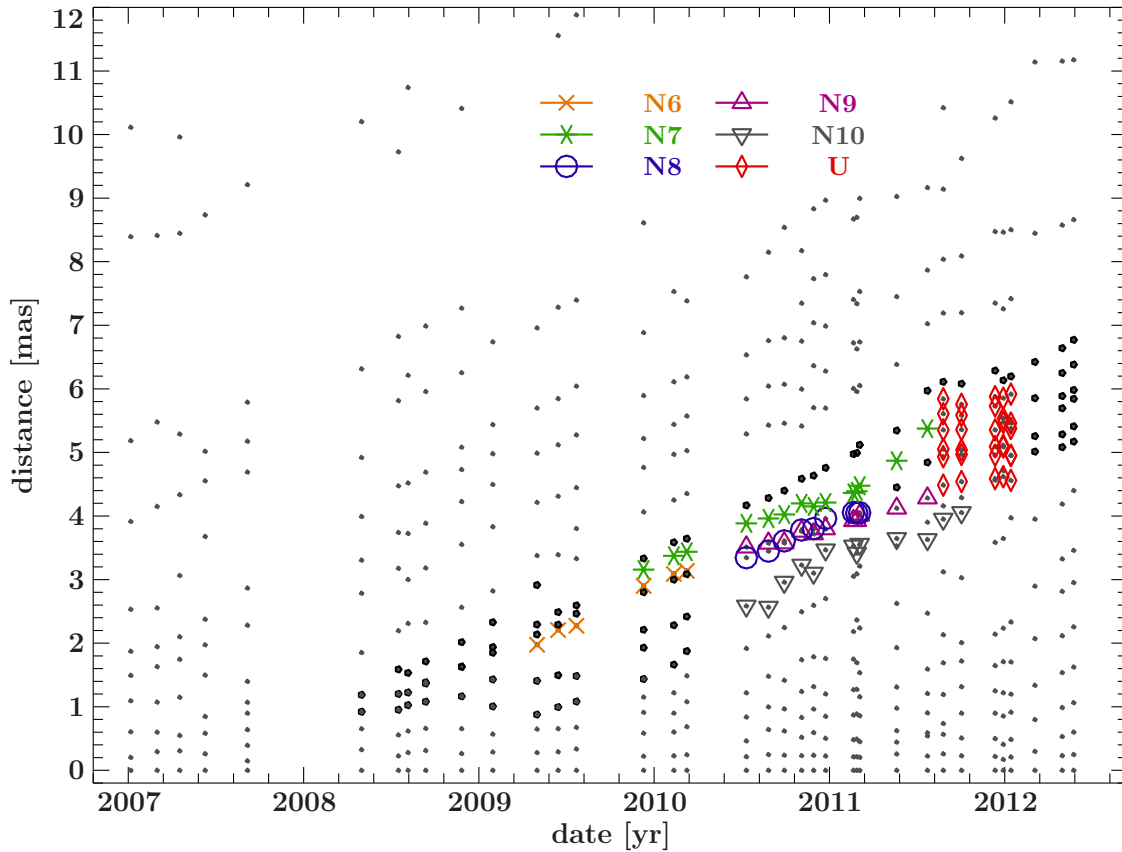


Figure 4.26: The distance of ballistic components to the respective location of C1. The distance of all model components are shown in gray, while the components associated to the 2008 outbursts are shown as bold black dots. If multiple components were associated with one component they are depicted as circles in the color of the component.

Table 4.4: Name and attributes of all components appearing in positions related to ballistic components of 2008a. The columns in the order of their appearance list the names of the components, their vector speed, P.A., number of unique identifications, and if applicable the possible predecessor(s).

name	vector speed [masyr ⁻¹]	P.A. [yr]	counts [deg]	pos. predecessor
N6	1.41 ± 0.06	55.56 ± 4.17	6	
N7	1.22 ± 0.08	53.32 ± 7.64	14	
N8	1.26 ± 0.10	41.73 ± 30.93	9	C70a, N6
N9	0.81 ± 0.04	52.73 ± 4.38	11	C70a

N7 was resolved at a position close between B64a and B70a (see Fig 4.29). As for N6 the distance between N7 and its surrounding components B64a and B70a was ~ 0.4 mas, indicating again an expanding region or trailing components. The component was tracked based on its relative position with respect to the other model components. In Fig. 4.29

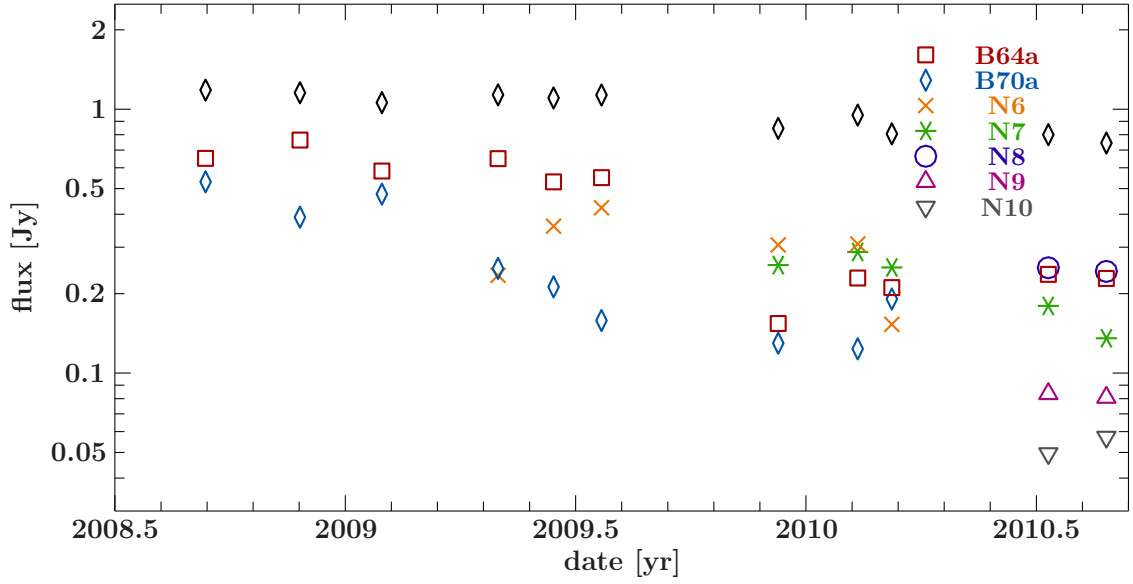


Figure 4.27: The flux density evolution of all components associated with outburst 2008a from 2008.5 to 2010.7. In colored symbols the flux density of the individual components is shown and in black the summed flux density.

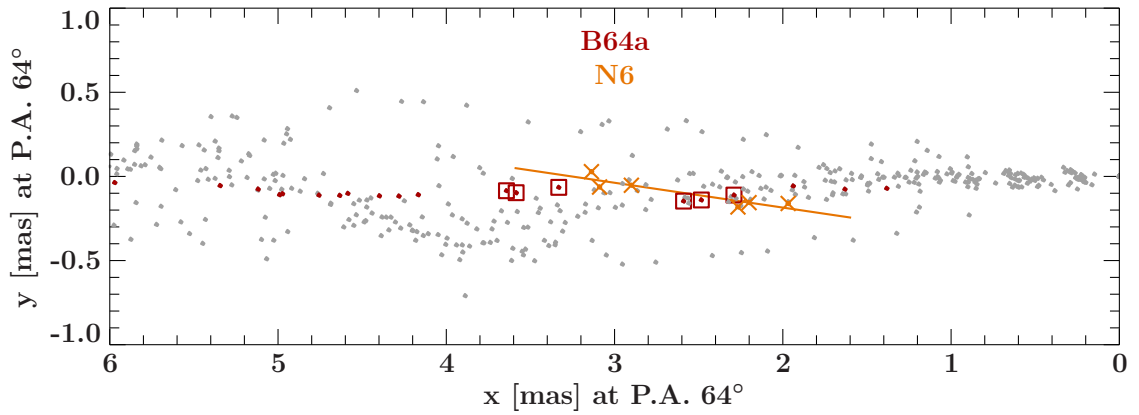


Figure 4.28: The positions of all model components rotated by 64° in gray. Orange crosses mark the model component positions of N6 which is overlaid by a fitted linear trajectory. The positions of component B64a at the same observational dates of N6 are shown in red square, while the positions of the other dates are shown as dots.

it can be seen that component N7 has a curved trajectory. A lower limit on the apparent motion of $1.22 \pm 0.08 \text{ mas yr}^{-1}$ is derived by a linear regression fit.

A comparison of the apparent motions favor N8 as the successor component of B70a with a vector speed of $1.26 \pm 0.10 \text{ mas yr}^{-1}$ while N9 only has $0.81 \pm 0.04 \text{ mas yr}^{-1}$. In both cases we note that the P.A. must have changed which was already indicated in the trajectory of B70a. In principle N6 could be the predecessor component of N8 (see Fig. 4.30).

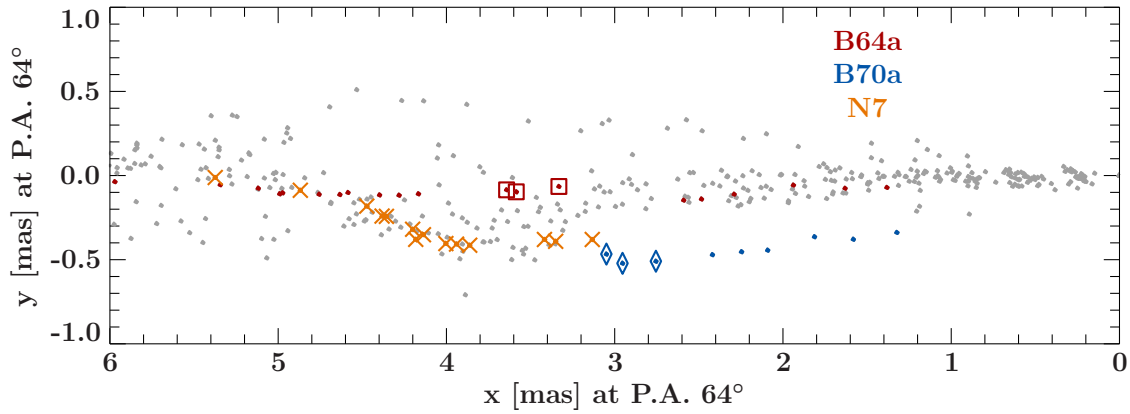


Figure 4.29: The positions of all model components rotated by 64° in gray. Orange crosses mark the model component positions of N7. The positions of component B64a and B70a during the first three epochs are shown in red crosses and blue diamonds, while the respective positions of other dates are shown as colored dots.

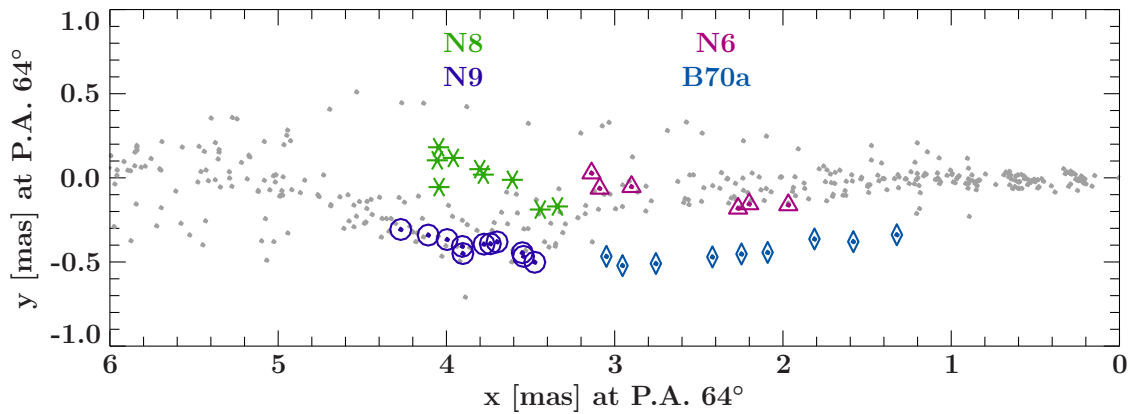


Figure 4.30: The positions of all model components rotated by 64° in gray. In blue diamonds, magenta triangles, green stars, and violet circles the components B70a, N6, N8, and N9 are depicted.

Considering the observation date difference of 0.3 yr and the small distance of 0.3 mas between the first model component of N8 and the last one of N6 this is unlikely. The derived vector speed would be 1.0 mas yr^{-1} , but we found the apparent motions of both components to be at least 20% higher.

No other prominent components could be clearly identified and traced in later observations with the exception for the time range from 2011.6 to 2012.1. At this time the region associated with the 2008 outbursts was modeled with 7-8 components. We find the positions of these components to be stationary, except for two components, which were slow with an apparent motion $< 0.5 \text{ mas yr}^{-1}$. The originally ballistic component B64a also appeared stationary during that time. An association of these components to the ones from previous observation is beyond the scope of this work due to the complexity of the region (changing from 5 to 8 model components between two adjacent epochs). A list of

Table 4.5: Name and attributes of all components in the region associated with the outburst 2008 observed between 2011.6 to 2012.1. The columns in the order of their appearance list the names of the components, their vector speed, and P.A..

name	vector speed [mas yr ⁻¹]	P.A. [deg]
B64a	0.30 ± 0.24	78.83 ± 6.92
U2	0.16 ± 0.48	9.37 ± 88.98
U3	0.52 ± 0.49	151.24 ± 70.45
U4	0.32 ± 0.07	83.43 ± 20.36
U5	0.45 ± 0.10	99.93 ± 51.58
U6	0.01 ± 0.22	37.63 ± 58.06
U7	0.07 ± 0.24	78.26 ± 26.49

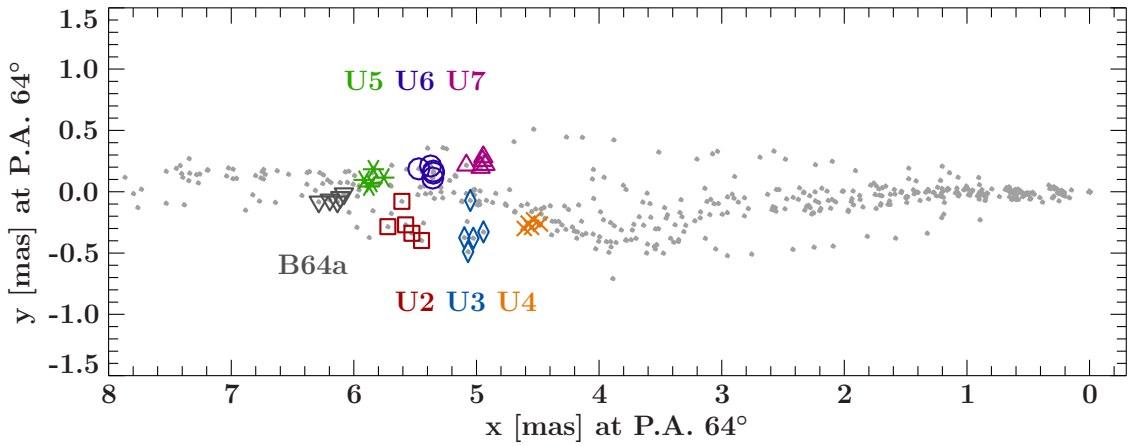


Figure 4.31: The projected position (P. A. 64°) for all stationary components during 2011.6 and 2012.1 and associated to the outburst 2008a are depicted in colored symbols. The positions for all model components found in the data set are marked with gray dots.

the attributes for these components is given in Tab. 4.5. The P.A. was derived by a linear regression fit to the model component positions in the (x, y) -plane while the velocity was derived by a linear regression fit from the distance to the mean position over time. The position angles of the components have usually very high uncertainties with the exception of B64a with a P.A. of $78.83^\circ \pm 6.92$. This value is different from the derived P.A. of $\sim 64^\circ$ for the B64a model component. The projected distance on a P.A. of 64° from C1 is between 4.5 and 6.5 mas for all of these components (see Fig. 4.31). The position of components U2 and U3 appears to be scattering in contrast to the position of the other model components. The summed flux density of all components associated with the outburst 2008 versus the date of observation (see Fig. 4.32) shows that the region decreased in total flux density from ~ 1.2 Jy to ~ 550 mJy in 3 years. Starting at the date coinciding with the appearance of the stationary model components the total flux density in the region increased by 150 mJy and decreased afterwards. From the evolution of the flux density

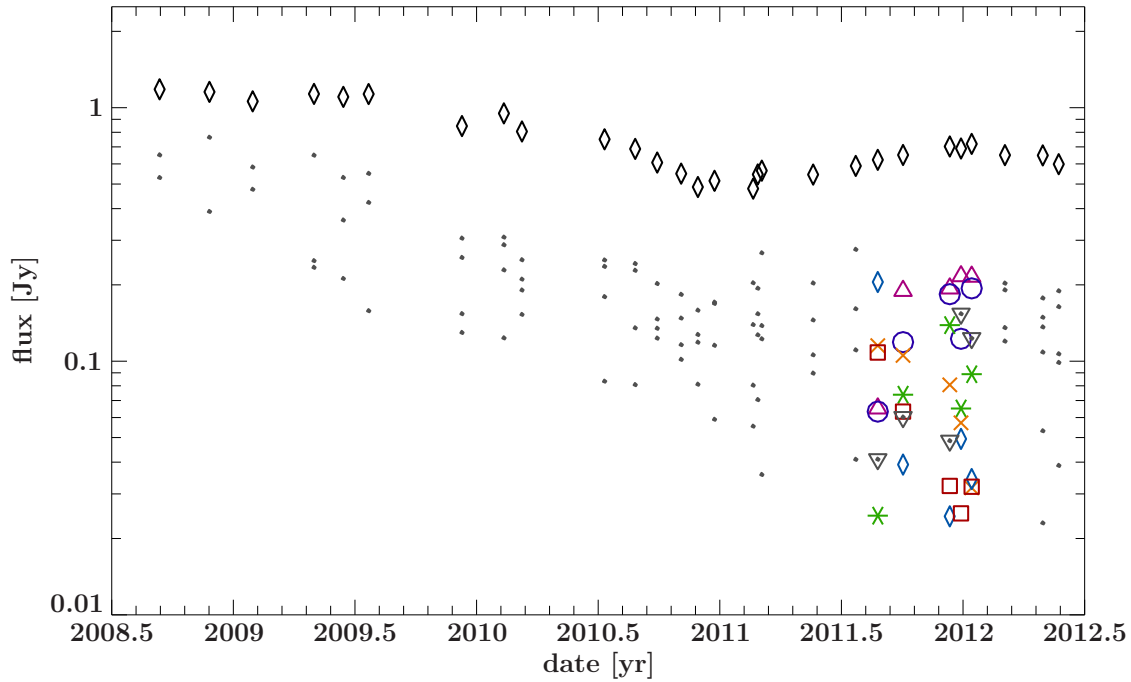


Figure 4.32: The flux density of all associated components to the outburst 2008a are shown as gray dots. The black diamonds mark the summed flux density for all of them. The colored symbols show the flux density of the “stationary” components in the time range of 2011.6 and 2012.1.

during 2011.6 and 2012.1 it appears that U2, U3, and U4 become fainter. Even though the region is subject to possible flux density exchange of spatially close components we think this is real since these three components are located at a larger spatial distance to the other components. Moreover in later epochs only 1 component is detected at the former position of U2, U3 and U4 which supports the idea that these components are vanishing. We note that the total flux density of this region associated with the 2008 outbursts explain the observed difference in flux density in the lightcurve at 14.5 GHz before 2004 and after 2012.

4.4.3 Kinematics of components associated with the 2009 outburst

Unlike to the previous prominent outbursts (2006 and 2008a) we find the emergence of new ballistic components being ejected in the declining phase of the 2009 outburst at 14.5 GHz instead of the rising phase. The associated jet structure is depicted in Fig. 4.33. An illustration of these identified components in the context of all other model components is shown in Fig. 4.34 and their properties presented in Table 4.6.

The fastest component in our analysis of 3C 111 was found to be B58a with an apparent motion of $1.95 \pm 0.03 \text{ mas yr}^{-1}$ (see Fig. 4.35) which also inherits the lowest P.A. of $58.48^\circ \pm 1.45^\circ$. The ejection date of 2009.57 ± 0.03 coincides with the peak of the outburst 2009b in the lightcurve at 14.5 GHz (see *top panel* Fig. 4.35). The component

Table 4.6: Name and attributes of all emerging ballistic components emerging after the prominent outburst 2008a. The columns in the order of their appearance list the names of the components, their vector speed, ejection date, and ejection angle.

name	vector speed [mas yr ⁻¹]	ejection date [yr]	P.A. [deg]	counts
B58a	1.95 ± 0.03	2009.57 ± 0.03	58.48 ± 1.45	15
B69a	1.68 ± 0.12	2009.84 ± 0.09	68.82 ± 0.49	10
B68d	1.33 ± 0.11	2009.93 ± 0.09	68.06 ± 2.85	9
B63b	1.19 ± 0.23	2010.12 ± 0.18	63.12 ± 2.18	5
B65a	1.65 ± 0.028	2010.62 ± 0.02	64.83 ± 1.18	11

could be tracked for 15 epochs but could not be directly traced to the inner jet region. Backextrapolating the trajectory finds the two candidate components UX in Fig 4.35. The combined flux density of these components (see Fig. 4.36) fit the trend of the flux density for B58a which decreases at first and later increases. The flux density of this component is between ~ 20 mJy and ~ 70 mJy. Besides the high speed and low P.A. angle the most striking attribute of B58 is its trajectory, which shows a continuous separation between B58 and the majority of components located at the same distance on the projected angle of 64° (see Fig. 4.37).

No other identified component outside the inner jet region shows a potential association with the outburst 2009a, but more ballistic components (B69a, B68d, B63b, B65a) are found at later epochs. No prominent counterparts are found in the lightcurve at 14.5 GHz. The maximum flux density for these components is less than 300 mJy and all display a rapid decay in their flux density (see Fig. 4.36). We determined their P.A. to be $\sim 63-69^\circ$ and their vector speeds in the order of $\sim 1.2-1.7$ mas yr⁻¹. As was already depicted in Fig. 4.25 the overall flux density of these components is lower than the ones associated with the prominent outbursts which makes modeling and associating these components quite challenging. Despite the difficulties in the identification process component B65a could be clearly identified in more than 10 epochs and shows nearly no divergence from ballistic motion. It also coincides with a small bump in the lightcurve at 14.5 GHz lightcurve. The flux density of B65a declines by an order of one magnitude per year.

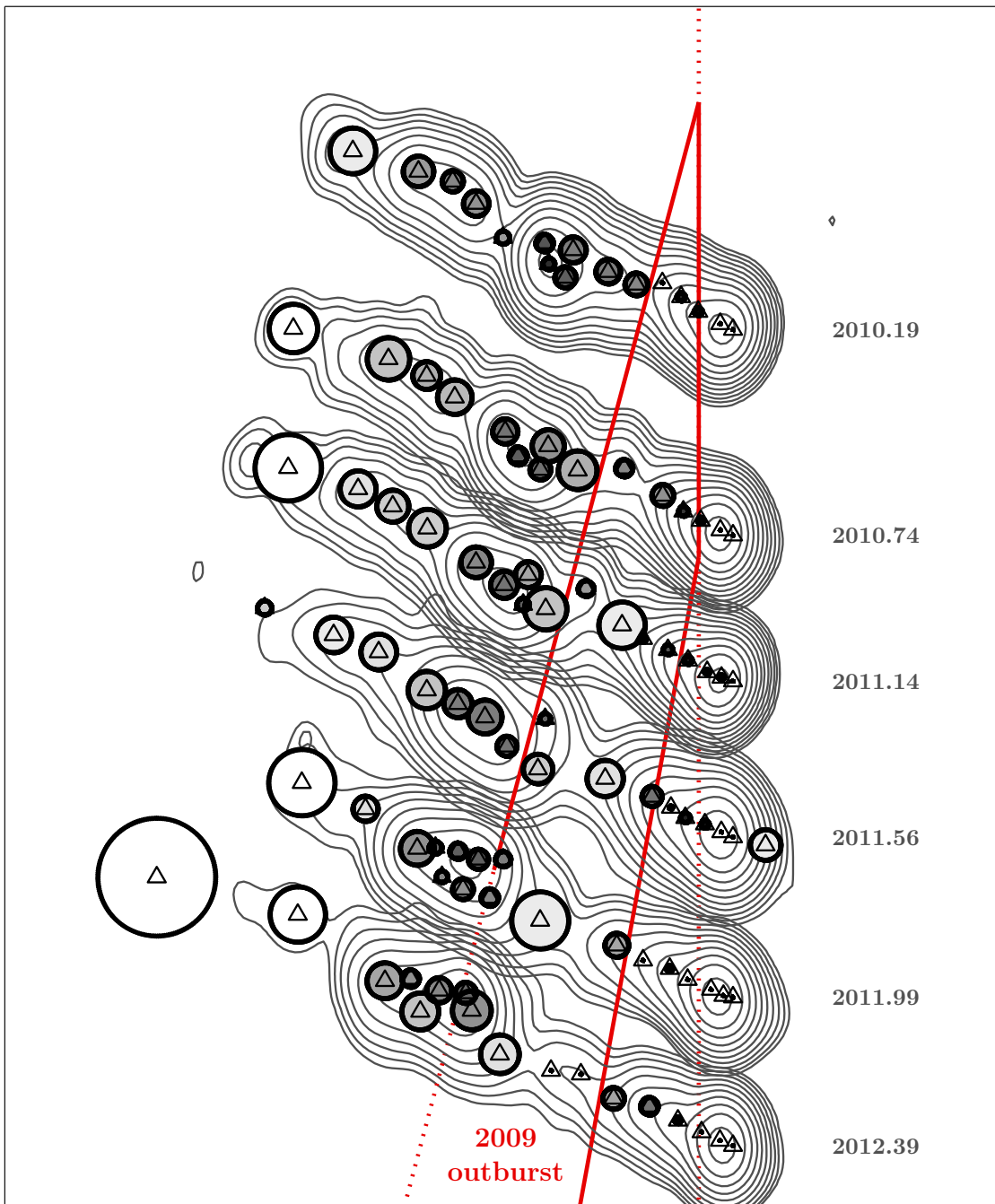


Figure 4.33: Illustration of the region in the jet associated with the 2009 outburst. The contours of selected clean images start at a 10σ background level. The separation of individual images is scaled to the time of the observation. Position and size of the circular model components for each observation are overlaid and color coded according to their respective brightness temperature (white: $T_B < 10^8$ K and black $T_B > 10^{11}$ K).

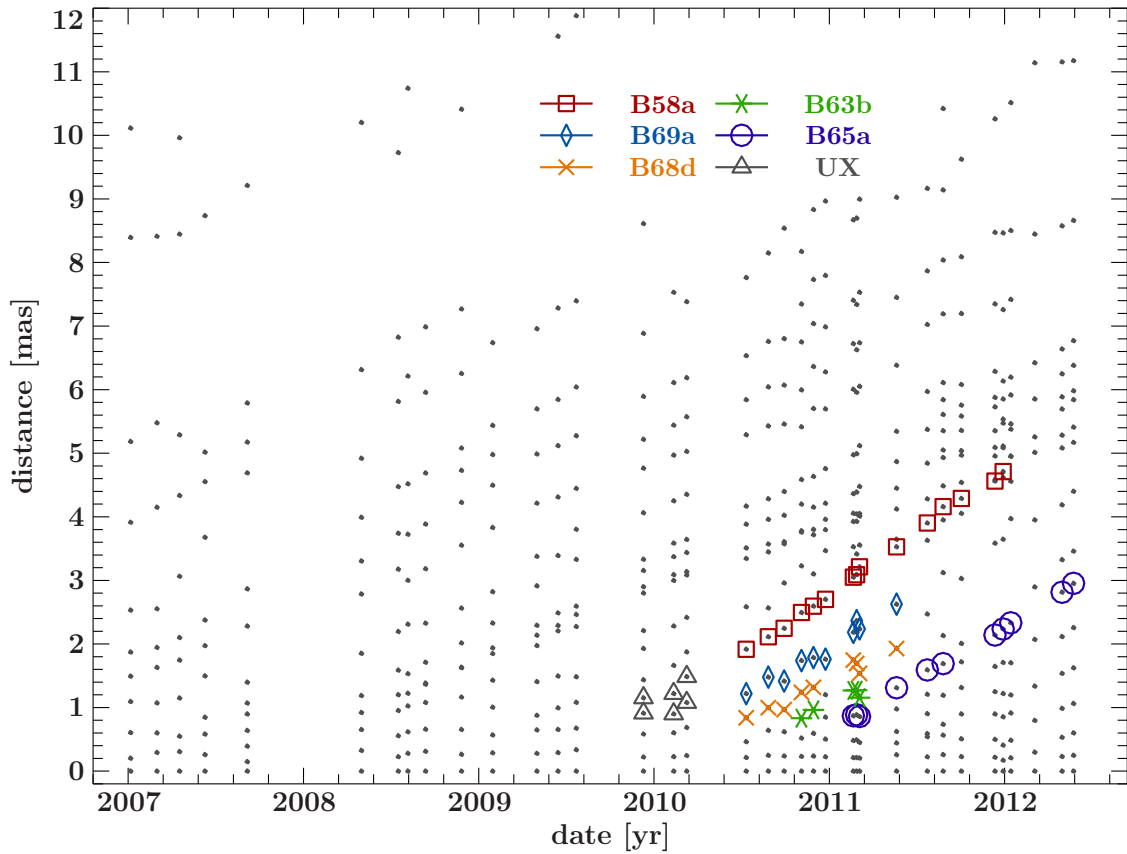


Figure 4.34: The distance of ballistic components to the respective location of C1. The distance of all model components are shown in gray, while the components associated to the 2009 outbursts are shown as bold black dots. If multiple components were associated with one component they are depicted as circles in the color of the component.

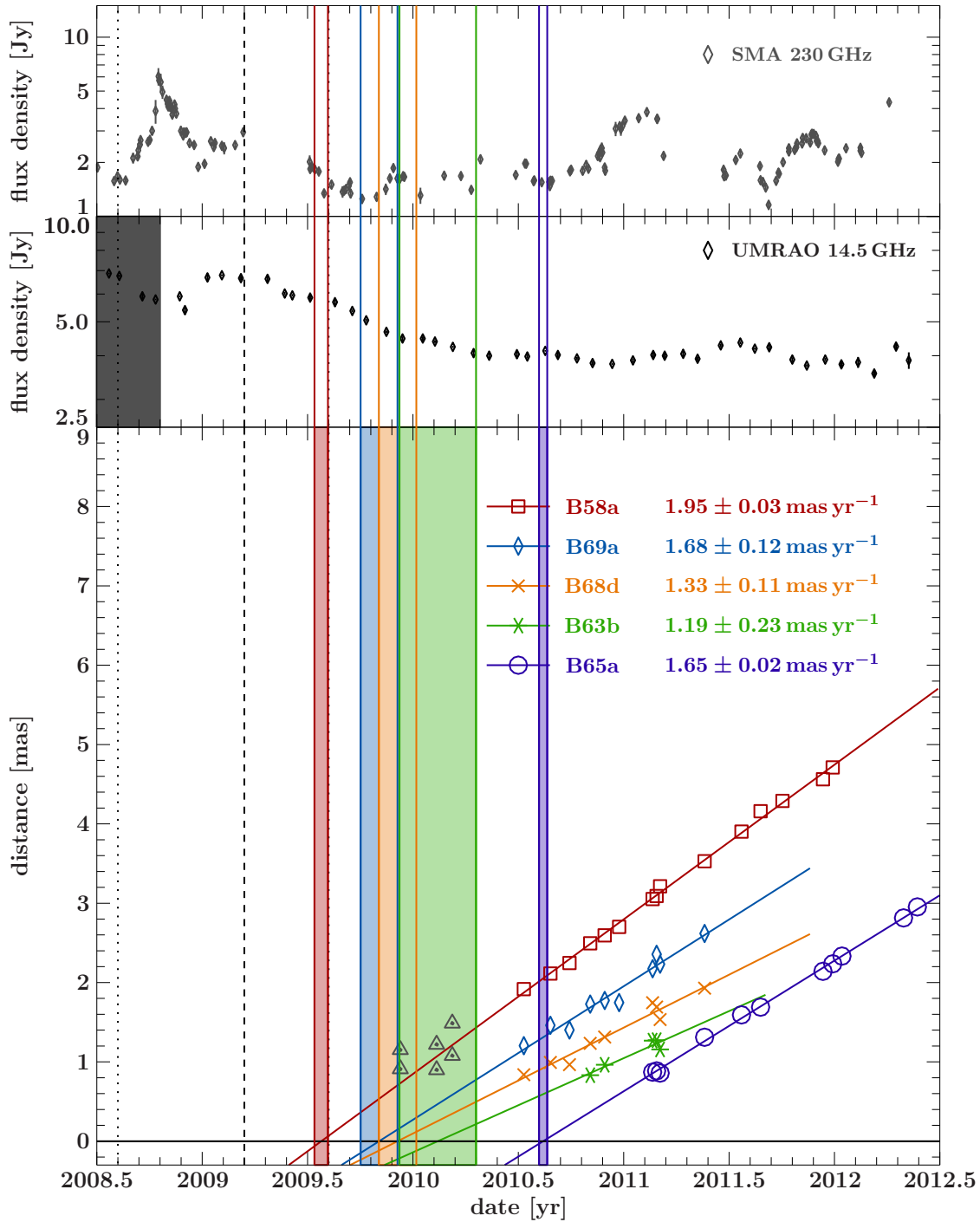


Figure 4.35: *top:* SMA lightcurve at 230 GHz. The colored lines mark the range of ejection dates for all ballistic components shown in the bottom panel. *mid:* UMRAO lightcurve at 14.5 GHz. The shaded regions mark the rise and decline phase of prominent outbursts. The colored lines are the same as in the top panel. *bottom:* The distance of ballistic components to the respective location of C1* over time and overlaid with linear regression fits. The derived ejection times (by extrapolating the fits) are shown as shaded regions in the corresponding color of the component. The dashed black lines mark the peak time of the prominent outburst in the light curve at 14.5 GHz, while the dotted black lines mark minor outbursts.

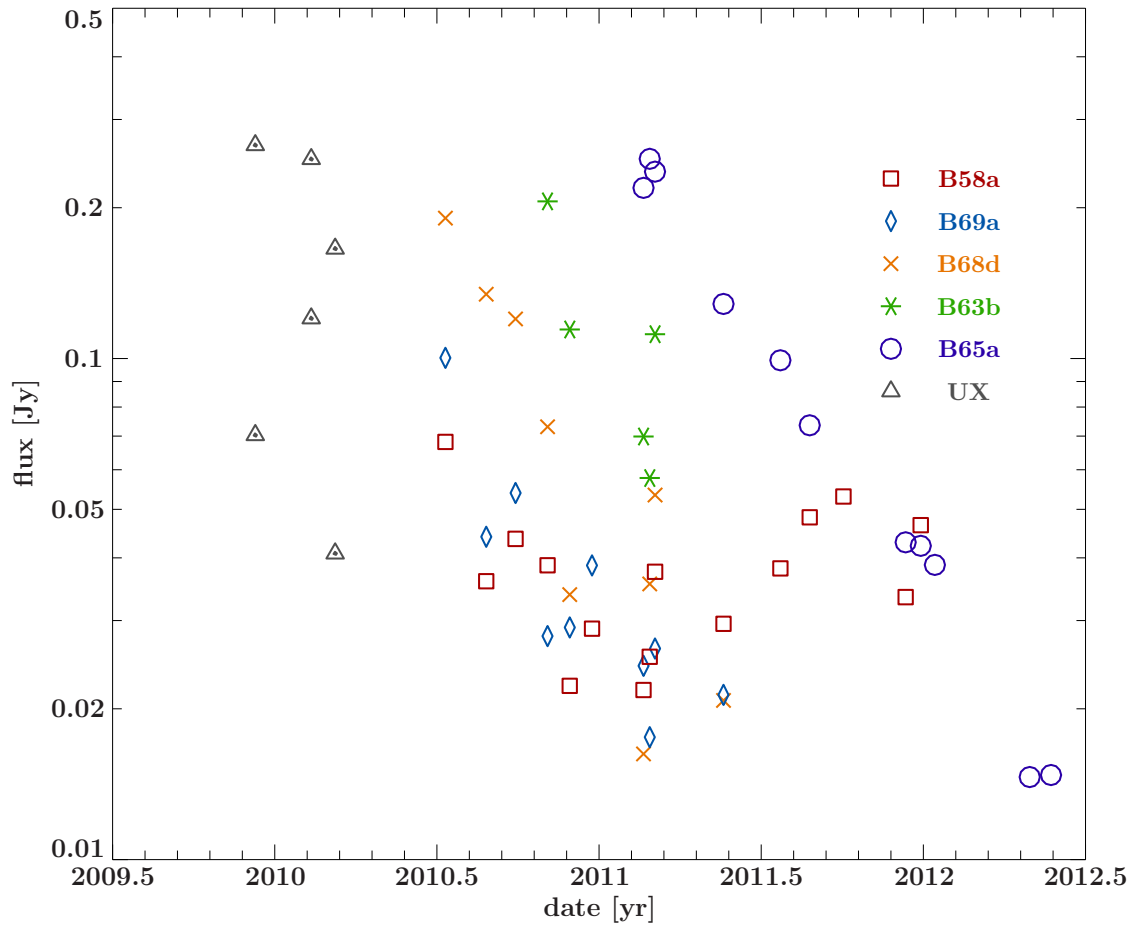


Figure 4.36: The flux density evolution for the different ballistic components associated with outburst 2009a is displayed in same color and symbols as in Fig. 4.35. The colored dots show associated components but these were not considered in the determination of characteristics.

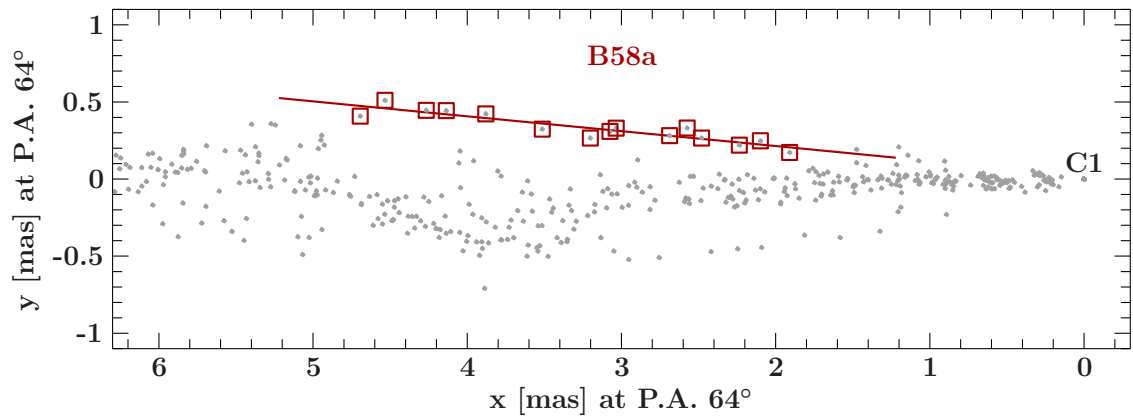


Figure 4.37: The projected positions of component B58a with a P.A. of 64° are shown in color, with a linear regression fit applied. The positions of all model components are depicted in gray.

4.5 Summary & Outlook

We find the ejection of ballistic components close to the inner jet region associated to the outbursts of the radio light curve at 230 GHz. The number of ejected components for each outburst appears to be connected to the observed flux density of the outburst at 14.5 GHz – the stronger the outburst the more components emerge.

A comparison of the components of the 2008 outburst with the found ballistic components associated with outburst 2006 reveal a similar pattern in the ejection events, except for the additional component B70a in the outburst 2008a. In the order of their appearance in the data set a fast component is observed first, followed by a component with a higher P.A. but lower vector speed, and finally a component with an even lower vector speed at an even higher P.A. angle. After a short time delay new, but weak, components are ejected at a lower P.A. but with increasing apparent motions. This can be a sign for jet precession and will be investigated in future works with the analysis of the inner jet region.

The ejected ballistic components can typically be traced for 1 to 2 years before we find a change in their direction or observe new components. These components resemble the trailing features observed by [Kadler et al. \(2008\)](#) although appearing at different distances to the core and will be explored in more details in upcoming works. [Kadler et al. \(2008\)](#) did not observe the curved trajectories, typically at a distance of 3 mas to 5 mas from the core, although a change in the flux density was noted for that region. The reason being that the sampling rate was not high enough. Before this analysis the source was only observed once or twice a year, and if we assume an apparent motion of 1.2 mas yr^{-1} we have at most three observations of a component in this region. To clearly identify a component one would need at least 5 observations and, to even measure the curvature (acceleration), more than 10 identifications are needed (e.g., [Lister et al., 2013](#)). Our plan is investigate this accelerating behavior considering various models, e.g., the projection of a particles moving on the surface area of a cone.

In addition we identified two untypical ballistic components, appearing at an offset to the majority of components. These components inherit the highest and lowest apparent motions with the P.A. being at a low and high value in comparison to the typical components observed in 3C 111. These untypical components could resemble instabilities at the border regions of a jet interacting with the ambient medium or only be components ejected with different inclination angles to the line of sight. More work will be needed to discuss the nature of these components.

Only one ballistic component is found to maintain its linear trajectory while all others either change their P.A. or seem to disappear. This could be an indication for a component which is thought to be charged plasma, being ejected parallel to the magnetic field where the curved trajectories are due to the acceleration of charged particles in the magnetic field. We will investigate this scenario in our future works.

We will also simultaneously fit multiple data sets to test different kinematic scenarios with the new analyzing techniques of Sect. 3.3 and try to estimate the frequency core shift by using the data and models of [Schulz \(2012\)](#) at 43 GHz and 86 GHz.

5

Multi-frequency evolution study of the jet in 3C 84

5.1 Source overview

The Perseus cluster (Abell426) is one of the most famous galaxy clusters in the celestial sky and the brightest in the X-rays (e.g., [Boehringer et al., 1993](#)). At its very center one finds a giant elliptical galaxy, NGC 1275, which is classified as a Seyfert 1.5 ([Véron-Cetty & Véron, 2010](#)). The bright radio source 3C 84 at a redshift of $z = 0.018$ (e.g., [Strauss et al., 1992](#)) is associated with NGC 1275 ([Pedlar et al., 1990](#)). Studies with the X-ray satellites *ROSAT* and *Chandra* by, e.g., [Boehringer et al. \(1993\)](#) and [Fabian et al. \(2000b, 2006\)](#) revealed cavities in the hot cluster gas surrounding it, suggesting that the jet of 3C 84 played a large part in their creation.

Observations with the Very Large Array (VLA) by [Pedlar et al. \(1990\)](#) showed a bright core, emission at a P.A. 160° up to 30 arcsec away from the core, and a second emission component further down the jet at a P.A. of 235° . Zooming into the core region with VLBI (e.g., [Walker et al., 2000](#); [Asada et al., 2006](#); [Lister et al., 2013](#)) to parsec scales led to the findings of a southern jet component at a mean distance of ~ 15 mas and a weak jet component to the north considered to be the counter-jet.

The kinematics of these components was subject of many investigations (e.g. [Walker et al., 1994, 2000](#); [Asada et al., 2006](#); [Lister et al., 2009b, 2013](#)). The most recent kinematic analysis at 15.4 GHz with more than 10 years of data by [Lister et al. \(2013\)](#) revealed an apparent motion of $\sim 0.25 \text{ mas yr}^{-1}$ for the southern component and approximately half of that for the northern lobe.

[Strong & Bignami \(1983\)](#) reported on the detection of γ -rays at a position coinciding with NGC 1275 between 1975 and 1979 with the *COS B* instrument. The lack of any positional uncertainties for *COS B* data makes the unique identification of the gamma-rays' production site with the source impossible. In the 1990's no evidence for the emission of γ -rays in NGC 1275 was found with *EGRET* ([Reimer et al., 2003](#)) although the sensitivity was

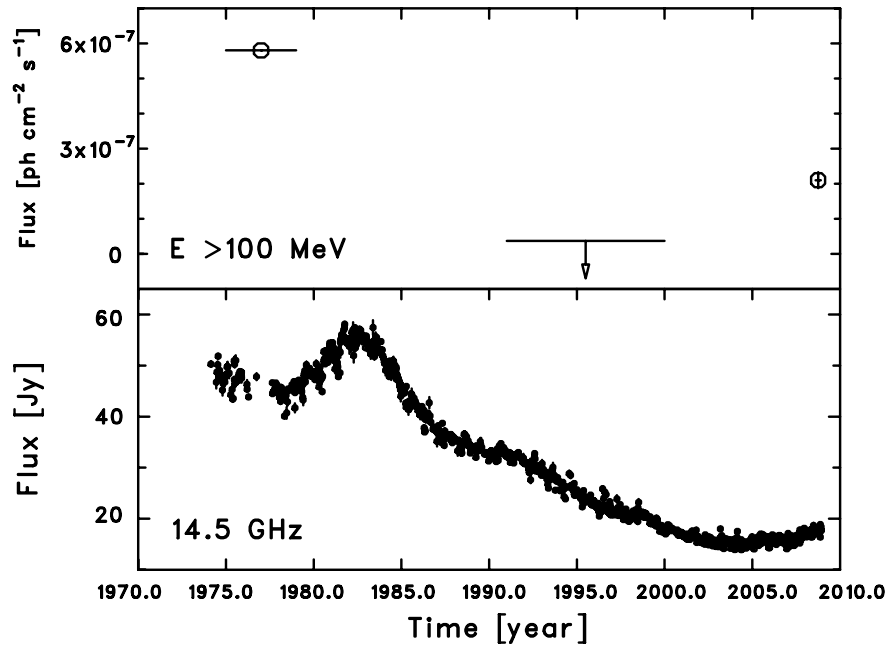


Figure 5.1: *top:* γ -ray lightcurve from historical data above 100 MeV. *bottom:* daily binned lightcurve at 14.5 GHz obtained by UMRAO. (Credit: [Abdo et al., 2009](#))

a factor higher than with *COS B*. Starting at the beginning of the observations with the *Fermi*-satellite, the source was again detected in the γ -rays at energies >100 MeV with a flux 7 times higher than the upper limit derived by *EGRET* ([Abdo et al., 2009](#)). The long term radio lightcurve at 14.5 GHz obtained by UMRAO shows similar trends to those of the observed gamma-ray flux (see Fig. 5.1 [Abdo et al., 2009](#)). After the observations with *COS B*, the radio flux density was at its highest reaching the maximum in the early 1980's with more than 60 Jy. This was followed by a continuous drop of the flux density over the next two decades, coinciding with the non-detection by *EGRET*. The radio lightcurve has been in an rising phase since the beginning of the *Fermi* observations. [Abdo et al. \(2009\)](#) also reported on a core brightening (see Fig. 5.3) in the radio at sub-parsec scales (data obtained within the MOJAVE program) during their time of observation with *Fermi* which might be related to the detection of 3C 84 in the γ -rays.

This is of special interest since 3C 84 is among the few radio galaxies detected in the γ -rays ([Abdo et al., 2010b](#)) while most extragalactic γ -ray sources are typically of the blazar type (e.g., [Hartman et al., 1999](#)). Amongst the γ -ray detected radio galaxies, no time variability was observed except for NGC 1275 ([Kataoka et al., 2010](#)).

These findings triggered a series of papers by e.g., [Nagai et al. \(2010, 2012, 2013\)](#) and [Suzuki et al. \(2012\)](#), studying the recurrent radio activity and their connection to the γ -rays. Based on VLBI measurements with VERA and the VLBA at various frequencies they reported on the restarting of the jet activity by the appearance of a new component C3 within the central parsec region of 3C 84 where ejection time coincides with the increasing flux density in the radio lightcurves. The innermost region of the jet with its

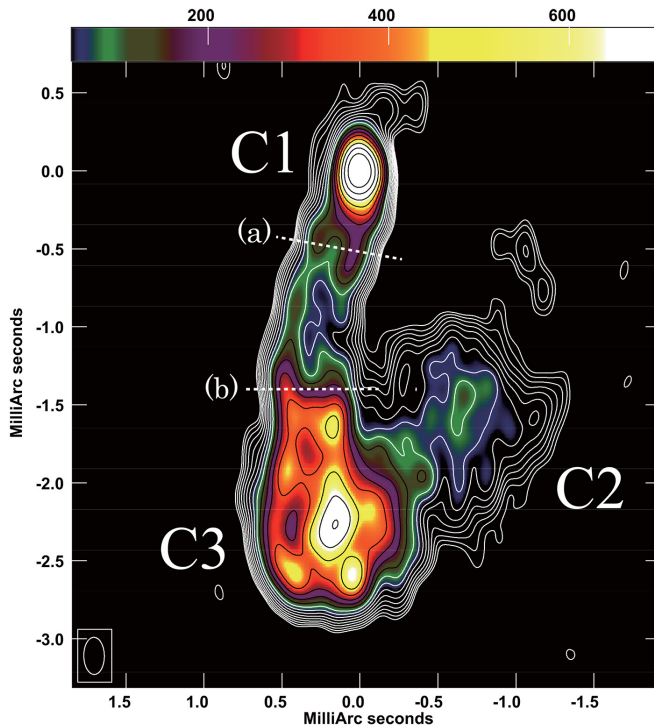


Figure 5.2: A 43 GHz full intensity image of 3C 84 by Nagai et al. (2014) showing the limb brightened structure. The different regions for C1, C2, and C3 are indicated. The range from $100 \text{ mJy beam}^{-1}$ to $700 \text{ mJy beam}^{-1}$ is color coded.

three main regions C1 (core), C2, and C3 as shown in Nagai et al. (2014) is depicted in Fig. 5.2). Note that this image is of a higher resolution than the ones used in previous studies by Nagai et al. (2010, 2012) and Suzuki et al. (2012) and the regions C1, C2 and C3 were represented as single components in their analysis.

Using VERA observations at 22 GHz between 2007 and 2009 Nagai et al. (2010) found an apparent motion of 0.23 mas yr^{-1} for component C3. In contrast Suzuki et al. (2012) found that C3 was accelerating with $0.07 \pm 0.01 \text{ mas yr}^{-2}$ based on snap shot observations with the VLBA at 43 GHz between 2002 and 2009. The vector speed of C3 was initially $0.09 \pm 0.04 \text{ mas yr}^{-1}$ and $0.41 \pm 0.07 \text{ mas yr}^{-1}$ in 2009 (Suzuki et al., 2012). The component C3 was ejected at a P.A. of $\sim 160^\circ$ with the motion mainly in the north-south direction and slightly to the east-west.

Nagai et al. (2012) and Suzuki et al. (2012) found that Metsahovi radio lightcurve at 37 GHz (Terasranta et al., 1998) was constant until to 2005 when the flux density started to increase. A rapid change of the flux density was observed after 2008 to 2009 and coincided with an increasing flux density of C1 and C3 at 22 GHz and 43 GHz (Nagai et al., 2010; Suzuki et al., 2012). The lightcurve showed a similar behavior afterwards with the flux density only moderately increasing from 2009 to 2011.5 before it changed to rapidly increasing again. In their analysis of the MOJAVE data set at 15.4 GHz Nagai et al. (2012)

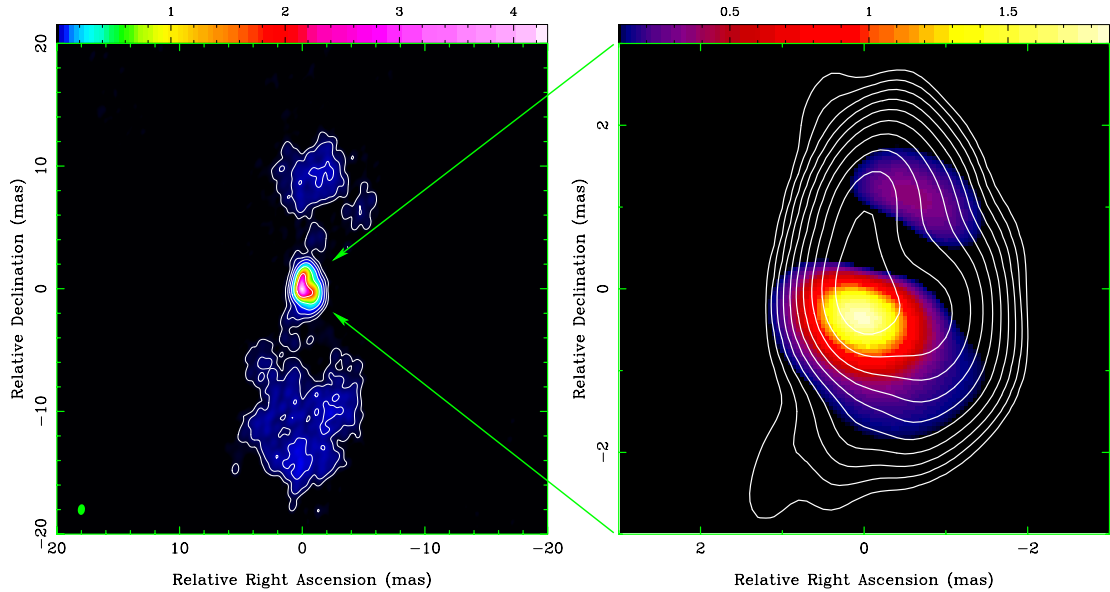


Figure 5.3: The naturally weighted VLBI image of 3C 84 at 15.4 GHz including contours (*left*) and a zoom to the inner region (*right*) as displayed in [Abdo et al. \(2009\)](#). The colors in the figure to the *right* shows the difference between two images separated by 1 year.

found that only component C3 continued to become brighter while the core component (C1) and the stationary feature (C2) remained constant at ~ 5 Jy.

No connection of the γ -ray flare in 2010 ([Brown & Adams, 2011](#)) with the time variability in the Metsahovi radio lightcurve at 37 GHz could be established when taking into account the found timescale of the γ -ray variability ([Nagai et al., 2012](#)).

Based upon one observation with the VLBA at 43 GHz [Nagai et al. \(2013, 2014\)](#) noted that the “restarted” jet, associated with the radio outburst in 2005, showed evidence of a limb-brightened structure (see Fig. 5.2).

5.2 Data & Fit

I analyzed multiple VLBI data sets of 3C 84 at different frequencies. The first calibrated data set was obtained by the MOJAVE project ([Lister et al., 2009a](#)) and contained observations from 2006 to 2013 at 15.4 GHz. The second set of data was obtained and calibrated by the Boston University blazar monitoring program ([Jorstad et al., 2005](#)) and included observations at 43 GHz starting from November 2010 to early 2013. These two data sets were used in addition to six simultaneous observations at 24 GHz and 43 GHz which we acquired during 2010.5 and early 2011. Initial total intensity data calibration for our data sets were performed in the standard manner using the Astronomical Image Processing System (AIPS) ([Greisen, 2003](#)). The DIFMAP software package ([Shepherd, 1997](#)) was

used in order to image, self calibrate, and model the (u, v) -data. The data were exclusively fit with circular Gaussian components. Additional steps of self-calibration (phase only) were applied during the model fit process.

5.3 Morphology

The morphology of 3C 84 is very complex and sometimes more than 30 model components were needed to describe the data. We divided the jet into the spatial regions C1, C2, and C3 resembling the components modeled in e.g. Nagai et al. (2012); Suzuki et al. (2012). We found two symmetric streams of model components connecting region C1 to C3 at 43 GHz (see Fig. 5.4). Similar streams are indicated in some models at 24 GHz (see Fig. 5.5) but not for all. At 15 GHz we found no evidence for the existence of these streams (see Fig. 5.6).

We also found model components to the north and east of C1 at all frequencies. These model components were not needed in all observations but were predominantly found in the ones with good (u, v) -coverage.

Based on Figure 5.4 which shows the contours and model components for two epochs at 43 GHz with the core centered at 0/0 in the (x, y) -plane it already becomes apparent that the jet structure is expanding into the southern direction. This is also observed in the images and models at 15 GHz.

A full kinematic study of all model components in the complex region C3 is beyond the scope of this work. Therefore we only derive and estimate on the apparent motion of the region C3 by first calculating the flux weighted mean position of all components given by

$$x = \sum_{i=1}^N \frac{f_i x_i}{F} \quad (5.1)$$

with x_i denoting the position of each model component in C3, f_i their flux density, N the total number of components in C3 and F the total flux density of all model components in region C3. This position is depicted in Fig. 5.7 for all analyzed epochs at 15 GHz and 43 GHz. We found a P.A. of $\sim 187^\circ$ of the flux weighted mean positions in both data sets. We restricted our data at 15.4 GHz to only contain data after 2010 for this analysis since a clear identification of components is impossible before that time with the fixed zones C1, C2, and C3.

In a second step we applied a linear regression fit to the distance evolution of this flux weighted mean position and the core component (see Fig. 5.8). We found a vector speed of 0.24 mas yr^{-1} at 15.4 GHz and 43 GHz which is less than the derived apparent motion by Suzuki et al. (2012). The same vector speed can be derived for 24 GHz although only six epochs are available and therefore the result is very susceptible to errors.

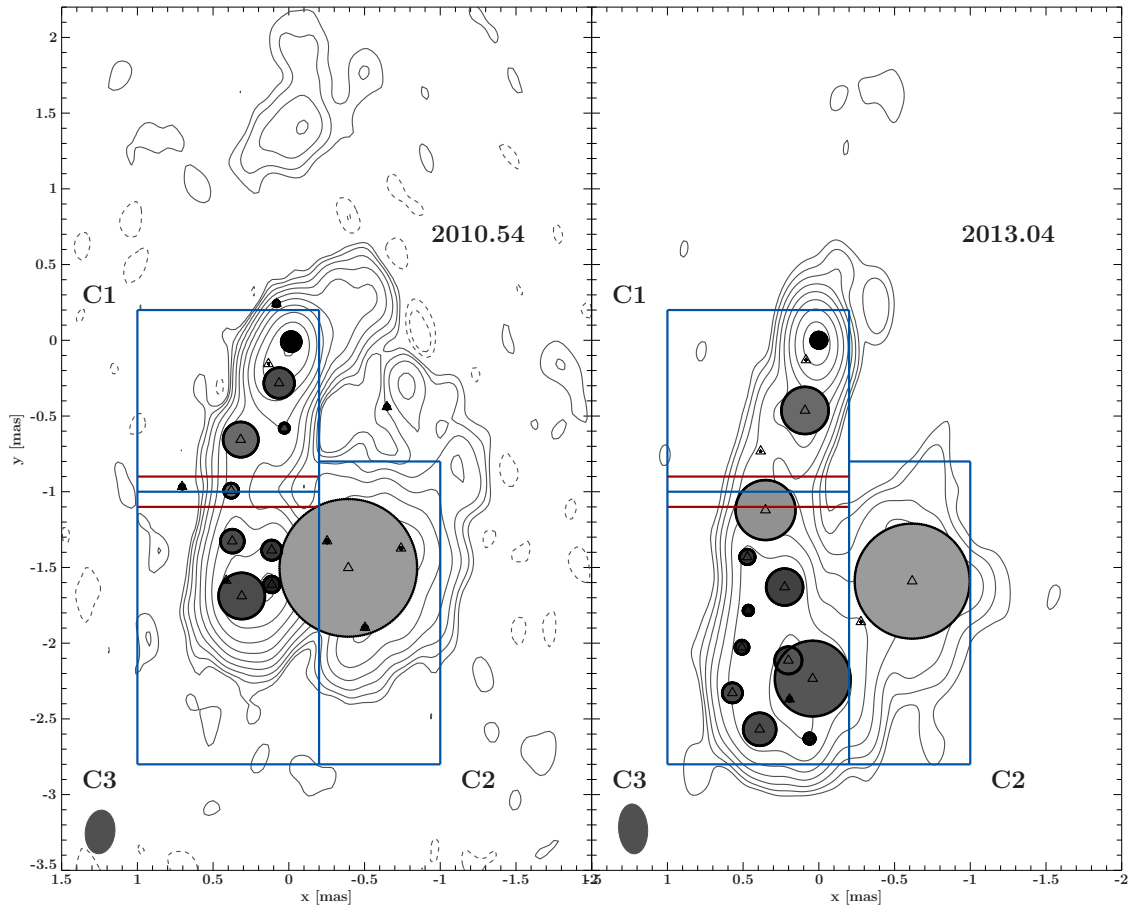


Figure 5.4: Contours of selected clean images for 3C 84 at 43 GHz starting at a 3σ background level and natural weighting. Position and size of the circular model components for each observation are overlaid and color coded according to their respective brightness temperature (white: $T_B < 10^8$ K and black $T_B > 10^{11}$ K). The regions C1, C2, and C3 are overlaid in blue and a zone with red border lines marks the transition region between C1 and C3.

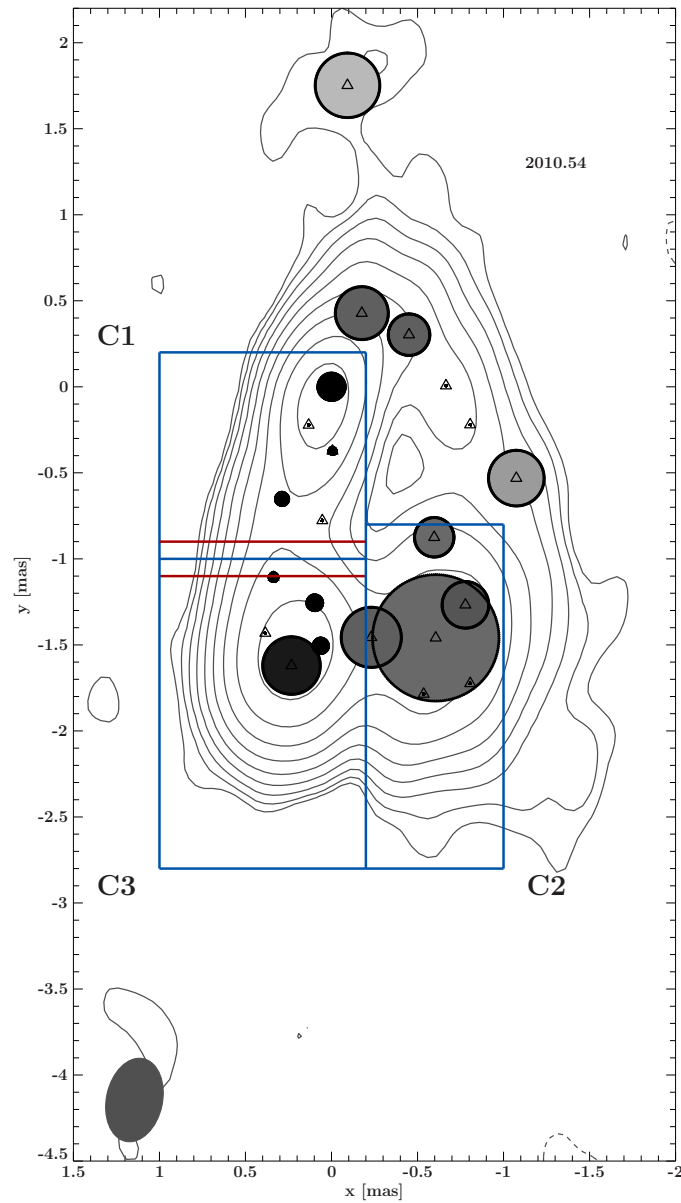


Figure 5.5: Contours of a clean image for 3C 84 at 24 GHz starting at a 3σ background level and natural weighting. Position and size of the circular model components for each observation are overlaid and color coded according to their respective brightness temperature (white: $T_B < 10^8$ K and black $T_B > 10^{11}$ K). The regions C1, C2, and C3 are overlaid in blue and a zone with red border lines marks the transition region between C1 and C3.

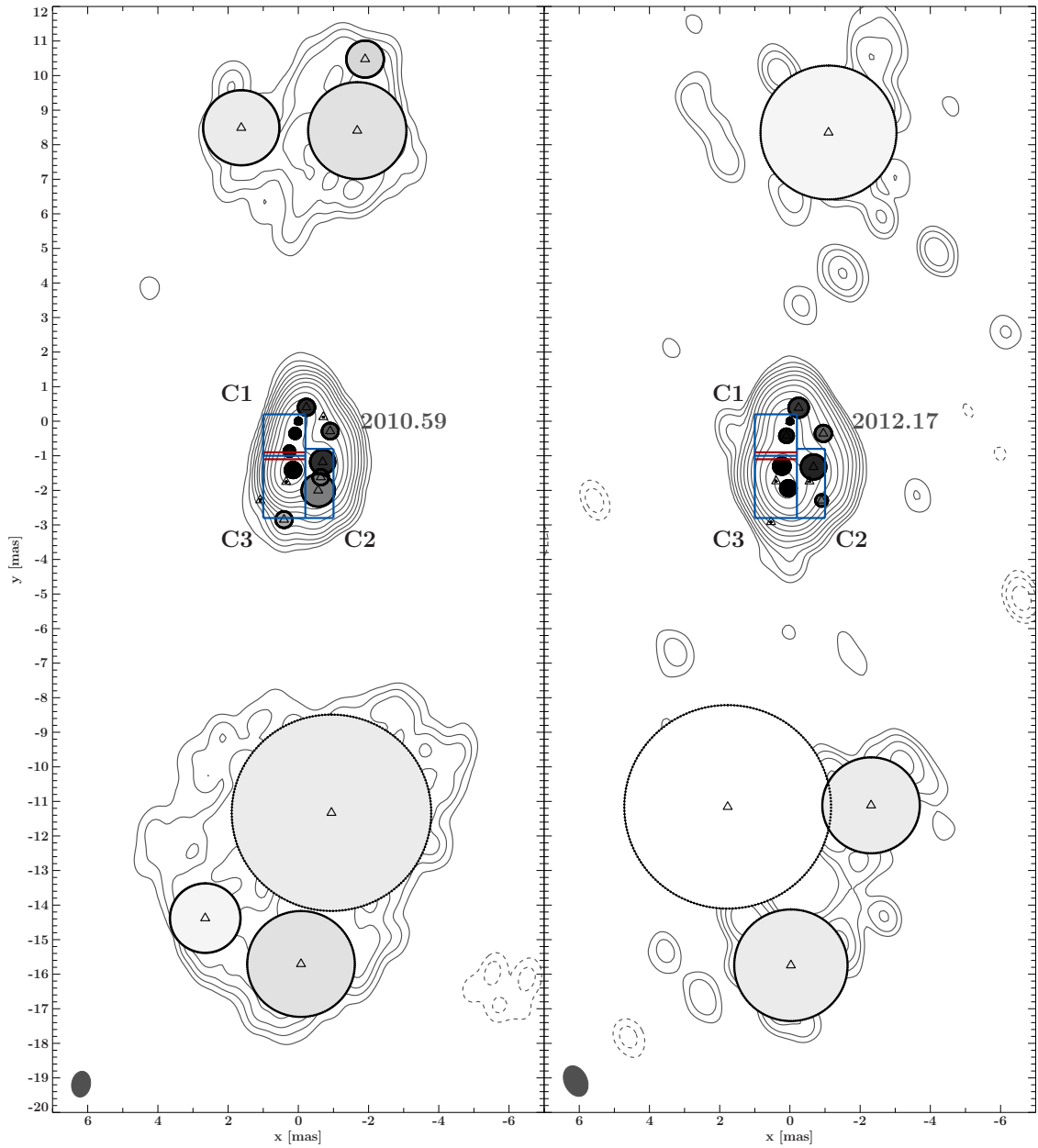


Figure 5.6: Contours of selected clean images for 3C 84 at 15 GHz starting at a 3σ background level and natural weighting. Position and size of the circular model components for each observation are overlaid and color coded according to their respective brightness temperature (white: $T_B < 10^8$ K and black $T_B > 10^{11}$ K). The regions C1, C2, and C3 are overlaid in blue and a zone with red border lines marks the transition region between C1 and C3.

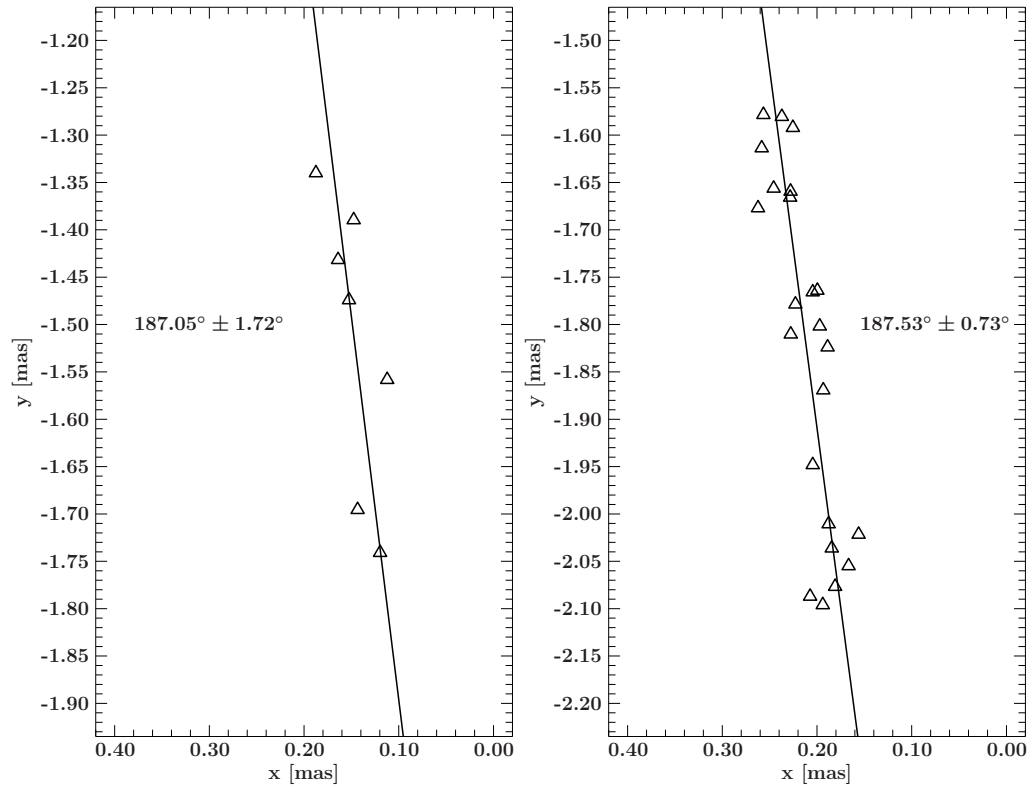


Figure 5.7: Flux weighted mean position of all components in zone C3 at 15.4 GHz (*left*) and 43 GHz (*right*). A two dimensional linear regression fit was applied to derive the position angle as displayed in the images including the uncertainties.

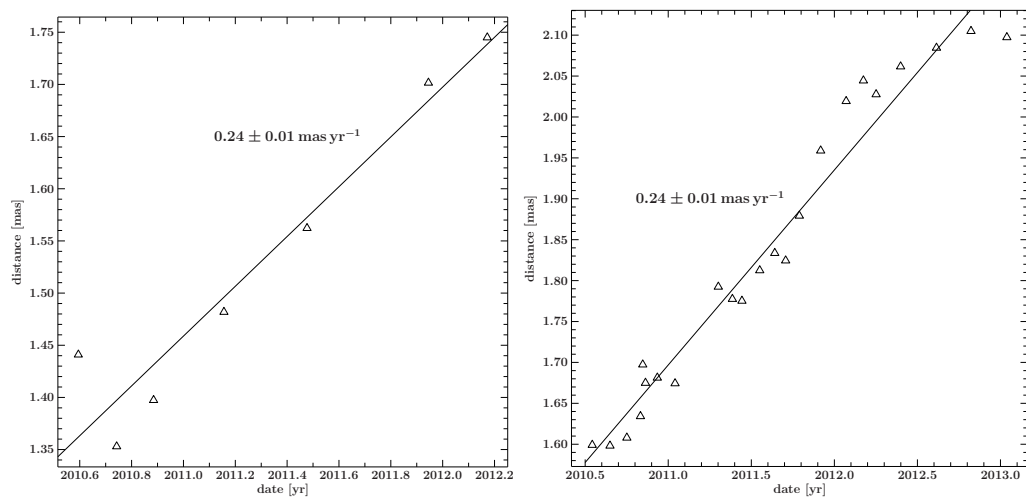


Figure 5.8: Distance of the flux weighted mean position of all components in zone C3 to the core component as a function of time at 15.4 GHz (*left*) and 43 GHz (*right*). A linear regression fit was applied to estimate the mean apparent motion of the region C3, which is $0.24 \pm 0.01 \text{ mas yr}^{-1}$ at both frequencies.

5.4 Light curves

The puzzle of the γ -ray activity in 3C 84 is still not solved. Therefore we investigated the γ -ray light curve obtained by the *Fermi* satellite above 100 MeV (priv. comm. Michael Dutka). The light curve was adaptively binned with an algorithm developed by [Lott et al. \(2012\)](#) and is shown in Fig. 5.9. The size of the bins are set in an iterative way to have a constant relative flux uncertainty and thus time intervals with significant flux become tightly sampled. This has some similarities to the method of Bayesian-Blocks by [Scargle \(1998\)](#), which adapts the time binning of a light curve to have bins of constant flux.

The outburst noted by [Brown & Adams \(2011\)](#) is clearly visible and started ~ 2010.5 and is marked in red. In addition we find an increasing γ -ray activity starting in 2010 which lasts approximately 1 year and is shown as the gray shaded region in Fig. 5.9.

We derived a radio light curve for each defined zone (C1, C2, and C3) and observing frequency by using the sum of the flux density of all model components contained in these zones. To account for the fact that we arbitrarily defined these zones but do not know exactly the exact separation between C1 and C3, we defined a transition zone. The transition zone is centered on the border of C1 to C3 and extends 0.1 mas into both zones. Any component located in this zone is used as a measure of the uncertainty of the light curve in these zones and is displayed as error bars in Fig. 5.10 and 5.11.

The light curves at 15.4 GHz are depicted in Fig. 5.10. We find that the flux density of region C2 is constant at ~ 5 Jy for all observations. Before 2010.5 a clear distinction between components in C1 and C3 appears to be impossible based on the flux density of components observed in the transition zone. We note an overall increase in flux density for the sum of both regions until early to mid 2011 which is followed by a rapid increase. In the light curve after 2010.5 the core region C1 appears to be constant at the same flux density level as C2. C3 is the only region to depict a flux density growth which was even stronger after early 2011. This suggests that the observed flux density increase for the sum of C1 and C3 before 2010.5 was only due to the model components forming the region C3 at later epochs. Therefore a light curve based on moving zones, taking the mean apparent motion of zone C3 into account, would be more appropriate to investigate that time range and will be investigated in future works.

At 24 GHz and 43 GHz (see Fig. 5.11) the region C2 is again at a constant flux density level of respectively ~ 2 Jy and ~ 3 Jy for all observations. Region C1 was also found to be constant, except for some smaller variability. This minor variability might be a calibration issue, since component C2 is usually observed at a constant flux density but undergoes smaller changes at times coinciding with a strong variability of C1, which is even more prominent in C3. The region C3 appeared to be constant with the indication of a slightly increasing flux density before 2011. In early 2011 the flux density evolution of C3 changes from constant to a steady increase, doubling its flux density of 5 Jy to 10 Jy in only a half a year. A strong variability of the flux density is observed for C3 (and C1) after 2012 which might be due to the previously mentioned calibration issue.

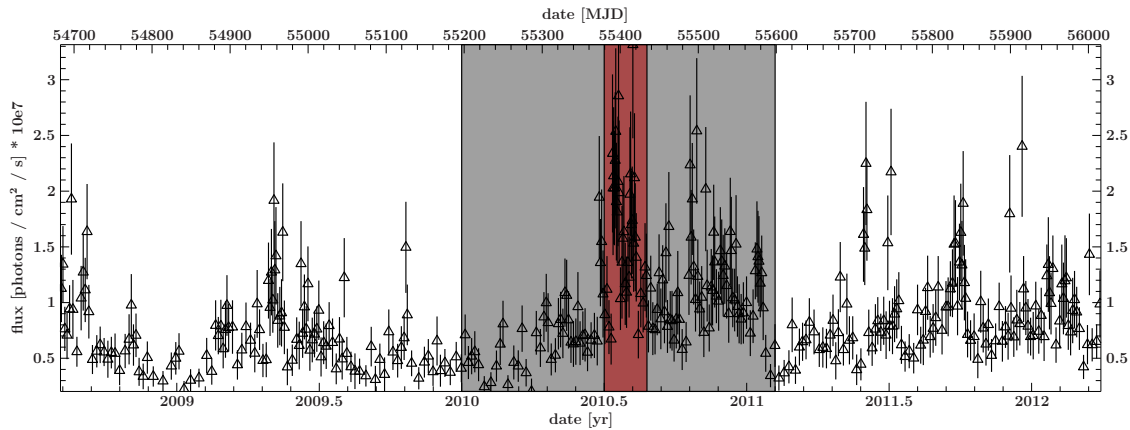


Figure 5.9: Adaptive binned *Fermi* light curve of 3C 84 above 100 MeV. The gray shaded area marks the time range of an overall rise in the flux level while the red box marks a time range of an outburst.

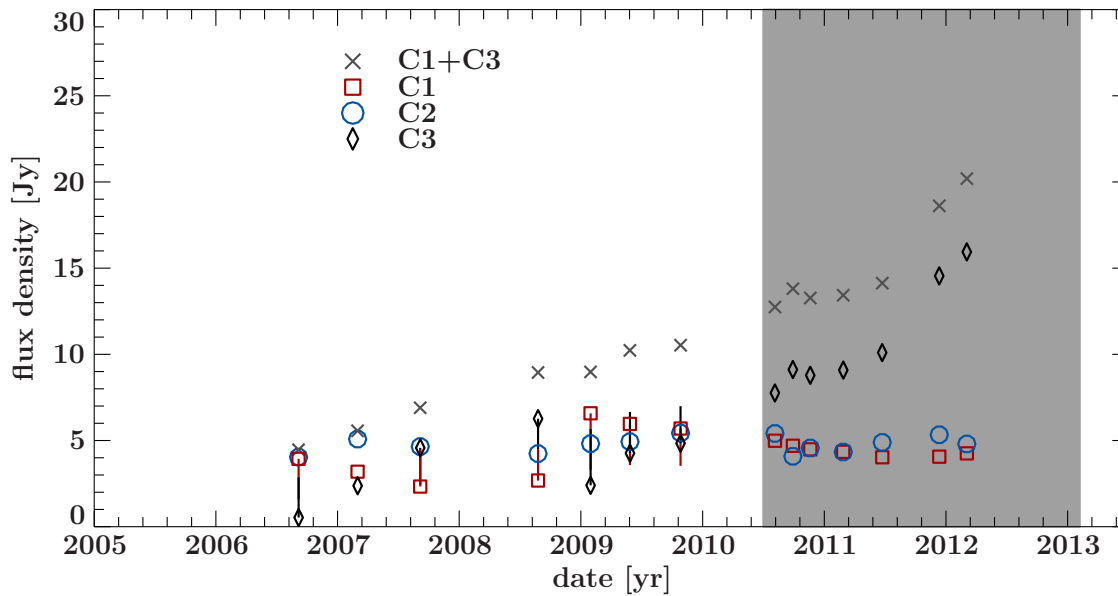


Figure 5.10: Light curve of the zones C1, C2, and C3 at 15.4 GHz. The flux density was derived by summing the flux density of all model components in each region. The uncertainties are based on the transition region marked, represented by the red lines in Fig. 5.6. The gray shaded area marks the same time range for which we obtained a light curve at 43 GHz.

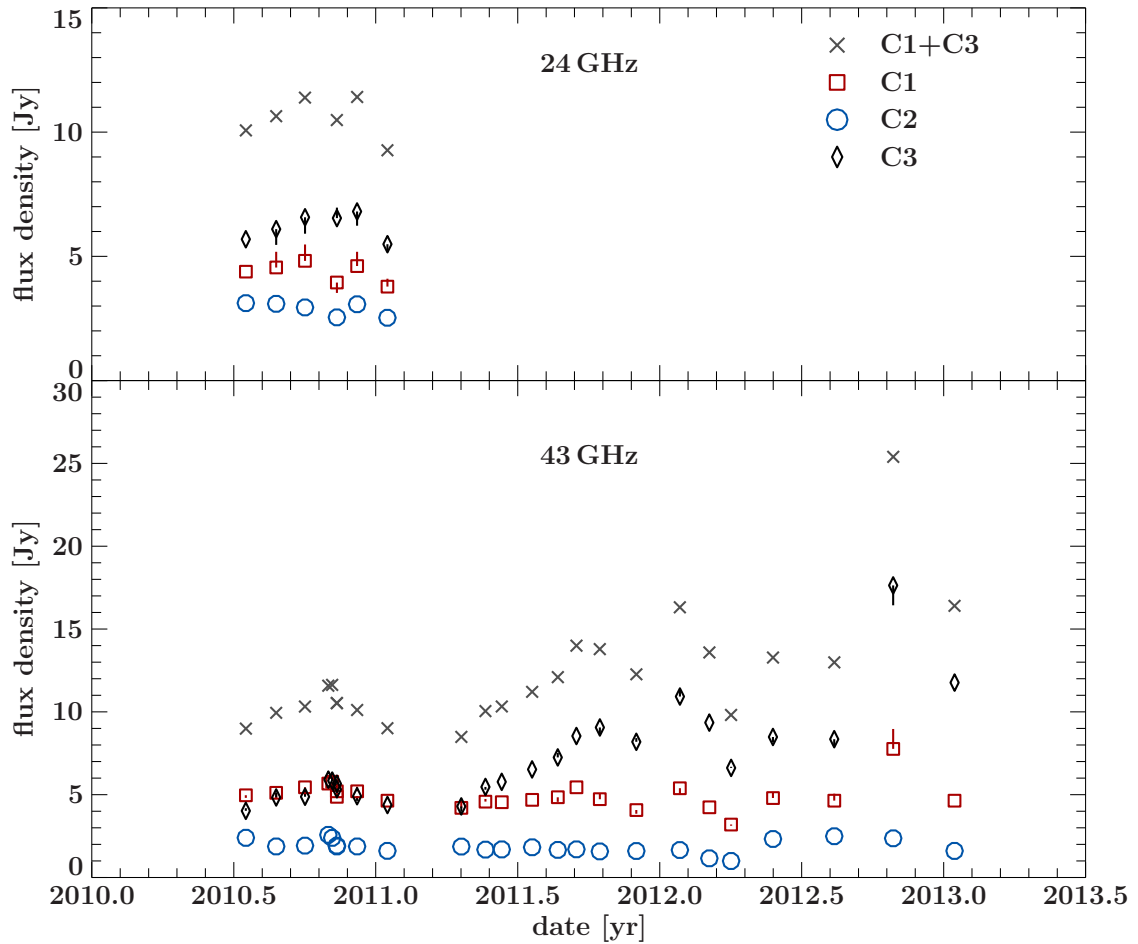


Figure 5.11: Light curve of the zones C1, C2, and C3 at 24 GHz and 43 GHz. The flux density was derived by summing the flux density of all model components in each region. The uncertainties are based on the transition region marked, represented by the red lines in Fig. 5.5 and 5.4.

5.5 Discussion

In the analysis of multiple 24 GHz and 43 GHz data sets we detected streams of model component which were not apparent at 15.4 GHz. This led to the conclusion that we have resolved the jet in the transverse direction at higher frequencies and agrees well with the observed limb-brightened structure by Nagai et al. (2013) and Nagai et al. (2014).

We find that the apparent motion of C3 between 2010.5 and 2013 to be $\sim 0.24 \text{ mas yr}^{-1}$ which is less than the expected vector speed of $\sim 0.5 \text{ mas yr}^{-1}$, based on the acceleration found in the data set between 2002 and 2009 by Suzuki et al. (2012). This result could be an indication that the region of C3 is decelerating, which is supported by a possible change in the distance evolution in Fig. 5.8 after 2012 at 43 GHz. The direction of the apparent motion of C3 is in agreement with the one shown Suzuki et al. (2012)

Interestingly Nagai et al. (2010) noted an apparent motion close to the ones we found which would indicate a ballistic motion that cannot be ruled out from the data shown in Suzuki et al. (2012). Moreover this vector speed is also similar to the one given in Lister et al. (2013) for the southern component at a distance $\sim 15 \text{ mas}$. This gives rise to the idea that this southern region was created by a similar mechanism to the ones which led to the ejection of C3.

No evidence for a bright and fast radio component ejected close to the core which could account for the increasing flux density of C3 after 2011.25 was found. The reason being that region C1 was observed at a constant flux density level at all frequencies and if a strong emission component was ejected close to the core we must see a variability of the flux density in region C1, given the time coverage of our data set. The fact that the core region C1 shows a constant flux density at all frequencies is very unusual since the core is found to be variable especially for sources considered to be gamma bright (e.g. Kovalev et al., 2005, 2009). This constant flux density of C1 is agreement with the analysis of the MOJAVE data by Suzuki et al. (2012). Our results also suggest that C1 stopped getting brighter between 2009 and 2010.5 at 43 GHz when taking into account the works by Nagai et al. (2012).

The constant moderate increasing flux density of C3 is in agreement with the analysis by Nagai et al. (2012), which also found first indications of a change to rapidly increasing after 2011.5.

If we assume that the increase in flux density of C3 in early 2011 to 2012 was triggered by the γ -ray outburst in mid 2010.5 we can estimate the location of the γ -ray production side by backextrapolating the flux weighted mean position of the emission region C3 to that time. The position of C3 was at a distance of $\sim 1.8 \text{ mas}$ away from the core in 2011.25 at 43 GHz and using the derived mean vector speed of 0.24 mas yr^{-1} the location of the production side would have been $\sim 1.6 \text{ mas}$ away from the core. If the increased radio emission in C3 was due to the overall increase in γ -ray activity starting in 2010, then the production side would only be a little bit closer to the core but still more than 1 mas away from it.

Based on the summed flux density of region C3 at different frequencies one could derive the spectral index of the region during the time of increasing flux density. The spectral

index is defined as

$$\alpha = \frac{\log(S_i) - \log(S_j)}{\log(f_i) - \log(f_j)} \quad (5.2)$$

with i and j denoting the different frequencies. The sparse sampling rate of observations at 15.4 GHz and the need for an investigation of the calibration at 43 GHz after 2012 prevents a detailed study of it. Based on five out of the six obtained simultaneous observations at 24 GHz and 43 GHz the spectral index of C3 is determined prior to the onset of the flux density increase. We excluded one observation at 24 GHz since the position of C3 had a large offset in comparison to the majority of positions which was still evident when apparent motion of that component was taken into account. In future works we will re-calibrate and model that particular observation.

As shown by, e.g. [Kovalev et al. \(2008b\)](#), the frequency dependent core-shift can be measured by aligning the model component position for an optically thin feature, assuming frequency independent peak position. We found a mean spectral index of $\alpha \simeq -0.48 \pm 0.09$ which is considered to be optically thin. Therefore, comparing the flux weighted mean position of C3 at both frequencies allows us to derive an estimate on the mean frequency core shift, which is found to be 0.06 ± 0.03 mas. The results are consistent with the ones of [Suzuki et al. \(2012\)](#) who reported a spectral index of -0.86 ± 0.30 for the C3 component measured between the frequencies of 43 GHz and 22 GHz and a core shift of the order 0.1 mas.

We also derived the spectral index of C3 for two observations at 15 GHz with observations at 24 GHz and 43 GHz which were separated by 10 days or less from the ones at 15 GHz. Unfortunately we could only use one observation at 24 GHz due to the reasons mentioned above. The spectral index of the C3 region between 43 GHz and 15 GHz was found to be -0.48 and -0.6 with a core shift of 0.26 mas in both cases. A spectral index of -0.74 was derived for C3 between 24 GHz and 15 GHz with a core shift of 0.22 mas. In general we note a shift of the core position to the north with a slight shift to the west with increasing frequency values.

- Abdo A.A., Ackermann M., Ajello M., et al., 2009, *ApJ* 699, 31
- Abdo A.A., Ackermann M., Ajello M., et al., 2010a, *ApJ* 720, 912
- Abdo A.A., Ackermann M., Ajello M., et al., 2010b, *ApJ* 720, 912
- Agudo I., Gómez J.L., Martí J.M., et al., 2001, *ApJ* 549, L183
- Alef W., Preuss E., Kellermann K.I., Gabuzda D., 1998, In: Zensus J.A., Taylor G.B., Wrobel J.M. (eds.) *IAU Colloq. 164: Radio Emission from Galactic and Extragalactic Compact Sources*, ASP Conf. Ser. 144, 129
- Alfvén H., Herlofson N., 1950, *Phys. Rev.* 78, 616
- Aller H.D., Aller M.F., Latimer G.E., Hodge P.E., 1985, *ApJS* 59, 513
- Angelakis E., Fuhrmann L., Nestoras I., et al., 2012, *Journal of Physics Conf. Ser.* 372, 012007
- Antonucci R.R.J., 1984, *ApJ* 278, 499
- Antonucci R.R.J., Miller J.S., 1985, *ApJ* 297, 621
- Asada K., Kamenon S., Shen Z.Q., et al., 2006, *PASJ* 58, 261
- Baade W., Minkowski R., 1954, *ApJ* 119, 206
- Ballo L., Braito V., Reeves J.N., et al., 2011, *MNRAS* 418, 2367
- Bardeen J.M., Press W.H., Teukolsky S.A., 1972, *ApJ* 178, 347
- Beckmann V., Shrader C.R., 2012, *Active Galactic Nuclei*, Wiley-VCH Verlag GmbH & Co. KG
- Bennett A.S., 1962, *Mem. RAS* 68, 163
- Bevington P.R., Robinson D.K., 1992, *Data reduction and error analysis for the physical sciences*, McGraw-Hill, New York
- Blandford R.D., Königl A., 1979, *ApJ* 232, 34
- Blandford R.D., McKee C.F., Rees M.J., 1977, *Nat* 267, 211
- Blandford R.D., Payne D.G., 1982, *MNRAS* 199, 883
- Blandford R.D., Znajek R.L., 1977, *MNRAS* 179, 433
- Bloom S.D., Marscher A.P., Gear W.K., et al., 1994, *AJ* 108, 398
- Boehringer H., Voges W., Fabian A.C., et al., 1993, *MNRAS* 264, L25
- Boettcher M., Harris D.E., Krawczynski H., 2012, *Relativistic Jets from Active Galactic Nuclei*, Wiley, Berlin
- Bridle A.H., Perley R.A., 1984, *Annual Review of Astronomy and Astrophysics* 22, 319
- Brown A.M., Adams J., 2011, *MNRAS* 413, 2785
- Burbidge E.M., 1970, *ApJ* 160, L33
- Burrows D.N., Hill J.E., Nousek J.A., et al., 2005, *Space Sci. Rev.* 120, 165
- Chatterjee R., Marscher A.P., Jorstad S.G., et al., 2011, *ApJ* 734, 43
- Clark B.G., 1999, In: Taylor G.B., Carilli C.L., Perley R.A. (eds.) *Synthesis Imaging in Radio Astronomy II*, ASP Conf. Ser. 180, 1
- Cohen M.H., Cannon W., Purcell G.H., et al., 1971, *ApJ* 170, 207
- Cohen M.H., Jauncey D.L., Kellermann K.I., Clark B.G., 1968, *Science* 162, 88
- Cohen R.D., 1983, *ApJ* 273, 489
- Cornwell T., Fomalont E.B., 1999, In: Taylor G.B., Carilli C.L., Perley R.A. (eds.) *Synthesis Imaging in Radio Astronomy II*, ASP Conf. Ser. 180, 187
- Cornwell T.J., Wilkinson P.N., 1981, *MNRAS* 196, 1067
- Curtis H.D., 1918, *Publications of Lick Observatory* 13, 9
- Dame T.M., Hartmann D., Thaddeus P., 2001, *ApJ* 547, 792
- Dauser T., Wilms J., Reynolds C.S., Brenneman L.W., 2010, *MNRAS* 409, 1534
- Dent W.A., 1965, *Science* 148, 1458
- Di Matteo T., Springel V., Hernquist L., 2005, *Nat* 433, 604
- Diamond P.J., 1995, In: Zensus J.A., Diamond P.J., Napier P.J. (eds.) *Very Long Baseline Interferometry and the VLBA*, ASP Conf. Ser. 82, 227
- Dove J.B., Wilms J., Maisack M., Begelman M.C., 1997, *ApJ* 487, 759
- Edge D.O., Shakeshaft J.R., McAdam W.B., et al., 1959, *Mem. of the RAS* 68, 37
- Elitzur M., 2007, In: Ho L.C., Wang J.W. (eds.) *The Central Engine of Active Galactic Nuclei*,

- ASP Conf. Ser. 373, 415
- Eracleous M., Halpern J.P., 2004, *ApJS* 150, 181
- Fabian A.C., 2012, *ARA&A* 50, 455
- Fabian A.C., Iwasawa K., Reynolds C.S., Young A.J., 2000a, *PASP* 112, 1145
- Fabian A.C., Sanders J.S., Etori S., et al., 2000b, *MNRAS* 318, L65
- Fabian A.C., Sanders J.S., Taylor G.B., et al., 2006, *MNRAS* 366, 417
- Fanaroff B.L., Riley J.M., 1974, *MNRAS* 167, 31P
- Fanidakis N., Baugh C.M., Benson A.J., et al., 2011, *MNRAS* 410, 53
- Fasano G., Vio R., 1988, *Bulletin d'Information du Centre de Donnees Stellaires* 35, 191
- Fath E.A., 1909, Ph.D. thesis, University of California, Berkeley.
- Ferrarese L., Merritt D., 2000, *ApJ* 539, L9
- Ferrarese L., Pogge R.W., Peterson B.M., et al., 2001, *ApJ* 555, L79
- Fomalont E.B., 1999, In: Taylor G.B., Carilli C.L., Perley R.A. (eds.) *Synthesis Imaging in Radio Astronomy II*, ASP Conf. Ser. 180, p. 301
- Fossati G., Maraschi L., Celotti A., et al., 1998, *MNRAS* 299, 433
- Freyberg M.J., Budau B., Burkert W., et al., 2008, In: Turner M.J.L., Flanagan K.A. (eds.) *Space Telescopes and Instrumentation 2008: Ultraviolet to Gamma Ray*, Proc. SPIE 7011, 701117
- Friedrich P., 2013, Status of the Mirror System, Consortium Presentation, Garching, https://wiki.mpe.mpg.de/eRosita/erosita_consortium_meeting_oct2013?action=AttachFile&do=get&target=eROSITA_MM_status_14OCT2013.pdf
- Gaskell C.M., 2009, *New Astron. Rev.* 53, 140
- Gebhardt K., Bender R., Bower G., et al., 2000, *ApJ* 539, L13
- Ghisellini G., Haardt F., Matt G., 1994, *MNRAS* 267, 743
- Ghisellini G., Tavecchio F., 2008, *MNRAS* 387, 1669
- Giacconi R., Bechtold J., Branduardi G., et al., 1979, *ApJ* 234, L1
- Giacconi R., Gursky H., Paolini F.R., Rossi B.B., 1962, *Physical Review Letters* 9, 439
- Giacconi R., Murray S., Gursky H., et al., 1972, *ApJ* 178, 281
- Gierlinski M., Zdziarski A.A., Done C., et al., 1997, *MNRAS* 288, 958
- Giommi P., Padovani P., Polenta G., et al., 2012a, *MNRAS* 420, 2899
- Giommi P., Polenta G., Lähteenmäki A., et al., 2012b, *A&A* 541, A160
- Golombek D., Miley G.K., Neugebauer G., 1988, *AJ* 95, 26
- Götz M.M.A., Alef W., Preuss E., Kellermann K.I., 1987, *A&A* 176, 171
- Greisen E.W., 1990, In: Longo G., Sedmak G. (eds.) *Acquisition, Processing and Archiving of Astronomical Images*, 125
- Greisen E.W., 1998, In: Albrecht R., Hook R.N., Bushouse H.A. (eds.) *Astronomical Data Analysis Software and Systems VII*, ASP Conf. Ser. 145, 204
- Greisen E.W., 2003, *Information Handling in Astronomy - Historical Vistas* 285, 109
- Gu Q., Huang J., 2002, *ApJ* 579, 205
- Gurwell M.A., Peck A.B., Hostler S.R., et al., 2007, In: Baker A.J., Glenn J., Harris A.I., Mangum J.G., Yun M.S. (eds.) *From Z-Machines to ALMA: (Sub)Millimeter Spectroscopy of Galaxies*, ASP Conf. Ser. 375, 234
- Haardt F., Maraschi L., 1993, *ApJ* 413, 507
- Hanke M., 2011, Ph.D. thesis, Friedrich-Alexander University, Erlangen
- Harrison F.A., Craig W.W., Christensen F.E., et al., 2013, *ApJ* 770, 103
- Hartman R.C., Bertsch D.L., Bloom S.D., et al., 1999, *ApJS* 123, 79
- Hartman R.C., Kadler M., Tueller J., 2008, *ApJ* 688, 852
- Hasinger G., Miyaji T., Schmidt M., 2005, *A&A* 441, 417
- Hazard C., Mackey M.B., Shimmins A.J., 1963, *Nat* 197, 1037
- Healey S.E., Romani R.W., Taylor G.B., et al., 2007, *ApJS* 171, 61
- Heckman T.M., 1980, *A&A* 87, 152

- Hirabayashi H., Hirosawa H., Kobayashi H., et al., 2000, PASJ 52, 955
- Hogan B.S., Lister M.L., Kharb P., et al., 2011, ApJ 730, 92
- Högbom J.A., 1974, A&AS 15, 417
- Homan D.C., Ojha R., Wardle J.F.C., et al., 2001, ApJ 549, 840
- Homan D.C., Ojha R., Wardle J.F.C., et al., 2002, ApJ 568, 99
- Houck J.C., Davis J.E., Huenemoerder D., et al., 2013, ISIS: Interactive Spectral Interpretation System, Astrophysics Source Code Library
- Hubble E., 1929, Proceedings of the National Academy of Science 15, 168
- Hughes P.A., Aller H.D., Aller M.F., 1991, ApJ 374, 57
- Jansen F., Lumb D., Altieri B., et al., 2001, A&A 365, L1
- Jansky K.G., 1933, Nat 132, 66
- Jorstad S.G., Marscher A.P., Lister M.L., et al., 2005, AJ 130, 1418
- Kadler M., 2002, Diplomarbeit, Rheinischen Friedrich-Wilhelms-University, Bonn
- Kadler M., Ros E., Perucho M., et al., 2008, ApJ 680, 867
- Kadler M., Wilms J., 2010, Active Galactic Nuclei, University Lecture
- Kardashev N.S., Khartov V.V., Abramov V.V., et al., 2013, Astronomy Reports 57, 153
- Kataoka J., Stawarz Ł., Cheung C.C., et al., 2010, ApJ 715, 554
- Kellermann K.I., 2013, Bulletin of the Astronomical Society of India 41, 1
- Kellermann K.I., Moran J.M., 2001, ARA&A 39, 457
- Kellermann K.I., Sramek R., Schmidt M., et al., 1989, AJ 98, 1195
- Konigl A., 1981, ApJ 243, 700
- Kovalev Y.Y., Aller H.D., Aller M.F., et al., 2009, ApJ 696, L17
- Kovalev Y.Y., Kellermann K.I., Lister M.L., et al., 2005, AJ 130, 2473
- Kovalev Y.Y., Lobanov A.P., Pushkarev A.B., Zensus J.A., 2008a, A&A 483, 759
- Kovalev Y.Y., Lobanov A.P., Pushkarev A.B., Zensus J.A., 2008b, Journal of Physics Conf. Ser. 131, 012058
- Kraemer S.B., Crenshaw D.M., 2000, ApJ 544, 763
- Krichbaum T.P., Bach U., Graham D.A., et al., 2008, In: The role of VLBI in the Golden Age for Radio Astronomy, Proc. of Science
- Krolik J.H., 1999, Active galactic nuclei : from the central black hole to the galactic environment, Princeton University Press, Princeton New Jersey
- Laing R.A., 1981, MNRAS 195, 261
- Linfield R., 1981, ApJ 244, 436
- Linfield R., Perley R., 1984, ApJ 279, 60
- Lister M., 2003, Bull. AAS 35, 1246
- Lister M.L., Aller H.D., Aller M.F., et al., 2009a, AJ 137, 3718
- Lister M.L., Aller M.F., Aller H.D., et al., 2013, AJ 146, 120
- Lister M.L., Cohen M.H., Homan D.C., et al., 2009b, AJ 138, 1874
- Lister M.L., Homan D.C., 2005, AJ 130, 1389
- Lobanov A.P., 1996, Ph.D. thesis, New Mexico Institute of Mining Technology, Socorro
- Lott B., Escande L., Larsson S., Ballet J., 2012, A&A 544, A6
- Lovell J., 2000, In: Hirabayashi H., Edwards P.G., Murphy D.W. (eds.) Astrophysical Phenomena Revealed by Space VLBI, ISAS, Tokyo, 301
- Malzac J., Jourdain E., 2000, A&A 359, 843
- Marchesini D., Celotti A., Ferrarese L., 2004, MNRAS 351, 733
- Marscher A.P., 2010, Jets in Active Galactic Nuclei. In: Belloni T. (ed.) The Jet Paradigm Lecture Notes in Physics 794, 173 Springer, Berlin
- Marscher A.P., Gear W.K., 1985, ApJ 298, 114
- Marscher A.P., Jorstad S.G., Gómez J.L., et al., 2002, Nat 417, 625
- Marshall F.E., Mushotzky R.F., Boldt E.A., et al., 1978, Nat 275, 624
- Massardi M., Bonaldi A., Negrello M., et al., 2010, MNRAS 404, 532
- Meidinger N., 2013, eROSITA detectors,

- Consortium Presentation, Garching, https://wiki.mpe.mpg.de/eRosita/erosita_consortium_meeting_oct2013?action=AttachFile&do=get&target=eROSITA_consortium_Meidinger_final.pdf
- Meidinger N., Andritschke R., Elbs J., et al., 2011, In: Tsakalakos L. (ed.) UV, X-Ray, and Gamma-Ray Space Instrumentation for Astronomy XVII, Proc. SPIE 8145, 814502
- Meier D.L., 2003, *New Astronomy* 47, 667
- Meier D.L., 2009, In: Hagiwara Y., Fomalont E., Tsuboi M., Yasuhiro M. (eds.) Approaching Micro-Arcsecond Resolution with VSOP-2: Astrophysics and Technologies, ASP Conf. Ser. 402, 342
- Merloni A., Heinz S., 2008, *MNRAS* 388, 1011
- Merloni A., Heinz S., 2013, Evolution of Active Galactic Nuclei. In: Oswalt T., Keel W. (eds.) Planets, Stars and Stellar Systems Springer Netherlands, Dordrecht, p.503
- Merloni A., Predehl P., Becker W., et al., 2012, ArXiv e-prints
- Meyer E.T., Fossati G., Georganopoulos M., Lister M.L., 2011, *ApJ* 740, 98
- Mitsuda K., Bautz M., Inoue H., et al., 2007, *PASJ* 59, 1
- Nagai H., Haga T., Giovannini G., et al., 2014, arXiv:1402.5930
- Nagai H., Orienti M., Kino M., et al., 2013, In: Gómez J.L. (ed.) The Innermost Regions of Relativistic Jets and Their Magnetic Fields, EPJ Web of Conferences 61, 04008
- Nagai H., Orienti M., Kino M., et al., 2012, *MNRAS* 423, L122
- Nagai H., Suzuki K., Asada K., et al., 2010, *PASJ* 62, L11
- Napier P.J., Bagri D.S., Clark B.G., et al., 1994, *IEEE Proceedings* 82, 658
- Nolan P.L., Abdo A.A., Ackermann M., et al., 2012, *ApJS* 199, 31
- Osterbrock D.E., Ferland G.J., 2006, *Astrophysics of gaseous nebulae and active galactic nuclei*, University Science Books, Sausalito, CA
- Osterbrock D.E., Koski A.T., 1976, *MNRAS* 176, 61P
- Padovani P., 2007, *Ap&SS* 309, 63
- Pavlinsky M., Akimov V., Levin V., et al., 2011, In: O'Dell S.L., Pareschi G. (eds.) Optics for EUV, X-Ray, and Gamma-Ray Astronomy V, Proc. SPIE 8147, 814706
- Pavlinsky M., Akimov V., Levin V., et al., 2012, In: Takahashi T., Murray S.S., den Herder J.A. (eds.) Space Telescopes and Instrumentation 2012: Ultraviolet to Gamma Ray Proc. SPIE 8443, 84431T
- Pavlinsky M., Arefiev V., Churazov E., et al., 2007, In: O'Dell S.L., Pareschi G. (eds.) Optics for EUV, X-Ray, and Gamma-Ray Astronomy III, Proc. SPIE 6688, 66880L
- Pavlinsky M., Hasinger G., Parmar A., et al., 2006, In: Turner M.J.L., Hasinger G. (eds.) Space Telescopes and Instrumentation II: Ultraviolet to Gamma Ray, Proc. SPIE 6266, 62660O
- Pavlinsky M., Sunyaev R., Churazov E., et al., 2008, In: Turner M.J.L., Flanagan K.A. (eds.) Space Telescopes and Instrumentation 2008: Ultraviolet to Gamma Ray, Proc. SPIE 7011, 70110H
- Pavlinsky M., Sunyaev R., Churazov E., et al., 2009, In: O'Dell S.L., Pareschi G. (eds.) Optics for EUV, X-Ray, and Gamma-Ray Astronomy IV, Proc. SPIE 7437, 743708
- Pearson T.J., 1999, In: Taylor G.B., Carilli C.L., Perley R.A. (eds.) Synthesis Imaging in Radio Astronomy II, ASP Conf. Ser. 180, 335
- Pedlar A., Ghataure H.S., Davies R.D., et al., 1990, *MNRAS* 246, 477
- Pence W.D., 1992, *Bull. AAS* 24, 750
- Pence W.D., Chiappetti L., Page C.G., et al., 2010, *A&A* 524, A42
- Perley R.A., Chandler C.J., Butler B.J., Wrobel J.M., 2011, *ApJ* 739, L1
- Perucho M., 2014, *International Journal of Modern Physics Conf. Ser.* 28, 60165
- Perucho M., Agudo I., Gómez J.L., et al., 2008, *A&A* 489, L29
- Peterson B.M., 1997, *An Introduction to Active Galactic Nuclei*, New York Cambridge University Press, Cambridge
- Peterson B.M., 2006, In: Gaskell C.M., McHardy I.M., Peterson B.M., Sergeev S.G. (eds.) AGN Variability from X-Rays to Radio

- Waves, ASP Conf. Ser. 360, 191
- Piner B.G., Mahmud M., Fey A.L., Gospodinova K., 2007, *AJ* 133, 2357
- Predehl P., 1999, In: Siegmund O.H., Flanagan K.A. (eds.) *EUV, X-Ray, and Gamma-Ray Instrumentation for Astronomy X*, Proc. SPIE 3765, 172
- Predehl P., 2012, In: Takahashi T., Murray S.S., den Herder J.A. (eds.) *Space Telescopes and Instrumentation 2012: Ultraviolet to Gamma Ray*, Proc. SPIE 8443, 84431R
- Predehl P., 2013, eROSITA Status, Presentation, Garching, https://wiki.mpe.mpg.de/eRosita/TalksPresentations?action=AttachFile&do=get&target=Predehl_SRG-eROSITA_Status+Juni_2013.pptx
- Predehl P., Andritschke R., Becker W., et al., 2011, In: Siegmund O.H. (ed.) *UV, X-Ray, and Gamma-Ray Space Instrumentation for Astronomy XVII*, Proc. SPIE 8145, 81450D
- Predehl P., Andritschke R., Böhringer H., et al., 2010, In: Arnaud M., Murray S.S., Takahashi T. (eds.) *Space Telescopes and Instrumentation 2010: Ultraviolet to Gamma Ray* Proc. SPIE 7732, 77320U
- Predehl P., Andritschke R., Bornemann W., et al., 2007, In: Siegmund O.H.W. (ed.) *UV, X-Ray, and Gamma-Ray Space Instrumentation for Astronomy XV*, Proc. SPIE 6686, 668617, Bellingham, WA
- Predehl P., eROSITA Team 2013, *Mem. Societa Astronomica Italiana* 84, 770
- Predehl P., Hasinger G., Böhringer H., et al., 2006, In: Turner M.J.L., Hasinger G. (eds.) *Space Telescopes and Instrumentation II: Ultraviolet to Gamma Ray*, Proc. SPIE 6266, 62660P
- Preuss E., Alef W., Kellermann K.I., 1988, In: Reid M.J., Moran J.M. (eds.) *The Impact of VLBI on Astrophysics and Geophysics*, IAU Symposium 129, 105
- Pringle J.E., 1981, *ARA&A* 19, 137
- Pudritz R.E., Hardcastle M.J., Gabuzda D.C., 2012, *Space Sci. Rev.* 169, 27
- Purcell G.H., 1973, Ph.D. thesis, California Institute of Technology
- Reimer O., Pohl M., Sreekumar P., Mattox J.R., 2003, *ApJ* 588, 155
- Rybicki G.B., Lightman A.P., 1979, *Radiative processes in astrophysics*, Wiley-Interscience, New York
- Ryle M., Hewish A., 1960, *MNRAS* 120, 220
- Ryle M., Neville A.C., 1962, *MNRAS* 125, 39
- Salpeter E.E., 1964, *ApJ* 140, 796
- Sanders D.B., Soifer B.T., Elias J.H., et al., 1988, *ApJ* 325, 74
- Sargent W.L.W., 1977, *ApJ* 212, L105
- Sarma Kuchibhotla H., Lister M., MOJAVE Collaboration 2010, *Bull. AAS* 36, 602
- Scargle J.D., 1998, *ApJ* 504, 405
- Schinzel F., 2011, Ph.D. thesis, Universität zu Köln
- Schmid C., 2012, Ph.D. thesis, Friedrich-Alexander University, Erlangen
- Schmidt M., 1963, *Nat* 197, 1040
- Schmidt M., Green R.F., 1983, *ApJ* 269, 352
- Schmidt M., Matthews T.A., 1964, *ApJ* 139, 781
- Schmitt J.L., 1968, *Nat* 218, 663
- Schulz R., 2012, Master's thesis, University of Würzburg, Germany
- Schulz R., Kadler M., Ros E., et al., 2013, *ArXiv e-prints*
- Scott P.F., Ryle M., Hewish A., 1961, *MNRAS* 122, 95
- Seyfert C.K., 1943, *ApJ* 97, 28
- Sguera V., Bassani L., Malizia A., et al., 2005, *A&A* 430, 107
- Shakura N.I., Sunyaev R.A., 1973, *A&A* 24, 337
- Shepherd M.C., 1997, In: Hunt G., Payne H. (eds.) *Astronomical Data Analysis Software and Systems VI*, ASP Conf. Ser. 125, 77
- Shields G.A., 1999 111, 661
- Sholomitskii G.B., 1965, *Soviet Ast.* 9, 516
- Sikora M., Begelman M.C., Rees M.J., 1994, *ApJ* 421, 153
- Skrutskie M.F., Cutri R.M., Stiening R., et al., 2006, *AJ* 131, 1163
- Soldi S., Türler M., Paltani S., et al., 2008, *A&A* 486, 411
- Springel V., Di Matteo T., Hernquist L., 2005, *MNRAS* 361, 776

- Stoche J.T., Morris S.L., Gioia I.M., et al., 1991, *ApJS* 76, 813
- Strauss M.A., Huchra J.P., Davis M., et al., 1992, *ApJS* 83, 29
- Strong A.W., Bignami G.F., 1983, *ApJ* 274, 549
- Suzuki K., Nagai H., Kino M., et al., 2012, *ApJ* 746, 140
- Swanenburg B.N., Hermsen W., Bennett K., et al., 1978, *Nat* 275, 298
- Swenson, Jr. G.W., 1969, *ARA&A* 7, 353
- Taylor G.B., Carilli C.L., Perley R.A., 1999, *ASP Conf. Ser.* 180
- Tchekhovskoy A., McKinney J.C., Narayan R., 2012, *Journal of Physics Conf. Ser.* 372, 012040
- Teraesranta H., Tornikoski M., Mujunen A., et al., 1998, *A&AS* 132, 305
- Thompson A.R., 1999, In: Taylor G.B., Carilli C.L., Perley R.A. (eds.) *Synthesis Imaging in Radio Astronomy II*, *ASP Conf. Ser.* 180, 11
- Trippe S., Krips M., Piétu V., et al., 2011, *A&A* 533, A97
- Trümper J., 1982, *Advances in Space Research* 2, 241
- Trümper J., 1992, *Q. J. R. Astron. Soc.* 33, 165
- Turner T.J., Miller L., 2009, *Astron. Astrophys. Rev.* 17, 47
- Ueda Y., Akiyama M., Ohta K., Miyaji T., 2003, *ApJ* 598, 886
- Ungerer V., Mauron N., Brillet J., Rieu N.Q., 1985, In: Serra G. (ed.) *Nearby Molecular Clouds*, *Lecture Notes in Physics* 237, 68, Springer, Berlin
- Urry C.M., Padovani P., 1995, *PASP* 107, 803
- Venturi T., 2010, In: *10th European VLBI Network Symposium and EVN Users Meeting: VLBI and the New Generation of Radio Arrays*, *Proc. of Science*
- Véron-Cetty M.P., Véron P., 2010, *A&A* 518, A10
- Walker R.C., Dhawan V., Romney J.D., et al., 2000, *ApJ* 530, 233
- Walker R.C., Romney J.D., Benson J.M., 1994, *ApJ* 430, L45
- Weisskopf M.C., Brinkman B., Canizares C., et al., 2002, *PASP* 114, 1
- Whitney A.R., Shapiro I.I., Rogers A.E.E., et al., 1971, *Science* 173, 225
- Wille M., 2011, Master's thesis, Friedrich-Alexander University, Erlangen
- Wills D., Wills B.J., 1976, *ApJS* 31, 143
- Wilms J., Kreykenbohm I., Schmid C., 2009, *Near Real Time Data Analysis Software Design*, eRO-RSB-DD-63-01_2
- Winkler C., Courvoisier T.J.L., Di Cocco G., et al., 2003, *A&A* 411, L1
- Winkler H., 1992, *MNRAS* 257, 677
- Wolter H., 1952, *Annalen der Physik* 445, 94
- Woltjer L., 1959, *ApJ* 130, 38
- Woo J.H., Treu T., Barth A.J., et al., 2010, *ApJ* 716, 269
- Wootten A., Thompson A.R., 2009, *IEEE Proc.* 97, 1463
- Zel'dovich Y.B., Novikov I.D., 1964, *Soviet Physics Doklady* 9, 246

A

Tables for Chapter 3.3

A.1 Model parameters and uncertainties

Table A.1: Table of all component parameters for the different models of the observations 05 September 2005 and 23 September 2005. The positional parameters x and y are given in respect to the core position. Parameter values for which no uncertainties are given were frozen in this particular model.

model	id	date	S [Jy]	x [mas]	y [mas]	major [mas]	ratio	ϕ [deg]
1	C0	2005.68	1.236 ± 0.008	$(0.00^{+0.26}_{-0.25}) \times 10^{-3}$	$(0.0 \pm 0.5) \times 10^{-3}$	0	1	—
1	C0	2005.73	1.268 ± 0.006	$(0.0 \pm 2.1) \times 10^{-4}$	$(0 \pm 4) \times 10^{-4}$	0	1	—
2	C0	2005.68	$1.28794^{+0.00015}_{-0.00327}$	$(0.00^{+0.06}_{-0.54}) \times 10^{-3}$	$(0.0^{+0.5}_{-0.8}) \times 10^{-3}$	0.044 ± 0.006	≤ 0.27	$-60.9^{+8.3}_{-2.4}$
2	C0	2005.73	1.311 ± 0.012	$(0 \pm 5) \times 10^{-4}$	$(0.0 \pm 0.6) \times 10^{-3}$	$0.0486^{+0.0030}_{-0.0033}$	≤ 0.34	74 ± 6
3	C0	2005.68	$1.236^{+0.022}_{-0.008}$	$(0.00^{+0.26}_{-0.52}) \times 10^{-3}$	$(0.0^{+1.0}_{-0.5}) \times 10^{-3}$	$0.004^{+0.019}_{-0.004}$	1	—
3	C0	2005.73	$1.344^{+0.017}_{-0.018}$	$(0^{+5}_{-4}) \times 10^{-4}$	$(0.0^{+0.9}_{-1.0}) \times 10^{-3}$	$0.051^{+0.004}_{-0.005}$	1	—
1	C1	2005.68	0.0329 ± 0.0011	-1.08 ± 0.05	7.68 ± 0.06	$4.15^{+0.16}_{-0.15}$	$0.345^{+0.025}_{-0.022}$	-39.5 ± 1.6
1	C1	2005.73	0.0360 ± 0.0013	-1.03 ± 0.05	7.65 ± 0.07	$4.93^{+0.08}_{-0.20}$	0.36 ± 0.05	$-26.9^{+1.9}_{-2.0}$
2	C1	2005.68	$0.0328^{+0.0008}_{-0.0011}$	$-1.08^{+0.04}_{-0.05}$	$7.68^{+0.05}_{-0.06}$	$4.15^{+0.10}_{-0.15}$	$0.344^{+0.018}_{-0.022}$	$-39.5^{+1.6}_{-1.5}$
2	C1	2005.73	0.0345 ± 0.0013	-0.96 ± 0.05	$7.61^{+0.07}_{-0.06}$	$4.61^{+0.18}_{-0.16}$	0.37 ± 0.05	-29.2 ± 2.1
3	C1	2005.68	$0.0310^{+0.0015}_{-0.0014}$	-1.07 ± 0.05	$7.52^{+0.06}_{-0.05}$	2.75 ± 0.13	1	—
3	C1	2005.73	$0.0350^{+0.0015}_{-0.0013}$	-0.90 ± 0.06	7.58 ± 0.06	$3.32^{+0.13}_{-0.12}$	1	—
1	C2	2005.68	0.0133 ± 0.0005	$0.089^{+0.015}_{-0.016}$	1.613 ± 0.020	0.59 ± 0.04	1	—
1	C2	2005.73	$(0.582 \pm 0.030) \times 10^{-2}$	$0.257^{+0.020}_{-0.021}$	$1.14^{+0.05}_{-0.04}$	0	1	—
2	C2	2005.68	0.0129 ± 0.0004	0.094 ± 0.015	$1.625^{+0.018}_{-0.019}$	1.63 ± 0.04	1	—
2	C2	2005.73	0.0144 ± 0.0008	$0.111^{+0.027}_{-0.026}$	1.23 ± 0.05	1.24 ± 0.10	1	—
3	C2	2005.68	0.0135 ± 0.0005	$0.085^{+0.015}_{-0.016}$	1.625 ± 0.020	1.63 ± 0.04	1	—
3	C2	2005.73	$0.0142^{+0.0008}_{-0.0007}$	$0.105^{+0.028}_{-0.027}$	1.33 ± 0.06	1.34 ± 0.11	1	—
1	C3	2005.68	$0.570^{+0.008}_{-0.007}$	-0.0685 ± 0.0007	0.1412 ± 0.0012	0.1569 ± 0.0023	1	—
1	C3	2005.73	0.558 ± 0.006	-0.0686 ± 0.0007	$0.1429^{+0.0011}_{-0.0010}$	0.1585 ± 0.0020	1	—
2	C3	2005.68	$0.519^{+0.014}_{-0.013}$	$-0.06750^{+0.00018}_{-0.00079}$	$0.14668^{+0.00025}_{-0.00055}$	0.1615 ± 0.0012	1	—
2	C3	2005.73	0.511 ± 0.012	-0.0721 ± 0.0012	$0.1499^{+0.0026}_{-0.0025}$	0.166 ± 0.005	1	—
3	C3	2005.68	$0.570^{+0.008}_{-0.021}$	$-0.0685^{+0.0007}_{-0.0016}$	$0.1411^{+0.0025}_{-0.0013}$	0.157 ± 0.005	1	—
3	C3	2005.73	$0.479^{+0.018}_{-0.016}$	$-0.0736^{+0.0017}_{-0.0016}$	0.149 ± 0.004	0.166 ± 0.006	1	—

A.2 Comparison of model parameter uncertainties with conservative estimates

Table A.2: Table comparing the parameter values, including their uncertainties, of components C0, C1, and C2 for two observations with a conservative estimate for the uncertainty. The uncertainty for the flux value is 5% of the maximum flux value of both observations, while the positional uncertainty is the scatter between the two positions.

component	model	parameter	05 Sep 05	23 Sep 05	cons. uncertainty
C0	1	flux	1.236 ± 0.008	1.268 ± 0.006	0.063
C0	2	flux	$1.28794^{+0.00015}_{-0.00327}$	1.311 ± 0.012	0.066
C0	3	flux	$1.236^{+0.022}_{-0.008}$	$1.344^{+0.017}_{-0.018}$	0.067
C0	1	x	$(-1.3^{+2.6}_{-2.5}) \times 10^{-4}$	$(-2.3 \pm 2.1) \times 10^{-4}$	0.000
C0	2	x	$(-2.26^{+0.06}_{-0.54}) \times 10^{-3}$	$(-0.7 \pm 0.5) \times 10^{-3}$	0.002
C0	3	x	$(-0.00^{+0.26}_{-0.52}) \times 10^{-3}$	$(0.1^{+0.5}_{-0.4}) \times 10^{-3}$	0.000
C0	1	y	$(-0 \pm 5) \times 10^{-4}$	$(0.4 \pm 0.4) \times 10^{-3}$	0.000
C0	2	y	$(2.6^{+0.5}_{-0.8}) \times 10^{-3}$	$(1.5 \pm 0.6) \times 10^{-3}$	0.001
C0	3	y	$(0.0^{+1.0}_{-0.5}) \times 10^{-3}$	$(-0.1^{+0.9}_{-1.0}) \times 10^{-3}$	0.000
C0	2	major	0.044 ± 0.006	$0.0486^{+0.0030}_{-0.0033}$	-
C0	3	major	$0.004^{+0.019}_{-0.004}$	$0.051^{+0.004}_{-0.005}$	-
C0	2	ratio	≤ 0.27	≤ 0.34	-
C0	2	phi	$-60.9^{+8.3}_{-2.4}$	74 ± 6	-
C1	1	flux	0.0329 ± 0.0011	0.0360 ± 0.0013	0.002
C1	2	flux	$0.0328^{+0.0008}_{-0.0011}$	0.0345 ± 0.0013	0.002
C1	3	flux	$0.0310^{+0.0015}_{-0.0014}$	$0.0350^{+0.0015}_{-0.0013}$	0.002
C1	1	x	-1.08 ± 0.05	-1.03 ± 0.05	0.058
C1	2	x	$-1.08^{+0.04}_{-0.05}$	-0.96 ± 0.05	0.125
C1	3	x	-1.07 ± 0.05	-0.90 ± 0.06	0.173
C1	1	y	7.68 ± 0.06	7.65 ± 0.07	0.023
C1	2	y	$7.68^{+0.05}_{-0.06}$	$7.61^{+0.07}_{-0.06}$	0.065
C1	3	y	$7.52^{+0.06}_{-0.05}$	7.58 ± 0.06	0.060
C1	1	major	$4.15^{+0.16}_{-0.15}$	$4.93^{+0.08}_{-0.20}$	-
C1	2	major	$4.15^{+0.10}_{-0.15}$	$4.61^{+0.18}_{-0.16}$	-
C1	3	major	2.75 ± 0.13	$3.32^{+0.13}_{-0.12}$	-
C1	1	ratio	$0.345^{+0.025}_{-0.022}$	0.36 ± 0.05	-
C1	2	ratio	$0.344^{+0.018}_{-0.022}$	0.37 ± 0.05	-
C1	1	phi	-39.5 ± 1.6	$-26.9^{+1.9}_{-2.0}$	-
C1	2	phi	$-39.5^{+1.6}_{-1.5}$	-29.2 ± 2.1	-

Table A.3: Table comparing the parameter values, including their uncertainties, of component C3 for two observations with a conservative estimate for the uncertainty. The uncertainty for the flux value is 5% of the maximum flux value of both observations, while the positional uncertainty is the scatter between the two positions.

component	model	parameter	05 Sep 05	23 Sep 05	cons. uncertainty
C2	1	flux	0.0133 ± 0.0005	$(0.582 \pm 0.030) \times 10^{-2}$	0.001
C2	2	flux	0.0129 ± 0.0004	0.0144 ± 0.0008	0.001
C2	3	flux	0.0135 ± 0.0005	$0.0142^{+0.0008}_{-0.0007}$	0.001
C2	1	x	$0.089^{+0.015}_{-0.016}$	$0.257^{+0.020}_{-0.021}$	0.168
C2	2	x	0.092 ± 0.015	$0.110^{+0.027}_{-0.026}$	0.018
C2	3	x	$0.085^{+0.015}_{-0.016}$	$0.105^{+0.028}_{-0.027}$	0.021
C2	1	y	1.613 ± 0.020	$1.14^{+0.05}_{-0.04}$	0.476
C2	2	y	$1.628^{+0.018}_{-0.019}$	1.23 ± 0.05	0.395
C2	3	y	1.625 ± 0.020	1.33 ± 0.06	0.290
C2	1	major	0.59 ± 0.04	$\equiv 0$	-
C2	2	major	$0.569^{+0.027}_{-0.034}$	$0.94^{+0.06}_{-0.05}$	-
C2	3	major	0.60 ± 0.04	0.98 ± 0.06	-
C3	1	flux	$0.570^{+0.008}_{-0.007}$	0.558 ± 0.006	0.029
C3	2	flux	$0.519^{+0.014}_{-0.013}$	0.511 ± 0.012	0.026
C3	3	flux	$0.570^{+0.008}_{-0.021}$	$0.479^{+0.018}_{-0.016}$	0.029
C3	1	x	-0.0687 ± 0.0007	-0.0688 ± 0.0007	0.000
C3	2	x	$-0.06976^{+0.00018}_{-0.00079}$	-0.0728 ± 0.0012	0.003
C3	3	x	$-0.0685^{+0.0007}_{-0.0016}$	$-0.0735^{+0.0017}_{-0.0016}$	0.005
C3	1	y	0.1411 ± 0.0012	$0.1434^{+0.0011}_{-0.0010}$	0.002
C3	2	y	$0.14932^{+0.00025}_{-0.00055}$	$0.1514^{+0.0026}_{-0.0025}$	0.002
C3	3	y	$0.1411^{+0.0025}_{-0.0013}$	0.149 ± 0.004	0.008
C3	1	major	$0.2144^{+0.0019}_{-0.0018}$	0.2286 ± 0.0017	-
C3	2	major	$0.2219^{+0.0032}_{-0.0027}$	0.2174 ± 0.0026	-
C3	3	major	$0.2140^{+0.0020}_{-0.0018}$	$0.2237^{+0.0021}_{-0.0022}$	-

Acknowledgements

I would like to say thank you to my supervisors Jörn Wilms and Matthias Kadler, who gave me the unique opportunity to write this thesis. They always helped and supported me as best as possible and without them this thesis would not have been possible. Thanks to them I could also attend many scientific conferences and made contact with many colleagues.

I am extremely grateful for my colleague Ingo Kreykenbohm at the Dr. Karl Remeis-Observatory, who always had to listen to my problems and gave me great advice, even though the questions were sometimes outside of his field of expertise. I thank all the former and present colleagues in Bamberg who made working there quite the joy. I would like to particularly mention Moritz Böck for his great advice, expertise in the field of jets and helping me improve my programming skills with ISIS and S-LANG. On the topic of jets I would also like to thank Cornelia Müller, Jonas Trüstedt, Eduardo Ros, Manel Perucho, Matthias Kadler, Jörn Wilms, Michael Dutka, Roopesh Ojha and especially Robert Schulz who, like me, worked on the peculiar source 3C 111.

I would also like to thank the rest of the Würzburg team led by Matthias Kadler, who always made me feel welcome.

For the help of parallel programming and error calculations I would like to thank Matthias Kühnel, Thomas Dauser and Fritz Schwarm. Many thanks to administrators, Manfred Hanke, Thomas Dauser, Fritz Schwarm, and Ingo Kreykenbohm who always fixed any computer related problems as quickly as possible and maintained the computer systems. Furthermore I would like to thank the eROSITA team in Bamberg, Christian Schmid for the simulations of eROSITA survey data, Ingo Kreykenbohm for our work on the pre-processing software package, Michael Wille for our fruitful discussions. Thanks also to the leader of the eROSITA software team Hermann Brunner from the Max-Planck-Institute in Garching.

A big thank you to my former and present office mates in Bamberg, Refiz Duro, Thorsten Brand, Victoria Grinberg, Cornelia Müller, Eugenia Litzinger, Natalie Hell, and Ivica Miškovičová, who made my time spent there unforgettable. I also like to thank Ingo Kreykenbohm, Alex Markowitz, Macarena Sagredo, Robert Schulz, and Thorsten Brand reviewing my thesis and for their helpful and constructive feedback.